Saint-Petersburg State University

20th International School-Conference

Magnetic resonance and its applications

proceedings

20

Spinus

27 March — 30 March 2023
Saint-Petersburg, Russia

20th International School-Conference

MAGNETIC RESONANCE AND ITS APPLICATIONS

Proceedings

March 27 — 30, 2023
Saint Petersburg, Russia

Schola Spinus

20th International School-Conference
MAGNETIC RESONANCE AND ITS APPLICATIONS SPINUS-2023

ORGANIZING COMMITTEE
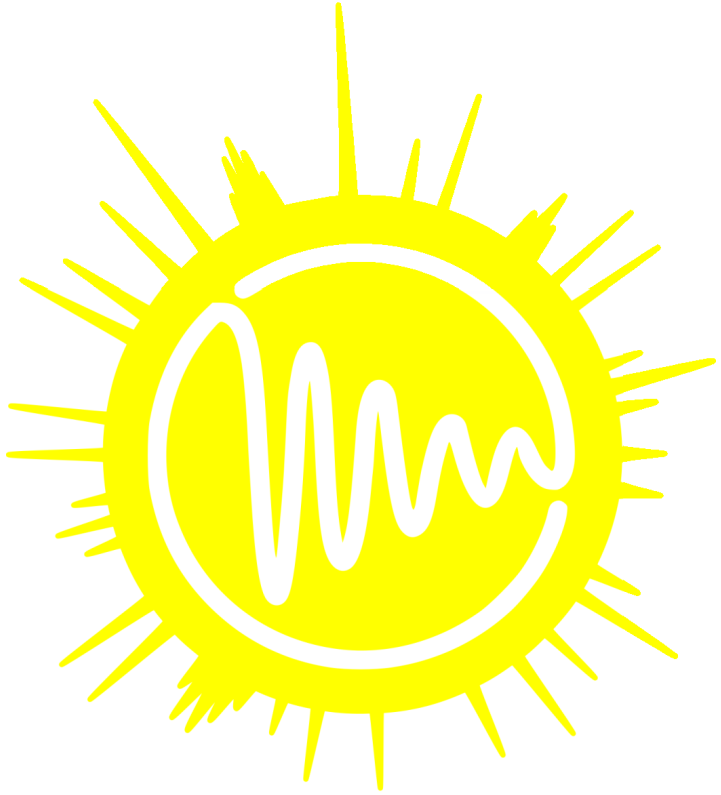
Chairman	Prof. Denis Markelov, SPSU
Vice-chairman	M. Sc. Alexandr Ievlev, researcher, SPSU
Committee members	Dr. Andrey Egorov, associate professor, SPSU Dr. Andrey Komolkin, associate professor, SPSU Prof. Marina Shelyapina, SPSU Dr. Pavel Kupriyanov, associate professor, GTU (Gebze, Turkey) Dr. Nadezhda Sheveleva, assistant, SPSU M. Sc. Timofey Popov, SPSU
Layout of Proceedings	M. Sc. Aleksandra Koroleva
Reviewer of Proceedings	Vasily T. Lebedev, Doctor of Physics and Mathematics, Head of Laboratory of Neutron Physicochemical Research, PNPI RAS

CONTACTS
1, Ulyanovskay st., Peterhof, 198504, St. Petersburg, Russia
Department of Nuclear Physics Research Methods
St. Petersburg State University

Tel.:	+7-953-350-0640
Fax.:	+7-812-428-7240
E-mail:	spinus@spinus.spb.ru
Website:	spinus.spb.ru

PROGRAM COMMITTEE

SCIENTIFIC ADVISER
OF THE SCHOOL-CONFERENCE

Vladimir Chizhik   Honored Scientist of Russian Federation
Honorary Professor of Saint Petersburg State University

ADVISORY BOARD

C. Cabal   Professor, Havana University, Cuba

V. I. Chizhik   Professor, St. Petersburg State University, Russia

S. V. Dvinskikh   Professor, Royal Institute of Technology, Stockholm, Sweden

L. Yu. Grunin   Associate Professor, CEO, Resonance Systems, Russia

B. Rameev   Professor, Gebze Technical University, Turkey

N. R. Skrynnikov   Professor, St. Petersburg University, Russia

M. S. Tagirov   Professor, Kazan Federal University, Russia

L. M. Varela   Professor, University Santiago de Compostela, Spain
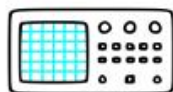
S. Vasiliev   Professor, University of Turku, Finland

Spinus

Saint Petersburg State University
spbu.ru

P&L Scientific Company
plscientific.se

ELEMENT Company
element-msc.ru

Magicplot Systems, LLC
magicplot.com

TerraQuanTech, LLC

MRRC "Spinus" SPbU, LLC
magres.ru

Contents

9

Schedule

20th International School-Conference

«Magnetic Resonance and its Applications.

Spinus-2023»

March 27 - 30, 2023

St. Petersburg

	MONDAY – 27 March 2023
10:00 – 10:10	**Opening**
10:10 – 10:40	**Vladimir Chizhik (Saint-Petersburg, Russia)** **Lecture:** Start and passage of the School-Conference "Magnetic Resonance and its Applications" (Spinus) (to the 20th meeting of the conference)
10:40 – 11:20	**Yury Bunkov (Moscow, Russia)** **Lecture:** Magnon-magnon interaction through phonons
11:20 – 11:40	**Igor Yanilkin (Kazan, Russia)** **Oral report:** Engineering the Exchange Spin-Waves in Graded Thin Ferromagnetic Films
11:40 – 12:00	**'COFFEE' BREAK**
12:00 – 12:40	**Elena Charnaya (Saint-Petersburg, Russia)** **Lecture:** Application of NMR to studies of nanocomposites
12:40 – 13:20	**Sergey Dvinskikh (Stokholm, Sweden)** **Lecture:** Hydrogen bonding in bulk and nanoconfined ionic liquid crystals

13:20 – 13:40	**Alexey Soloninin (Ekaterinburg, Russia)** **Oral report:** Comparison of ion dynamics in a carbon-substituted closo-hydroborates $NaCB_9H_{10}$, $NaCB_{11}H_{12}$ and solid-solution $Na_2(CB_9H_{10})(CB_{11}H_{12})$: ^1H and ^{23}Na NMR studies
13:40 – 14:00	**Daria Pomogailo (Moscow, Russia)** **Oral report:** Photochemical transformations of O-containing radical-cations at low temperatures in CF_3CCl_3 matrix
14:00 – 14:15	Dmitriy Fedorov **(Ekaterinburg, Russia)** **Oral report:** Sodium diffusion in scheelite-type $Na_5M(MoO_4)_4$ (M=Bi, La, Y)
14:15 – 14:30	**Vladislav Liamin (Saint-Petersburg, Russia)** **Oral report:** Development and characterization of new membranes based on polyphenylene oxide and its block copolymer with polydimethylsiloxane for enhanced pervaporation
14:30 – 15:30	**LUNCH**
15:30 – 15:50	**Enza Di Gregorio (Torino, Italy)** **Oral report:** Targeted nanosystems for treatment of triple negative breast cancer and MRI Imaging
15:50 – 16:10	**Nikolay Anisimov (Moscow, Russia)** **Oral report:** Technological applications on a 0.5 T clinical MRI scanner
16:10 – 16:30	**Mikhail Gulyaev (Moscow, Russia)** **Oral report:** Fluorine-19 (^{19}F) magnetic resonance imaging in 1.5 T
16:30 – 16:50	**Dmitriy Blokhin (Kazan, Russia)** **Oral report:** Structural studies of human semen amyloid peptides by NMR spectroscopy and molecular dynamics
16:50 – 17:05	**Alexander Fedotov (Saint-Petersburg, Russia)** **Oral report:** Passively detunable wireless coil for 1.5T breast imaging
17:05 – 17:20	**Zilya Badrieva (Saint-Petersburg, Russia)** **Oral report:** Multi-Echo Spin Echo based T_2 mapping: how can we handle the issue of variations among slices?
17:20 – 17:35	**Fabian Tamayo Delgado (Santiago de Cuba, Cuba)** **Oral report:** Plasma dynamic viscosity in Multiple Myeloma patients measured using NMR
17:35 – 17:50	**Fabian Tamayo Delgado (Santiago de Cuba, Cuba)** **Oral report:** Dalcetrapib and Reduced Glutathione effect on Hemoglobin S polymerization studied by NMR
	TUESDAY – 28 March 2023
10:00 – 10:40	**Richard Shi (Vice President of Magnetic Resonance ZHONGTAI, Hefei, China)** **Anton Cherkasov (leading specialist of the company "ELEMENT", Ekaterenburg, Russia)** **Lecture:** Development of ZHONGTAI W-band EPR Spectrometer

10:40 – 10:55	**Pavel Zasimov (Moscow, Russia)** **Oral report:** An EPR study on the radiolysis of isolated ethanol molecules in solid argon and xenon: matrix control of radiation-induced generation of radicals in cryogenic media
10:55 – 11:10	**Margarita Sadovnikova (Kazan, Russia)** **Oral report:** The Symmetry of the Hyperfine and Quadrupole Interactions of the Boron Vacancy in a Hexagonal Boron Nitride
11:10 – 11:25	**Igor Veyshtort (Saint-Petersburg, Russia)** **Oral report:** Polarization dependence of the ODMR spectrum of spin 3/2 vacancy centers in 6H and 15R silicon carbide polytypes
11:25 – 11:40	**Fan Liu (Beijing, China)** **Oral report:** The DNA binding mechanism of virulence-associated protein Ler from pathogenic Escherichia coli
11:40 – 12:00	**'COFFEE' BREAK**
12:00 – 12:40	**Peter Tolstoy (Saint-Petersburg, Russia)** **Lecture:** NMR study of hydrogen and halogen bonds with P=O groups
12:40 – 12:55	**Mark Kaplanskiy (Saint-Petersburg, Russia)** **Oral report:** The factors determining ^{1}H NMR chemical shift in complexes with centrally symmetric hydrogen bonds
12:55 – 13:10	**Anna Titova (Saint-Petersburg, Russia)** **Oral report:** Investigation of the mutual influence of NH-N hydrogen bonds in heterodimers of substituted diaminopyridines by means of quantum chemistry
13:10 – 13:25	**Elizaveta Kononenko (Novosibirsk, Russia)** **Oral report:** Obtaining High Resolution NMR Spectra in Inhomogeneous Magnetic Fields in Experiments with Antiphase Magnetization
13:25 – 13:40	**Edem Chakalov (Saint-Petersburg, Russia)** **Oral report:** Homoconjugated anions of phosphoric and phosphinic acids: spectral and structural peculiarities probed by low-temperature NMR spectroscopy
13:40 – 13:55	**Daria Novikova (Saint-Petersburg, Russia)** **Oral report:** Estimation of long-range interproton distances in tetrahydropyrazolo[1,5-a]pyrimidines using NOE data
13:55 – 14: 10	**Semyon Egorov (Saint-Petersburg, Russia)** **Oral report:** ^{31}P NMR Spectroscopy within Investigation of Compounds Based on Hexachlorocyclotriphosphazene
14:10 – 14:30	**Eugeny Pestryaev (Ufa, Russia)** **Oral report:** What is hidden under the FID noise of entangled polymer melt?
14:30 – 15:30	**LUNCH**
15:30 – 16: 30	Oral blitz reports of young scientists (5 min × 12)

16:30 – 18:30	**POSTER SESSION I**
	WEDNESDAY – 29 March 2023
10:00 – 10:40	**Sergey Vasil'ev (Chernogolovka, Russia)** **Lecture:** Multiple-quantum NMR dynamics in quasi-one-dimensional zigzag proton spin chains in hambergite single crystal
10:40 – 10:55	**Daniil Shitov (Saint-Petersburg, Russia)** **Oral report:** Handling of the strength of hydrogen bonds involving imidazole ring through the formation of additional non-covalent interactions
10:55 – 11:10	**Julia Pronina (Saint-Petersburg, Russia)** **Oral report:** Diastereoisomers of 3-azabicyclo[3.1.0]hexanes spiro-fused with a benzo[4,5]imidazo[1,2-a]indole fragment: structure determinations using NMR methods
11:10 – 11:40	**Galina Kupriyanova (Kaliningrad, Russia)** **Lecture:** Nuclear Quadrupole Resonance and its Applications
11:40 – 12:00	**'COFFEE' BREAK**
12:00 – 12:40	**Janez Stepišnik (Ljubljana, Slovenia)** **Lecture:** Chemical exchange rate study by NMR CPMG method
12:40 – 13:00	**Oleg Shushakov (Novosibirsk, Russia)** **Oral report:** An example of the Bloch-Siegert effect in magnetic-resonance sounding
13:00 – 13:20	**Aleksandra Kusova (Kazan, Russia)** **Oral report:** Translational diffusion as a protein-protein interaction marker
13:20 – 13:35	**Ksenia Panicheva (Moscow, Russia)** **Oral report:** Translational self-diffusion of α-tocopherol in a new water-soluble form
13:35 – 13:50	**Adeliya Garaeva (Kazan, Russia)** **Oral report:** NMR relaxation of helium-3 in contact with 20-200 nm DyF_3 particles
13:50 – 14:10	**Ayşe Maraşlı (Gebze-Kocaeli, Turkey)** **Oral report:** Time Domain Nuclear Magnetic Resonance Investigations of Benign and Threat Liquids
14:10 – 14:30	**Leonid Grunin (Yoshkar-Ola, Russia)** **Oral report:** Solid State NMR: Validity of Relaxation Times Approach
14:30 – 15:30	**LUNCH**
15:30 – 15:50	**Andrei Komolkin (Saint-Petersburg, Russia)** **Oral report:** Master programs in Physics at Saint Petersburg State University
15:50 – 16:35	Oral blitz reports of young scientists (5 min × 9)

16: 35 – 18:30	**POSTER SESSION II**
	THURSDAY – 30 March 2023
10:00 – 10:40	**Marina Shelyapina (Saint-Petersburg, Russia)** **Lecture:** Recent advances in NMR of hierarchically organized zeolites
10:40 – 10:55	**Milosh Ubovich (Saint-Petersburg, Russia)** **Oral report:** The state of concomitant water in system "ionic liquid - aluminum salt"
10:55 – 11:10	**Nadezhda Pokhvishcheva (Saint-Petersburg, Russia)** **Oral report:** Diffusion studies in polymeric membranes plasticized by ionic liquids
11:10 – 11:25	**Kirill Mukhin (Saint-Petersburg, Russia)** **Oral report:** Local structure and dynamics in concentrated ''water-in-salt'' mixed LiOAc and KOAc solutions according to data of NMR
11:25 – 11:45	**Nikita Slesarenko (Chernogolovka, Russia)** **Oral report:** Local motion of water molecules and Li^+, Na^+, Cs^+ cations in sulfonic cation-exchange membranes studied by spin relaxation of ^1H, ^7Li, ^{23}Na, ^{133}Cs nuclei.
11:45 – 12:00	**'COFFEE' BREAK**
12:00 – 12:20	**Georgy Mozzhukhin (Gebze-Kocaeli, Turkey)** **Oral report:** The detection of NQR signals with use of the single-turn toroid
12:20 – 12:40	**Cengiz Okay (Istanbul, Turkey)** **Oral report:** Microwave (MW) Dielectric Spectroscopy investigations of benign and threat liquids
12:40 – 13:00	**Ilya Yakovlev (Novosibirsk, Russia)** **Oral report:** Hydrogen pulverization of metallic cobalt observed by ^{59}Co Internal Field NMR of Co-Zr cermet precursor
13:00 – 13:15	**Anton Kashnikov (Surgut, Russia)** **Oral report: On the spin properties of cement and its components**
13:15 – 13:30	**Sergei Bystrov (Saint-Petersburg, Russia)** **Oral report:** NMR to Industry: developing the portable NMR solution
13:30 – 13:50	**Pavel Kupriyanov (Gebze-Kocaeli, Turkey)** **Oral report:** Detection of organophosphorus liquids by NMR in the Earth's magnetic field
13:50 – 14:30	**Pavel Yushmanov (Stockholm, Sweden)** **Lecture:** Electrophoretic NMR and applications
14:30 – 15:30	**MEETING** **OF AWARDING COMMISSION**
15:30 – 16:00	**AWARDING and CLOSING**

			POSTER SESSION I (TUESDAY, 15:30 – 18:30)
1	Ivan	Adyukov	Homo- and heteronuclear NMR spectroscopy experiments in studying structure of 3-bromo-3-nitro-1-phenylprop-2-en-1-one
2	Dmitry	Aleshin	Analysis of thermodynamics properties of Fe(II) spin-crossover complexes by the ^{1}H chemical shifts analysis
3	Andrey	Bagautdinov	Induced nonlinear frequency shift of an active ring resonator on a magnonic crystal
4	Marcel	Bakirov	Increasing the effective relaxation time in Carr-Purcell-Meiboom-Gill sequence
5	Valerii	Bezrodnyi	Molecular dynamics simulation of lysine based peptide dendrimers with neutral and protonized histidine
6	Viktor	Demidov	ESR spectroscopy of temperature accessible lowest electronic triplet biradical states of d-elements biologically active 1,10-phenanthrocyanines (bi-1,10-phenanthrolylenes), soft colloidal glasses
7	Nina	Djapic	Eugenol and piperine proton spectra
8	Mariia	Dmitrenko	Development and characterization of novel pervaporation mixed matrix membranes based on carboxymethyl cellulose modified with Zn-based MOF for hybrid process
9	Maria	Egorova	Water molecules mobility in microporous mordenite by molecular dynamics simulation
10	Albina	Gafarova	EPR study of mechanically activated calcium gluconate monohydrate irradiated with gamma quanta
11	Kirill	Gomonov	Study of the structure of reaction products of acetyl-containing furancarboxylates with hydrazine hydrate by 1D and 2D NMR spectroscopy
12	Timur	Islamov	Pravastatin with transition metal ion studied by NMR
13	Alexander	Khudozhitkov	Deuterium Isotope Effects in Protic Ionic Liquids
14	Aleksandr	Koltsov	Nuclear magnetic resonance in eutectic Cs-Li-OAc-H$_2$O "water-in-salt" solution
15	Alexandr	Kondrashov	Ways of optimization of the magnonic reservoir computer performances
16	Vladilina	Koryakina	Solid-State ^{13}C NMR of Annealing Nanodiamonds
17	Andrei	Zolotarev	Development and characterization of novel ultrafiltration membranes based on cellulose acetate modified with Zn-based MOFs
18	Anastasia	Nikitina	Investigation of NMR relaxation properties of contrast agents based on magnetic nanoparticles
19	Denis	Lyozov	Homo- and heteronuclear NMR methods for signal assignments in ^{1}H and ^{13}C specta of 1-aminoacyloxygermatran
20	Darya	Melkova	Tautomeric transformations N- and C-acyl derivatives of tetrahydro-1,4-diazepines
21	Ivan	Mershiev	Cogwheel phase cycling for T_2-T_2 exchange NMR
22	Igor	Neelov	Investigation of complex formation by Lys-2Leu dendrimer with oligopeptides of different degree of hydrophobicity
23	Kenan	Mamedgasanov	Molecular Dynamics Study of the Process of Extraction Purification of Model Fuel

			POSTER SESSION II (WEDNESDAY, 15:50 – 18:30)
1	Igor	Neelov	The SCF study of micelle formation of the amphiphilic hybrid molecules consisting of a polylysine dendron with several hydrophobic tails
2	Igor	Neelov	Molecular dynamics study of complex formation of the dendrigraft DG2 with charged oligopeptides AED, GED and ED
3	Andrey	Nikitin	Modeling of nonlinear spin-wave transient processes in magnonic active-ring oscillators
4	Anna	Kuzminova	Novel pervaporation membranes based on poly(ester-block-amide) modified with MOFs.
5	Anastasia	Nikitina	New methods of magnetic resonance theranostics
6	Boris	Nikolaev	Low-field Bench-top NMR analysis of pharmaceutical, food products in chemical laboratory
7	Vasilii	Pelipko	Configuration Determination of Regioisomeric Spirocyclopropanes Using NMR Spectroscopy Methods
8	Alina	Petrova	Investigation of biosilification mechanisms by experimental EPR methods and calculated DFT method on the example of orthosilicic acid oligomers
9	Andrey	Rochev	Slowdown of spin-lattice relaxation of quadrupole nuclei in crystals by additional magnetic excitation
10	Alexey	Salin	Synthesis and NMR structure of Michael adducts derived from phosphine-catalyzed reaction of sesquiterpene lactone arglabin with nucleobases
11	Leila	Sharipova	The environment effect on the intramolecular mobility of pillar[5]arene
12	Anzhelika	Sheremeta	Identification of diosmin in Hyssopus officinalis L by ^{1}H NMR spectroscopy.
13	Semen	Shestakov	Optimization of the duration of ^{31}P-NMR analysis of lignin functional composition
14	Nadezhda	Sheveleva	Mechanical Relaxation of PPI and PAMAM Dendrimers of Low Generations
15	Mark	Smirnov	Application of ^{1}H and ^{13}C NMR spectroscopy for the determination of the key parameters of vegetable oils
16	Vladislav	Stanishevskiy	Topical problems of ^{15}N NMR spectroscopy.
17	Milosh	Ubovich	Effect of addition of lithium and aluminum salts on molecular mobility in ethylammonium nitrate. A molecular dynamics simulation study
18	Andrey	Uskov	Atomic mobility in metallic sodium confined to porous glass
19	Allisher	Vasilev	Freezing and melting transitions and atomic mobility in the nanoconfined Ga-Sn eutectic alloy
20	Vitalii	Vitko	Investigation of transmission characteristics of active ring resonator on nonlinear ferrite-ferroelectric delay line
21	Vladimir	Voronov	On the possibility of using nuclear magnetic resonance to create a quantum computer based on a top-down approach
22	Timophey	Zhivotikov	Applied possibilities of using the ^{35}Cl NQR line in KClO$_3$
23	Anna	Kuzminova	Development and characterization of novel membranes based on sodium alginate modified with Zr-MOFs.
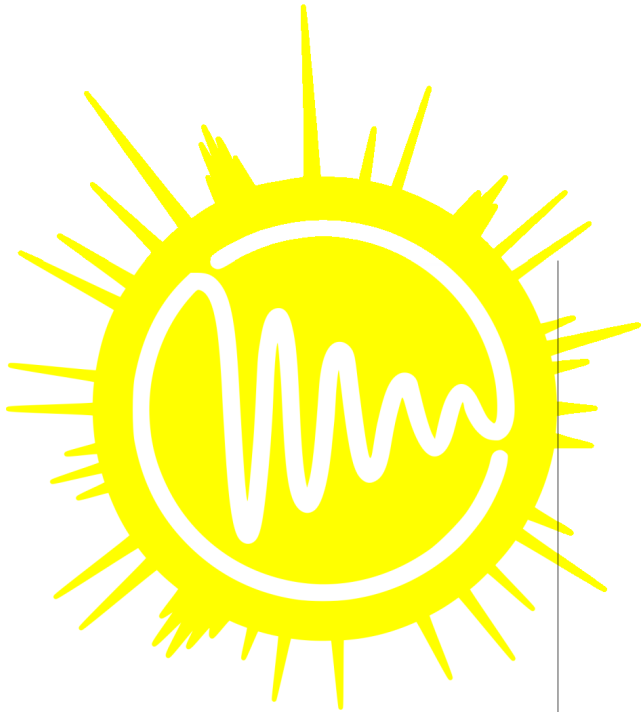
Spinus

The School-Conference "Spinus" of Saint Petersburg State University

The St. Petersburg State University (SPSU) holds International School-Conference "Magnetic resonance and its application" (Spinus) since 2004. "Spinus" is organized in according to the subjects of researches and Master Programs, which have been developed and implemented in the SPSU. In modern physics, the term "magnetic resonance" refers to a set of phenomena accompanied with the emission or absorption of electromagnetic waves of the radiofrequency diapason by quantum systems (nuclei, electrons, atoms, molecules, etc.). These phenomena, the physical nature of which is of independent interest, provided the basis of radiospectroscopic methods for studying the structure of matter and physical-chemical processes in it. They are also used for the creation of quantum generators, amplifiers, and magnetometers. For the development of ideas and applications of magnetic resonance six Nobel Prizes were awarded in the areas of physics, chemistry, biology, physiology and medicine (the latter was in 2003).

Primarily, magnetic resonance methods are:

- Nuclear Magnetic Resonance (NMR)
- Electron Paramagnetic Resonance (EPR)
- Nuclear Quadrupole Resonance (NQR)

These methods, being contactless, do not destroy an object under a study, that makes them unique and in demand not only in physics and chemistry, but also in medicine, geology, biology and archeology. Now, any medical center with high reputation has a magnetic resonance imaging (MRI). In Russia, NMR is used in oil well logging, laboratory analysis of the productivity of oil-bearing reservoirs, analysis of oil content and moisture of seeds; EPR technique is used for geological research, non-destructive control of precious stones, as well as for the dating of paleontological artifacts; there are NQR applications for remote detection of solid explosives and narcotics. Magnetometry methods based on magnetic resonance are indispensable for carrying out archaeological researches.

Selected papers of participants are published in a special issue of the journal "Applied Magnetic Resonance"

Earlier the school organizers worked at the Department of quantum magnetic phenomena (QMPh) of the St. Petersburg State University, which was founded in 1993 on the initiative of Professor V. I. Chizhik on the basis of the laboratory, created in the 50s of the last century by F. I. Skripov at the Department of Radio Physics (the branch "Quantum Radiophysics"). On January 1, 2014, the Department of QMPh joined the united Department of nuclear-physics research methods (Head of the Department is Corresponding Member of the Russian Academy of Sciences, Professor Mikhail Kovalchuk). The QMPh collective has a number of priority works in the field of nuclear magnetic resonance. One of the most significant achievements was the first in the world implementation (in 1958) of the Fourier transform of a free induction signal in order to obtain a NMR spectrum (see the details in [1]). Concurrently with the research activity, the staffs of the department are actively involved in the development of practical applications of magnetic resonance. The department graduates work not only in Russia and the CIS, but also in Sweden, USA, New Zealand, England, Cuba, Germany, France, Italy, Turkey, occupying positions from a highly advanced operator of radiospectrometers to a professor.

The main research areas developing in the team of quantum magnetic phenomena:

- Nuclear magnetic resonance in liquids (spectra, relaxation, diffusometry, …);
- Nuclear magnetic resonance in solids;
- NMR in liquid crystals;
- NMR in heterogeneous systems;

- MRI in weak magnetic fields;
- The quantum magnetometry in archeology;
- Nuclear magnetic resonance in the magnetic field of the Earth;
- Computing modeling in magnetic resonance.

It is evident from the above that the scope of our research interests is quite wide. We are always open for the collaboration with researchers from various fields of science.

Our team has published a series of monographs, textbooks and training manuals on Magnetic Resonance. For example:

1. Vladimir I. Chizhik, Yuri S. Chernyshev, Alexey V. Donets, Viatcheslav Frolov, Andrei Komolkin, Marina G. Shelyapina. Magnetic Resonance and Its Applications. 2014, Springer-Verlag. 782 pp. *(Now about 40000 chapter downloads).*
2. Квантовая радиофизика: магнитный резонанс и его приложения. Учеб. пособие. 2-е изд., перераб. Под ред. В. И. Чижика. – СПб.: Изд-во С.-Петерб. ун-та, 2009. 700 с.
3. В. И. Чижик. Ядерная магнитная релаксация. Учеб. пособие. 3-е изд. – СПб.: Изд-во С.-Петерб. ун-та, 2004. 388 с.
4. Практикум по магнитному резонансу. Учебное пособие. Под ред. В. И. Чижика. – СПб.: Изд-во С.-Петерб. ун-та, 2003. 184 с.

Due to current problems in the organization of public events, the Organizing Committee of "Spinus-2023" decided to implement the School-Conference in the on-line format using ZOOM (not in a face-to-face format). We hope that next "Spinus 2024" will be held the usual format!

Welcome to the annual Spinus!

Dr. Sci., Professor, SPSU, Denis A. Markelov
Chairman of Organizing committee of
the 20th School-conference
"Magnetic resonance and its applications"
Spinus-2023

References

1. V.I. Chizhik. On the history of the Fourier transform in NMR spectroscopy. 2018, BULLETIN DU GROUPEMENT AMPERE, 67, № 4 (273), p 5-6.

Lectures

Magnon-magnon interaction through phonons

Yu.M. Bunkov
Russian Quantum Center, Skolkovo, 143025 Moscow, Russia.
Email: y.bunkov@rqc.ru

Magnon Bose-Einstein condensation (MBEC) was discovered in the famous experiments on pulsed NMR in superfluid 3He, in which it led to a narrowing of the magnetic resonance line by a thousand times [1]! Then magnonic BEC was discovered in antiferromagnets [2] and finally in a film of yttrium iron garnet (YIG) at room temperature [3, 4]. The unique properties of MBEC open new possibilities for its application to quantum computing. Unlike the traditional quantum system based on several oscillators, the magnon BEC is a collective macroscopic system of magnons in the same coherent quantum state. It has several fundamental advantages over previously developed systems for quantum computing.

1. **Critical temperature**. The critical temperature that destroys the quantum memory of quantum qubit is determines by its working frequency ω. For the qubit to function, its temperature must be significantly lower than $h\omega/k$. In the case of MBEC, we are dealing with a macroscopic ensemble of oscillators in a single coherent state. Their number can reach values of the order of 10^{18}! Therefore, the absorption of a finite number of thermal excitations cannot change the state of the MBEC. To destroy quantum memory, the number of excitations must be increased by a factor of N or SQRT(N), where N is a density of particles in MBEC. In any case, we are reaching temperatures above room temperature. This means that a quantum qubit based on MBEC can operate at room temperature.

2. **Temperature.** Currently, the most developed are qubits based on superconductivity, which exists at temperatures of several kelvins. Even lower temperatures require qubits based on atomic BEC. Magnons are quasiparticles, and the formation of MBEC requires not a decrease in temperature, but the excitation of a sufficient number of nonequilibrium magnons. Theoretically, it is shown that for the formation of MBEC at room temperature, it is sufficient to deviate the equilibrium magnetization in yttrium iron garnet (YIG) by an angle of more than 3° [5].

3. **Quantum information.** Usually, reading the state of a qubit leads to its destruction. In the case of MBEC, the use of a certain number of magnons for reading information does not change the state of the qubit. Therefore, the process of quantum computing and reading information can be continuous.

4. **Permanent state of MBEC.** Magnons are quasiparticles whose density decreases with time. Therefore, a magnon qubit can operate at times much shorter than the decay time, or under conditions of continuous pumping of magnons. In the latter case, it should be taken into account that the newly born magnons fall into the MBEC state according to the laws of quantum mechanics and therefore do not destroy the quantum state of the qubit.

5. **Permanent read out.** Usually, reading the state of a qubit leads to its destruction. In the case of MBEC, the use of a certain number of magnons for reading information does not change the state of the qubit. Therefore, the process of quantum computing and reading information can be continuous.

At the Russian Quantum Center, we are working on the creation of quantum qubits based on magnon Bose condensate. In particular, a 5 mm MBEC platform was obtained, on which the MBEC exists continuously in the region far from RF pumping area. In addition, we managed to create an optical readout of the magnon density [6,7]. The report will present

projects of possible qubits based on MBEC [8, 9]. Finally, new results on the coupling of magnons in two YIG disks through phonons to the substrates will be presented.

Acknowledgments

References

1. A.S. Borovik-Romanov, et al. JETP Letters, 40, 1033 (1984).
2. Yu. M. Bunkov, et al., Phys. Rev. Lett. 108, 177002 (2012).
3. Yu. M. Bunkov, et al., Scientific Reports, 11, 7673 (2021).
4. M. Schneider, et al., Nat. Nanotechnol. 15, 457–461 (2020).
5. Yu. M. Bunkov and V. L. Safonov, J. Magnetism Magnetic Materials, 452, 30–34 (2018).
6. P. E. Petrov, et al., Optics Express 30, 1737 (2022).
7. P. E. Petrov, et al., Optics Express 31, 8335 (2023).
8. P. M. Vetoshko, et al., JETP Lett., 112, 299 (2020).
9. Yu. M. Bunkov, JETP, 131, 18 (2020).

Application of NMR to studies of nanocomposites

Elena V. Charnaya, Denis Yu. Nefedov, Andrei V. Uskov, Allisher A. Vasilev,
Dmitrii Yu. Podorozhkin

Faculty of Physics, St. Petersburg State University, St. Petersburg 198504 Russia
E-mail: e.charnaya@spbu.ru

Introduction

A review of recent NMR applications to studies nanocomposites based on porous silica templates with metallic and ferroelectric inclusions is presented. The enhancement of polymorphism under nanoconfinement, alterations in atomic mobility for liquid and solid nanoparticles, and size-effects on phase transitions are discussed.

Polymorphism under nanoconfinement

NMR provides unique information about changes in structure of confined metals and alloys. We observed the stabilization of the β-Ga structure in the gallium-rich segregates within binary and triple alloys. The remarkable increase in the temperature of the polymorph phase emergence was found for metallic sodium embedded into a glass template. Polymorphism was shown to affect strongly the melting and freezing processes in confined substances.

Atomic mobility

NMR is a powerful probe to study local atomic mobility in confined metals, alloys and ferroelectrics. Drastic slowdown of self-diffusion was observed for liquid metals and alloys, which was evidenced by a strong increase in the correlation time of atomic mobility. Acceleration of atomic mobility was observed for some crystalline metals and alloys. Changes of mobility in confined ferroelectric nanoparticles were revealed in measurements of spin-lattice relaxation.

Phase transitions under nanoconfinement

The liquid-liquid phase transition was observed unambiguously in melted gallium and gallium alloys under nanoconfinement using measurements of the Knight shift and spin relaxation. Within a range of this transition, the NMR lines split into two components. Structural phase transitions in ferroelectrics were shown to be shift remarkably depending of pore size and geometry. Melting and freezing transitions in fine confined metallic sodium particles were found to occur with formation of some intermediate states.

Acknowledgments

Start and passage of the School-Conference "Magnetic Resonance and its Applications" (Spinus) (to the 20th meeting of the conference)

Vladimir I. Chizhik[*]

Faculty of Physics, Saint-Petersburg State University, Russia
E-mail: v.chizhik@spbu.ru

The School-Conference "Magnetic Resonance and its Applications" was first held by St. Petersburg State University in 2004. Since then it has been held annually. The lecture will cover the specifics and formats of the School Conference during different periods, including the time of the COVID 2019 pandemic.

In recent years, the conference was annually attended by scientists from about 15 countries (Australia, Brazil, Great Britain, Germany, Italy, Cuba, USA, Turkey, Finland, France, Sweden and others).

One of the goals of the lecture is to stimulate the discussion about the appropriate formats of holding a School-conference in the future.

---

[*] Chairman of the Program Committee of the School-Conference

Hydrogen bonding in bulk and nanoconfined ionic liquid crystals

Sergey V. Dvinskikh

KTH Royal Institute of Technology, Stockholm, Sweden.
E-mail: sergeid@kth.se

Ionic liquid crystals have the typical characteristics of ionic liquids and, at the same time, a nanoscale-organized structure of liquid crystals [1]. The formation of liquid-crystalline phases in ionic liquids is driven by a balance between hydrogen bonding, electrostatic interactions, and dispersion forces. A small shift of the force balance can lead to discernible changes in phase behaviour and local molecular ordering and dynamics. Trends in mesophase window and ionic orientational order are well correlated with physicochemical properties of the anions such as ionic radius, charge delocalization, and the ability for hydrogen bonding [1-3]. Modification of the hydrogen-bonding network by hydration further contributes to mesophase stabilization in ionic liquid crystals despite decreasing the orientational order and accelerated ion translational dynamics [3, 4].

Hydrogen-bonding interactions have also been studied in nanoconfined ionic liquids, presenting a class of hybrid composites combining the functional properties of ionic liquids and porous solids. Due to non-covalent interactions with the solid interface, confined ionic liquids exhibit distinct structural, orientational, and dynamic preferences different from the bulk.

Previously, we have studied the dynamic and the orientational ordering behaviour of ionic mesophases using heteronuclear dipolar NMR spectroscopy and pulsed-field-gradient diffusion NMR [2-6]. In the present work, we discuss cation–anion hydrogen-bonding interactions in imidazolium-based ionic liquid crystals. We apply solid-state ^{1}H NMR and heteronuclear ^{1}H-^{13}C spectroscopy (HETCOR) to access proton chemical shift interactions in Hydrogen-bonding centers [7]. Hydrogen bonding effects are compared in isotropic, liquid crystalline, and solid phases of ionic liquid crystals as well as in the nanoconfined state. The influence of anion properties, cation structures, ion dynamics, and orientational order on hydrogen bond strength is discussed.

References

1. K. Goossens, K. Lava, C. W. Bielawski, K. Binnemans, *Chem. Rev.* (2016), 116, 4643.
2. J. Dai, D. Majhi, B. B. Kharkov, S. V. Dvinskikh. *Crystals* (2019), 9, 495.
3. D. Majhi, J. Dai, A. V. Komolkin, S. V. Dvinskikh. *PCCP* (2020), 22, 13408.
4. S. V. Dvinskikh. *Liq. Cryst.* (2020), 47, 1975.
5. D. Majhi, S. V. Dvinskikh. *Sci. Rep.* (2021), 11, 5985.
6. M. Cifelli, V. Domenici, V. I. Chizhik, S. V. Dvinskikh. *Appl. Magn. Reson.* (2018) 49,553.
7. D. Majhi, J. Dai, S. V. Dvinskikh. *PCCP* (2022), 24, 23532.

Nuclear Quadrupole Resonance and its Applications

G.S. Kupriyanova[1], *G.V. Mozzhukhin*[2]

[1]*Immanuil Kant Baltic Federal University, Kaliningrad, Russian Federation.*
Email: galkupr@yandex.ru
[2]*Gebze Technical University, 41400 Gebze/Kocaeli, Turkey*

Introduction

Nuclear quadrupole resonance (NQR) is based on the electrical interaction of nonspherical nuclei with an electric field gradient created by the electrons surrounding the nucleus. The main physical parameters that can be extracted from the NQR spectrum under favorable conditions are the quadrupole interaction tensor and the electric field gradient on the nucleus. Thus, NQR is a sensitive method for determining the local environment of the nucleus. NQR makes it possible to obtain detailed information about crystal symmetry, defects in crystals, phase transitions, the presence of polymorphic structures, and others. Although NQR is not observed in liquids, quadrupole interactions manifest themselves in relaxation processes. NQR also has an important advantage associated with the dependence of the NQR spectra on the local electrical gradient, which is unique for each substance. Thus, NQR has the property of identifying chemicals. This property is very important for the detection of drugs, explosives, drug identification. However, the signal-to-noise ratio (SNR) in NQR depends on the resonant frequency, which is often small. In recent years, much effort has been made to develop methods that allow increasing the SNR, as well as expanding the information content of NQR.

Basic NQR theory

In the coordinate system associated with the principal axes of the electric field gradient tensor, the quadrupole interaction Hamiltonian has the form:

$$H_Q = \frac{e^2 q_{ZZ} Q}{4I(2I-1)} \{3I_Z^2 - I^2 + \eta(I_X^2 - I_Y^2)\}$$

(1)

where I_x, I_y, I_z are the components of the nuclear angular moment spin operator, η is the asymmetry parameter of the EFG, and $e^2 Q q_{zz}$ is quadrupole coupling constant of the nucleus.

Application NQR for the identification of chemical substances

The task of identifying chemicals is very important for transport security, humanitarian demining, and pharmacy security. Although the use of NQR has been proposed for more than forty years, the development of experimental techniques has made it possible to significantly improve the signal-to-noise ratio and the reliability of this approach. New methods include the development of double NMR/NQR, the use of highly sensitive sensors (magnetometers and HTS sensors), the development of a remote detection technique [1], and advanced processing techniques (neural network and machine learning). A special device and methods for the identification of medicinal substances have been developed.

Application NQR in Pharmacy

A hot topic in pharmacy is polymorphism. Polymorphism associated with the property of substances to exist in several crystalline forms [1]. In this case, NQR makes it possible to detect polymorphic forms and distinguish between these forms. In recent years, NQR has been used for the authentication and analysis of medicines, vitamins, nutritional supplements, etc [2].

References

1. Rameev, B., Mozzhukhin, G. & Aktaş, B. Magnetic Resonance Detection of Explosives and Illicit Materials. *Appl Magn Reson* **43**, 463–467 (2012)
2. Janez Seliger, Veselko Žagar, Tomaž Apih, Alan Gregorovič, Magdalena Latosińska, Grzegorz Andrzej Olejniczak, Jolanta Natalia Latosińska,Polymorphism and disorder in natural active ingredients. Low and high-temperature phases of anhydrous caffeine: Spectroscopic (^{1}H–[14]N NMR–NQR/^{14}N NQR) and solid-state computational modelling (DFT/QTAIM/RDS) study, European Journal of Pharmaceutical Sciences, Volume 85, 2016, Pages 18-30

Development of ZHONGTAI W-band EPR Spectrometer

Dr. Richard Shi

Vice President of Magnetic Resonance, ZHONGTAI
E-mail: gml@grgo gpv′o ue0 w

The design and performance of a W-band EPR continuous-wave (CW) and pulsed electron paramagnetic resonance (EPR) spectrometer are reported.

The instrument contains a microwave bridge, a hybrid magnet system, a probe head with a TE011 cavity, a variable-temperature system as well as the control system and software. The frequency range is 93.5 – 94 .5 GHz. The maximum microwave power is 50 mW at CW-EPR mode and 1 W at pulsed-EPR mode. There are four fixed phases ($\pm$X and $\pm$ Y) with fixed identical amplitude in the pulse forming unit. A second microwave source for ELDOR experiment is equipped. In pulsed-EPR mode, the length of $\pi/2$ pulse is 20 ns at a resonator Q-value of 2000. The magnet system consists of a 6 T horizontal split-coil superconducting magnet and a fast sweep coil. The magnet can be swept over the full range from 0 to 6 T. The sweep coil has a $\pm$1000 gauss range. The magnet system is cooled by two cryocoolers. The variable-temperature system is a continuous flow-type that works from 4 to 300 K range.

Recent advances in NMR of hierarchically organized zeolites

<u>M.G. Shelyapina</u>[1], D. Nefedov[1], A.S. Mazur[1], R. Yocupicio-Gaxiola[2], V. Petranovskii[2]

[1]*Saint Petersburg State University, 7/9 Universitetskaya nab., Saint Petersburg 199034, Russia*
[2]*Centro de Nanociencias y Nanotecnología, Universidad Nacional Autónoma de México, Ensenada, B.C., 22860 México*
E-mail: marina.shelyapina@spbu.ru

In recent years, hierarchical zeolites combining microporosity and meso- or macroporosity have attracted increasing attention due to their higher mass transfer and molecular accessibility that helps to overcome steric and diffusion limitations, as well as limitations of coke formation in catalytic reactions inherent to microporous zeolites [1, 2]. When developing synthetic strategies for hierarchical zeolites aimed at solving a specific problem, it is necessary to establish a correspondence between the synthesis method, the topology of pores, the structure of their surface and other properties that affect the mass transfer of guest molecules, effectiveness of catalytic reactions and other target characteristics. Nuclear magnetic resonance (NMR) is a unique tool that provide an access to the study not only zeolitic matrices (Brønsted and Lewis sites, pore sizes and connectivity) but also to guest-host interactions inside pores, diffusivity of adsorbed molecules, and *in situ* monitoring of zeolite growing and catalytic reactions [3-7].

In this lecture we provide a brief overview of recent advances in NMR studies of hierarchically organized zeolites for emerging applications.

Acknowledgments

References

1. S. Mitchell, A.B. Pinar, J. Kenvin, P. Crivelli, J. Kärger. J. Pérez-Ramírez. – Nat. Comm. **6**, 8633 (2014).
2. M. Hartmann, M. Thommes, W. Schwieger. – Adv. Mater. Interfaces **8**, 2001841 (2021).
3. M.G. Shelyapina R.I. Yocupicio-Gaxiola I.V. Zhelezniak, M.V. Chislov, J. Antúnez-García, F.N. Murrieta-Rico, D. Homero Galván, V. Petranovskii. S. Fuentes-Moyado, – *Molecules* **25** 4678 (2020).
4. D. Wisser, M. Hartmann. – Adv. Mater. Interfaces **8**, 2001266 (2021).
5. M.G. Shelyapina, A. Mazur, R.I. Yocupicio‑Gaxiola, U. Caudillo‑Flores, A. Urtaza, I.A. Rodionov, I.A. Zvereva, V. Petranovskii. – Appl. Mag. Res. **53**, 1609 (2022)
6. M.G. Shelyapina, E.A. Krylova, A.S. Mazur, A.A. Tsyganenko, Y.V. Shergin, E.A. Satikova, V. Petranovskii. – Catalysts **13**, 344 (2023)
7. I.I. Ivanova, E.P. Andriako. – Microp. Mesopor. Mat. Available online 19 November 2022, 112363, doi: 10.1016/j.micromeso.2022.112363
8. Rameev, B., Mozzhukhin, G. & Aktaş, B. Magnetic Resonance Detection of Explosives and Illicit Materials. *Appl Magn Reson* **43**, 463–467 (2012)

Chemical exchange rate study by NMR CPMG method

Janez Stepišnik[1], Aleš Mohorič [1,2]
[1]*Faculty of mathematics and physics, University of Ljubljana, Slovenia,*
[2]*Institute Jozef Stefan, Ljubljana, Slovenia*
E-mail: janez.stepisnik@fmf.uni-lj.si
https://users.fmf.uni-lj.si/stepisnik/index.html

Introduction

Various nuclear magnetic resonance (NMR) method, which manipulate the spin dynamic of atomic nuclei in order to convey information about their environment i.e. the structure and dynamics in matter, are used in chemistry, physics, material science, biology, and medicine. In NMR studies of liquids in sub-MHz frequencies range and at high temperatures, we assume a rapid molecular motion on the pico- or nanosecond time scale that completely cancels out both near- and long-range spin dipole-dipole interactions and first-order quadrupole interactions, if not taking into account their effect on the spin relaxation times. But the interactions of spins with electrons in molecular orbitals, i.e. the chemical shifts of spectral lines, nor the indirect dipolar interaction between spins in different molecular conformations mediated by electrons of molecular orbitals, i.e. the line splitting by j-coupling, cannot neglected. In liquids we have to take also in account the effects of molecular and chemical dynamics causing fluctuations in these interactions. Particularly useful NMR method for the study of the correlation fluctuation functions is the Carr-Purcell-Meiboom-Gill sequence (CPMG)[1] with a train of π-radiofrequency (RF) pulses, which was originally introduced to provide reliable spin measurements relaxation by eliminating the spin echo attenuation effect created by the spin motion in the non-uniform magnetic field of the old magnets. Later on it turned out that the method, which combines CPMG with an inhomogeneous magnetic field, the magnetic field gradient (MFG), known as the modulated gradient spin echo (MGSE)[4] provides the direct insight into the spectrum of the molecular velocity auto-correlation (VAS), which is the key dynamic quantity of molecular translation motion by containing details about the underlying nature of molecular interactions. Thermally induced molecular and chemical dynamics cause spin parameter fluctuations, which are usually analyzed in a quasi-classical manner using the Bloch-Torey equation in the case of diffusion or the Bloch-McConnell equations[2] in the case of chemical exchange. Such an approach cannot reveal some details that can only be obtained within the framework of a quantum mechanical (QM) derivation. Like QM treatment of the MGSE method[4,5] here we study the effects of molecular conformation changes to get insight into the correlation functions of chemical exchanges. Study of spins in liquids gives the amplitude of the induced spin echo along the y direction

$$E(t) = \hbar\gamma \frac{d}{dt} \sum_{ij} Tr\rho_r(t)\widehat{I_{ylj}}$$

$$\approx \sum_{ij} Tr\widehat{I_{y,l,J}}\,^2 J_{s\,i\,j}(t)^{n_j} e^{-i\Delta\omega_{ij}(t)f(t)} \langle e^{i\int_0^t \xi_{ij}(t')f(t')dt'}\rangle, (1)$$

in which the factor $J_{sij}(t)^{n_j}$ gives signal undulation due to j-coupling and where

$$\Delta\omega_{ij} = \omega_{Csij}(t) + \gamma\boldsymbol{G}\,\boldsymbol{r}_{ij}(t) + \frac{2\pi}{\hbar}\sum_{ih} J_{ijh}(t)\hat{S}_{zih}$$

are oscillations due to the effects of chemical shifts, spin displacements in the gradient field and j-coupling of hetero-nuclear spins. Signal phase is the time average of the phase, which is the integral over the product of the spin phase modulation function f(t) and the rate of

fluctuation $\xi_{i,j,q}(t) = \frac{d}{dt}\Delta\omega_{i,j}(t)$, which is caused by either chemical exchange or changes due to movements in an inhomogeneous magnetic field. If the fluctuations rate, $\xi_{ij}(t)$, is considered as a random variable, the exponent can be expanded into the cumulant series, which gives, in the Gaussian phase approximation, the attenuation of the echo peaks[3], i.e. t=NT, as

$$\beta_j(NT) = \int_0^{NT}\int_0^t \langle\xi_{ijc}(t)\xi_{ijc}(t')\rangle f(t')f(t)dt'dt = \frac{1}{\pi}\int_0^\infty k_j(\omega)|f(\omega,NT)|^2 d\omega$$

in which $k_j(\omega)$ is the spectrum of chemical exchange rate and the spectrum of spin echo pulse sequences is

$$\langle f(\omega,N)\rangle^2 = \frac{8sin^4\left(\frac{T\omega}{4}\right)sec^2(\frac{T\omega}{2})(1-(-1)^N \cos(NT\omega))}{\omega^4},$$

in which T is the period of CPMG sequence. Assuming that the frequency variation of $k_j(\omega)$ is negligible in the interval of the spectrum width of the CPMG sequence, which is determines by the length of CPMG sequences1/NT, as shown in Fig.2, $\langle f(\omega,N)\rangle^2$ can be approximated by the delta function to get the contribution of the j-th spin to the peak of the induction signal as

$$E_j(NT) \approx J_{sj}(NT)^{n_j}e^{-\frac{8}{\pi^2\omega_m^2}k_j(\omega_m)NT+NT/T_2},$$

where T_2 is the spin relaxation time. It shows the decay of the spin echo peak, which is directly proportional to the chemical exchange rate spectrum at the value of the spin phase modulation frequency, when the decay due to T_2 is subtracted.
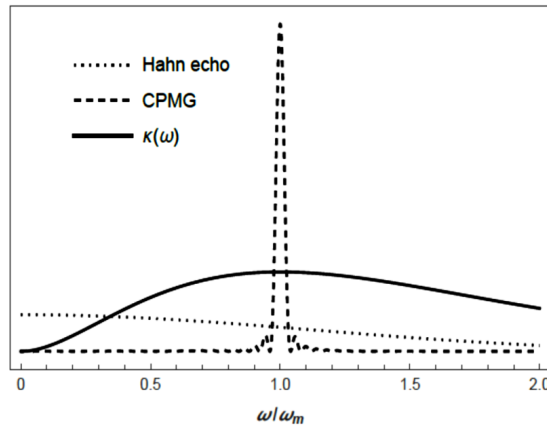
Figure 1. Spectrum of chemical exchange rate and the spectra of Hahn echo sequence with N=1 and the CPMG sequence with N=50

Experiment

NMR spectrometer with 100 MHz proton Larmor frequency was used to measure the spectrum of chemical exchange rate in the sugar/water solution at room temperatures by the CPMG method. The shape of $k_j(\omega)$ is measured by changing the repetition time T of the π-

RF pulses. The spectrometer allows measurements with a high signal to noise ratio with the top frequency limited to 3 kHz by the power of RF transmitter. Figure 2 shows the results of our measurement, where the spectrum of chemical exchange was obtained from the echo decays after subtraction the extrapolated value of effective decay in the high frequency limit.
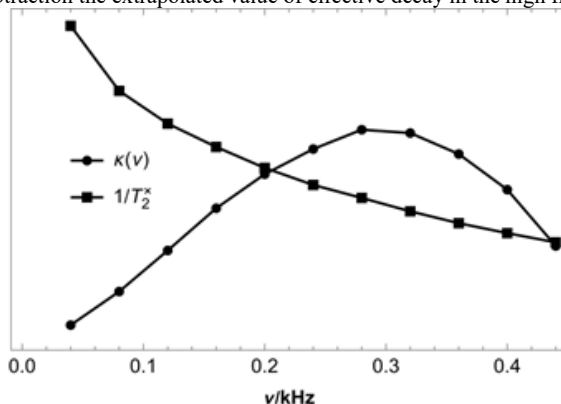
Figure 2. Spectrum of chemical exchange rate in aqueous sugar solutions obtained from the effective relaxation decay $1/T_2^*$ measured by the CPMG method.

Conclusion

However, we must note that the CPMG measurement might not provide just a chemical exchange spectrum between only two molecular conformations; it could result from several exchanges effecting the molecular conformation of spin. In addition, in the spin echo the chemical shifts of all homonuclear spins in the molecule are refocused. Thus, the measured signal may contain the sum of several chemical exchanges, which can only be distinguished by frequency analysis of the signal, i.e. by measuring the high-resolution NMR spectrum. However, we must take into account that in the frequency analysis, the area of the spectral lines is proportional to the spectrum of the chemical exchange rate.

Acknowledgments

References

1. Carr, H.Y., Purcell, E.M. Phys. Rev., Vol. 94, Iss. 3, (1954), 630–638.
2. McConnell, H.M., J. Chem. Phys., 28 (1958), 430–431.
3. Stepišnik J., Physica 104B (1981) 350–361.
4. Callaghan P.T., Stepišnik, J. Advances in Magnetic and Optical Resonance, ed.Warren S. Warren, Vol. 19, (1996), pp. 326–389.
5. Stepišnik J., Mattea C., Stapf S., Mohorič A., Physica A 553 (2020) 124–171.

NMR study of hydrogen and halogen bonds with P=O groups

Peter M. Tolstoy[1],
Valeriia V. Mulloyarova,[1] *Mikhail A. Kostin,*[1] *R.E. Asfin,*[2] *Edem R. Chakalov,*[1] *Daniil M. Ivanov,*[1] *Omar Alkhuder,*[1] *Alexei S. Ostras,*[1] *Aleksander S. Antonov*[1]
[1]*Institute of Chemistry, St.Petersburg State University, St. Petersburg, Russia*
[2]*Faculty of Physics, St.Petersburg State University, St. Petersburg, Russia*
E-mail: peter.tolstoy@spbu.ru
https://chem.spbu.ru/ptchem.html

Introduction

The formation and strengthening of hydrogen and halogen bonds are manifested in changes of geometric and spectral characteristics of complexes. Both types of non-covalent interactions are fully described by their electronic structure while all other parameters – energetic, geometric, and spectroscopic – are consequences. However, in real-world examples, it is often quite challenging to extract detailed electronic information, so that spectroscopic parameters become essential probes and markers for geometric and energetic properties of complexes. For example, as such spectroscopic probe one can use NMR and IR characteristics of a P=O functional group acting as a proton or halogen acceptor.

Previous usages of P=O group for spectral characterization

The P=O fragment appears in the chemical structures of phosphine oxides, phosphinic, phosphoric or phosphonic acids and their anions (Figure 1). The ^{31}P is a sensitive spin-½ nucleus with a large span of chemical shifts, while the stretching vibrations of the P=O group lead to characteristic bands in the IR spectra.
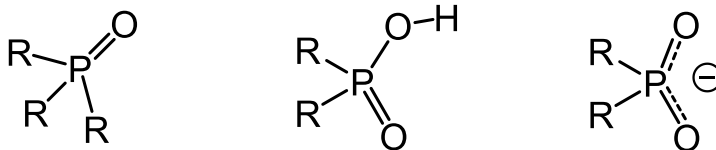
Figure 1. Main chemical sources of P=O groups

The relatively large span of ^{31}P NMR chemical shift changes of phosphine oxides due to their complexation (up to 75 ppm) was used previously to characterize the electron acceptor properties of solvents and other compounds exhibiting Lewis acidity (the so-called Gutmann-Beckett scale of acceptor numbers AN) [1]. Later on, the reports on using ^{31}P NMR of phosphine oxides for hydrogen bond characterization have appeared, though the main focus was on the possibility to estimate pK_a values of proton donors [2].

Complexes studied in this work

In this work we test if and how ^{31}P NMR chemical shifts could be used to establish geometry and energy of hydrogen and halogen bonds formed with participation of P=O and POOH/POO$^-$ groups. We discuss experimental and computational challenges of obtaining non-averaged values of NMR chemical shifts and interpreting them in terms of intermolecular distances and complexation energies, which was attempted by us in a series of recent publications [3–8].
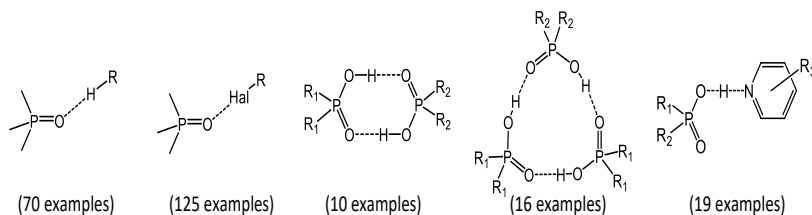
Figure 2. Types of complexes, studied in this work

Figure 2 shows general structures of the studies complexes, while Figure 3 shows two individual complexes of *tert*-butylphosphonic acid, which helped us to identify H-bonding patters exhibited and preferred by the anions of this acid.
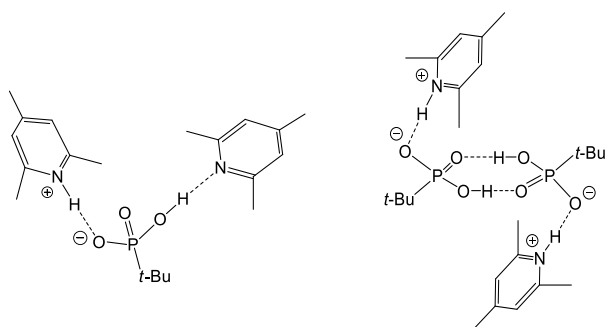
Figure 3. Examples of complexes formed by anions of tert-butylphosphonic acid

Working with sets of complexes allowed us to generalize and propose several correlational dependencies which could be of practical value. As an example of such correlation, in Figure 4 are plotted halogen and hydrogen bond energies as a function of changes of ^{31}P NMR chemical shift upon complexation. This dependence seems to be fairly linear over a broad range of energies of non-covalent interactions.
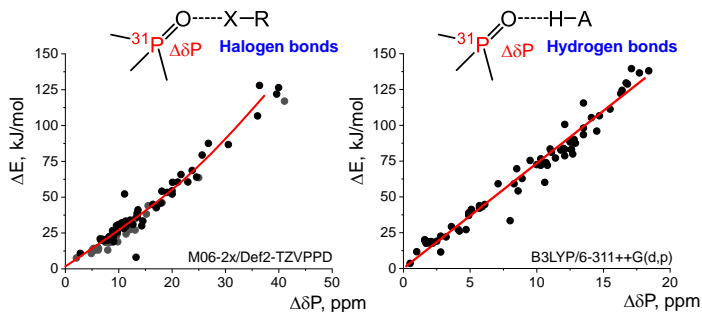
Figure 4. Examples of correlations between changes of ^{31}P NMR chemical shifts of trimethylphosphine oxide and halogen (left) and hydrogen (right) bond energies.

Acknowledgments

References

1. Zheng, S. Bin Liu, F. Deng, *Chem. Rev.* 2017, *117*, 12475.
2. E. Pires, J.M. Fraile, *Phys. Chem. Chem. Phys.* 2020, *22*, 24351.
3. M.A. Kostin, S.A. Pylaeva, P.M. Tolstoy, *Phys. Chem. Chem. Phys.* 2022, *24*, 7121.
4. A.S. Ostras', D.M. Ivanov, A.S. Novikov, P.M. Tolstoy, *Molecules* 2020, *25*, 1406.
5. E.R. Chakalov, E.Yu. Tupikina, E.V. Bartashevich, D.M. Ivanov, P.M. Tolstoy, *Molecules* 2022, *27*, 4848.
6. V.V. Mulloyarova, D.O. Ustimchuk, A. Filarowski, P.M. Tolstoy, *Molecules* 2020, *25*, 1907.
7. I.S. Giba, P.M. Tolstoy, V.V. Mulloyarova, *Phys. Chem. Chem. Phys.* 2022, *24*, 11362.
8. I.S. Giba, P.M. Tolstoy, *Symmetry* 2021, *13*, 258.

Multiple-quantum NMR dynamics in quasi-one-dimensional zigzag proton spin chains in hambergite single crystal

G.A. Bochkin[1], A.V. Fedorova[1], E.B. Fel'dman[1], E.I. Kuznetsova[1], I.D. Lazarev[1,2], K.V. Panicheva[1,2], <u>S.G. Vasil'ev</u>[1]

[1]*Federal Research Center of Problems of Chemical Physics and Medicinal Chemistry RAS, Ac. Semenov avenue 1, Chernogolovka, Moscow Oblast 142432, Russia*
[2]*Faculty of Fundamental Physical-Chemical Engineering, Lomonosov Moscow State University, GSP-1, Leninskie Gory, Moscow 119991, Russia*
E-mail: svasilev@icp.ac.ru, viesssw@mail.ru

Introduction

Multiple quantum (MQ) NMR refers to the techniques exploiting the nominally forbidden degrees of freedom in a collection of nuclear spins in a large magnetic field. The superposed states with the difference between Zeeman quantum numbers other than ± 1 are accessed through the specially designed pulsed sequences in two-dimensional experiments. Early applications focused on the characterization of distribution and clustering of spins in solid materials, simplification of spectra of anisotropic liquids whose complex structure results from the dipolar couplings in large groups of spins [1, 2]. Later, the development of concepts in the field of quantum information has brought renewed interest to the MQ experiments. The development of MQ coherences is associated with the formation of networks of correlated spins (qubits) which provides a model of a quantum register.

In general, MQ dynamics is complicated from the theoretical viewpoint, but for the linear and alternating infinite one-dimensional spin chains analytical results in the approximation of the nearest-neighbor interactions were derived [3, 4]. The interactions with only nearest neighbors preclude the development of the MQ coherences with order higher than two. The time evolution of MQ coherences represents an oscillatory exchange of the intensities of 0th and $\pm 2^{\text{th}}$ orders. In the present work we investigate the MQ dynamics experimentally in recently discovered quasi-one-dimensional alternating spin chains formed by protons in hambergite (Be_2BO_3OH) single crystals [5] and compare the results with theory.

Materials and methods

The spin chain formed by the hydroxyl protons of hambergite lies in the direction of c-axis. The protons are evenly spaced along the chain and the angle formed by a vector connecting two neighbors and the c-axis is approximately $16.7°$. In such a zig-zag arrangement the vectors connecting next nearest neighbors is exactly parallel to the c-axis. The distance between nearest neighbors in the chain is 2.312 Å. All chains lie in parallel planes. We used the crystals of natural hambergite from Malkhan pegmatite field for investigation. The crystal was cut into the plate's perpendicular to the direction of the spin chain, which can be identified by eye as longest dimension of the crystal. Then the two cylinders (samples S1 and S2) with orthogonal axes were cut from these plates. For both of these crystals the rotation of the sample corresponds to the change of the angle between the spin chain axis and the external magnetic field, but the angles formed by the filed and zigzag plane are different. When the spin chains are parallel to the magnetic field the chains are homogeneous (equal dipolar couplings with nearest neighbors). With increasing inclination angle the alternating character reveals. Two orientations in the magnetic field were chosen for MQ experiments: $10°$ for S1 and $15°$ for S2.

MQ experiments were performed on a Bruker Avance III 400 NMR spectrometer using the 8-pulse Baum-Pines sequence [1] on ^{1}H nuclei. The pulse sequence used preparation

period was $X\overline{X}\overline{X}X$, where X and $\overline{X}$ designate the phase of the pulse pair $(\Delta/2)\text{-}(\pi/2)\text{-}(\Delta')\text{-}(\pi/2)\text{-}(\Delta/2)$, gives the average MQ Hamiltonian:

$$H_{MQ} = \frac{1}{3}\left(H_{yy} - H_{xx}\right) = -\frac{1}{2}\sum_{i<j} D_{ij}\left(I_i^+ I_j^+ + I_i^- I_j^-\right)$$

where γ is the gyromagnetic ratio, r_{ij} is the distance between spins i and j, $\hbar$ is the Planck's constant, θ is the angle between the applied magnetic field and the vector connecting two spins, $I_{i\alpha}$ and $I_{j\alpha}$ are the α-projections ($\alpha = x;\ y;\ z$) of the spin angular momenta. The measurements were performed in a 2.5 mm solenoidal coil orthogonal to the external magnetic field on single-crystal samples inserted inside glass tubes at room temperature. The orientation of the crystal with respect to the external magnetic field was adjusted by the rotation of the tube around the coil axis. The duration of a $\pi/2$ pulse was 1.2 μs, duration of the 8-pulse cycle was 26.4 μs, 16 phase increments for the separation of coherences were used. The mixing period was equivalent to the preparation period with the 90° phase shift of all pulses.

Results and discussion

The long spin-lattice relaxation times in hambergite present a severe problem for an experiment. Our previous investigation has shown that T_1 values for protons are in the range of 35-46 minutes depending on the orientation of the crystal in the magnetic field. This makes the two-dimensional MQ experiments impractically long, especially when we interested in the time development of MQ coherences under two-spin/double-quantum Hamiltonian. The presence of the defects accelerating the relaxation is desirable. We introduced such defects by subjecting the crystals to gamma-ray irradiation on Gammatok-100 apparatus with the ^{60}Co source of radiation [6]. The effect of irradiation is demonstrated in Table 1 for the perpendicular orientation of the spin chains.

Table 1. Spin-lattice relaxation times measured after the irradiation with 270 Mrad

Time (days)	T_1 (s)	T_1 (minutes)
Non-irradiated	2200 ± 140	37
0	240 ± 3	4
107	470 ± 37	8
149	669 ± 13	11
254	594 ± 7	10

For the following MQ experiments we employed 500 Mrad dose. The measurements were performed right after the irradiation. The relaxation times were 211 s and 247 s for samples S1 and S2, respectively. The recovery delay was set to 660 s and 800 s for samples S1 and S2, respectively, to satisfy RD>3*T_1.

The intensities of MQ NMR coherences as a function of the preparation period for samples S1 and S2 are shown in Fig. 1. The data show oscillating exchange between zero and second order coherences. The small signals of the 4th order MQ coherences start to appear after approximately 90 μs and reach the values of 10-12% of the overall observed coherences at the largest time of 152 μs investigated in the present experiments and are not shown. The oscillatory evolution of MQ coherences in the alternating chains have more complicated character, compared to homogeneous chain, which depend on the ratio of the dipolar coupling constants. The frequency spectrum of the oscillations of 0th and 2nd order MQ coherences contain the information required to determine the dipole–dipole coupling constants in the alternating chain
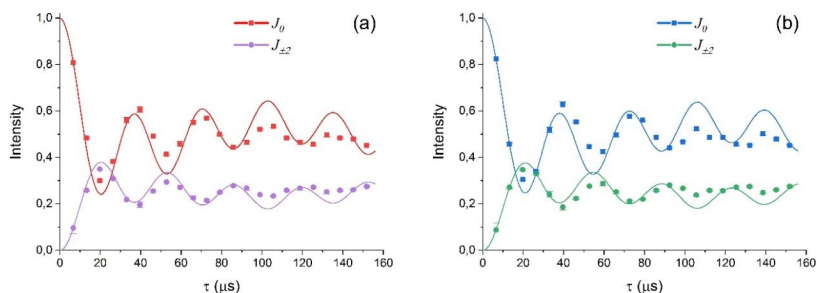
Figure 1.Comparison of the experimental MQ intensities of the 0 and ±2 order coherences (dots) with the theory (solid lines) for alternating spin chains with nearest neighbor interactions for sample S1 (a) and S2 (b)

The development of the MQ NMR coherences is restricted mostly to the oscillations of intensities between the 0 and $\pm 2^{th}$ orders showing a good isolation of the spin chains in hambergite. The character of these oscillations was ascribed to the peculiarities of MQ dynamics in the alternating spin chains according to the results of the comparison with the theory of MQ dynamics in inhomogeneous spin chains with nearest neighbor couplings developed earlier. We believe that the results will be useful in the future investigations of quantum information transport, decoherence and entanglement.

Acknowledgments

References

1. J. Baum, M. Munowitz, A.N. Garroway, A. Pines - *J. Chem. Phys.* 83, 2015–2025 (1985)
2. E.E. Burnell, C.A. de Lange, W. Leo Meerts, in: *Nucl. Magn. Reson. Spectrosc. Liq. Cryst.*, 1–35, WORLD SCIENTIFIC (2009)
3. G.A. Bochkin, E.B. Fel'dman, S.G. Vasil'ev - *Appl Magn Reson,* 53, 1439–1448 (2022)
4. S.G. Vasil'ev, A.V. Fedorova, E.B. Fel'dman - *Appl Magn Reson*, 52, 831–842 (2021)
5. G.A. Bochkin, E.B. Fel'dman, E.I. Kuznetsova, I.D. Lazarev, S.G. Vasil'ev, V.I. Volkov - *J. Magn. Reson.* 319, 106816 (2020)
6. D.P. Kiryukhin, G.A. Kichigina, S.R. Allayarov, E. R. Badamshina - *High Energy Chem,* 53, 228–237 (2019)

Electrophoretic NMR and applications

Pavel Yushmanov

P&L Scientific, Stockholm, Sweden
E-mail: pavel@plscientific.se

Electrophoretic NMR (eNMR), having been introduced more than 30 years ago, is a useful yet not very widespread methodology. It is based upon applying a voltage and thereby an electric field across the sample volume. When done so, ionic species are set into motion that can be detected by experiments exploiting pulses of magnetic field gradients that are parallel to the direction of the applied electric field. Hence, pulse sequences of eNMR experiments are often similar to those of diffusion NMR experiments with the major differences being (i) the need for electric field pulses and (ii) the information in the form of electrophoretic mobilities μ extracted from the signal phase instead of signal attenuation[1,2].
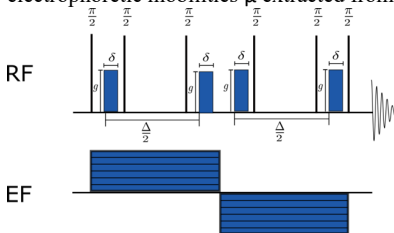
Fig.1. Electrophoretic NMR (eNMR) pulse sequence is based on pulsed field gradients, akin to diffusion NMR
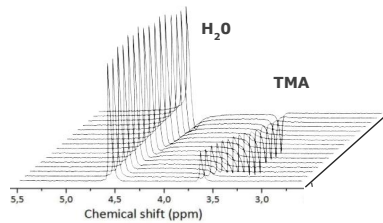
Fig.2. Resulting series of spectra for TMA in D_2O solvent

eNMR is a desirable methodology for determining μ because of the unparalleled chemical selectivity of the detection method NMR. Also, based on the results of the e-NMR experiment, one can determine the electrophoretic mobility of particles, their charge, and belonging (association with other particles, etc.). A wide range of materials studied - electrolytes, gels, ionic liquids, and all kinds of ionic solutions - determines the great practical importance of this method.

Possible applications include:

- optimization of electrolyte parameters for modern batteries, in particular, those based on ionic liquids and gels
- determination of the structure of substances, in particular, complex ionic solutions
- determination of properties and search for hidden phase transitions of process fluids
- study of biomolecules and their association
- study of the structure of supramolecular complexes according to the degree of their charge
- study of proton conductivity in Nafion membranes
- study of solid electrolytes

Thus, the e-NMR method is of great importance for the following applications [2]:

- Fundamental and applied research in the field of physical, organometallic, and analytical chemistry, as well as biotechnology
- The pharmaceutical industry and applied research of properties and materials
- Development of battery and fuel cell technology
- Studying the properties of various process fluids used as cleaning, lubricants, etc.

While the capability of applying field-gradient pulses is commonplace in modern NMR spectrometers, applying electric field pulses requires additional instrumentation that is

commercially less widespread. The additional instrumentation encompasses both suitable power supplies providing the electric field pulses and probe arrangements that enable the electric field to be applied over the chosen sample volume.

Our company has developed the complete set of eNMR equipment that is presently distributed worldwide in various NMR research laboratories and research centers [3].

$$\mu = \frac{\phi}{\gamma \delta g \Delta_E E} \qquad z = \frac{\mu k_B T}{De}$$
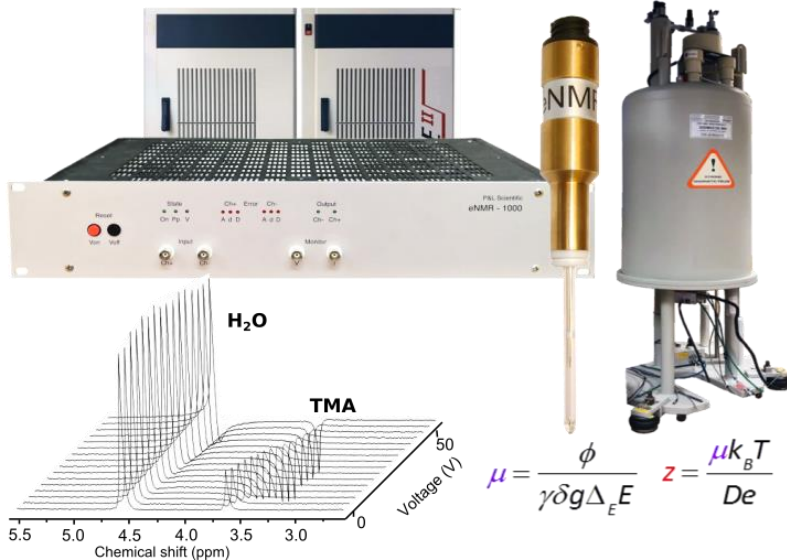
Figure 3. The complete set of eNMR equipment including Bruker NMR spectrometer and magnet

However, even when the required instrumentation is at hand, eNMR suffers from some limitations that, so far, severely restricted eNMR experiments in terms of permissible samples and phenomena. Various forms of motional artifacts constitute the most important limitations. In very conductive samples, the electric field, while setting the ions into motion, also generates an electric current that leads to Joule heating and, typically, to a temperature gradient that in turn results in thermal convection [5, 6]. This constitutes the first motional artifact. The second artifact is electroosmosis which appears in a manner that is strongly dependent on the sample, and the material and dimensions of the sample container [4]. The third major artifact is the electrode reactions that also produce gases and yields bubbles that may detach from the electrodes and travel through the signal-yielding volume.

Various solutions were developed to diminish those artifacts. Among others, those are:

- Coating the sample tube with the slightly conductive media to reduce electroosmosis [5]
- Using the Carr-Parcell version of eNMR pulse sequence [4]
- Well-symmetric construction of eNMR cell [2]
- Installation of the porous plug in the bottom of the eNMR sample and performing the experiment in current stabilization mode [1]

As result, the achieved values of the recorded phase shifts may allow the so-called 2D electrophoretic mobility ordered spectroscopy (2D-MOSY) where the resulting 2D spectra are provided by Fourie transform in the F1 direction. For certain samples, this approach is beneficial vs. DOSY providing a better selection of the components in the F1 axis [7].
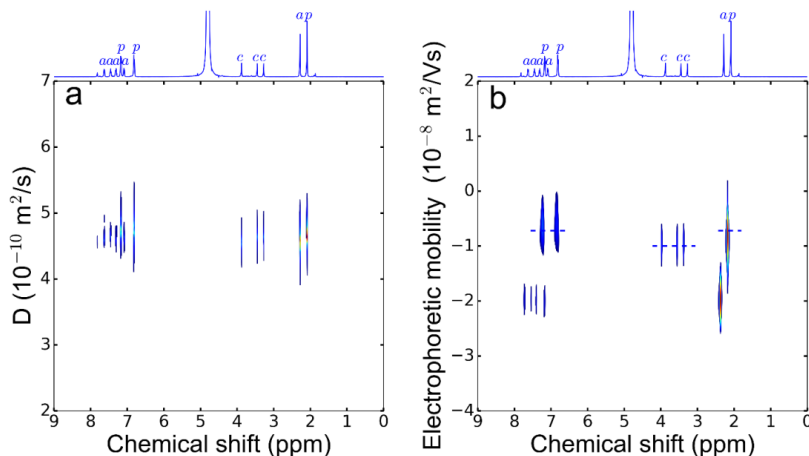
Figure 4. (a) - 2D-MOSY vs. (b)- 2D- DOSY analysis of components of Thomapyrin medical substance

References

1. Yuan Fang, Pavel V. Yushmanov, István Furó, Improved accuracy and precision in electrophoretic NMR experiments. Current control and sample cell design. Journal of Magnetic Resonance 318 (2020) 106796
2. P. Stilbs, Diffusion and electrophoretic NMR, De Gruyter, Berlin, Boston, 2019.
3. http://plscientific.se/?eNMR/References-and-selected-literature
4. M. Bielejewski, M. Giesecke, I. Furó, On electrophoretic NMR. Exploring high conductivity samples, J. Magn. Reson. 243 (2014) 17–24.
5. F. Hallberg, I. Furó, P.V. Yushmanov, P. Stilbs, Sensitive and robust electrophoretic NMR: instrumentation and experiments, J. Magn. Reson. 192 (2008) 69–77.
6. E. Pettersson, I. Furó, P. Stilbs, On experimental aspects of electrophoretic NMR, Concepts Magn. Reson., Part A 22A (2004) 61–68.
7. Y. Fang, P. V. Yushmanov, and I. Furó, Assessing 2D electrophoretic mobility spectroscopy (2D MOSY) for analytical applications, *Magn. Reson. Chem.* **55** doi: 10.1002/mrc.4558 (2017).

Quantum Diamond Atomic Force Microscope

High quality diamond probe

Quantitatively non-invasive magnetic imaging

High magnetic field sensitivity ~1 uT/(Hz 1/2)

High spatial resolution ~ 10 nm

50 ps timing accuracy

Compatible with both ambient conditions and low temperature high vacuum

Quantum Diamond Atomic Force Microscope (QDAFM) is a magnetic imaging instrument based on both NV center in diamond and AFM scanning imaging technology. By quantum control and readout of the spin state in the diamond probe, the magnetic property of samples is acquired quantitatively and non-invasively. With nanoscale spatial resolution and ultra-high detection sensitivity, QDAFM is an nnovative technology to develop and study magnetic textures, high-density magnetic storage, and spintronics.

QDAFM has extensive applications in material science, biology, physics and so on.

element-msc.ru

Moscow	Ekaterinburg	Novosibirsk
(495) 514-00-47	(343) 278-34-64 (-65-69)	(383) 21-12-726
msc@element-msc.ru	ekb@element-msc.ru	nsk@element-msc.ru

Oral Reports

Technological applications on a 0.5T clinical MRI scanner

Nikolay V. Anisimov[1], Arina A. Tarasova[2], Ivan A. Usanov[2], Olga S. Pavlova[1,2],
Mikhail V. Gulyaev[1], Yury A. Pirogov[2]
[1]*Faculty of Fundamental Medicine, Lomonosov Moscow State University, 119991, Russia*
[2]*Faculty of Physics, Lomonosov Moscow State University, 119991, Moscow, Russia*
E-mail: anisimovnv@mail.ru

Introduction/Purpose

Typical magnetic resonance (MR) scanners are focused on medical diagnostics - non-invasive imaging of human organs. MRI also has significant potential for technological applications – material diagnostics, MR microscopy, food analysis, etc. The purpose of this work was to test some of these applications. In particular, the visualization of objects that do not directly give an NMR signals, including metal objects. We did not find publications with corresponding illustrations. So we took measurements to make up for the lack of demo material. It was supposed to use multinuclear methods for this – detection of not only protons (^{1}H), but also fluorine (^{19}F) and sodium (^{23}Na) nuclei. The measurements were carried out on a clinical MRI scanner with a field of 0.5 Tesla. This is a relatively low field, which makes it difficult to detect weak signals. In our case, this is relevant – the molar receptivity of the ^{23}Na isotope is 10.8 times less than ^{1}H, and the signal from fluorine is detected from the gase perfluorcyclobutane (PFCB, C_4F_8), whose density is 113.4 times less than for water. And the detection of proton signals from some of the solid objects we studied was difficult because of the short transverse relaxation times – T_2=4 ms. But since in our case, there are no fundamental limitations on the scanning time, it was supposed to obtain acceptable results by repeatedly accumulating the signal.

Materials and Methods

The experiments were carried out on a 0.5T clinical scanner Bruker Tomikon S50. The spins were excited by a linearly polarized RF field from a coil 60 cm in diameter built into the gap of the magnet. MR signals were received on modified proprietary coils, some of which were tuned to the Larmor frequencies of ^{23}Na and ^{19}F [1]. Scanning was carried out using the gradient echo method with the following parameters: TR/TE=26/3.5 ms (^{1}H), 50/14 ms (^{23}Na), 100/10 ms (^{19}F). Flip angle was set equal to 10° when detecting protons, and 90° when detecting ^{23}Na or ^{19}F nuclei. Accordingly, the voxel size (VS) was 1 mm^3 and 8 mm^3, and the scanning time was 10 min and up to 3 hours.

Results

1. MRI of coils

We obtained images of the probeheads used in MRI studies - specialized coils. Figure 1 shows images of proprietary coil designed for scanning human head. The MR signal was detected by the same coils, and the signal sources were their own facing and fastening elements made of hydrogen-containing materials – plastics.
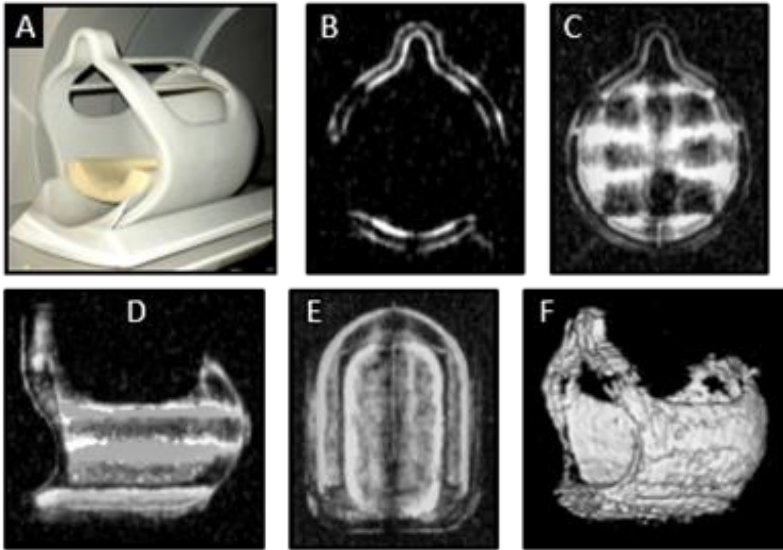
Figure 1. MRI of proprietary coil designed for scanning human head. A - photo of the coil at the magnet bore; B- individual slice; C, D, E - 3D MIP reconstructions; F - 3D rendering

2. MRI of metal and glass products

We obtained three-dimensional images of objects that do not directly give an NMR signal, including metal objects. We did this in two ways - by applying a hydrogen-containing substance to their surface - the method of surface application, as well as by the loss of a signal on the image when the object is immersed in a homogeneous, chemically neutral medium, which gives a powerful background NMR signal - signal void imaging (SVI) [2]. If, before 3D reconstruction, individual clusters in the data matrix are zeroed out, then unusual images of the object can be obtained, showing what a object would look like, if processed with some fantastic tools – for example, drilled (Figure 2D).

Figure 2. MRI of a glass goblet (B, C, D) and copper-silver goblet (F, G). A and E - photos of the goblets; B, F - central slices of the MR images; C, D, G - volumetric reconstructions 3D rendering

3. Incorporating text in an MR image using the surface application method

We applied the surface deposition method to incorporate textual information on the MR image. To do this, a suitably arranged set of plastic molds from a children's kit for learning the alphabet, filled with petroleum jelly, was placed next to the scanned organ.
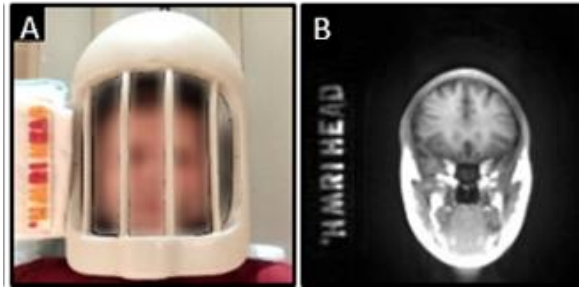
Figure 3. A – text elements for forming the text "1H MRI HEAD" an MR image are arranged to the right of the patient's head; B – MR image containing both diagnostic material and text.

4. Detection of ^{1}H, ^{19}F and ^{23}Na nuclei in the SVI method

We have shown that in the SVI method, the background medium can be not only hydrogen-containing (H_2O), but also containing sodium (NaCl solution) or fluorine (C_4F_8 gas), whose magnetic isotopes can be used to implement the method. If not for the problem with sensitivity, then the gas environment is preferable, since not all objects can be immersed in the aquatic environment without irreversible changes for them [3]. It is not the case for metal objects that we scanned by immersing them in water – Figures 2, 5, because the signal from it is two orders of magnitude stronger than from the gas, which simplifies its detection.
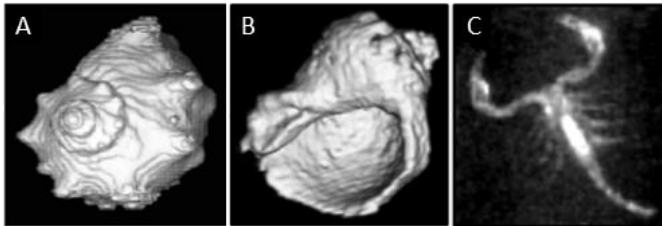
Figure 4. MR images obtained by SVI method using salt water – A -^{1}H MRI, B ^{23}Na MRI and PFCB gas – C - ^{19}F MRI. A and B - 3D rendering of a shell of mollusk (Bursa lissostoma); C – 3D MIP reconstruction of a dried scorpion (Palamnerus).

5. Resonance effects from a solenoid immersed in water

When scanning metal solenoids in the water, the possibility of amplifying the signal inside the solenoid by at least 3 times was noted. The analogy with a wireless coil, the oscillatory circuit of which is formed by lumped LC elements, can be seen [4]. In our case, these elements are not lumped. In particular, the role of the electric capacitance is performed by the filling liquid - water. An increase in the electrical conductivity of water due to impurities has the opposite effect - a decrease in the signal inside the solenoid. It is of interest to construct an adequate model of such a circuit with distributed parameters to assess its potential opportunities.
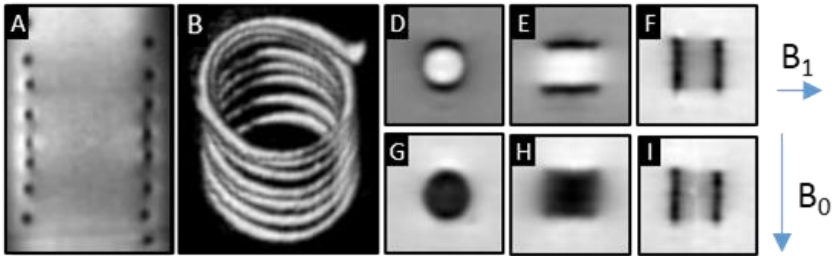
Figure 5. MRI of solenoid using the SVI method: A - individual slice (VS=1 mm^3), B – 3D rendering, D-I - images of the solenoid (VS=8 mm^3) in the coronal projection with different coil orientations relative to B_0 and B_1 (indicated by arrows); G-I - similar to D-F, but the ends of the solenoid are electrically connected by a thin wire.

Conclusion

In addition to obtaining volumetric reconstructions of objects from which it is difficult to obtain an NMR signal, developed approaches can be used to refine the design of MRI coils (probeheads), incorporate textual information into an image, and develop wireless coils without lumped capacitance.

Acknowledgments

References

1. N. V. Anisimov, et al. - *Appl. Magn. Reson.*, 52, 221-233 (2021).
2. N.V. Anisimov, S.S. Batova, Yu.A. Pirogov, Magnetic Resonance Tomography: Contrast Control and Interdisciplinary Applications, (MAKS Press, Moscow, 2013), p. 244.(*in Russian*)
3. N. V. Anisimov, et al. - *Appl. Magn. Reson.*, 53, 1575-1585 (2022).
4. M. Schnall, et al. - *J. Magn. Reson.,* 68, 161-167 (1986).

Multi-Echo Spin Echo based T_2 mapping: how can we handle the issue of variations among slices?

Zilya Badrieva[1], _Ekaterina Brui[1], Charles-Alexis de Manenne[2], Stanislas Rapacchi[3], Thomas Troalen[4], David Bendahan[3]_

[1]*School of Physics and Engineering, ITMO University, Saint Petersburg, Russian Federation*
[2]*Paris Science et Lettres, E´cole Supe´rieure de Physique et de Chimie Industrielle de la ville de Paris, Paris, France*
[3]*Centre de R´esonance Magn´etique Biologique et M´edicale, Aix-Marseille Universite, CNRS, Marseille, France*
[4]*Siemens Healthcare SAS, Saint-Denis, France*
E-mail: zilia.badrieva@metalab.ifmo.ru

Multi-echo spin-echo (MESE) pulse sequence is one of the most frequently used methods for T_2 mapping [1]. However, several limitations such as the presence of stimulated echo signals leading to distorted signal decay curves and biased T_2 values when fitted using an exponential function have been acknowledged. An original fitting method based on a preliminary simulation of MR signal decay curves (signal versus TE, or echo modulation curves - EMC) has been recently proposed [2]. This method allows generating a dictionary which is related to a set of EMC curves for a range of T_2 values and RF magnetic field (B_1^+) inhomogeneities and so for a particular pulse sequence. The experimentally obtained data can then be compared to the EMC curves from the dictionary so as select the best matching EMC curve and the corresponding T_2 value. However, limitations related to the variations between slices could be expected. Indeed, dictionaries have been generated for a single slice. During multi-slice acquisitions one can expect slice interference effects to occur and lead to T_2 biases. We have previously shown [3] that the use of MESE in a multi-slice mode with zero gap between slices led to T_2 biases among slices likely resulting from slice cross- talk effect.

The aim of the present study was to propose an improved version of the EMC method that takes into account slice-interference effects and allows reducing T_2 biases for multi-slice measurements.

Experiment

Agarose-based phantoms (Eurospin, Diagnostic Sonar, Livingston, UK) with $T_1 = 336.1/672.5/1235.2$ ms and $T_2 = 95.7/110.5/166.3$ (ground truth values) were scanned at 3T (Magnetom Vida, Siemens, Erlangen). Parameters of the MESE pulse sequence were as follows: TR = 2 s, first TE=11 ms, inter echo time = 11 ms, number of echo signals = 8, slice thickness = 2 mm, number of slices = 5, inter-slice gap = 0. This resulted in 8 multi-slice images for each phantom with different T_2 weighting. Thus, for each pixel in each slice of the phantom, a separate experimental EMC curve could be obtained.

Time-dependent changes of the magnetization during the MESE sequence was simulated using Bloch equation simulator [4] in one spatial dimension (z – slice selection direction). In order to take into account the slice cross-talk effect, a home-built Matlab simulating a multi-slice MESE acquisition was created. The multi-slice imaging mode implied a sequential acquisition of the signal from 5 slices in an interleaved order (1-3-5-2-4) within one TR. In other words, the third slice was excited after a TR/5 time delay from the excitation of the first slice, the fifth – after TR/5 time delay from the third slice, etc... For the simulation scheme, the magnetization was initially excited and repeatedly refocused in the first slice (including the area surrounding the slice) and let to freely evolved until TR/5. At this point, the magnetization profile was shifted by a distance equal to Δz = 2*slice thickness +2*slice gap thereby providing the initial conditions for the excitation of the third slice. The same principle was applied for the remaining slices, and the whole procedure was repeated for

55

several TR cycles in order to achieve steady state. This code allowed us to generate EMC dictionaries in both single-slice (without slice cross-talk, as originally proposed [2]) and multi-slice modes. Parameters of the dictionaries were as follows: B_1^+ = [80:1:120] %; T_2 = [90:1:240] ms for the phantoms № 1 and 2, and T_2 = [50:1:180] ms for the phantom # 3. After that, experimental EMC curves were matched (minimal L2-norm) with the single-slice and multi-slice dictionaries.

As a result, 2 T_2 maps were obtained for each phantom: when multi-slice data were fitted with single-slice dictionary (MS), and when multi-slice data were fitted with multi-slice dictionary (MM) (Figure 1). Figure 2(a) depicts the mean T_2 values measured in regions of interest (ROIs) in 5 slices of the phantom images. Coefficient of variation (CV) of the mean T_2 values was calculated among five slices as follows:

$$CV = \frac{SD_{T2}}{\frac{\sum_{i=1}^{N} T2_i}{N}} * 100\%$$

where T_{2i} - T_2 value measured from the slice number i, SD_{T2} – standard deviation of T_2 values computed in 5 slices and N = 5 is the quantity of slices.

The results are provided in Table 1. For the 3 phantoms, the second fitting approach (MM) led to a reduction of coefficient of variation. The most prominent effect was observed for phantom № 3, having the longest T_2 and T_1 times.
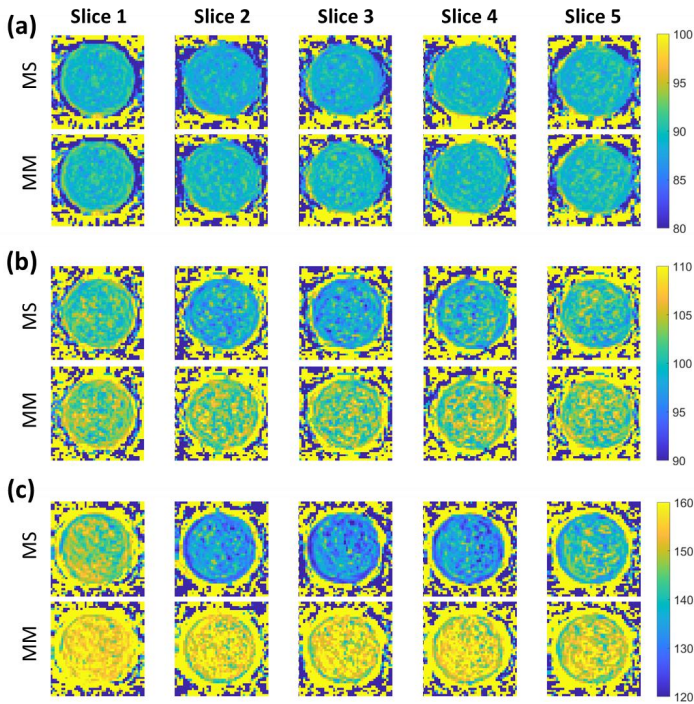
Figure 1. T_2 maps of phantoms based on multi-slice MESE: a) phantom № 3, b) phantom № 8, c) phantom № 15.

Table 1. Coefficient of variation of T_2 among 5 slices, %

Phantom №	1	2	3
MS	0.47	1.36	4.14
MM	0.29	0.26	0.65

In addition, relative error of T_2 estimation was calculated as:

$$\Delta T2_{GT} = \frac{\sum_{i=1}^{N}(T2_i - T2_{GT})}{N * T2_{GT}} * 100\%$$

where $T2_{GT}$ is the ground truth T_2 value. The results are depicted in Figure 2 (b) as a function of T_2 values. Our approach was related to a reduction of the relative errors for all phantoms, especially for phantom № 3: from -16.6% in MS case to -6.8% MM case.
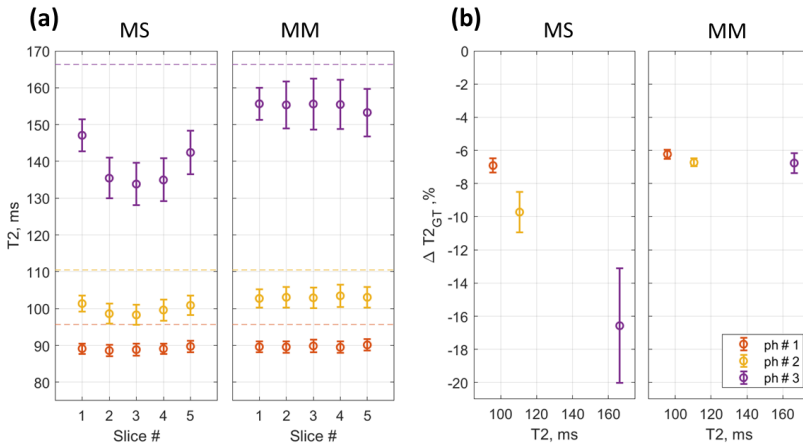
Figure 2. a) T_2 values extracted from T_2 maps based on multi-slice MESE. Horizontal dashed lines correspond to ground truth T_2 values. b) Errors of the multi-slice T_2 estimation with respect to the ground truth T_2 values.

Conclusions

In this work, an improved method for EMC dictionary generation taking into account slice cross-talk effect has been proposed. Experimental MESE data were matched to the generated EMC curves, and the multi-slice T_2 maps were obtained. Supportive of an improvement of the previously proposed single-slice dictionary method, a reduction of both inter-slice T_2 coefficients of variation and relative T_2 errors was reported.

Acknowledgments

References

1. Juras, V., Bohndorf, K., Heule, R., Kronnerwetter, C., Szomolanyi, P., Hager, B., Trattnig, S. (2016). A comparison of multi-echo spin-echo and triple-echo steady-state T_2 mapping for in vivo evaluation of articular cartilage. European radiology, 26, 1905-1912.
2. Ben-Eliezer, N., Sodickson, D. K., & Block, K. T. (2015). Rapid and accurate T_2 mapping from multi–spin-echo data using Bloch-simulation-based reconstruction. Magnetic resonance in medicine, 73(2), 809-817.
3. Badrieva, Z., Brui, E., de Manenne, C. A., Rapacchi, S., Troalen, T., & Bendahan, D. (2022, November). Effect of multi-slice MESE acquisition on inter-slice T_2 variability. In 2022 IEEE International Multi-Conference on Engineering, Computer and Information Sciences (SIBIRCON) (pp. 570-574). IEEE.
4. Bloch Equation Simulator: http://www-mrsrl.stanford.edu/brian/blochsim/

Structural studies of human semen amyloid peptides by NMR spectroscopy and molecular dynamics

Daria A. Osetrina, Maria O. Abramova, Aleksandra M. Kusova, Aydar R.Yulmetov, Aydar G. Bikmullin, Evelina A. Klochkova, Vladimir V. Klochkov, Dmitriy S. Blokhin
Kazan Federal University, Kremlevskaya Str., 18, 420008 Kazan, Russia
E-mail: dblohin@kpfu.ru/dmitr.blokhin@gmail.com

Amyloid fibrils were discovered in human semen. It was found that these fibrils are involved in the process of increasing the probability of HIV infection [1]. The surfaces of the semen amyloid fibrils are positively charged. Thus, semen amyloids increase the probability of HIV infection, by reducing the electrostatic repulsion between the HIV virion and the target cell [2, 3]. Semen amyloids consist of peptide fragments of three semen proteins: prostatic acid phosphatase (PAP), semenogelin 1 (SEM1), and semenogelin 2 (SEM2) [4]. Nine peptide fragments were identified: PAP(248-286), PAP(85-120), SEM1(45-107), SEM2(45-107), SEM1(49-107), SEM2(49-107), SEM1(68-107), SEM2(68-107), and SEM1(86-107). Structural studies of amyloid fibrils by experimental methods are difficult. Therefore, the main method for their study is molecular simulations of amyloids. To run the calculations, the structure of the peptides is required. In this regard, for the study of amyloids, an actual task is to establish the spatial structure of amyloid peptides.

In our work we studied spatial structure of human semen amyloid peptides. To study peptides in solution, the methods of nuclear magnetic resonance spectroscopy, circular dichroism spectroscopy, and molecular dynamic simulations were used. We had studied structures of peptides: PAP(85-120), SEM1(86-107), SEM1(68-85), SEM1(68-107), and the structure of the SEM1(86-107) peptide in solution with dodecylphosphocholine micelles. Micelles acted as a model of membrane charged surface. The obtained results are planned to be further applied to the simulations of semen amyloids.

Acknowledgments

References

1. J. Munch, et al., Semen-derived amyloid fibrils drastically enhance HIV infection. Cell, 2007, Vol. 131(6), P. 1059–1071.
2. J. Münch, et al., Effect of semen and seminal amyloid on vaginal transmission of simian immunodeficiency virus. Retrovirology, 2013, Vol. 10(148), P. 1–9.
3. P. Rusert, et al., Quantification of infectious HIV-1 plasma viral load using a boosted in vitro infection protocol. Virology, 2004, Vol. 326(1), P. 113-129.
4. N.R. Roan, et al., Peptides released by physiological cleavage of semen coagulum proteins form amyloids that enhance HIV infection. Cell Host Microbe, 2011, Vol. 10(6), P. 541–550.

NMR to Industry: developing the portable NMR solution

Bystrov S. S. [1,2], Khrustalev A.A. [3], Kirilenko V. D. [4], Zolotov D. R. [5]
[1]*Department of Nuclear-Physics Research Methods, St. Petersburg State University*
[2]*LLC "TerraQuantTech" (VAT Number: 7819045984), Peterhof, Saint-Petersburg*
[3]*Bachelor of Engineering in Mechatronics And Robotics, ITMO University*
[4]*Wydział Matematyki i Informatyki, Uniwersytet Łódzki, Łódź, Poland*
[5]*TRASSIR GLOBAL FZC, LLC "DSSL" (Digital Security Systems Lab), Moscow, Russia*
E-mail: terraquanttech@gmail.com
http://terraquant.tech

Introduction

During the past decades, NMR has established itself as a powerful and versatile tool in terms of chemical and structural research tasks. NMR has proved to be an indispensable method for diagnosing diseases, a method unrivaled by any other in a wide range of applications: scaling from the level of simple molecules to complex biological systems.

Unfortunately, despite the vast potential in obtaining of all kind of useful information, in practice it turns out that the widespread implementation of the NMR technique for solving household and industrial problems is greatly hindered by the enormous price of NMR facilities caused by the high cost of superconducting magnets as well as the imminent need to bear regular expenses for the maintenance of the highly qualified personnel and keeping spectrometers performance at its operational level.

However, possible implementation of NMR research methods at different stages of technological processes, at intermediate stages of production chains in a wide variety of modern industries (from food to oil refinery) - is an up-and-coming and seemingly underestimated area [1], which can lead to a reduction in the cost of products for the end consumers, as well as to the improvement of quality control in production, provided that it is possible to reach a compromise concerning the main shortcoming of NMR - high costliness.

Market demand

Despite the established attitude to the issue described above, researchers and entrepreneurs in different parts of the world, are still making consistent attempts to introduce technologies based on nuclear magnetic resonance albeit focusing on highly specialized areas [2]. At the moment, a more or less developed direction on the market aimed to increase the affordability of NMR spectrometers for small enterprises, is associated with the advent of benchtop NMR spectrometers. Most of the major players in the NMR market have already presented their variations of such devices, incl. Magritek's Spinsolve, Nanalysis, Oxford Instruments and Bruker Fourier 80.

From general point of view all representatives of this type of devices have a rather similar design in core: they all have a powerful electromagnetic coil or permanent magnet inside developed for resonant frequencies of the order of 60-90 MHz (Magnetic field strength 0.3-1.5T) and as a consequence having an imposing weight in a range from 60 to 100 kg. Furthermore, samples are measured using standard 5 mm NMR tubes and spectrometers are controlled through an external computer, thus, almost completely reproducing the way operator interact with the instrument as for the case of a full-ledge superconducting spectrometers from the same manufactures.

Furthermore, these devices do not solve the problem of the affordability of spectrometers in any way; they still require a significant amount of money per item (average benchtop solution are distributed at a price of 50k to 120k dollars apiece), yet have a number of significant drawbacks: such as strong temperature dependence of the magnets used to generate the main magnetic field which, in turn, additionally forces the user to place the

device on some special mounting plate or portable trolleys with continuous power supplies and a bunch of cables into the bargain.

Modern solution

A more modern approach to expanding the coverage of nuclear magnetic resonance possible areas of application (as well as all other resonant research methods) is to maintain the focus while developing solution on a particular specific consumer demand, leading, as a consequence, to a significant reduction in the market cost of spectrometers on the world market in general, due to an overall increase of the appearance of such devices in various enterprises workflow.

There are several possible realizations of creating artificial demand in "measurement instruments" markets ones may find already over-crowded.

The first approach is to fully target the development process on one specific industry area consistently fulfilling all the tricky problems that area may have faced. A striking example of the successful application of the such approach is SpinLock (Argentina)[4]. Since the beginning of 2006, this company has succeeded in developing and implementing multiphase in-line flow NMR analyzers in most Argentina oilfields that allow continuous NMR measurements and phase separation of oil components using a 4-inch drill located directly inside the oilfields.

Another notable example is Fine Instrument Technology (FIT) (Brazil). The research group was able to develop a simple but effective approach in quantifying macro-characteristics of various components of food products (in particular, the chemical composition of the Brazil nut, on the basis of which many by-products are made in Brazil, such as nut milk) using an ultra-low-field spectrometer manufactured within the same company (SpecFIT Spectrometer, 0.33 T, probe diameter 40 mm) and classic spin-echo pulse sequence (TD-NMR) [5]. It is worth noting that due to the fact that the team of researchers was able to persuasively demonstrate the effectiveness of their approach in the separation of the aflatoxin components, it was accepted by the Brazilian Health Regulatory Agency (ANVISA) as a normative approach for determining the quality of nuts in the country. The presence of aflatoxins, produced by fungi (e.g., *Aspergillus Flavus*, *A. Nomius*, and *A. Parasiticus*) has been shown to be associated with human liver cancer.

Portable NMR analyzer

The second approach to expand the potential customer base is to effectively minimize the final product cost while trying to maintain the maximum accuracy that the instrument can provide as much as possible. A self-cost advantage of one or more orders in magnitude (e.g. 8k dollars per item) relative to competitive benchtop NMR instruments could open up the opportunity for many small and medium-sized entrepreneurs as well as small scientific groups and other enthusiasts not only to finally try one of the most potent research methods in their business processes without unacceptable expenses, but also due to the fact that a much more significant amount of people will be able to buy that spectrometer, it may potentially reveal some new previously unknown aspects of nuclear magnetic resonance.

A reasonable question immediately arises, how to achieve such characteristics of the device. In the proposed solution, we tried to combine several modern technologies that have not been used in NMR spectrometers before.

First of all, in order to get an inexpensive device, we use the field of our planet as an external magnetic field; it is homogeneous and can be accessed everywhere on the planet. On the other hand, NMR in the Earth's field for a long time was extremely unclaimed, because it requires many conditions to be met in order to carry out the experiment correctly. First, the strength of the Earth's magnetic field has a relatively small absolute amplitude (of the order of 50 μT), which imposes strict requirements on the design of the measuring coil of the device.

Therefore, during the development process, we have put together several options for the implementation of measuring coils, highly compensated from external electromagnetic interference. Thus, we managed to obtain good noise immunity.

Secondly, the Earth's field is constantly fluctuating, which means that the value of its magnetic induction constantly floats over time. To solve this problem, we have developed an automatic matrix of 14 capacitors on short reed relays, which, together with a ring of four 4-axis magnetic sensors, allows one to continuously tune to the current resonance frequency in Earth field at any given point in space and do not receive significant attenuation of the NMR signal during the experiment.

Thirdly, a system of two orthogonal shimming coils was implemented in the device in order to create a linear field gradient inside the measuring coil; this allows one to work with our device even indoors, in a case when the resulting magnetic field inside the room differs from the actual Earth magnetic field value, i.e., where it is significantly challenging to obtain a long NMR signal.

Fourth, in order to obtain a complete information about the substance under study, a system of two orthogonal excitation coils was implemented, making it possible to carry out not only NMR spectra measurements, but also relaxometric studies on the device.

Fifth, even despite all the engineering and technical optimizations that were applied to the device, the NMR signal is still quite noisy (S/N = 30), so to implement an effective classification algorithm based on the raw signals received, we developed and included in the device firmware a multimodal neural network classifier that allows you to predict the characteristics of a substance faster and more accurately than with the classical accumulation of spectra.

Acknowledgments

References

1. "Process NMR Spectroscopy: Technology and On-line Applications" John C. Edwards, and Paul J. Giammatteo, Chapter 10 in Process Analytical Technology: Spectroscopic Tools, Blackwell-Wiley, 2010
2. "A Review of Applications of NMR Spectroscopy in Petroleum Chemistry" John C. Edwards, ASTM Books, 2011.
3. J. Braz. Chem. Soc. vol.32 no.7 São Paulo, July 02, 2021, https://doi.org/10.21577/0103-5053.20210039
4. Inline NMR relaxometry for complex multiphase (Oil/Gas/Water) flow metering. The potential to solve a historical and industry-wide challenge", Dante Pusiol (Spinlock), Proceedings of the conference "BENCHTOP NMR: FROM ACADEMIA TO INDUSTRY"
5. "Process and Quality control in food and agroindustry using TD-NMR", D. Consalter, Proceedings of the conference "BENCHTOP NMR: FROM ACADEMIA TO INDUSTRY"

Homoconjugated anions of phosphoric and phosphinic acids: spectral and structural peculiarities probed by low-temperature NMR spectroscopy

Edem R. Chakalov[1] and Peter M. Tolstoy[1]

[1]*Institute of Chemistry, Saint Petersburg State University, Saint Petersburg, Russia*
E-mail: st086266@student.spbu.ru

Introduction

Hydrogen bonding (H-bonding) is ubiquitous and profoundly influences numerous chemical and solvation processes and is paramount in the understanding of molecular structure. Phosphorous-containing acids (phosphoric, phosphinic and phosphonic) in H-bonded complexes can act simultaneously as a proton donors and acceptors possessing POH and P=O groups. A number of works dedicated to the study of electroneutral self-associates [1] and heteroassociates [2] of phosphorus-containing acids in solid, liquid and gas phase have been published so far by some of us (Fig. 1).

The homoconjugated ions, *i.e.* H-bonded complexes of acids (bases) with their conjugate bases (acids) are of fundamental interest being one of the most famous types of complexes with the shortest and strongest hydrogen bonds (HBs) [3]. It is assumed that homoconjugated anions (HCAs) of phosphorus-containing acids are formed in several practically important systems, including polymer electrolyte membrane fuel cells based on polyphosphoric acids [4], reactions of asymmetric organocatalysis by chiral organophosphorus acids [5], as well as proton-coupled electron transfer reactions [6]. Nevertheless, the homoconjugation phenomena of phosphorus-containing acids remains poorly studied: there are very few publications discussing their structure as well as mutual influence (cooperative effects) of HBs in HCAs of non-equimolar composition [7].
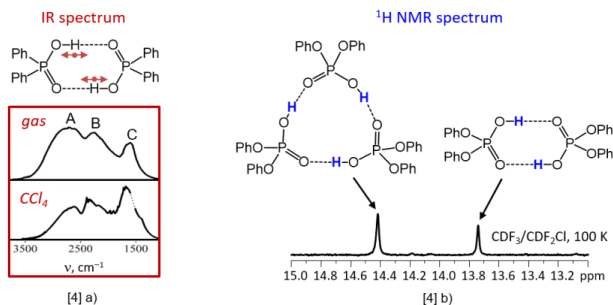
Figure 1. Examples of POOH-containing acids self-associates.

Methods and objects

The low-temperature liquid NMR spectroscopy remains one of the most informative methods for studying H-bonded complexes: their lifetime increases by slowing down the dynamic processes of proton and molecular exchange [8]. Thus, it becomes possible to observe resolved bridging proton signals of complexes of different stoichiometry (including isotopologues) and conformation.

We have studied the HCAs of diphenylphosphoric (**1**), dimethylphosphoric (**2**), diphenylphosphinic (**3**) and phenylphosphinic (**4**) acids (Fig. 2) by low-temperature ^{1}H and ^{31}P{^{1}H} NMR spectroscopy (solvent: liquefied freon CDF_3/CDF_2Cl mixture, temperature down to 100 K). Comparison of relative integral intensities in pair-wised ^{1}H and ^{31}P{^{1}H} NMR spectra of the samples with different acid/base ratio reveals the stoichiometry of the

HCAs and allows one to compare the cooperativity effects on their coupled HBs. Experiments have been supplemented by density-functional theory (DFT) calculations, including a numerical solution of the Schrödinger equation for bridging particle (proton and deuteron) motion in the anharmonic double-well potential to predict the expected values of primary and secondary H/D isotope effects.
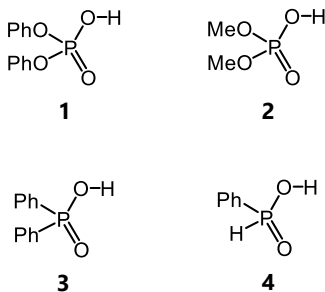
Figure 2. Phosphorus-containing acids studied in this work.

Results and discussion

As an example, in Fig. 3 we show the pair-wised ^1H (low-field part) and $^{31}P\{^1H\}$ NMR spectra of **3** with 1,8-*bis*(dimethylamino)naphthalene (DMAN; an efficient and kinetically inert in NMR time scale organic superbase used for the synthesis of HCAs [9]) with different acid/base ratio at 100 K.
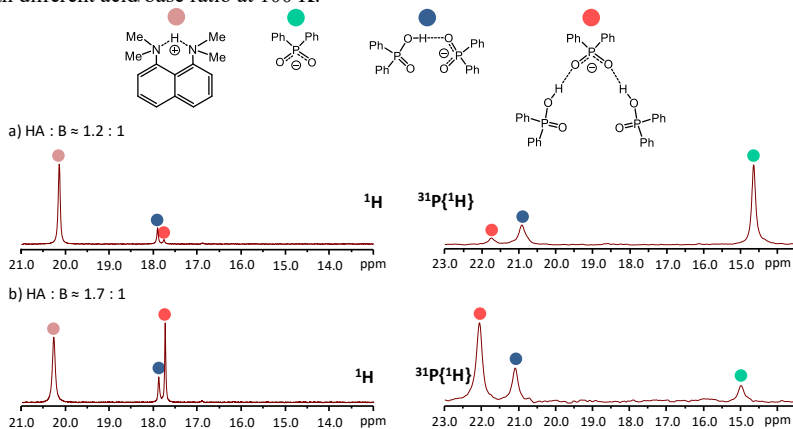
Figure 3. Pair-wised ^1H and $^{31}P\{^1H\}$ NMR spectra of the sample discussed in this work.

The observation of ^1H single signal of the HCA of $(AH)_2A^-$ type indicates the chemical equivalence of two bridging protons, characteristic for the "head-to-head" complexation type, $[A–H\cdots A\cdots H–A]^-$, with the charge localized on the central anion (see structure depicted in Fig. 3). In turn, the ^{31}P single signal indicates an effective chemical equivalence of all three POO^- fragments due to the fast in NMR time scale intramolecular HB jump of a given terminal acid to the other and simultaneous proton transfer in the neighbor HB without dissociation of the complex (Fig. 4), similarly to what was previously found for HCAs of carboxylic acids [10]. Furthermore, the closeness of ^1H signals of AHA^- and $(AH)_2A^-$

complexes allows one to draw an unexpected conclusion about the geometrical resemblance of strong $[O\cdots H\cdots O]^-$ bonds in them, *i.e.* an insignificant effect of anticooperative coupling of two HBs (i.e. mutual weakening (lengthening) of them due the opposite directions of the electronic polarization at central POO^- moiety) in the $(AH)_2A^-$ complex.
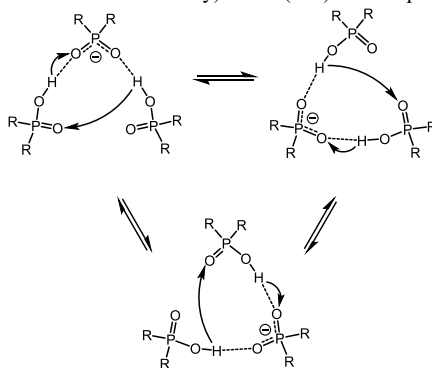
Figure 4. Proposed scheme of intramolecular proton exchange resulting in the effective chemical equivalence of all bridging protons and ^{31}P nuclei in the HCAs of $(AH)_2A^-$ type.

Acknowledgments

References

1. (a) I. S. Giba, P. M. Tolstoy. – *Symmetry (Basel)*, 13(2), 1–12 (2021). (b) V. V. Mulloyarova, I. S. Giba, M. A. Kostin, G. S. Denisov, I. G. Shenderovich, P. M. Tolstoy. – *Phys. Chem. Chem. Phys.*, 20(7), 4901–4910 (2018). (c) R. E. Asfin, G. S. Denisov, D. N. Poplevchenkov, K. G. Tokhadze, T. V. Velikanova. – *Polish J. Chem.*, 76(9), 1223–1231 (2002). (d) R. E. Asfin, G. S. Denisov, K. G. Tokhadze. – *J. Mol. Struct.*, 790(1–3), 11–17 (2006).
2. V. V. Mulloyarova, D. O. Ustimchuk, A. I. Filarowski, P. M. Tolstoy. – *Molecules*, 25(8), 1907–1923 (2020).
3. (a) P. G. Wenthold, R. R. Squires. – *J. Phys. Chem.*, 99(7), 2002–2005 (1995). (b) T. B. McMahon, P. Kebarle. – *J. Am. Chem. Soc.*, 108(21), 6502–6505 (1986).
4. C. Dreßler, G. Kabbe, D. Sebastiani. – *Fuel Cells*, 16(6), 682–694 (2016).
5. D. Jansen, J. Gramüller, F. Niemeyer, T. Schaller, M. C. Letzel, S. Grimme, H. Zhu, R. M. Gschwind, J. Niemeyer. – *Chem. Sci.*, 11(17), 4381–4390 (2020).
6. N. Berg, S. Bergwinkl, P. Nuernberger, D. Horinek, R. M. Gschwind. – *J. Am. Chem. Soc.*, 143(2), 724–735 (2021).
7. C. Detering, P. M. Tolstoy, N. S. Golubev, G. S. Denisov, H. H. Limbach. – *Dokl. Phys. Chem.*, 379(1–3), 191–193 (2001).
8. N. S. Golubev., S. N. Smirnov, V. A. Gindin, G. S. Denisov, H. Benedict, H. H. Limbach. – *J. Am. Chem. Soc.*, 116(26), 12055–12056 (1996).
9. F. Hibbert. – *J. Chem. Soc.*, *Perkin Trans.*, 2(15), 1862–1866 (1974).
10. P. M. Tolstoy, P. Schah-Mohammedi, S. N. Smirnov, N. S. Golubev, G. S. Denisov, H. H. Limbach. – *J. Am. Chem. Soc.*, 126(17), 5621–5634 (2004).

Dalcetrapib and Reduced Glutathione effect on Hemoglobin S polymerization studied by NMR

Lilian M. Delgado[1], Manuel A. Lores Guevara[1], Juan Carlos García Naranjo[1], Joseph Eric Niesor[2], Anne Perez[2], Inocente Rodriguez[3], Samuel Rosales[3], Fabian Tamayo Delgado[1]
[1]Centro de Biofísica Médica. Universidad de Oriente. Patricio Lumumba S/N. CP: 90500. Santiago de Cuba, Cuba.
[2]Hartis Pharma, Suiza.
[3]Hospital General "Dr. Juan Bruno Zayas Alfonso", Santiago de Cuba, Cuba.
E-mail: lilian.somoano@gmail.com
http://www.uo.edu.cu

Summary

The effects of dalcetrapib (dal) and reduced glutathione (GSH) on hemoglobin S (HbS) polymerization process are quantitatively evaluated using proton (^{1}H) magnetic relaxation. The HbS samples were obtained, using classical methods (centrifuging, decanting and freezing-thawing cycles), starting from whole blood of voluntary patients suffering Sickle Cell Disease (SCD). The transversal ^{1}H magnetic relaxation time (T_2) was determined at 360C using the Carr-Purcell-Meiboom-Gill (CPMG) experiment (echo time: 1000 μs, 1000 echoes, 90˚and 180˚pulses of equal amplitude and with 5 μs and 10 μs of width respectively) and its temporal behavior was used to obtain the initial (T_{2i}) and final (T_{2f}) values of T_2 as well as the delay time (td) of the HbS polymerization process. Both compounds showed effect on the HbS polymerization process with increments of td in the 60 % of the samples treated with GSH, as well as, an increasing of T_{2i} and T_{2f} in the 100% of the samples treated with dal. The changes in these parameters indicate, in both cases, an inhibition of the HbS polymerization processes.

Plasma dynamic viscosity in Multiple Myeloma patients measured using NMR

Fabián Tamayo Delgado[1], Yamirka Alonso Geli[1], Manuel Arsenio Lores Guevara[1], Yulianela Mengana Torres[1], Samuel Jorge Rosales Rodríguez[2], Lidia Clara Suárez Beyries[2], Haydee Cruz Vadell[3], Briseida Joa Rabionet[2], Martha Menéndez Rivera[2], Juan Carlos García Naranjo[1], Inocente Rodríguez Reyes[2]

[1]*Laboratorio de Relajación Magnética Nuclear. Centro de Biofísica Médica, Universidad de Oriente. Santiago de Cuba, Cuba.*
[2]*Hospital General "Juan Bruno Zayas Alfonso", Santiago de Cuba, Cuba.*
[3]*Facultad de Enfermería-tecnología. Instituto Superior de Ciencias Médicas, Santiago de Cuba, Cuba.*
E-mail: lilian.somoano@gmail.com
http://www.uo.edu.cu

Summary

The dynamic viscosity of the blood plasma was determined in patients with Multiple Myeloma during steady state and when they suffer the hiperviscosity syndrome. Proton magnetic relaxation was used to determine dynamic viscosity starting from the transverse proton magnetic relaxation time value, which was measured employing the Carr-Purcell-Meiboon-Gill pulse sequence. The values of the blood plasma dynamic viscosity during steady state statistically match with those determined in samples from healthy individuals and are increased in those patients suffering the hiperviscosity syndrome. Was possible to monitor dynamic viscosity during the treatment of the patients with hyperviscosity syndrome observing a remarkable dercreasing of this parameter.

Targeted nanosystems for treatment of triple negative breast cancer and MRI Imaging

Enza Di Gregorio[1], Chiara Romiti[1], Antonino Di Lorenzo[1], Laura Conti[1], Giuseppe Ferrauto[1].

[1]*Department of Molecular Biotechnology and Health Sciences, University of Turin, Italy.*
E-mail: enza.digregorio@unito.it

Introduction

Breast cancer (BCa) still represents the most prevalent cancer in women. Even if several therapeutic approaches are available (surgery, chemo-, radio-, immune-, hormone-therapy), systemic chemotherapy remains the primary choice, especially for treatment of triple negative breast cancers (TNBC). [1] However, it causes numerous side effects and damages to distal organs and generally requires high doses of drug to achieve the therapeutic concentration in the tumor region. Delivery of drugs by targeted nanosystems can allow overcoming these drawbacks [2].

Method

Poly (lactic-co-glycolic acid) (PLGA) Nanoparticles (NPs) and liposomes were prepared with the emulsification solvent evaporation or with the hydration of thin lipidic film method, respectively. They were bound to cyclic RGD to target $\alpha v \beta 3$ integrins.

NPs were loaded with the proper drug (docetaxel or CU-CPT22 in PLGA and doxorubicin in liposomes), with Gd-complexes (MRI probe) and carboxyfluorecein (optical probe). Physicochemical properties were determined by DLS, 1H NMRD Relaxometry, 1H-NMR. In vitro cytotoxicity was analysed by MTT assay. Intracellular uptake of Gd was imaged with T_{1w} MRI and measured with ICP-MS.

In vivo, the therapeutic effect of the two NPs (eventually in combination) was assessed on transplantable TNBC murine models. Outcome of therapy was followed by multiparametric MRI.

Results and Discussion

In the first part of the study, the efficiency of targeted NPs in treatment of BCa was assessed by comparing, both in cellular systems and in vivo, RGD-tageted NPs with untargeted NPs and free drug. For this study, NPs were filled with Docetaxel, Gd-contrast agents and carboxyfluorescein. MRI and ICP-MS data showed a stronger number of NPs delivered to the tumour region when RGD targeting is used (Fig.1). This resulted in an improved efficiency of treatment and lower side effects. Mice treated with RGD-PLGA NPs showed a stronger reduction of tumor size (Fig.2A,B) and a significant reduction of cardiotoxicity (Fig.2C). In the second part of the study, RGD-targeting liposomes were prepared and loaded with Doxorubicin. They were used in combination with PLGA loaded with CU-CPT22, a Toll-like receptor 2 (TLR-2) inhibitor. The two NPs were characterized and tested in vitro and in vivo. The use of TLR2 inhibitors in vivo reduces tumor growth and potentiates doxorubicin efficacy with no negative impact on the host immune system.

Conclusions

NPs were stable in physiological conditions, with a good efficiency of drug encapsulation. The RGD-targeted PLGA displayed a higher tumor accumulation than untargeted NPs, resulting in a higher hampering of tumor progression either compared to the control PLGA or the free drug. The use of NPs strongly reduced side effects. The combined delivery of two NPs loaded with different drugs strongly improved the efficiency of the treatment.
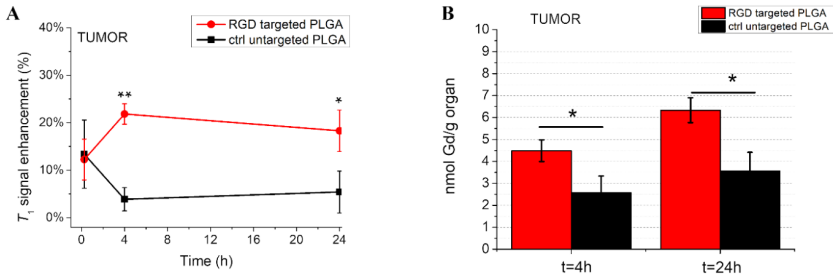
*Figure 1 In vivo biodistribution of RGD_PLGA and Ctrl_PLGA A) T_1^{enh} in the tumor region at different time points upon administration of RGD_PLGA or Ctrl_PLGA. **B**) Quantification of Gd retained in the tumor by Inductively Coupled Plasma – Mass Spectrometry (ICP-MS), at t = 4 h and t = 24 h.*
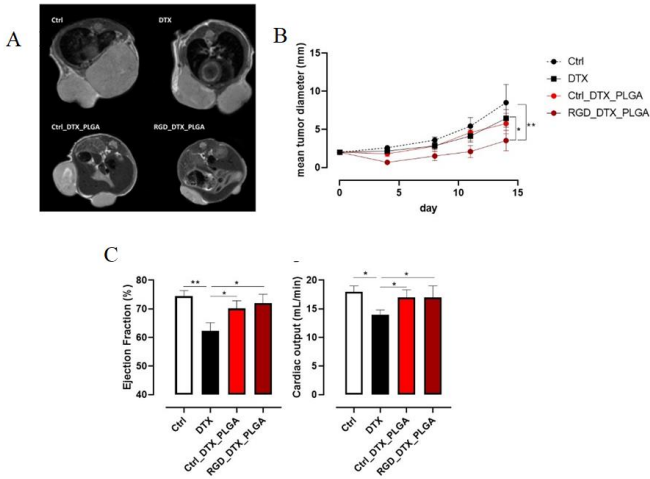
*Figure 2 In vivo effect of PLGA-NPs. (**A**) Representative axial T_{2w}-MR images of tumor region in mice treated with physiological saline solution as a control, free Docetaxel (DTX), Ctrl_DTX_PLGA or RGD_DTX_PLGA (N = 6 per group). (**B**) mean tumor diameter during the treatment (**C**) Heart Ejection Fraction (EF%) and Heart Cardiac Output (CO) as assessed by cardio MRI.*

References

1. Sung H, Ferlay J, Siegel RL, Laversanne M, Soerjomataram I, Jemal A, et al. Global cancer statistics 2020: GLOBOCAN estimates of incidence and mortality worldwide for 36 cancers in 185 countries. CA: a cancer journal for clinicians. 2021.
2. Yu Z, Gao L, Chen K, Zhang W, Zhang Q, Li Q, et al. Nanoparticles: A New Approach to Upgrade Cancer Diagnosis and Treatment. Nanoscale Res Lett. 2021; 16: 88.

^{31}P NMR spectroscopy within investigation of compounds based on hexachlorocyclotriphosphazene

Egorov S.S.[1], Selyutin A.A.[1], Tupikina E.Yu.[1]
[1]Institute of Chemistry, Saint Petersburg State University, Saint Petersburg, Russia
E-mail: st076062@student.spbu.ru

Introduction

Nowadays phosphazenes are an intensively developing and prospective class of inorganic and hybrid compounds, which are an object of interest of fundamental chemistry and material science. These compounds form various species, such as linear, cyclic ones, as well as polymers, due to the alternating nitrogen and phosphorus atoms. Hexachlorocyclotriphosphazene (Fig. 1) and its derivatives are the most famous representatives of this type of compounds.
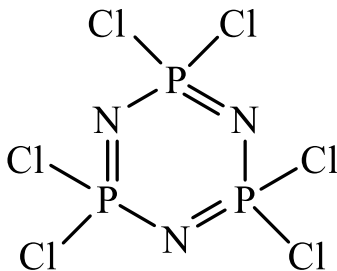
Figure 1. Hexachlorocyclotriphosphazene.

Using various organic functional groups as substituents, it's possible to obtain substances with diverse properties [1]. It's currently known that phosphazenes could be used as catalysts, fire retardants, antibacterial agents etc [2].

Problem statement

It is considered that NMR spectroscopy is the widespread method of reaction mixture analysis and investigation of the substances structure. Due to the high natural abundance of phosphorus-31 isotope and absence of the quadrupole moment, ^{31}P NMR spectroscopy is the suitable method for characterization of compounds containing the phosphazene core as it contains phosphorus atom. Unfortunately, there is still a small amount of research aimed to ^{31}P NMR spectroscopy of phosphazenes and influence of organic substituents on the chemical shifts of ^{31}P nuclei.

As a reaction mixture normally contains polymers and products of different-type substitutions by polyfunctional organic compounds, it's important to separate their signals on ^{31}P NMR spectra (Fig. 2).

The process of nucleophilic substitution of chlorine atoms in the structure of phosphazene is explored within our research. Our aim is to obtain the relative position of signals on ^{31}P NMR spectra for the series of phosphazene-containing compounds and their conformers. For modeling substituent, 2-aminoethanol is chosen because of the two reaction centers it contains. Indeed, the chlorine atom in the phosphazene structure could be replaced by either oxygen or nitrogen atoms. Moreover, 2-aminoethanol could connect two phosphazene cores leading to polymer formation (Fig. 3).
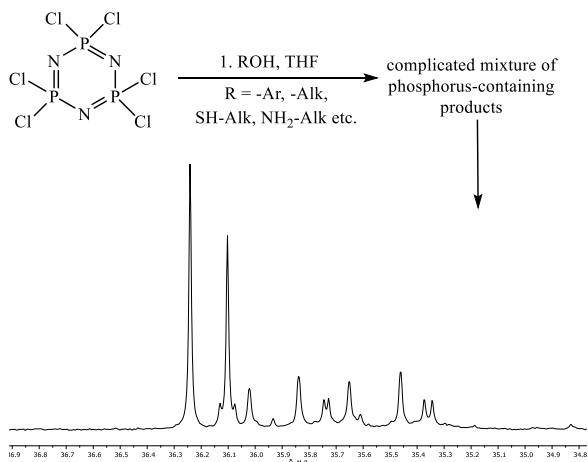
Figure 2. The example of complicated ^{31}P NMR spectrum of phosphazene-containing mixture
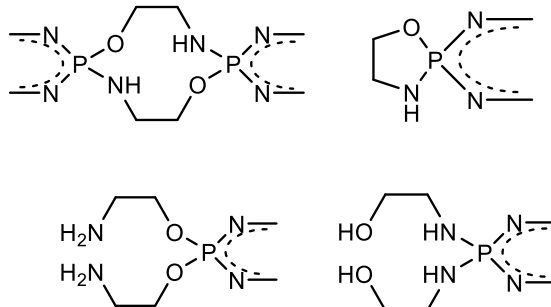
Figure 3. Different-type products of nucleophilic substitution

This data would simplify the analysis of more complicated ^{31}P NMR spectra in the future.

Methods

Equilibrium geometries and harmonic vibrational frequencies were calculated using Gaussian16 software package using B3LYP DFT functional in a combination with def-2-TZVP basis set. The spectral NMR parameters were obtained within GIAO method.

Acknowledgments

References

1. Nikovskii, I.A., et al. Russ. J. Gen. Chem., 2017
2. Jeevananthan, V. et al. ChemistrySelect, 2021

Sodium diffusion in scheelite-type $Na_5M(MoO_4)_4$ (M=Bi, La, Y)

<u>*Fedorov D.S.*</u>[1,2], *Buzlukov A.L.*[1], *Baklanova Y.V.*[2], *Tyutyunnik A.P.*[2], *Korona D.V.*[3], *Maksimova L.G.*[2], *Denisova T.A.*[2], *Medvedeva N.I*[2], *Spiridonova T.S.*[4], *Zolotova E.S.*[5]

[1]*M.N. Mikheev Institute of Metal Physics, Ural Branch, Russian Academy of Sciences, Ekaterinburg, 620137, Russia*

[2]*Institute of Solid State Chemistry, Ural Branch, Russian Academy of Sciences, Ekaterinburg, 620108, Russia*

[3]*Ural Federal University, Ekaterinburg, 620002, Russia*

[4]*Baikal Institute of Nature Management, Siberian Branch, Russian Academy of Sciences, Ulan-Ude, 670047, Russia*

[5]*Institute of Inorganic Chemistry, Siberian Branch, Russian Academy of Sciences, Novosibirsk, 630090, Russia*

E-mail: <u>*Fedorov@ihim.uran.ru*</u>

Introduction

The development of advanced technologies for electric energy storage (battery technologies) is a crucial problem in the field of world energy. This is due to the widespread occurrence of portable electronic devices, increased interest in creating electrical and hybrid vehicles, to the development of renewable energy sources, etc. Today, the technology based on lithium-ion batteries appears to be the most promising in terms of performance (high charge/discharge voltage and specific energy capacity), small size and light weight. It should be noted however that the search for lithium substitutes is continuing because of expensiveness of lithium-based devices. Sodium, being chemically similar to lithium, is much cheaper and less toxic. Although sodium-ion batteries have a considerably lower specific energy than lithium-ion counterparts, the former are of choice for stationary units with high power consumption.

Structure

The $Na_5M(MoO_4)_4$ (M = La, Y, Bi) belongs to the wide group of compounds with the scheelite-like crystal structure. Figure 1 shows structure of $Na_5M(MoO_4)_4$.
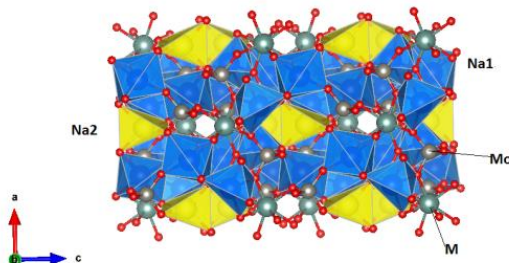
Figure 1. Structure of $Na_5M(MoO_4)_4$ M= (La, Y, Bi)

Conductivity

Figure 2 shows the temperature dependences of ion conductivity for sodium molybdates $Na_5M(MoO_4)_4$ (M=Bi, La, Y).
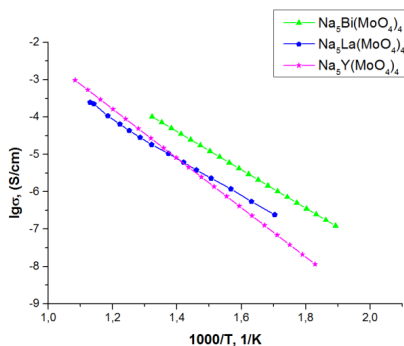
Figure 2. Temperature dependences of ion conductivity for the compounds Na₅M(MoO₄)₄
(M=Bi, La, Y)

NMR-spectroscopy

The ^{23}Na NMR spectra for Na$_5$M(MoO$_4$)$_4$ with M = Y, La, Bi have been acquired in the temperature range 300 – 700 K. Figure 3 presents the characteristic NMR spectra for Na$_5$La(MoO$_4$)$_4$ compound; for all other samples, the temperature variation of the NMR spectra is qualitatively similar. At temperature below 600 K, the spectrum is a superposition of two quadrupole split lines with quadrupole frequencies, $\nu_Q \approx 1000$ and 1500 kHz, and with the asymmetry parameters of EFG tensor, $\eta_Q \approx 0.7$ and 0. These values are in good agreement with theoretical estimates for sodium atoms in structural positions Na1 (16f) and Na2 (4b). In addition, the relative intensities of the corresponding signals are close to those expected from the occupation of distinct sites. Thus, two observed NMR signals have been attributed to the Na1 (16f) and Na2 (4b) positions in the Na$_5$M(MoO$_4$)$_4$ structure. An increase in temperature is accompanied by a significant change in the shape of NMR spectrum. It is interesting to note that the temperature changes for the signal corresponding to Na1 atoms are rather weak (on the order of 20% of the initial η_Q and ν_Q values), meanwhile the Na2 line shape changes drastically. This is most clearly seen in Fig. 4, which shows the temperature behavior of the quadrupole frequency, ν_Q, and the asymmetry parameter of EFG tensor , η_Q, for two types of structural positions in the Na$_5$La(MoO$_4$)$_4$, Na$_5$Y(MoO$_4$)$_4$, and Na$_5$Bi(MoO$_4$)$_4$ compounds.
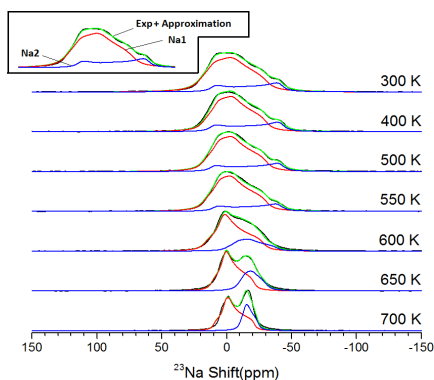
Figure 3. ^{23}Na NMR spectra acquired for the Na$_5$La(MoO$_4$)$_4$ in the temperature range 300 – 700 K

The observed features suggest the motion of Na atoms in the $Na_5M(MoO_4)_4$ compounds, which occurs through the jumps Na1 ↔ Na1, Na2 ↔ Na2 and Na1 ↔ Na2. It can be seen also that the temperature of the onset of motional distortions of the NMR spectrum shape shifts towards lower temperatures when Y is replaced by La and Bi. Thus, we can assume that the ion dynamics in $Na_5M(MoO_4)_4$ compounds increases in the series Y → La → Bi. The motional changes in NMR spectrum are expected at a temperature at which the ion jump frequency, τ_d^{-1}, becomes comparable with the characteristic frequencies of interaction determining the shape of NMR spectrum (in our case, these are the second-order quadrupole effects). On this basis, we can estimate the frequency of sodium ion jumps to be approximately 10^3–10^4 s^{-1} at T near 650 K for $Na_5Y(MoO_4)_4$, 600 K for $Na_5La(MoO_4)_4$ and 550 K for $Na_5Bi(MoO_4)_4$.
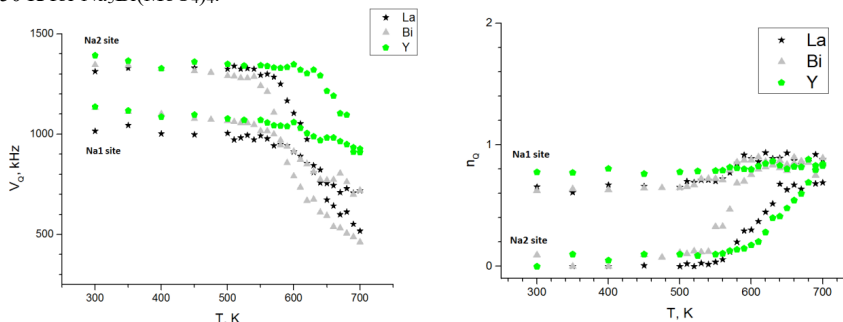
Figure 4. Temperature dependences of the quadrupole frequency and the asymmetry parameter of EFG tensor for Na₅M(MoO₄)₄ (M=La, Bi, Y), measured in the temperature range 300 – 700 K.

Acknowledgments

Passively detunable wireless coil for 1.5 T breast imaging

Alexander Fedotov[1], *Pavel Tikhonov*[1], *Georgiy Solomakha*[1], *Victor Puchnin*[1], *Anatolii Levchuk*[1, 2], *Alena Shchelokova*[1], *and Anna Hurshkainen*[1]

[1]*Department of Physics, ITMO University, St. Petersburg, Russian Federation*
[2]*Department of Radiology, Federal Almazov North-West Medical Research Center, Saint Petersburg, Russia*
E-mail: aleksandr.fedotov@metalab.ifmo.ru
https://physics.itmo.ru/

Abstract

Wireless radiofrequency (RF) coils have emerged as an attractive option for clinical applications due to their compatibility with MRI scanners of different vendors. These coils wirelessly connect to MRI body coils using inductive electromagnetic coupling. However, the use of wireless coils often requires manual calibration of reference RF input voltage. It assumes adjustment of reference voltage to take into account increased transmit efficiency of body coil due to inductive coupling with wireless coil. This study aims to overcome the disadvantage of manual calibration by development of the first Rx-only wireless coil for dedicated human breast MRI.

Introduction

Wireless RF coils offer several advantages over conventional dedicated cable-connected coils in clinical applications [1-3]. Due to inductive coupling with MRI body coil, there is no need to use RF cables with proprietary connectors providing compatibility across different MRI systems. Additionally, wireless RF coils provide increased patient comfort during MRI exams due to wire-free technology providing more freedom of movement. Another advantage is reduced electromagnetic interference with other equipment in the MRI room due to wire-free connection. Overall, the benefits of wireless RF coils provide an attractive option for clinical MRI applications.

However, due to the significant increase in B_1^+ compared to body coil, which is usually used as Tx coil, wireless coils often require manual reference voltage adjustment. Enhancement of transmit efficiency in the region of interest is caused by inductive coupling between resonant wireless coil and MRI body coil. In this work, we propose the first Rx-only wireless coil for breast MRI to address the need for improved patient comfort and imaging capabilities. To achieve this goal, we have designed and evaluated a wireless unilateral breast coil based on Helmholtz resonator equipped with a passive detuning circuit. Numerical simulations were conducted as well as coil prototype was built and experimentally studied to evaluate its performance.

Preliminary results of MRI studies demonstrate the feasibility and potential advantages of the proposed wireless coil. Further studies and optimization of the design will be necessary to fully assess its clinical utility.

Rx-only wireless coil design

A Helmholtz resonator, consisting of two electrically connected coils each having one turn, was selected as the wireless coil for human breast MRI. The resonator's dimensions (157x152x50 mm) were chosen based on the average size of the targeted region of interest, particularly, of a human breast. To achieve the primary objective of creating an Rx-only coil, a passive detuning circuit was inserted into the gap of the resonator's conductor. The main view of the numerical model and the detuning circuit is illustrated in Figure 1. The detuning circuit consists of a resonant LC-circuit with a frequency close to the tuning frequency of the Helmholtz coil, as well as a pair of anti-parallel pin-diodes inserted in series with the inductance of the LC-circuit.

To simulate the coil's operation during both transmit and receive modes, two different equivalent circuits of anti-parallel pin-diodes were considered. During low current or receive mode, the diode exhibits a high reactive resistance and can be described as a 1 pF capacitor with a resistor in parallel. In high current or transmit mode, it can be considered as a 1 Ohm resistor. The goal of the passive detuning circuit is to reduce coupling between the wireless coil and the body coil during transmit mode and exhibit resonant behavior of wireless coil during receive mode.

C_LC	159.76 pF
L_LC	54.78 nH
R1	1 Ohm
R2	5 kOhm
C2	1 pF
L_parasitic	1 nH
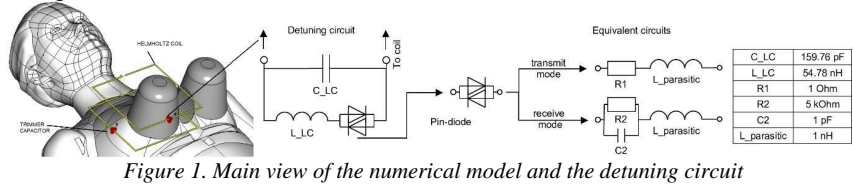
Figure 1. Main view of the numerical model and the detuning circuit

Numerical simulations

In order to evaluate the wireless coil properties full-wave numerical simulations were performed using CST Studio 2021 software (Dassault Systèmes). A birdcage coil was considered in simulations as a transmit body coil, driven in quadrature mode by two discrete ports. A homogeneous phantom with averaged properties of the human body was used in simulations. To tune the Helmholtz coil to the Larmor frequency of 63.8 MHz, a 3.3 pF capacitor was inserted in series to the conductor of the coil.

Since the studied coil is considered as Rx-only coil,, in transmission mode wireless coil inductively coupled with birdcage coil should demonstrate transmit efficiency similar to birdcage coil alone.

Figures 2a and 2b show the distributions of circularly polarized magnetic field B_1^+ magnitude corresponding to the birdcage coil in the presence of the wireless coil operating in the transmit mode(a), as well as in the absence of the wireless coil(b), respectively. Figures 2c and 2d show B_1^+ magnitude distributions of birdcage coil in the presence of the wireless coil operating in the receive mode(c), as well as in the presence of the wireless coil without a detuning circuit (d).

The depicted maps demonstrate the circuit's effective ability to detune. In both the transmit and receive modes, the magnetic field values in the targeted region of interest differ no more than 10% compared to the reference cases.
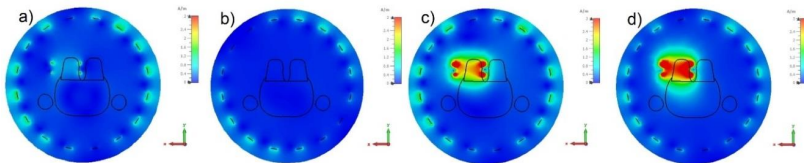
Figure 2. Distributions of the amplitude of the magnetic field of circular polarization for wireless coil with detuning circuit operating in transmit mode(a), absence of the wireless coil(b), wireless coil with detuning circuit operating in the receive mode(c), wireless coil without a detuning circuit (d).

Experimental verification

An experimental sample of the coil was done using a 3D-printed plastic holder with dimensions of 157x152x50 mm. Conductors of the Helmholz resonator were done using copper tape applied to the lateral surfaces of the holder, LC-circuit and tuning capacitance were realized using discrete non-magnetic reactive elements.

Experimental verification of the proposed solution was done using "Espree 1.5 T" (Siemens) MRI scanner. Plastic phantoms filled with nickel chloride solution (3.3685 g/L NiCl$_2$ 6H$_2$O and 2.4 g/L NaCl) mimicking a female breast were used for MRI tests. The reference voltage applied to the MRI scanner body coil under such a load is 309 V. The MR image obtained using birdcage coil only is shown in Figure 3a. In the presence of a wireless coil without a detuning circuit, the reference voltage was 53.1 V after manual calibration. The respective MR image is shown in Figure 3b.

Results

MR images of the phantom obtained in the presence of a wireless coil with a detuning circuit as well as for a reference case of the wireless coil without detuning circuit. The corresponding images are shown in Figures 3c and 3b, respectively. The signal-to-noise ratio for the image in Figure 3a (birdcage coil alone) is 68, for the image in Figure 3b is 872 (wireless coil without detuning circuit) and for the image in Figure 3c (wireless coil with detuning circuit) it is 756. In the presence of the detuning circuit coil, the MRI scanner was automatically calibrated to 429 V. This value is different from the reference voltage while using the body coil alone since the wireless coil slightly saves its resonant properties in transmit mode.
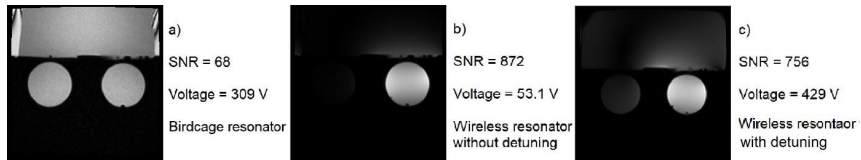
Figure 3. MR images obtained during experimental verification of the Birdcage resonator (a), wireless coil without a detuning circuit (b) and wireless coil with detuning circuit (c).

Numerical simulations and experimental results illustrate the effective detuning capabilities of the considered circuit and possibility of Rx-only wireless coil creation.

Lures and terms

Table 1. Useful terms

Term	Explanation
A birdcage resonator	A type of radiofrequency (RF) coil used in magnetic resonance imaging (MRI) that consists of a set of capacitive plates and inductive elements arranged in a cylindrical geometry resembling a birdcage. It generates a homogenous magnetic field for imaging.
Detuning circuit	A circuit inserted into the wireless coil to reduce the coupling between the coil and the Birdcage resonator during transmit mode and to save the working of the wireless coil during receive mode.

Acknowledgments

References

1. Shchelokova, Alena V., et al. "Volumetric wireless coil based on periodically coupled split-loop resonators for clinical wrist imaging." Magnetic resonance in medicine 80.4 (2018): 1726-1737.
2. Shchelokova, Alena, et al. "Ceramic resonators for targeted clinical magnetic resonance imaging of the breast." Nature communications 11.1 (2020): 1-7.
3. Puchnin, Viktor, et al. "Quadrature transceive wireless coil: Design concept and application for bilateral breast MRI at 1.5 T." Magnetic Resonancein Medicine (2022)

NMR relaxation of helium-3 in contact with 20-200 nm DyF$_3$ particles

A. M. Garaeva^a, E. M. Alakshin $^{a, b}$, E.I. Boltenkova^a, K.R. Safiullin,
V.V. Kuzmin^a, I. V. Romanova^a, M.S. Tagirov^a
^{a}*Kazan Federal University, Institute of Physics, Kazan, Russia*
^{b}*Tatarstan Academy of Sciences, Kazan, Russia*
E-mail: _adeliagaraeva84@gmail.com_

Dysprosium fluoride DyF$_3$ is a dipole ferromagnet with an easy magnetization axis along the [010] axis of the crystal lattice; the Curie temperature is 2.55 K along the [010] axis for a single crystal [1]. The compound has unique properties, which allows it to be used as a high-field MRI contrast agent [2] and as an additive to Nd-Fe-B magnets to increase the coercive force [3].

Powders of DyF$_3$ and LaF$_3$ with a characteristic particle size of 20 nm were obtained by hydrothermal synthesis according to the nitrate reaction [4], a powder with a size of 220 nm × 150 nm was obtained by the reaction through chloride [5]. Control of the chemical composition and confirmation of crystallinity were carried out using X-ray phase analysis on a diffractometer Bruker D8 Advance Cu Kα, λ=1.5418 Å. Photographs obtained by transmission electron microscopy on a HitachiHT Exalens microscope were used to determine the shape and characteristic size of particles in the resulting powders.

In this work, the rates of longitudinal and transverse relaxation of helium-3 nuclei in contact with DyF$_3$ (99.67%) and LaF$_3$ (0.33%) powder in the adsorbed layer, in the bulk of the liquid, and in the case of coating particles with a helium-4 layer were measured depending on the temperature in the range of 1.5-3 K in the fields of 173 and 505 mT. In the case of liquid helium-3, in the absence of helium-4 coating of particles, a two-component relaxation of the longitudinal and transverse magnetization is observed. A possible explanation for this phenomenon is proposed.

Acknowledgments

References

1. Savinkov A. V. et al. *Journal of Physics: Condensed Matter*, 2008, 20, 48, 485220.
2. González-Mancebo D. et al. *Particle & Particle Systems Characterization*, 2017, 34, 10, 1700116.
3. Xu F. et al. *Scripta Materialia*, 2011, 64, 12, 1137-1140.
4. Alakshin E. M. et al. *Journal of Nanomaterials*, 2016.
5. Alakshin E. et al. *Nanoscale*, 2022, 14, 31, 11353-11358.

Solid State NMR: Validity of Relaxation Times Approach

Leonid Grunin, Maria Ivanova, Innokenty Nikolaev, Roman Zhitnikov

Resonance Systems, Yoshkar-Ola, Russia

E-mail: mobilenmr@hotmail.com

Transverse relaxation in rigid-state materials below glass-transition point happens to be exponential in very rare cases, mostly showing up complex shape that may authors try to fit within a mixture of Gaussian, Abrahamian, Pake and Lorentzian lines, though for many samples even such variative models do not work perfectly.
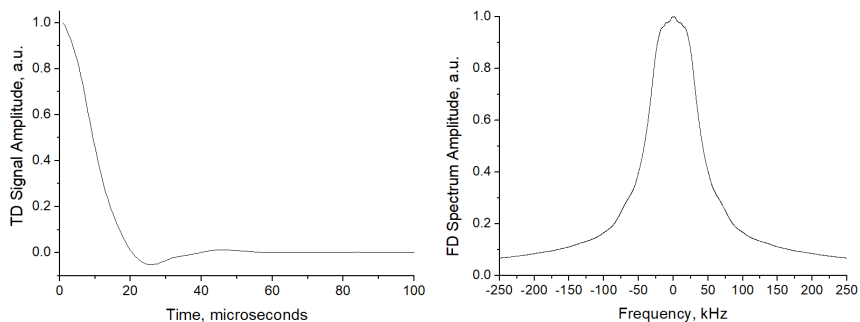
Fig.1. FID-MSE (on the right) and ^{1}H-NMR Spectrum of Allulose sample

The approach to characterize structures and dynamics of solids that involves moments of spectral lines is becoming more adequate and promising because the moments can be directly calculated using integration of FFT spectrum and not relying on ambiguous muti-component approximation of the TD-NMR Free Induction Decay (FID).

On the other hand, the huge community of scientists in applied areas where TD-NMR is considered as only one of the measuring tools are educated in the way of simple relaxation times approach and the use of second moments M_2 expressed in squared Gauss occurs far less convenient and demonstrative than the T_2 in microseconds.

The contribution pretends to bring up the way to recalculate second moments corresponding to various line shapes into timely parameter T_2^{**} with minimal distortion of information about structure of solid-state materials.

Fluorine-19 (^{19}F) magnetic resonance imaging at 1.5 T

Mikhail V. Gulyaev[1], Olga S. Pavlova[1,2], Dmitry S. Dmitriev[3], Aleksandr G. Pistrak[3], Kirill N. Ryabikov[3], Viktor P. Tarasov[3,4], Nikolay V. Anisimov[1], Yury A. Pirogov[2]

[1]*Faculty of Medicine, Lomonosov Moscow State University, 119991, Moscow, Russia*
[2]*Faculty of Physics, Lomonosov Moscow State University, 119991, Moscow, Russia*
[3]*«S.P. HELPIC» LTD, 117485, Moscow, Russia*
[4]*Federal* Research Center *of Problems of Chemical Physics and Medicinal Chemistry Russian Academy of Sciences, 142432, Moscow region, Chernogolovka, Russia*
E-mail: gulyaev@physics.msu.ru

Introduction

Currently, only ^{1}H MRI is used in clinical trials. Undoubtedly, this method has many advantages and therefore has become one of the most popular and effective methods for medical diagnosis [1]. However, like most methods, it has limitations. For example, since protons are distributed throughout the body, some pathology can sometimes be invisible against the background of signals from normal tissues. Another problem is the visualization of air-filled tissues, such as the lungs.

These issues do not exist in ^{19}F MRI because there is no fluorine in the body. The ^{19}F NMR signal is obtained only from the external signal source – fluorinated substances in liquid or in gaseous state [2]. Thus, the ^{19}F MR images are acquired without background signals. Particularly promising for the ^{19}F MRI method is the visualization of the lungs using fluorinated gas [3].

A number of foreign scientific laboratories have been conducting MRI developments on ^{19}F nuclei in human for 20 years, however, in Russia the ^{19}F MRI studies were carried out only on a low-field 0.5 T MRI scanner [4]. As has been shown by our studies in 0.5 T, the method is very promising. It seems rational to implement it on MR scanners with a high magnetic field, for example, on clinical 1.5 T.

In this work, the retuning of the transmit-receive path of 1.5 T MR scanner was done, and the ^{19}F MR images of phantoms were obtained.

Retuning of the transmit-receive path of the 1.5 T MR scanner

For the successful completion of this work, the following works were sequentially solved:

- The quadrature divider was retuned to ~60.0 MHz. The adjustment of the decoupling between the ports was carried out.
- The resonant frequencies of the transmitter and receiver RF coils were retuned from ~63.8 MHz (^{1}H) to ~60.0 MHz (^{19}F).
- For the transmitter coil, the additional capacitors were added to the RF circuit.
- For the receiver coil, the new matching RF circuits were calculated and then replaced.
- The matching of the RF coils to 50 Ω was tested at ~60.0 MHz.

^{19}F MR imaging of the phantoms

The ^{19}F MR images were obtained from two phantoms. One phantom was a ~60 ml glass container filled with octafluorocyclobutane (OFCB, C4F8) in liquid state. A second phantom was an inflatable balloon of ~15L filled with OFCB gas.

The ^{19}F MR images of the phantoms were obtained using gradient echo pulse sequence. The following scan parameters were identical for both phantoms: TR = 5.8 ms, TE = 2.4 ms, FA = 90°, matrix = 192 × 176, number of slices = 9 (3 for each projection – axial, sagittal, coronal), number of averages = 1, bandwidth = 200 kHz, total scan time = 10 s. For the first phantom, the slice thickness was 8 mm, FOV was 25 cm × 25 cm, so the spatial

resolution was 0.130 cm × 0.142 cm. For the second phantom, the slice thickness was 150 mm, FOV was 45 cm × 45 cm, so the spatial resolution was 0.234 cm × 0.255 cm.

In Fig. 1A, the photo of the first phantom located inside the receiver coil is shown. In Fig. 1B, the ^{19}F MR image of this phantom is presented.

In Fig. 2A, the photo of the second phantom inside the coils in the magnet is shown. In Fig. 2B-D, the ^{19}F MR images acquired from the second phantom are presented.

Figure 1. A: photo of the first phantom inside the receiver coil. B: [19]F MR image of the phantom in axial projection
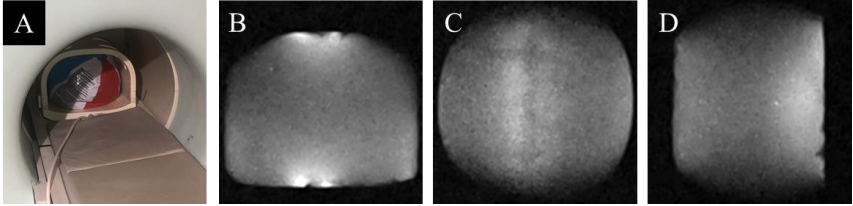
Figure 2. A: photo of the second phantom inside the receiver coil in the magnet. B-D: [19]F MR images of the second phantom in axial, coronal and sagittal projection, respectively

Conclusion

The ^{19}F MR images of the phantoms are obtained without visible distortions and artifacts. Thus, the transmit-receive path of the 1.5 T MR scanner was reconfigured correctly. Subsequently, the ^{19}F MRI studies of human lungs will be investigated on 1.5 T MR scanner using fluorinated gas OFCB.

Acknowledgments

References

1. V.P. Groverb, et al. – *J. Clin. Exp. Hepatol.*, 5, 246-255 (2015).
2. J. Ruiz-Cabello, et al. – *NMR Biomed.*, 24, 114-129 (2011).
3. M.J. Couch, et al. – *J Magn Reson Imaging*, 49, 343-354 (2019).
4. O.S. Pavlova, et al. – *Magn. Reson. Med.*, 84, 2117–2123 (2020).

The factors determining 1H NMR chemical shift in complexes with centrally symmetric hydrogen bonds

Kaplanskiy M.V., Tolstoy P.M., Tupikina E.Yu.
Institute of Chemistry, Saint Petersburg State University, Russia
E-mail: mark2402@mail.ru

Introduction

Speaking about the investigation of hydrogen bonds in solution or in gas phase, it is worth remembering that their geometry, strictly speaking, cannot be determined experimentally directly (compared to the solid state, where X-ray diffraction techniques are available to evaluate the geometry of the complex). That is why researchers must obtain information about the geometry of hydrogen bonds from indirect indicators, most often spectral parameters (IR or NMR). [1] The process of "reconstruction" of the geometry (or energy) of molecular complexes from known values of spectral parameters is known as the solution to the *inverse spectroscopic problem*. This idea lies at the basis of many correlation equations proposed in the literature, in which it is supposed to substitute the value of the experimentally measured spectral parameter and to obtain some property of the molecular complex (most frequently: geometry or energy). It is important to remember, however, that the accuracy of these equations may be limited by the «type» of systems, the specificity of the experimental conditions, the set of model complexes on the basis of which it is obtained, and, of course, the parameters of approximation. For instance, the following equation that can be used for restoration hydrogen bond geometry [2]:

$$\delta_H = \delta_H^0 + (\delta_H^{max} - \delta_H^0) \cdot e^{-6.2 \cdot q_1^2} \qquad (1)$$

Parameter q_1 is calculated as the half-difference of the distances between heavy atoms X and Y within X–H···Y hydrogen bond $q_1 = 0.5 \cdot (r_{XH} - r_{HY})$ and represents the "asymmetry" of a proton position within a given hydrogen bond. This equation demonstrates that $\boldsymbol{\delta_H(q_1)}$ is a bell-shaped curve. $\boldsymbol{\delta_H^{max}}$ is a maximal chemical shift value along the proton transfer coordinate which is usually observed for centrally symmetric hydrogen bridges ($q_1 \approx 0$). The magnitude of δ_H^{max} is highly dependent on the type of a system and cannot be directly related to the strength of a hydrogen bond.

In this computational work, we investigate the factors that determine the maximal value of the proton chemical shift in order to develop simple methods for predicting it. Most attention is paid to features of the electronic structure, such as topology and qualitative characteristics of electron density basins.

Model systems

As model complexes we considered a set of small formally-symmetric complexes with hydrogen bonds FHF, OHO, NHN (Fig. 1). The set of complexes contains different types of complexes: charged and neutral, with various heavy atoms, their hybridization and different strength of hydrogen bond.
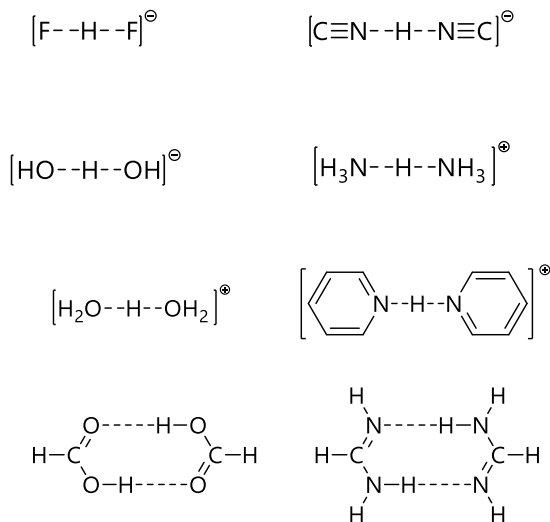
Figure 1. Complexes investigated in this work.

Methods

Computations were performed using Gaussian16 software package. Geometries of studied complexes were optimized using MP2/def2-TZVP level of theory. Quasi-adiabatic proton transfer was modelled by using a modredundant scheme. Two-dimensional potential energy surfaces were obtained for each complex by varying interatomic distances between hydrogen atom and each nearest heavy atoms. Proton transfer pathway was determined as a path through the regions with the lowest electronic energy gradient. Interatomic distances were ranged from 0.8 Å to 2.0 Å with the 0.05 Å as a step. NMR parameters were calculated using GIAO approach using the same computational level. Topological analysis of electron density was performed using Multiwfn 3.8 software package.

References

1. Tolstoy P.M., Tupikina E.Y. IR and NMR Spectral Diagnostics of Hydrogen Bond Energy and Geometry //Spectroscopy and Computation of Hydrogen-Bonded Systems. – 2023. – p. 345-407.
2. Limbach, H.H., Tolstoy, P.M., Pérez-Hernández, N., Guo, J., Shenderovich, I.G., & Denisov, G.S. (2009). OHO hydrogen bond geometries and NMR chemical shifts: from equilibrium structures to geometric H/D isotope effects, with applications for water, protonated water, and compressed ice. *Israel Journal of Chemistry*, *49*(2), 199-216.

On the spin properties of cement and its components

Anton A. Kashnikov[1], Larisa V. Tsyro[1]
[1]*Institute of Natural and Technical Sciences, Surgut State University, Lenina avenue 1,*
Surgut, Russian Federation
E-mail: twk3n@icloud.com
http://www.surgu.ru

Introduction

By the method of electron spin resonance, it was experimentally established that almost all rocks have molecules with open orbitals, and the specific number of spins per unit volume of the sample is comparable to the Avogadro number [1-3]. Experimental data on the so-called hardness salts have appeared. They precipitate out of domestic and industrial water systems during boiling, and have paramagnetism very similar to the paramagnetism of rocks [4]. This indicates that the prevalence of spin phenomena is much greater than it has been taken into account by researchers so far.

Cement is also a prominent representative of systems with spin properties. Portland cement (PC) is the most popular type of cement in construction. Produced from Portland cement clinker, gypsum and special additives. Clinker is obtained from limestone, clay and additives by firing. Clinker is an intermediate product; its composition is always unchanged. It is limestone and clay mixed in a ratio of 3:1. After cooling, the clinker grains are sent for grinding. They are crushed; a powdered product of a certain size is obtained. The resulting powder is mixed with the necessary additives that determine the brand and properties of the product. Apatites, fluorspar, silica, alumina, etc. are used as additives.

Portland cement is usually made from cheap raw materials that contain significant amounts of chromium, manganese and iron. Limestones contain 0,3–1% Fe_2O_3, clays - 5-15% Fe_2O_3. The greenish-gray color of Portland cement is due to the presence of chromium, manganese, iron, copper, vanadium, nickel, and titanium in its chemical composition. Their number in white cement is minimized.
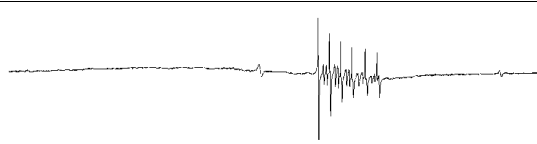
Research Methods

The electron spin resonance (ESR) method was used to analyze the samples. The sample was placed in a quartz glass ampoule, and the ampoule was placed in the resonator of the ESR spectrometer. The SE/X brand spectrometer operating in the X–band was used in the work. The device was tuned (the corresponding microwave modulation was selected), the spectrum was recorded. Spectrum shooting conditions: a) field width 550 mT; b) scan time 16 min; c) frequency 9 GHz; d) sensitivity was selected depending on the sample. The microwave modulation was selected in such a way that the sample did not saturate.

Results

Table 1 shows the data of the electron spin resonance method for the initial components of cement. It can be seen from the data in the table that the ESR spectrum of clay is a broad unresolved line. For limestone and gypsum, a hyperfine structure (HFS) of the spectrum is observed, which is characteristic of elements with a nuclear spin of 5/2. These elements can be aluminum, magnesium, manganese. In the case of gypsum, a complex line is obtained, which may be the result of the interaction of the magnetic moment of an electron with more than one nucleus. Each line of the limestone sextet is split into two. Perhaps this is due to the superposition of lines of hyperfine interaction formed from two different nuclei with a nuclear spin of 5/2. For clay and gypsum, a line is observed in the region g ~ 4.2, which is associated with the presence of ferric iron.

Table 1. Spin properties of the initial components of cement

Sample name	Spectrum view	C_{SC}, spin/g	sextet g-factor
limestone		$6,10*10^{20}$	2,1508 2,0895 2,0359 1,9833 1,9203 1,8708
clay		$3,18*10^{22}$	–
gypsum		$3,06*10^{19}$	2,1504 2,0885 2,0338 1,9813 1,9230 1,8717
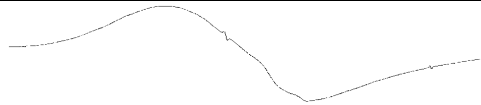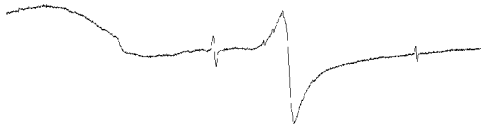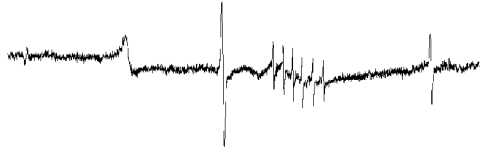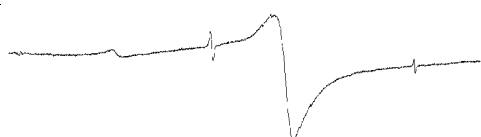
Finished Portland cement is 70-80% calcium silicates, the rest is gypsum and corrective additives. The chemical composition of cement grade M400: CaO – 67%; SiO_2 – 22%; Al_2O_3 – 5%; Fe_2O_3 – 3%; other elements – 3%. The brand determines the maximum strength of the cement. Grade 400 shows that in laboratory tests, the cement withstood a load of 400 kg/cm^2.

The properties of cements obtained by the ESR method are shown in Table 2. Table 2 shows data for different cements, but the ESR spectra of the samples: Portland cement M400, gray fast-hardening M500 D20, straining NC10 M400 are the same. The ESR spectra of white and gray cements are different. This is due to the use of white koalin clays, chalk, pure limestones, which significantly reduces the iron content in the production of white cement. This is reflected in the spectrum: in the case of gray cement there is a wide unresolved line, for white cement, as a rule, a sextet line is observed, as well as a small peak in the area g ~ 4.2. The total number of spin centers (SC), regardless of the brand of cement, is characterized by a large value, which varies from 10^{19} to 10^{22} spin/g.

A distinctive feature of white cements is the high fineness of their grinding. It is about 4500 cm^2/g, while for gray cements this figure is 3500 cm^2/g according to GOST (GOST 31108-2003). Due to this, white cement quickly hardens - the material gains 60% strength after 16 hours after pouring. Gray cement requires 3 to 4 weeks for this. The degree of hardening, in addition to the characteristics taken into account according to GOST, is associated with the presence of SC in the source material. These centers characterize the system during hardening by analyzing the spectrum in a wide range of magnetic field sweeps using direct radiospectroscopy. In [5], it was shown that in the process of mixing cement with water, a decrease in SC occurs.

Cement is characterized by a short shelf life according to GOST. It can be extended to six months or a year (depending on storage conditions). For the "white M500" sample, after 1 year, $C_{SC} = 7,71 \cdot 10^{19}$ spin/g, and for the "gray construction M400" – $7,91 \cdot 10^{20}$ spin/g. For white cement, the concentration of spin centers practically did not change; for gray cement, it decreased by an order of magnitude. The data obtained also indicate that the smaller the SC, the more stable the cement.

Table 2. Spin properties of cement

Sample name	Spectrum view	C_{SC}, spin/g
portland cement M400		$4,63*10^{22}$
gray building M400		$9,44*10^{21}$
gray fast hardening M500 D20		$4,30*10^{22}$
white M500		$8,86*10^{19}$
straining NC10 M400		$4,63*10^{22}$
straining NC20 M400		$2,21*10^{21}$

Consideration of the chemistry of cement, taking into account the spin characteristics of the material, can make it possible to resolve issues of improving its properties, as well as answer questions about the nature of the forces that contribute to the hardening and strength of the cement stone.

References

1. L.V. Tsyro, A.A. Pichugina, F.G. Unger. – Magnetic resonance and its applications. Spinus – 2018. Abstract book. Sant Petersburg State University, 253–255 (2018).
2. L.V. Tsyro, A.A. Pichugina. – Magnetic Resonance and its Applications. Spinus-2019. Proceedings. Saint Petersburg State University, 271−273 (2019).
3. A.S. Rakhimova, A.A. Pichugina, L.V. Tsyro. – Magnetic Resonance and its Applications. Spinus-2021. Proceedings. Saint Petersburg State University, 162−164 (2021).
4. A.A.Pichugina, L.V. Tsyro, F.G. Unger. – Magnetic Resonance and its Applications. Spinus-2022. Proceedings. Saint Petersburg State University, 128−130 (2022).
5. L.V. Tsyro, A.A. Pichugina. – Magnetic Resonance and its Applications, Spinus-2021, Proceedings, Saint Petersburg State University, 168−170 (2021).

Obtaining High Resolution NMR Spectra in Inhomogeneous Magnetic Fields in Experiments with Antiphase Magnetization

Elizaveta S. Kononenko[1,2], Ivan V. Skovpin[2] and Igor V. Koptug[2]
[1]Novosibirsk State University
[2]International Tomography Center SB RAS (ITC SB RAS), Novosibirsk
E-mail: elizaveta.kononenko@tomo.nsc.ru

Introduction

Nuclear magnetic resonance (NMR) methods are widely used for operando studies of heterogeneous catalytic processes. Because these methods are non-invasive, unique information about the operation of heterogeneous reactors can be obtained. But despite the wide range of possible studies, there are a number of limitations. One of them is the relatively low sensitivity of the method. It can be overcome using hyperpolarization techniques, such as parahydrogen-induced polarization (PHIP). Another significant limitation of the operando studies of heterogeneous reactors is the inhomogeneity of the magnetic field induced by a catalyst layer, which leads to a decrease in the spectral resolution. In addition, the experiments using PHIP at high magnetic fields (PASADENA experiments) are characterized by an antiphase NMR line shape. The positive and the negative parts of such signals cancel each other upon line broadening, which leads to a significant reduction in the sensitivity. Earlier we have already shown that conversion of an antiphase signal into an inphase one significantly increases the signal-to-noise ratio in MRI, but it does not lead to an improvement in the spectral resolution in NMR [1]. Therefore, it is necessary to develop methods that are based on the specifics of such experiments and allow one to obtain high-resolution spectra in an inhomogeneous magnetic field. This will make it possible to determine the spatial distribution of reactants and products and estimate the degree of substrate conversion inside a heterogeneous reactor.

Simulation of high-resolution NMR spectra

In this work, we investigate the possibilities of using multiple quantum coherences to obtain high-resolution spectra in experiments with antiphase magnetization in an inhomogeneous magnetic field. At the first stage we simulated 2D NMR spectra of the AX spin system in an inhomogeneous magnetic field under the action of the COSY (COrrelated SpectroscopY) pulse sequence. Spectra were obtained for various initial states: inphase magnetization ($\hat{I}_{1Z} + \hat{I}_{2Z}$), antiphase magnetization ($2\hat{I}_{1Z}\hat{I}_{2Z}$) and in the case of transformation of inphase magnetization into antiphase by the Sarkar module of pulse sequence (Figure 1).
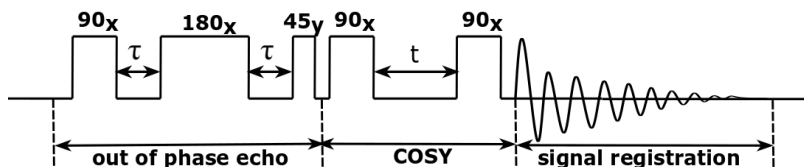
Figure 1. Scheme of the COSY pulse sequence with preliminary application of a pulse sequence module that converts inphase magnetization into antiphase (the Sarkar module of pulse sequence).

Experimental results

Further, the simulation results were verified experimentally. β-Nitrostyrene was chosen as a model AX spin system (Figure 2A). In the one-dimensional (1D) NMR spectrum (Figure

2D) obtained in an inhomogeneous magnetic field, the lines are broadened and the useful signal from the CH group overlaps with the signals of the solvent (chloroform-d). At the same time, a one-dimensional slice of the 2D NMR spectrum (Figure 2B) at the maximum of the signals of interest provides a high-resolution NMR spectrum, in which only high-intensity useful signals are present (Figure 2E). The result is also in agreement with a simulated spectrum (Figure 2C).
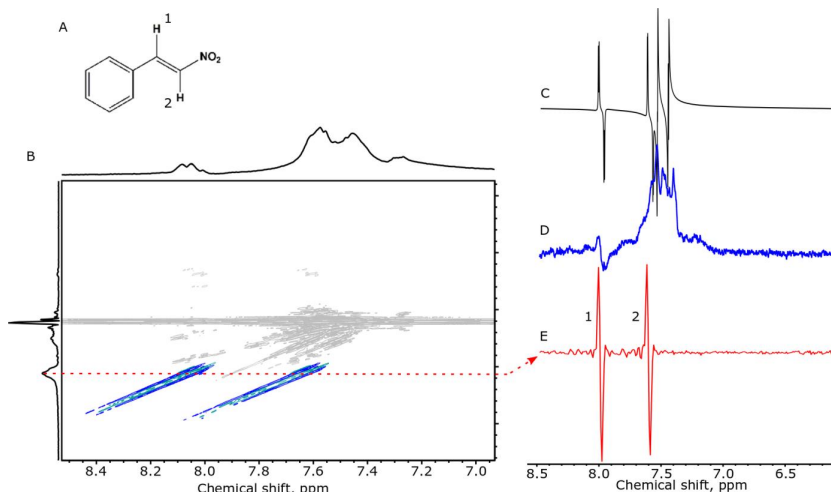
Figure 2. A – β-nitrostyrene molecule. B – 2D NMR spectrum of β-nitrostyrene obtained using the COSY pulse sequence with preliminary application of the Sarkar module of pulse sequence (useful signal in the spectrum is highlighted, blue corresponds to the positive part of the signal, light blue - negative). C – the simulated NMR spectrum of β-nitrostyrene. D – 1D NMR spectrum of β-nitrostyrene in an inhomogeneous magnetic field. E – one-dimensional slice of the 2D NMR spectrum at the maximum of the useful signals.

In addition, we began to investigate the effectiveness of this approach for obtaining high-resolution NMR spectra in experiments using PHIP in heterogeneous hydrogenation reactions. The performed studies demonstrate the possibility of using the COSY pulse sequence to obtain high-resolution NMR spectra in experiments with antiphase magnetization. It will expand the scope of NMR for studying heterogeneous catalytic hydrogenation processes using PHIP.

Acknowledgments

References

1. E.S. Kononenko, A. I. Svyatova et al. J. Phys. Chem. C, 126, 35, 14914–14921 (2022).

Detection of organophosphorus liquids by NMR in the Earth's magnetic field

Rifat Gimatdin[1], Pavel Kupriyanov[1,2], Georgy Mozzhukhin[1], Bulat Rameev[1,3,4], Vladimir Chizhik[2]

[1]*Physics Department, Gebze Technical University, Gebze, Kocaeli, Turkey*
[2]*Saint-Petersburg State University, St. Petersburg, Russian Federation*
[3]*Kazan State Power Engineering University, Kazan/Tatarstan,*
[4]*Zavoisky Physical-Technical Institute – Subdivision of the FRC "Kazan Scientific Center of Russian Academy of Sciences", Kazan/Tatarstan, Russian Federation*
E-mails: pavel@gtu.edu.tr

Abstract

NMR in high magnetic fields is usually preferred for analyzing organic substances because the spectral resolution increases with resonance frequency. However, indirect spin-spin coupling (J-coupling) can be probed by NMR in low or ultra-low fields (e.g. in Earth's magnetic field). The spectral splitting in the NMR spectra due to the J-coupling interaction make it possible to distinguish various liquids. In this work, Earth's magnetic field NMR-spectra from three different organophosphorus liquids have been measured using simple and inexpensive equipment. We have shown that the EFNMR spectra can be used to distinguish between various liquids of similar structure.

Introduction

NMR-investigations of organic substances usually are carried out in strong magnetic fields, because the chemical shift carries a wealth of information about the proton (or another nucleus) environment and the local electronic structure of a molecule. At first glance, very small chemical shift absolute values in low-field (e.g. in Earth's magnetic field) make this method absolutely useless. However, NMR spectra in the Earth's magnetic field include the information about indirect spin-spin coupling (J-coupling) and it makes possible to distinguish various liquids quite well. This work is devoted to the study of NMR spectra in the Earth's magnetic field from organophosphorus liquids. The spectra were registered using the simple and inexpensive equipment.

Experimental results and their discussion

The differences between the spectra of the three organophosphorus liquids are shown in Fig. 1. One can see that the spectra are strikingly different from each other.

The NMR-spectrum of triethyl phosphate in a strong field consists of two bundles of lines: from methyl and methylene groups (Fig. 2). Fourteen lines are observed in the strong-field NMR-spectrum: both methyl and methylene groups split with doublet due to phosphorous interaction every line of doublet of methyl protons splits into three lines (with amplitude ratio 1:2:1) out of interaction two methylene protons and doublet methylene groups into four lines (with amplitude ratio 1:3:3:1) out of interaction three methylene protons (see fig. 2).
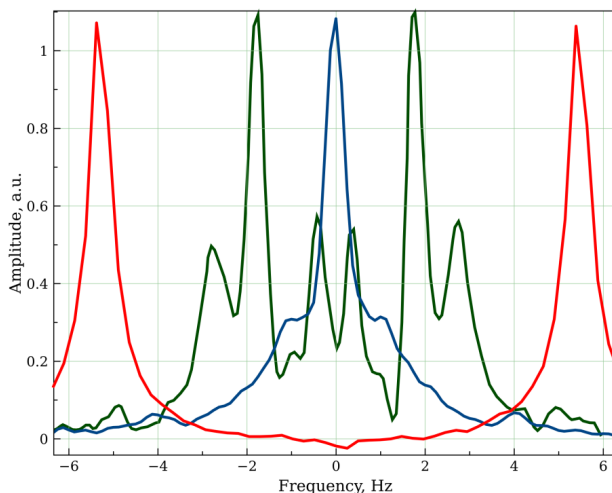
Figure 1. The NMR-spectra of trimethyl phosphate (red), triethyl phosphate (green), and tributyl phosphate (blue) in the Earth's magnetic field.
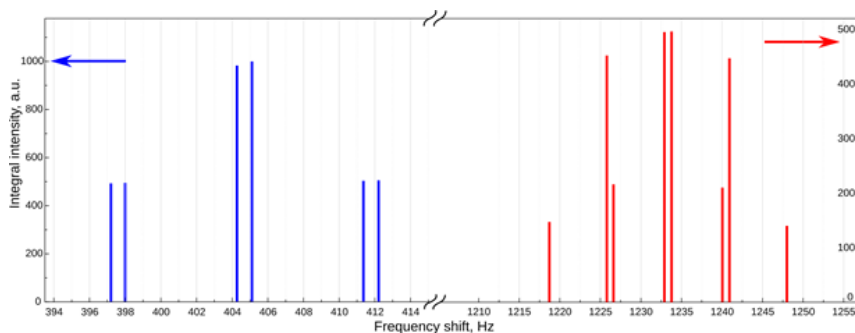
Figure 2. The ^{1}H NMR-spectrum of triethyl phosphate is based on data of SDBS (https://sdbs.db.aist.go.jp/sdbs/cgi-bin/landingpage?sdbsno=2164). Lines for the methyl group (left) and methylene one (right) at the resonance frequency 300-MHz.

In the Earth's field NMR, only 6 distinct lines are resolved in the spectra (see Fig. 1, green), and this is not due to the low resolution of NMR in the Earth's field. One can see that the distance between lines in the spectrum center is about 1 Hz between lines in the spectrum center. The number of spectral lines is reduced due to second-order effects. If the chemical shift between AB elements in a spin system becomes comparable to J-coupling then the shape of lines, splitted by spin-spin interaction, is distorted. Furthermore, the number and the distance between the lines are changed and the so-called "roofing" effect (changing arbitrary intensities of the lines) is observed. In detail, this effect is described in [1]. Stefan Appelt et al. offer the spring model of transformation of NMR spectra upon transition from strong to weak fields [2]. They also develop a mathematical apparatus that makes it possible to model NMR spectra in weak fields [3].

There is a decrease in line splittings with an increase in the length of chains of methylen groups in molecules of studied liquids. Tributyl phosphate has three methylene groups and its spectrum in strong-field NMR contains four multiplets. Various lines in Earth's field NMR spectrum of this material are already difficult to distinguish, but they may be deconvoluted by the software, e.g. in the MagicPlot program (Fig. 3).
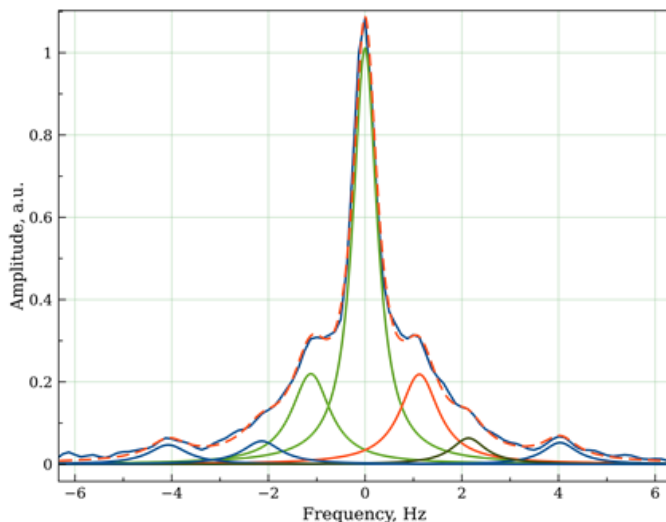
Figure 3. The EFNMR-spectrum of tributyl phosphate. Simulation of spectral lines and their sum (dashed line) were performed using the MagicPlot program.

Conclusion

We have shown that rich information about indirect spin-spin coupling (J-coupling) can be obtained by the Earth's magnetic field NMR. This work is devoted to the study of the NMR spectra in the Earth's magnetic field from three different organophosphorus liquids. Furthermore, the EFNMR experiments make it possible to distinguish various liquids with different molecular chain lengths.

References

1. Laurence M. Harwood and Timothy D. W. Introduction to Organic Spectroscopy. Claridge. 1996. 96 p.
2. Stephan Appelt, F. Wolfgang Häsing, Holger Kühn, Ulrich Sieling, Bernhard Blümich. Analysis of molecular structures by homo- and hetero-nuclear J-coupled NMR in ultra-low field. Chemical Physics Letters 440 (2007) 308–312
3. S. Appelt, F. W. Häsing, U. Sieling, A. Gordji-Nejad, S. Glöggler, B. Blümich. Paths from weak to strong coupling in NMR. Physical Review A 81, 023420 (2010)

Translational diffusion as a protein-protein interaction marker

A.M. Kusova, A.E. Sitnitsky, Yu.F. Zuev

Kazan Institute of Biochemistry and Biophysics, FRC Kazan Scientific Center of RAS,
Lobachevsky Str., 2/31 Kazan, Russian Federation
E-mail: alexakusova@mail.ru

Translational diffusion is the main way of molecular transport in organisms that defines numerous vital activities of the living systems. In simple cases, the diffusional process is well described by the classical Stokes–Einstein model. Translational diffusion of macromolecules significantly deviates from the classical representation in real living systems. Living systems contain various types of macromolecules such as DNA, RNA, proteins and there are many non-specific "soft" intermolecular interactions. Soft interactions include hydrogen bonds and charge–charge, solute–protein, van der Waals and hydrophobic interactions. Of these, only the strong electrostatic repulsion of like charged molecules prevents their approach. Other soft interactions are attractive and destabilizing because they favor expanded conformations that allow access to the attractive surfaces. Effect of the intracellular environment modulating protein-protein interactions (PPI) is important because the totality of weak interactions in cells forms the crowded cellular interior.

One of the commonly accepted approaches to estimate PPI in aqueous solutions is the analysis of their translational diffusion. Phenomenological approach was applied to analyze PPI effects via concentration dependencies of self- and collective translational diffusion coefficient for several spheroidal proteins derived from the pulsed field gradient NMR (PFG NMR) and dynamic light scattering (DLS), respectively [1,2]. The technique of pulsed field gradient nuclear magnetic resonance (PFG NMR) operates on time scales exceeding those of the intermolecular collisions. The long-time self-diffusion coefficient D_s is observed as the averaged result of protein diffusivity over a long observation time. In dilute solutions, the molecules move independently of each other, whereas in the semi-dilute solutions, the intermolecular interactions result in appearance of new class of motion-collective modes described by collective diffusion coefficient D_c (DLS) [3,4]. D_c depends on the microscopic fluctuations in the local concentration of particles and the corresponding local heterogeneities in the refractive index of the medium [5]. The self- and collective diffusion coefficients are always identical with diffusion coefficient in dilute solution when interactions between diffusing species are absent. At intermediate concentrations, D_c is different from D_0 and D_s and strongly depends on intermolecular interactions.

The concentration dependence of molecular diffusion coefficient contains information on the contributions of various types of PPI. The combination of protein concentration dependencies of self- and collective diffusion coefficients with phenomenological approach based on the formalism of non-equilibrium thermodynamics allows one to obtain sets of friction and virial coefficients. The second and higher virial coefficients were obtained for evaluation of paired and multi-particle intermolecular interactions in solution for chymotrypsin (ChTr), human serum albumin (HSA), α-casein (α-CN), and β-lactoglobulin (β-Lg). The McMillan–Mayer theory can be used for quantitative estimation of the non-specific PPI [6]. Balance of attraction-repulsion potentials between the two protein molecules in solution was considered within the electrostatic and van der Waals interactions in the framework of DLVO theory. The positive value of the second virial coefficient of spheroidal ChTr, HSA, α-CN, and β-Lg at low ionic strengths (0.003 M–0.01 M) indicates the dominance of the intermolecular repulsion. Increase of ionic strength (0.1–1.0M) leads to screening of the protein charges and, as a result, electrostatic potential decreasing was observed. The increase of the van der Waals attraction of ChTr and α-CN can be explained by

propensity to manifest weak unstable attractive interactions. The decrease of van der Waals interaction of β-Lg molecules is associated with well-known association process [7].

Self- and collective diffusion are sensitive differ to a short-lived HSA molecular forms. Short-time collective diffusion shows one type of diffusing species of pure HSA solution and two molecular forms of HSA with the presence of metal ions in the either concentration range. While the long-time diffusion detected an averaged self-diffusion coefficient among fast exchanging HSA oligomer forms.

References

1. Kusova AM, Sitnitsky AE, Faizullin DA, Zuev YF. Protein Translational Diffusion and Intermolecular Interactions of Globular and Intrinsically Unstructured Proteins. J Phys Chem A. 2019; 123(46):10190–6.
2. Kusova AM, Sitnitsky AE, Zuev YF. The Role of pH and Ionic Strength in the Attraction–Repulsion Balance of Fibrinogen Interactions. Langmuir [Internet]. 2021 Aug 17; Available from: https://doi.org/10.1021/acs.langmuir.1c01803
3. Sobac B, Dehaeck S, Bouchaudy A, Salmon J-B. Collective diffusion coefficient of a charged colloidal dispersion: interferometric measurements in a drying drop. Soft Matter. 2020; 16(35):8213–25.
4. Bowen WR, Mongruel A. Calculation of the collective diffusion coefficient of electrostatically stabilised colloidal particles. Colloids Surfaces A Physicochem Eng Asp. 1998; 138(2–3):161–72.
5. Dallari F, Jain A, Sikorski M, Möller J, Bean R, Boesenberg U, et al. Microsecond hydrodynamic interactions in dense colloidal dispersions probed at the European XFEL. IUCrJ. 2021; 8(5).
6. Haynes CA, Tamura K, Korfer HR, Blanch HW, Prausnitz JM. Thermodynamic properties of aqueous. alpha.-chymotrypsin solution from membrane osmometry measurements. J Phys Chem. 1992; 96(2):905–12.
7. Verheul M, Pedersen JS, Roefs SPFM, de Kruif KG. Association behavior of native β-lactoglobulin. Biopolym Orig Res Biomol. 1999; 49(1):11–20.

Development and characterization of new membranes based on polyphenylene oxide and its block copolymer with polydimethylsiloxane for enhanced pervaporation

Vladislav P. Liamin, Anastasiia D. Chepeleva, Anna I. Kuzminova, Anton S. Mazur, Anastasia V. Penkova, Mariia E. Dmitrenko

St. Petersburg State University, 7/9 Universitetskaya nab., St. Petersburg 199034, Russia
E-mail: lyamin.vlad.322@gmail.com

Introduction

One of the most popular separation and concentration methods are membrane technologies, related to sustainable processes. Pervaporation is a membrane method used to separate liquid mixtures of low molecular weight substances, which is an alternative to traditional separation methods (distillation, rectification, etc.) due to such advantages as environmental friendliness, low energy consumption, ease of automation and control, and the possibility of separating azeotropic mixtures without adding intermediate toxic reagents. The rapid development of pervaporation requires the search for new membrane materials and the creation of high-performance membranes based on them. One of the most effective directions for the development of new membrane materials is the combination of the properties of known polymers.

Membrane investigation

In the present work, novel membranes based on polyphenylene oxide and its block copolymer with polydimethylsiloxane were developed for enhanced pervaporation dehydration of ethanol. The block copolymer based on poly(2,6-dimethyl-1,4-phenylene oxide) (PPO) and polydimethylsiloxane (PDMS) was synthesized to create new highly efficient pervaporation membranes. For explanation of changes in membrane transport properties, the structure of the PPO and PPO-b-PDMS membranes was studied by spectroscopic methods such as FTIR and NMR, and atomic force and scanning electron microscopies.

Results

It was shown that membranes based on synthesized PPO-b-PDMS had significantly improved permeation flux compared to the pristine PPO membrane.

Acknowledgments

The DNA binding mechanism of virulence-associated protein Ler from pathogenic *Escherichia coli*

Fan Liu[1], Bo Duan[2], Bin Xia[1]

[1]*Beijing Nuclear Magnetic Resonance Center, College of Chemistry and Molecular Engineering, and School of Life Sciences, Peking University, Beijing 100871, China*
[2]*School of Biology & Basic Medical Sciences, Soochow University, Suzhou 215123, China*
E-mail: liufan33@pku.edu.cn

Horizontal gene transfer (HGT) is a major driving force for bacterial evolution and speciation, which can provide microbes with new genetic materials and adaptive traits. Many virulence factors and pathogenicity islands were transmitted among bacteria through HGT, such as the locus of enterocyte effacement (LEE) pathogenicity island of Enteropathogenic *Escherichia coli* (EPEC) and Enterohemorrhagic *Escherichia coli* (EHEC). The LEE pathogenicity island is mainly composed of five operons *LEE1-LEE5* and several smaller transcriptional units, which encode the components of a type III secretion system and some other virulence factors. The expressions of *LEE1-LEE5* operons are inhibited by xenogeneic silencer H-NS. The protein Ler, encoded by the first gene of *LEE1* operon, can antagonize the H-NS mediated inhibition of the transcription of *LEE2-LEE5* operons, which is essential for the virulence of EPEC and EHEC. However, the DNA binding mechanism and precise DNA binding specificity of Ler remain largely unknown.

In order to elucidate the DNA binding mechanism of Ler, we determined the solution structure of the C-terminal DNA binding domain of Ler (Ler$^{65-123}$) in complex with DNA d(CGCAAATTTGCG)$_2$. Ler$^{65-123}$ binds at the "AAATTT" region of the DNA, with residues Val88, Gly89 and Arg90 inserted into the minor groove, forming an "AT-hook-like" structure (Figure 1A). The binding is assisted by interactions of residues R68, R69, Q91, R93, K96, and K105 with DNA phosphate groups. *In vitro* mutagenesis studies confirmed that all of these residues contribute to the DNA binding ability of Ler$^{65-123}$, which further verifies the accuracy of our structural model (Figure 1B). The main chain NH groups of residues Gly89 and Arg90, and the sidechain guanidine group of Arg90 form hydrogen bonds with the O2 atoms of T bases in the minor groove. As a result, Ler binds to long contiguous A/T sequences with a preference towards the AATT motif, such as AAATTT and TAATTA (Figure 1C, D).

In summary, we have elucidated the DNA binding mechanism and binding specificity of the C-terminal domain of Ler, which will gain insight into the mechanism by which Ler antagonizes the transcription repression exerted by H-NS.
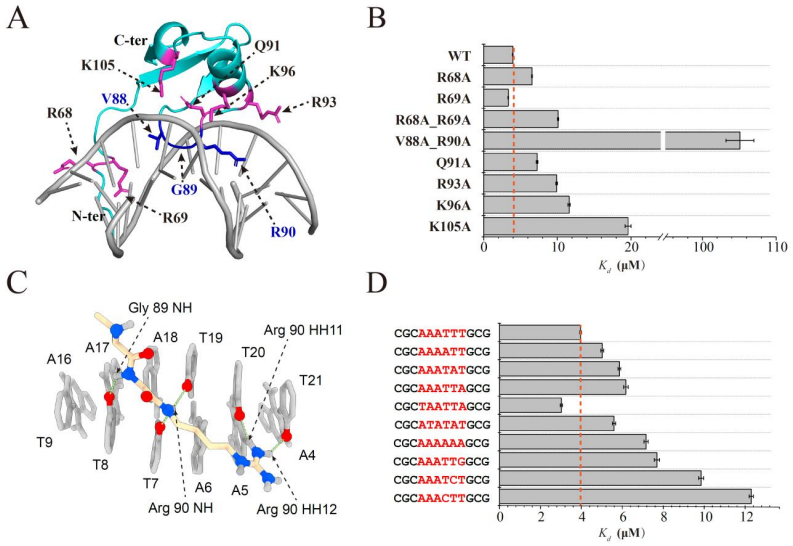
Figure 1. (A) Solution structure of Ler[65-123]/DNA complex. (B) Mutagenesis studies. (C) The interaction between "VGR" residues and DNA minor groove. (D) The DNA binding specificity studies of Ler[65-123].

Time Domain Nuclear Magnetic Resonance Investigations of Benign and Threat Liquids

Ayşe Maraşlı[1], Hacer İpek[1], Cengiz Okay[2], B. Z. Rameev[1,3,4]
[1]Department of Physics, Gebze Technical University, Kocaeli/Turkey
[2]Department of Physics, Marmara University, Göztepe-Istanbul, Turkey
[3]Kazan State Power Engineering University, Kazan/Tatarstan,
[4]Zavoisky Physical-Technical Institute – Subdivision of the FRC "Kazan Scientific Center of Russian Academy of Sciences", Kazan/Tatarstan, Russian Federation
E-mail: amarasli@gtu.edu.tr

Introduction

Detection of explosive and dangerous liquids is a very important problem for civil and military security measurements and practices. NMR one of the most powerful analytical methods for the investigation and identification of various substances, can also be used for the detection of explosives. However, using a (HF) NMR device for the detection of dangerous liquids at control points in transportation facilities brings with it a number of technical problems and very high costs. TD-NMR or NMR relaxometry technique is being studied intensively as an alternative method for explosive material detection, since it is much more economical, compact and easy to apply than (HF) NMR. Determination of NMR relaxation parameters makes it possible to distinguish between hazardous and non-hazardous liquid groups. The first study on using NMR method of detection of explosives and dangerous materials have been performed by Burnett and it has been published in 1994 [1]. Following years, Kumar and co-workers have been try to show practical usage of NMR in detection of explosives [2]. On August 10, 2006 the terrorists have tried to attack on more than one airplane which has flied from United Kingdom to United States and Canada simultaneously. Fortunately, they have been noticed and their explosion has been prevented. However, after this incident, severe restrictions have been applied in international airports. Because liquids explosives and explosive precursor materials are odorless, clear and resemble with water, it is difficult to determine whether dangerous or not. For this reason, research on development of a rapid, low-cost and effective method for determining liquid explosives has started. In the article [3],and patent [4] published by different research groups have obviously proved that the dangerous materials could be distinguished by evaluation of relaxation parameters NMR is an effective technique for the detection of large number of dangerous liquids [5,6].TD-NMR for the detection of dangerous liquids provides more accurate results and allows better evaluation of the measurement results comparing with the other techniques. In this study, relaxation times (T_1 and T_2) have been investigated as well as to classify (discriminate) between various kinds of benign and threat liquids.

Experimental

In this study, seven different liquid groups (63) were used as samples. The samples were placed in an 8 mm radius glass NMR tube with a height of 15 mm and conditioned at room temperature (25°C). Relaxation times were taken with the Bruker Minispec MQ20 device. The Inversion Recovery (IR) and Carr-Purcell-Meiboom-Gill (CPMG) pulse sequences were used for T_1 and T_2 measurements, respectively. Experimental parameters of the CPMG and IR measurements for the device are given Table 2. The relaxation parameters (T_2 and T_1) were calculated by exponential fittings($A = A_0 e^{-t/T_2}$), $A = A_0 \left(1 - 2e^{-t/T_1}\right)$ and parameters (T_{21} - T_{22}) and (T_{11} - T_{12}) were calculated by bi-exponential fittings($A = A_1 e^{-t/T_{21}} + A_2 e^{-t/T_{22}}$), $A = A_1 \left(1 - 2e^{-t/T_{11}}\right) + A_2 \left(1 - 2e^{-t/T_{12}}\right)$

Table 1. List of the samples groups.

Water	Uludağ Mineral Water	Eskipazar Mineral Water
	Top Water	Distilated Water
	Kuvartz Drinkable Water Kızılay	Damla Mineral Water
	Mineral Water	Beypazarı Mineral Water
Fruit Juice	Cappy Apricot	Dooy Cherry
	Cappy Cherry	Dooy Peach
	Cappy Peach	Lipton Ice Tea Peach
	Dimes Apricot	Lipton Ice Tea Lemon
	Dimes Cherry	Pınar Cherry
	Dooy Apricot	Pınar Apricot
	Dimes Peach	Pınar Peach
Soft Drink	Cocacola	Fruko
	Cocacola Light	Pepsi Zero
	Cocacola Zero	Pepsi
	Çamlıca Gazoz	Sprite
	Fanta	
Edible Oils	Virgin Olive Oil	
	Sunflower Oil	
	Riviera Olive Oil	
Beverages	Brendy (%40 Alcohol)	Baileys (%17 Alcohol)
	Tekirdağ Rakı (%45)	Terre Allegra Red Vine (%12)
Milks	İçim Milk Light	Pınar Milk Light
	İçim Milk Normal	Sek Milk Normal
	İçim Milk Rahat	Pınar Milk Lactose Free
	Pınar Milk Normal	Sütaş Milk Normal
Chemical Compounds and Solutions	Propanol	N-N Diethylformamide
	Isopropanol	Nitrobenzene
	Acetone	Mitromethane
	Acetonitrile	Methanole
	Chloroform	Tetrahydrofuran
	Dioxane	Toluene
	Formamide	EST Lemon Cologe
	Ethylenamide	Peroxide
	Glycerole Solution	

Table 2. Measurement parameters of CPMG and IR sequences.

Parameters for CPMG	Bruker Minispec	Parameters for IR	Bruker Minispec
B_1 Frequency	19.95 MHz	B1 Frequency	19.95 MHz
B_1 Field	1.76 mT	B_1 Field	1.76 mT
Echo Time	500 us	Max Delay	1500 ms
Number of Echoes	1500	Number of Steps	50
Repetition Time	2000 ms	Repetition Time	2000 ms
90^0 Pulse Length	3.32 us	90^0 Pulse Length	3.32 us
180^0 Pulse Length	6.4 us	180^0 Pulse Length	6.4 us
Receiver Gain	64 dB	Receiver Gain	64 dB
Number of Scans	4	Number of Scans	2

Result and discussion

The relaxation times of various liquids are given in Fig. 1. It is seen in Fig. 1a and Fig.1b that different liquids groups can be grouped according to their T_1 and T_2 values. However, there is a problem in the discrimination of some groups of liquids, e.g., water + mineral water group and chemicals have overlapping values of T_1 (T_2) values. We found in many cases, discrimination between various liquids could be improved by using bi-exponential fits (or even obtaining a continuous distribution of relaxation parameters by application of inverse Laplace transform). In this manner, we can increase the number of

scanned parameters to resolve better between various liquids. For instance, a ratio of relaxation times of T_{21}/T_{22} or T_{11}/T_{12} (Fig.2b) can be used.

(a)   *(b)*
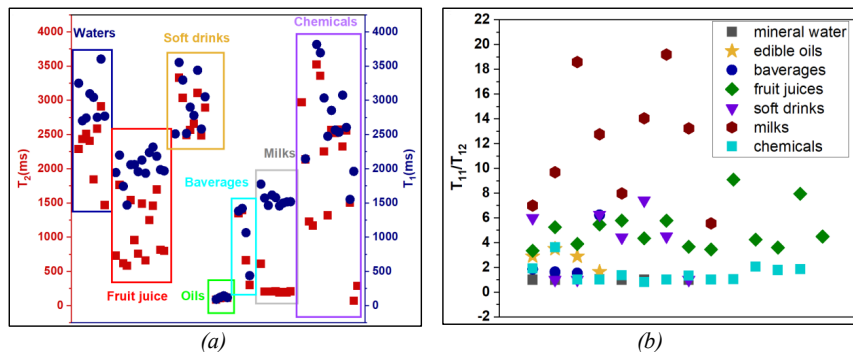
Figure 1. (a) T_1 and T_2 relaxation times of each samples, (b) Ratio of bi-exponential results of T_1 relaxation times of each samples.

Conclusions

We demonstrated TD-NMR is an efficient method to detect dangerous liquids in the case that advanced measurement and signal processing approaches are applied. It is also desirable to use an additional measurement technique based on other physical principles (e.g. measurements of dielectric permittivity or optical properties) to increase the reliability of identification further.

Acknowledgments

References

1. L.J. Burnett, Liquid explosives detection., Subst. Detect. Syst. 2092 (1994).
2. D.C.S. Sankaran Kumar, W. Casey McMichael, Y.-W. Kim, Alan G. Sheldon, Erik E. Magnuson, L. Ficke, T. K.-L. Chhoa, C. R. Moeller, Geoffrey A. Barrall, Lowell J. Burnett, Peter V. Czipott, J. Scott Pence, Screening sealed bottles for liquid explosives, Secur. Syst. Nonlethal Technol. Law Enforc. 2934 (1997).
3. A. Gradišek, T. Apih, NMR-Based liquid explosives detector, Appl. Magn. Reson. 38 (2010) 485–493. https://doi.org/10.1007/s00723-010-0145-9.
4. P.J. Prado, Detecting Hazardous Materals in Containers Utilizing Nuclear Magnetic Resonance Based Measurements, US 9,575,019 B2, 2017.
5. B. Rameev, G. Mozzhukhin, B. Aktaş, Magnetic Resonance Detection of Explosives and Illicit Materials, Appl. Magn. Reson. 43 (2012) 463–467. https://doi.org/10.1007/s00723-012-0423-9.
6. G. V. Mozzhukhin, G. V. Kupriyanova, S.S. Mamadazizov, A. Maraşlı, B.Z. Rameev, Low-field 14N nuclear magnetic resonance for detection of dangerous liquids, Chem. Phys. 513 (2018) 129–134. https://doi.org/10.1016/j.chemphys.2018.07.032.

The detection of NQR signals with use of the single-turn toroid

<u>G. V. Mozzhukhin[1]</u>, B.Çolak[1], P.A.Kupriyanov[1], M.Maksutoğlu[1], S. Kazan[1], H. İpek[1], A. Maraşlı[1], C.Okay[2], B. Z. Rameev[1,3,4]

[1]*Physics Department, Gebze Technical University, Gebze, Kocaeli, Turkey*
[2]*Department of Physics, Marmara University, 81040 Göztepe-Istanbul, Turkey*
[3]*Kazan State Power Engineering University, Kazan/Tatarstan,*
[4]*Zavoisky Physical-Technical Institute – Subdivision of the FRC "Kazan Scientific Center of Russian Academy of Sciences", Kazan/Tatarstan, Russian Federation*
Email: mgeorge@gtu.edu.tr

Introduction

In this report, we describe a system for the detection sample in volume with a low filling coefficient by the nuclear quadrupole resonance (NQR) method. NQR is a non-destructive method for the identification of solid chemical substances [1]. Identification of substances for the needs of transport security and industry is realized in conditions which are far from the laboratory ones. It means that a substance to be detected may occupy only a small part of the scanned volume, it may be partially shielded, and a scanned volume may contain conductive parts, etc. In this work, the conditions of work of NQR detection system which are close to real ones have been tested and their impact on the possibility of identification of nitrogen compounds has been estimated.

Experimental

Several types of RF coils can be used for the distant detection of NQR signals. There are solenoidal coils, flat disk coils, gradiometric coils, and others [2]. In our system, we tested a single-turn toroid coil as proposed in [3]. The coil has the advantage to be noise resilient [3] and it may be easily scaled for different sizes of objects. For successful use in practice the coil needs to produce a radiofrequency field of enough intensity, high sensitivity in a large part of its volume despite a low filling coefficient, possibility to tune its frequency.

Our NQR system consists of a two-channel Tecmag Scout console (0.1-100 MHz), linear amplifier TOMCO model BT04000-AlphaC, low noise preamplifier Miteq (0-100MHz), home-made low noise preamplifier (0.1-10 MHz) and homemade Q-spoiler. The RF coil is presented in Fig.1. The size of the one-turn coil made of copper is 170x90x 50cm. The volume used for the NQR detection in the gap of this coil is 50x50x55 cm. The resonance frequency of the coil is tunable near the resonance frequency (3305±5 kHz). The quality factor for the loaded coil is 180. For the experiments, we used the sample of hexamethylenetetramine (HMTA) $C_6H_{12}N_4$ with a ^{14}N NQR frequency of 3306 kHz at room temperature.

Before manufacturing, the distribution of the radiofrequency magnetic field inside the coil gap was modelled by the finite element method (FEM). The calculated distribution of the radiofrequency field is presented in Fig.2. Comsol MP Software was used in the simulations.

Results and discussion

Firstly, we tried to define a minimal weight of the HMT substance for robust detection of the NQR signal. The time of detection was in the interval of 1- 2 minutes. The sample was inside the backpack. We found that 500 g of HMT can be detected. The sample of smaller weight can be detected by increasing the detection duration or by increasing the quality factor of the RF probe.

Secondly, the influence of shielding the sample with foil on the possibility to detect NQR signals was tested. The weight of the sample was 2 kg with a size of about

180x180x90mm. A square hole with an area of 100 cm^2 was saved in the sample shielding to prevent a full shielding of sample material (Fig.3).
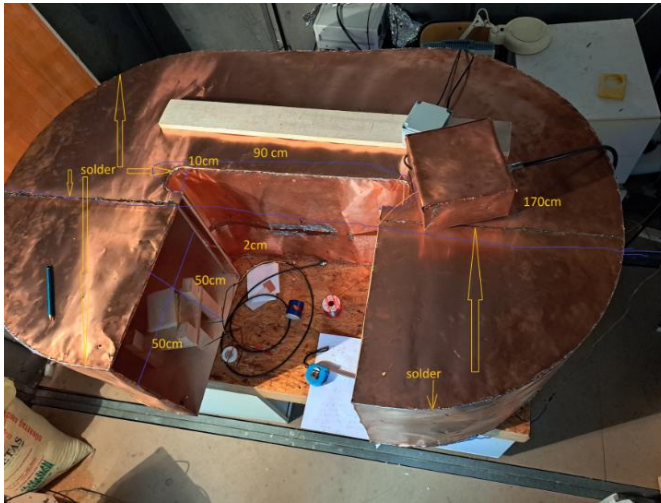
Figure 1. Photograph of one-turn toroid coil

a   b
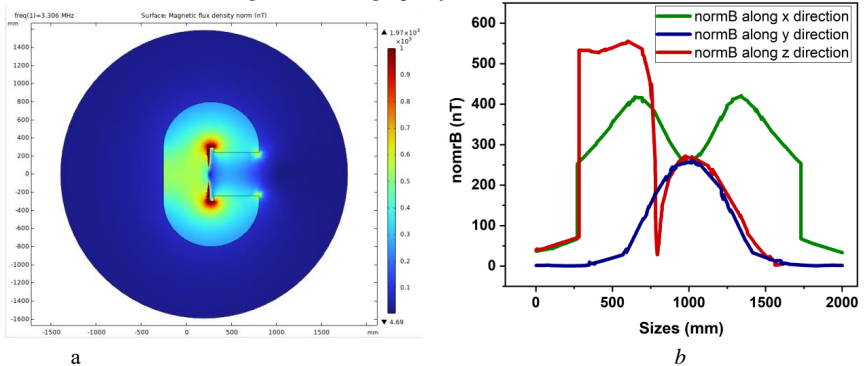
Figure 2. Magnetic field distribution in the one-turn toroid coil: a) the field induction in the longitudinal section (dark blue colour corresponds to the minimum field); b) dependence of the magnetic field induction on a position along different axes (x, y, z) passing through the center of the gap.

We measured the signal intensities depending on the window orientation relative to the central axis of the toroid opening (0°). The results are presented in Table 1. T of each measurement was nearly 8 minutes. It is clear that 0° and 180° orientations provide the maximum possible signal with respect to other geometries.

Figure 3. Sample of HMTA in the gap of the toroid coil.

Table 1. The magnitude of partially shielded samples for different orientations.

Position	Relative magnitude	The ratio of the signal in the shielded sample to the signal without shielding
0°	545151	~0.10
90°	116781	~noise
180°	553141	~0.10
270°	53594	~noise
Without shielding	6112860	1

Conclusion

We designed the system for the detection of samples by the ^{14}N NQR method. We studied the conditions optimal for the detection of NQR signals by a signal turn toroid coil. The distribution of the radiofrequency field in the gap of the RF probe was calculated by FEM modelling. The minimally detected sample quantity (500 g) for detection of the HMT compound by the constructed toroid coil for 2 minutes was defined. The possibility of the detection of a partially shielded sample of HMTA using the toroidal RF probe was tested. The dependence of signal intensities on the orientation of the hole in the sample shielding was studied.

Acknowledgments

References

1. G.V. Mozzhukhin, B.Z.Rameev, *Nuclear Quadrupole Resonance*, In Book: *Subsurface sensing* (*Eds.* A.S. Turk, A.K. Hocaoglu, A.A. Vertiy), Wiley-Interscience, ISBN: 978-0-470-13388-0, Hardcover, 920 pages, September 2011,(429-450)
2. J.B.Miller, G.A.Barrall, "Explosives Detection with Nuclear Quadrupole Resonance", American scientist, Vol. 93 (1), 50 (2005).
3. J.Barras, M.J.Gaskell, N.Hunt, R.I.Jenkinson, K.R.Mann. D.A.G.Pedder, G.N.Shilstone, J.A.S.Smith. Appl. Magn. Reson. 25, 411-437 (2004).

Local structure and dynamics in concentrated "water-in-salt" mixed LiOAc and KOAc solutions according to data of NMR.

Kirill A. Mukhin[1], Olga N. Pestova[1], Konstantin V. Tyutyukin[2], Vladimir V. Matveev[2]

[1]Department of General and Inorganic Chemistry, Chemistry Institute, Saint Petersburg State University

[2]Department of Nuclear Physics Research Methods, Saint Petersburg State University,

E-mail: st085268@student.spbu.ru , o.pestova@spbu.ru

Introduction

Electrolyte solutions are a key component of energy storage devices. Recent developments in aqueous electrolyte water-in-salt (WIS) research have demonstrated aqueous lithium-ion batteries that operate with a capacity and cycle life comparable to commercial non-aqueous lithium-ion batteries. Among these works, electrochemical studies of highly concentrated aqueous systems containing alkali metal acetates are distinguished: LiOAc-KOAc-H_2O, LiOAc-CsOAc-H_2O. The concentration of salts in the mixture has a significant effect on the mobility of ions, and consequently on the electrical conductivity of the WIS system.

The purpose of this work is to study particles mobility and local structure in the LiOAc-KOAc-H_2O system depending on salts concentration by NMR methods. In addition, the task of this study is to determine the density values for WIS electrolyte based on cesium acetate saturated solution with different lithium acetate content for further study of ions mobility and electrochemical properties.

The mobility of anions and cations was studied by measuring the diffusion coefficients and relaxation rates in the LiOAc-KOAc-H_2O system. The compositions of systems are taken following Ref. [1].

A series of WIS systems of the composition LiOAc-CsOAc(sat)-H_2O with different lithium acetate contents (including those described in Ref [2]) was prepared and the density of these systems was measured by the pycnometric method.

NMR spectra

In this work, 8 samples were studied (follow Ref. 1), which differ in the ratio of components, see below. Salt concentrations were reached first by preparation and then were verified using integral intensities of signals of the CH_3-group and water, see for example Fig.1.

Diffusion

We have measured the temperature dependence of the diffusion coefficients of the acetate anion and water using 1H nucleus and of the Li^+ cation using ^7Li nucleus. Measurements were carried out for 3 samples (3, 7, 8 in the table), and the results are shown in Fig. 2.

As evident from the figure the diffusion factors of the Li^+ and CH_3COO^- counter ions are equal. It means that these ions diffuse as a whole in all the investigated temperature range, i.e. the system consists of clusters and each cluster includes a number of counter ions. Also, one can conclude that counter ions in the cluster cannot be in a form of simple LiOAc molecules as in this case the conductivity of the system should be negligible.

Table 1. Composition of the samples

Sample №		3	4	5	6	7	8	9	10
Salt (mole fraction)	*LiOAc*	1,0		0.8	0.6	0.33	0.2	0.2	0.1
	KOAc		1,0	0.2	0.4	0.66	0.77	0.8	0.9
Molality	*LiOAc*	7.88		7.37	6.66	9.23	6.39	7.98	3.27
	KOAc		28,64	1.84	4.44	18.52	21.39	31.87	29.94
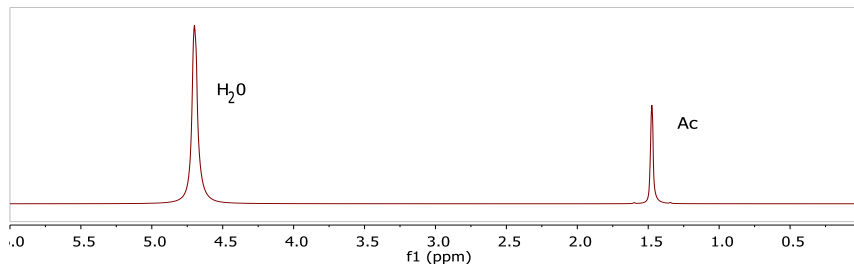
Fig. 1.A typical ^1H NMR spectrum of LiOAc – KOAc – water triple systems, sample №5.
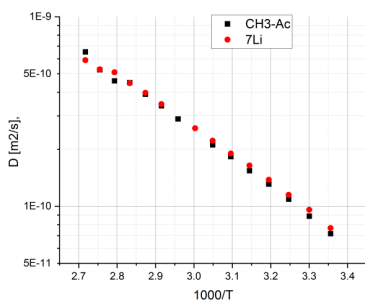
Fig. 2. Diffusion factors vs. temperature for the sample №3 with x(Li) = 1; 7.88m LiOAc in H_2O.
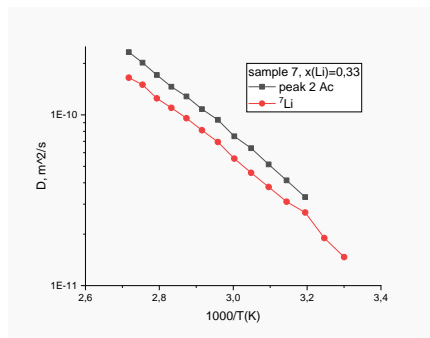
Fig. 3. Diffusion factors vs. temperature for the sample №7 with x(Li) = 0.33.

At the same time, in mixed solutions, the diffusion coefficients of the lithium cation and the acetate anion diverge, an example is shown in Fig. 3. Apparently, this means that the composition of the clusters changes with the Li/K ratio in the electrolyte. Unfortunately, it is impossible to measure the diffusion coefficient of the potassium cation by NMR diffusometry due to very short T_1 for 39K nucleus, so it is unclear if the diffusion factors of the potassium cation and the acetate anion are correlated.

Density Measurements

A logical continuation of the research on the properties of the lithium and potassium acetate system was the research of the ternary system lithium acetate – cesium acetate – water.

It is of particular interest because of the highest solubility of cesium acetate among other alkali metals. Therefore, the emphasis was placed on highly concentrated solutions of cesium acetate with different lithium acetate content. The preparation of solutions was carried out at 25^0C and stirring by the weight method. Systems containing different concentrations of lithium acetate were prepared by dissolving solid lithium acetate dihydrate in a 45 *m* solution of cesium acetate. The concentration values are given considering the water introduced by LiOAc•2H$_2$O dihydrate. The constant content of cesium acetate was achieved by adding an extra amount of CsOAc salt to the solution.

A series of obtained solutions with component concentrations is given on Table 2.

Table 2. Sample densities of the lithium acetate - cesium acetate - water system

Sample	Cesium concentration, mol /kg H$_2$O	Lithium concentration, mol/kg H$_2$O	Density, g/ml
CsOAc №1	30	-	2.110
CsOAc №2	35	-	2.146
CsOAc №3	45	-	2.149
Li-CsOAc №1	45	1	2.126
Li-CsOAc №2	45	3	2.098
Li-CsOAc №3	45	5	2.012
Li-CsOAc №4	45	7	2.146

As one of the physicochemical properties, the density of the prepared systems was measured. The measurement results are also presented on Table 2. Based on the results of density measurement, it can be concluded that when lithium salt is introduced into a saturated solution of caesium acetate, the density of the solution decreases, and the dependence of the density of the triple system on the concentration of lithium is anti–acid. The exception is the sample with the highest concentration for both components – Li-CsOAc No. 4, but its high density is explained by its proximity to the solubility limit for both salts.

Acknowledgments

References

1. Lukatskaya M.R., Feldblyum J.I., Mackanic D.G. *et al*. − Energy Environ Sci. 2018. V. 11. No. 3. P. 2876. doi:10.1039/c8ee00833g
2. Chen S., Lan R., Humphreys J., and Tao S. – Applied Materials Today 2020. V. 20. P. 100728. DOI:10.1016/j.apmt.2020.100728.

The Symmetry of the Hyperfine and Quadrupole Interactions of the Boron Vacancy in a Hexagonal Boron Nitride

Fadis F. Murzakhanov, Irina N. Gracheva, Margarita A. Sadovnikova, Georgy V. Mamin,
Bulat F. Gabbasov, Marat R. Gafurov
Institute of Physics, Kazan Federal University, 420008 Kremlyovskaya 18, Kazan, Russia
E-mail: murzakhanov.fadis@yandex.ru

Introduction

Optically polarized electron spins of defects in solids serve as a valuable platform for development of an advanced quantum technologies and are widely used as a tool to probe unconventional many body quantum physics in condensed matter. The development of solid-state technologies based on defects with a significant electron-nuclear interaction has been underway for several decades and has been implemented into diverse semiconductor crystal structures. The main explored solid-state platforms with these respects are diamond with negatively charged nitrogen vacancy defect (NV⁻) and silicon carbide (SiC) with NV⁻ and vacancy-related defects. Quantum magnetometers, nanoscale magnetic resonance imaging (MRI), sensors of thermal and electrical fields, masers operated at room temperature have been proposed and developed using advantages of these defects. The main approach of their use in mentioned above applications is that the high spin state ($S \geq 1$) of the defect is already split in zero magnetic field and can be initialized, manipulated, and subsequently read out by optical or radio frequency means utilizing principles of electron spin resonance (ESR) and optically detected magnetic resonance (ODMR). However, both diamond and SiC are three-dimensional (3D) crystals that prevents advanced nanoscale fabrication processing of these materials [1].

Distinctly new platform for potential realization of mentioned above scenarios has been recognized only recently by demonstration of optically addressable spin states of defects in two-dimensional van der Waals (vdW) material, namely hexagonal boron nitride (hBN). hBN is formed by 2D atomic layers of sp^2-hybridized nitrogen−boron atoms that are coupled through weak vdW interactions. Its ultra-wide-bandgap ($Eg \approx 6$ eV) naturally grants the existence of deep level defects with optical transitions well below its bandgap. Together with well-developed exfoliation technique allowing one to achieve fine tuning of the number of atomically-thin layers (down to the single layer), these make such kind of layered material particularly interesting for nanoscale quantum technologies and as a monolayer single-photon quantum emitter. Particularly, exploiting two-dimensional nature of hBN, defects emitting single photons has been successfully isolated in a single monoatomic BN layer, and the search for defects in hBN from the perspectives of their applicability for quantum sensing, and qubits has been launched [2].

One of the major advantages inherently given to the negatively charged boron vacancy in hBN through its high D_{3h} symmetry is that the spin density strongly bounded to the defect site is seems to be fully localized in a single two-dimensional layer of sp^2-hybridized boron and nitrogen atoms. The latter peculiarity preserves the spin properties of this defect, keeping them almost unchanged for the bulk crystal and for the single BN layer. This fact is well documented through *ab initio* calculations; however, it has not been rigorously probed experimentally. Driving on the mentioned above we focused here on study of anisotropy of hyperfine and nuclear quadrupole interactions associated with V_B electron spin and three nearest nitrogen nuclei (^{14}N, $I = 1$) by means of ESR and pulsed ENDOR techniques. Special attention is also paid to the study of the HFI because of its importance in determining the nature of the point defects in hBN and the effect on the coherent properties of the boron vacancy. Based on the results of these experiments we accomplishing study of the electron-

nuclear interactions of the V_B electron spin with nearest nitrogen shell and are able to demonstrate that V_B spin is localized in a single two-dimensional layer [3].

Results and Discussions

In this work, the features of electron-nuclear interactions of the boron vacancy V_B with surrounding equivalent nitrogen nuclei were investigated by the methods of stationary electron paramagnetic resonance (9.6 GHz) and high-frequency (94 GHz) pulsed electron-nuclear double resonance technique. In addition to the g - factor and fine splitting (D = 3.6 GHz) the detailed study of the angular dependence of the ESR spectra made it possible to determine all the components of the hyperfine interaction tensor ($A_\perp$ = 45.5 ± 0.9 MHz and $A_\parallel$ = 87 ± 0.5 MHz), and therefore to establish its axial symmetry. Established HFI values serves as an estimate of V_B electron spin density localization in a two-dimensional plane of sp^2-hybridized B-N atoms. Given the isotropic A_{iso} and anisotropic T contributions of HFI, we can conclude that nearly all spin density of the V_B density ($\approx$ 84%) is localized on the three nitrogen atoms in the 2D BN layer. The latter means that the number of layers in a single crystal will not have a significant effect on the ground state spin properties of the center, which means that it might be possible to obtain a monoatomic hBN layer with optically addressable structurally protected spin sublevels of color centers.

The electron-nuclear double resonance method applied at two different canonical orientations allows to determine the value of the quadrupole interaction C_q = 1.96 ± 0.05 MHz with an estimate of the asymmetry parameter η = -0.07 ± 0.005. Despite the fact that the fine structure tensor is directed along the crystallographic axis c, the quadrupole interaction has its maximum value along the dangling bond. The relatively small value of the asymmetry parameter η indicates the axial symmetry of the quadrupole interaction. Hence, in this work we explored all terms of the V_B spin Hamiltonian together with their symmetry reflecting interactions with the three nearest nitrogen atoms.

Acknowledgments

References

1. Awschalom, D.; Hanson, R.; Wrachtrup, J.; Zhou, B. B. Quantum technologies with optically interfaced solid-state spins. *Nat. Photonics* **2018**, *12*, 516–527.
2. Wolfowicz, G.; Anderson, C. P.; Yeats, A. L.; Whiteley, S. J.; Niklas, J.; Poluektov, O. G.; Heremans, F. J.; Awschalom, D. D. Optical charge state control of spin defects in 4H-SiC, *Nat. Commun*. **2017**, *8*, 1876.
3. Cassabois, G.; Valvin, P.; Gil, B. Hexagonal boron nitride is an indirect bandgap semiconductor, *Nat. Photonics* **2016**, *10*, 262–266.

Estimation of long-range interproton distances in tetrahydropyrazolo[1,5-a]pyrimidines using NOE data

Daria S. Novikova[1], Vyacheslav G. Tribulovich[1], Maxim N. Krivchun[1], Stanislav I. Selivanov[1,2]
[1]St. Petersburg State Institute of Technology (Technical University), 190013 St. Petersburg, Russia
[2]Laboratory of Biomolecular NMR, St. Petersburg State University, 199034 St. Petersburg, Russia
E-mails: dc.novikova@gmail.com , nmr.group.spbu@gmaill.com

Introduction

Almost all NMR applications in the field of structural and conformational analysis of molecules in liquid are associated with the use of nuclear Overhauser effect (NOE) data. This fact arises from the extremely strong sensitivity of the cross-relaxation rate σ_{ij} between the magnetic nuclei "i" and "j" on the distance between them r_{ij}, as well as from the dependence of σ_{ij} on the motion of the vector r_{ij}, which is determined by the overall rotational diffusion and intramolecular mobility of this pair of nuclei: $\sigma_{ij} \sim \tau_c^{\mathrm{eff}}(r_{ij})^{-6}$, where τ_c^{eff} is the effective correlation time of overall diffusional and internal motions. Thus, the analysis of 2D NOE data lies in the determination of cross-relaxation rates from the measured relaxation matrix.

There are two standard approaches to analyze NOE data: initial slope approximation and relaxation matrix analysis The former is more commonly used for small molecules (at the extreme narrowing limit $\omega_o\tau_c \ll 1$); it requires only the values of cross-peak volume integrals S_{ij} at different short mixing times τ_m normalized to the corresponding diagonal integrals (S_{ii} or S_{jj}) as input, no other experimental information is needed. This is an advantage over relaxation matrix analysis, which is more correct and the most appropriate for large molecules under spin diffusion conditions of $\omega_o\tau_c \gg 1$.

It is well known that the ability of NOE to detect long-range dipole-dipole interactions for small and large molecules differs by almost a factor of two: the long-range distance up to 12 Å can be detected in large molecules [1], while in small molecules it is only about 5 Å [2]. Considering this fact the highest possible accuracy in determining cross-peak volume integrals is required when studying small molecules. This is especially important when only long-range NOEs allow one to uniquely solve a structural or conformational problem [3]. This report presents the use of NOESY data to determine long-range interproton distances of model compounds obtained by reduction of pyrazolo[1,5-a]pyrimidine (**1**) with sodium borohydride (Scheme 1), consisting in selective reduction of the pyrimidine ring and formation of two enantiomer pairs (**2a**, **2b**) with different spatial orientation of the substituents.
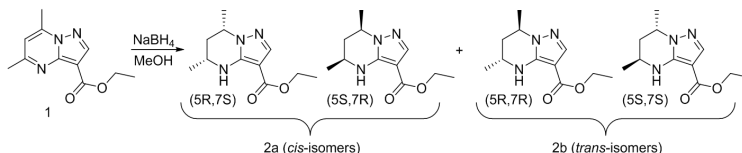
Figure 1. Synthetic scheme for the studied compounds

Experiments and results

There are some problems related to the registration and processing of extremely small cross-peaks in NOESY spectra corresponding to long-range distances. These are an insufficient correction of the base plane in the phase-sensitive NOESY spectra, an influence of so-called "t_1-noise" and "t_2-noise" on the volume integral accuracy and also overlapping of

proton signals and cross-peaks. It should be noted that the origin of t_1-noise and ways to deal with it are described much better [4] than the t_2-noise phenomenon. It is assumed that the latter may be associated with the receiver overload and/or with a slight mismatch between two channels of the quadrature detection system, as well as with insufficiently accurate phase correction of the 2D spectrum.

The studied tetrahydropyrazolo[1,5-a]pyrimidines (THPP) turned out to be extremely convenient models to analyze the indicated problems based on cross-peaks corresponding to long-range distances (about 4–6 Å) between two protons in the rigid part of the molecule and between such a proton and protons of rotating methyl groups. So, vertical lines of t_1-noise and horizontal lines of t_2-noise are clearly visible on a routine NOESY spectrum of compound **2a** at high gain (Fig. 1). Unfortunately, all our attempts to reduce the input of t_2-noise in NOESY spectra by a twofold and fourfold decrease in the receiver gain parameter (RG) had no result, and the experimental ratio of the noise and cross-peak integrals remained the same.
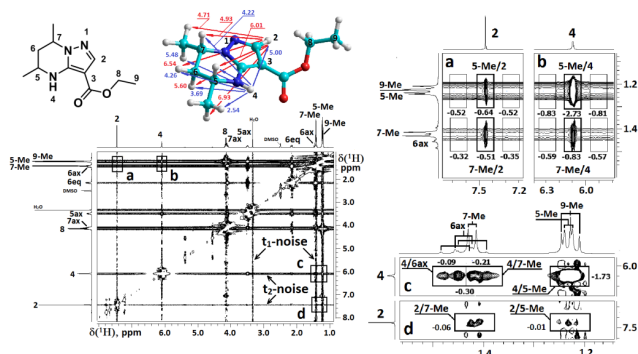
*Figure 2. NOESY spectrum of **2a** and magnified fragments at $\tau_m = 0.3$ s in DMSO-d_6*

To demonstrate the influence of noise bands on integral intensities of small cross-peaks, we considered four fragments containing the following 8 cross-peaks: 5-Me/2 and 7-Me/2, 5-Me/4 and 7-Me/4 (Fig. 2, *a*, *b*); 4/5-Me and 4/7-Me, 2/5-Me and 2/7-Me (Fig. 2, *c*, *d*). Among these cross peak pairs, only one corresponds to a short distance ($r_{4/7\text{-Me}} = 2.54$ Å), and the remaining distances are longer than 4.5 Å. Two pairs of the least intense cross-peaks are 2/7-Me and 2/5-Me (Fig. 2, *a*, *d*) corresponding to the distances of 4.71 Å and 6.93 Å, respectively. The calculated ratio of their integral intensities should be about 10:1. This relation holds relatively well when comparing the volume integrals of these cross-peaks in fragment *d* (0.06:0.01=6:1), but it turns out to be completely inverse when integrating the corresponding cross-peaks in fragment *a* (0.51:0.64≈0.8). It means that proton 2 is closer to protons of 5-Me than to those of 7-Me. This problem was solved by further integrating the left and right neighbourhood of the measured cross-peak within the same rectangle used to integrate the cross-peak (Fig. 3). The results of additional integrals were averaged and then subtracted from the original cross-peak intensity value. After such processing, the cross-peak ratio became equal to 1.5, which is more consistent with the calculated one.

Additional problems arise from partial overlapping of cross-peaks, as in the case of 7-Me/4 and 6ax/4. Since the 6ax signal is a doublet of triplets ($^2J_{6ax\text{-}6eq} = -13.4$ Hz, $^3J_{6ax\text{-}5ax} = {}^3J_{6ax\text{-}7ax} = 11.2$ Hz) and only a half of this signal overlaps with 7-Me doublet. It is convenient to separately integrate the total cross peak: ½$S_{4/6ax}$=0.09 and ½$S_{4/6ax}$+$S_{4/7\text{-Me}}$=0.21. The volume integral $S_{4/7\text{-Me}}$ is equal to 0.12 (40% of the total value). The integration accuracy when

normalized to one proton in the region without t_1- and t_2-noise bands was not worse than ±0.005%. The procedure for estimating the volume integration accuracy using additional measurements in the vicinity of 4/6eq and 2/6eq cross-peaks (corresponding to distances 4.26 and 6.54 Å, respectively) is shown in Fig. 3. The calculated ratio of these cross peaks is 13.1, while experimental value obtained base on analysis performed is equal to 0.104/0.009=11.6. Therefore, if we take the distance between 4 and 6eq protons as the reference one, the experimental value $r_{2/6eq}$ is only 0.14 Å less than the calculated one (2.2%).
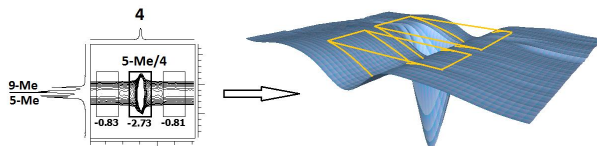
Figure 3. Three-dimensional representation of 5-Me/4 cross-peak (yellow lines indicate equal rectangles of volume integral limits for the cross-peak and close t_2-noise region)
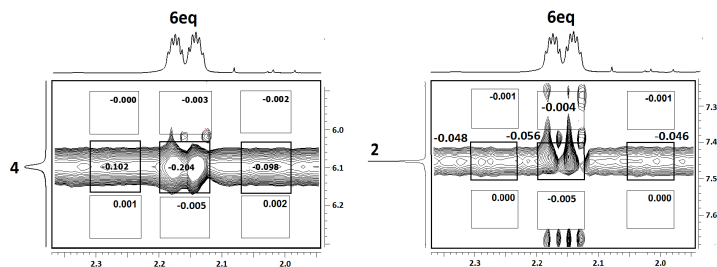
Figure 4. Three-dimensional representation of 5-Me/4 cross-peak (yellow lines indicate equal rectangles of volume integral limits for the cross-peak and close t_2-noise region)

The presented results demonstrate the possibility of quantitative estimation of long-range interproton distances (up to 6 Å and more) in small molecules using NOE data with the accuracy within 10% of the measured value. However, increased attention should be paid to the measurement of volume integrals in the presence of t_1- and t_2-noise distortions of the base plane in the NOESY spectra.

Acknowledgments

References

1. R. Sounier, L. Blanchard, J. Boisbouvier. – *J. Am. Chem. Soc.*, **129**, 472-473 (2007).
2. C. P. Butts, C. R. Jones, J. N. Harvey. – Chem. Commun., 47, 1193-1195 (2011).
3. Ju. A. Pronina, D. D. Komolova, V. M. Boitsov, A. V. Stepakov, S. I. Selivanov. – Appl. Magn. Reson., 53, 1677-1691 (2022).
4. H. Mo, J. S. Harwood, D. Yang, C. B. Post. – J. Magn. Reson., 276, 43-50 (2017).

Microwave (MW) Dielectric Spectroscopy investigations of benign and threat liquids

Cengiz Okay

Department of Physics, Marmara University, 81040 Göztepe-Istanbul, Turkey
E-mail: cokay@marmara.edu.tr

Abstract

The microwave dielectric spectroscopy technique, which is based on the interaction of electric dipoles in a material with an electromagnetic field, is highly sensitive to the real and imaginary components of permittivity. It can be used to scan various liquids for security reasons to detect the threat liquids. In this work, six groups of samples (threat materials, water-based drinks, juices, beverages milks and oils) were examined. We have shown that this technique is very efficient in the discrimination between threat and benign liquids.

Introduction

The detection of explosive and illicit materials is a very critical problem in the modern globalized world. In the case of aviation and public security, there is a need for devices for fast, reliable and non-invasive detection of explosive and illicit substances in the age, suits, underwear, etc. Today's air traveller deals with very lengthy queues, essential security delays and bothering scans. Meanwhile, the appearance of new and evolving security threats results in increasingly complex equipment and procedure at security checkpoints. The number of passengers increased very much in the last decades, therefore the scan procedures become increasingly slow and inconvenient. A number of various detectors have been developed [1-6]. However, a number of problems, such as sensitivity, reliability, shortening the detection time, decreasing the scanner cost, and false alarm response level, are still waiting to be resolved. Additional parameters and advanced measurement/analysis approaches are very desirable to resolve between various liquids. In this respect, an attractive approach is to apply dielectric spectroscopy at the microwave range. The mechanism of this technique is based on the interaction of electromagnetic (EM) waves with the electric dipoles of a material. The real component of the dielectric coefficient (ε) is a measure of the electric polarization of the dipoles, while the imaginary component expresses the energy loss due to the damping of the dipole oscillations [7-8]. Both these parameters are changing with the frequency of the EM field.

In this study, a laboratory study of dielectric constant ε_1 and ε_2 of six groups of liquid samples has been done to develop classification approaches to resolve between various kinds of benign and threat liquids.

Experimental procedure

We used six groups of samples: threat materials, water-based drinks, juices, beverages, milks and oils. All selected samples are given in Table.1.

Table 3. List of six groups of samples and their contents.

Threat materials	Acetone, Acetonitrile, Nitromethane, Tetrahydrofuran, Chloroform, N,N-Dimethylformamide, Toluene, Nitrobenzene, Methanol, Ethylenediamine, Dioxane, Peroxide %35, Ethanol, 1-Propanol, 2-Propanol, Isopropanol, Tert- Butanol, Glycerol solution.
Water based drinks	Coca-Cola Light, Pepsi Max Zero Calori, Coca-Cola Zero, Mineral Water (Kızılay), Sprite, Mineral Water (Eskipazar), Fanta, Fruko, Mineral Water (Beypazarı), Water (Tap), Water (DI), Coca-Cola Orginal, Water (Kuvars), Water (Saka), Pepsi Zero, Camlıca Gazoz,

	Mineral water (Uludag).
Juices	Sour Cherry (Cappy), Lipton Ice Tea Peach, Lipton Ice Tea Lemon, Sour Cherry (Pınar), Sour Cherry (Dooy), Sour Cherry (Dimes), Apricot (Dooy), Apricot (Pınar), Peach (Pınar), Peach (Dimes), Apricot (Cappy), Peach (Dooy), Sour Cherry (Tropicana), Peach (Cappy), Fuse Tea Lemon, Ayran (Eker), Peach (Tropicana), Apricot (Dimes).
Beverages	Brendy Konyak (%40 Alcohol), Rakı Tekirdag (%45 Alcohol), Terre Allegre Vine (%12 Alcohol), Baileys Vine(%17 Alcohol).
Milks	Milk (Icim Rahat), Milk (Pinar), Milk (Icim Light), Milk (Sütas), Milk (Pinar No Laktoz), Milk (Torku Light), Milk (Sek Normal), Milk (Icim Normal), Milk (Pinar Light).
Oils	Sunflower oil, Olive oil (Riviera), Olive oil (Sızma).

Experimental results and their discussion

Dielectric constant ε_1 and ε_2 measurements were performed by using an Agilent E8364B PNA series vector network analyzer and Agilent 85070E Dielectric Kit with Slim Form Probe. Calibration of the liquid test fixture was performed at 25^oC in air, distilled water and using a 50 Ohm load terminal.

Figure 1. Real part (left panel) and imaginary part (right panel) of permittivity at 1GHz for various benign (blue colour-left side) and threat liquids (red colour-right side).

In Figure 1 the real and imaginary permittivities of all groups of liquids measured at 1GHz are presented. We see that the real permittivities of three 3 threat liquids (hydrogen peroxide, nitrobenzene and dioxane) have values which are close to water-based drinks. We also see that two brands of olive oil and a tested brand of sunflower oil have very low permittivity value which is close to that of nitromethane (nitrobenzene). On the other hand,

the real permittivities of tap and drink water are very close to that of hydrogen peroxide. We note that in this work, the permittivity of liquids only at one (fixed) frequency (1 GHz) is presented. It is known that the permittivity of liquids depends essentially on the measurement frequency. Furthermore, this frequency dependence is a unique characteristic of each substance. Therefore, we concluded that probing the permittivity values at other (higher) frequencies would be desirable to discriminate better in a very large group of typically met liquid materials.

Acknowledgements

References

1. Rohman, Y. B. Che Man, A. Ismail, and P. Hashim, "Application of FTIR spectroscopy for the determination of virgin coconut oil in binary mixtures with olive oil and palm oil," JAOCS, J. Am. Oil Chem. Soc., vol. 87, no. 6, pp. 601–606, 2010, doi: 10.1007/s11746-009-1536.
2. M. J. Lerma-García, G. Ramis-Ramos, J. M. Herrero-Martínez, and E. F. Simó-Alfonso, "Authentication of extra virgin olive oils by Fourier-transform infrared spectroscopy," *Food Chem.*, vol. 118, no. 1, pp. 78–83, 2010, doi: 10.1016/j.foodchem.2009.04.092.
3. H. Lizhi, K. Toyoda, and I. Ihara, "Discrimination of olive oil adulterated with vegetable oils using dielectric spectroscopy," *J. Food Eng.*, vol. 96, no. 2, pp. 167–171, 2010, doi: 10.1016/j.jfoodeng.2009.06.045.
4. Cataldo, E. Piuzzi, G. Cannazza, E. De Benedetto, and L. Tarricone, "Quality and anti-adulteration control of vegetable oils through microwave dielectric spectroscopy," *Meas. J. Int. Meas. Confed.*, vol. 43, no. 8, pp. 1031–1039, 2010, doi: 10.1016/j.measurement.2010.02.008.
5. S. Ok, "Detection of olive oil adulteration by low-field NMR relaxometry and UV-Vis spectroscopy upon mixing olive oil with various edible oils," *Grasas y Aceites*, vol. 68, no. 1, pp. 1–13, 2017, doi: 10.3989/gya.0678161.
6. D. Šmejkalová and A. Piccolo, "High-power gradient diffusion NMR spectroscopy for the rapid assessment of extra-virgin olive oil adulteration," *Food Chem.*, vol. 118, no. 1, pp. 153–158, 2010, doi: 10.1016/j.foodchem.2009.04.088.
7. S. O. Nelson and S. Trabelsi, "Dielectric properties of agricultural products and applications," *Am. Soc. Agric. Biol. Eng. Annu. Int. Meet. 2009, ASABE 2009*, vol. 5, no. 2, pp. 2901–2919, 2009, doi: 10.13031/2013.27075.
8. H. Lizhi, Toyoda,K I.Ihara, "Dielectric properties of edible oils and fatty acids as a function of frequency, temperature moisture and composition." Journal of Food Engineering, pp. 151–158, 2008, [Online]. Available: Journal of Food Engineering.

Translational self-diffusion of α-tocopherol in a new water-soluble form

<u>Ksenia V. Panicheva</u>[1,2], Svetlana V. Kurmaz[1], Irina A. Avilova[1], Sergey G. Vasil'ev[1]

[1]*Federal Research Center of Problems of Chemical Physics and Medicinal Chemistry RAS, Ac. Semenov avenue 1, Chernogolovka, Moscow Oblast 142432, Russia*
[2]*Faculty of Fundamental Physical-Chemical Engineering, Lomonosov Moscow State University, GSP-1, Leninskie Gory, Moscow 119991, Russia*
E-mail: kseniap13@mail.ru

Introduction

(±)-α-Tocopherol (TP) belongs to the highly bioactive fat-soluble vitamins from the E family of tocopherols and tocotrienols. Lipophilic TP molecules are able to inactivate free radicals directly in the hydrophobic layer of membranes by transferring a hydrogen atom to a lipid peroxide free radical, thereby preventing the development of the lipid peroxidation chain. Free radical reactions are engaged in the pathogenesis of various diseases; thus, the study of new dosage forms of TP antioxidant properties is a topical task of biomedical chemistry. However, their intravenous use in the treatment of pathological conditions is limited due to the low water solubility of TP.

The hydrophilicity of drugs with low water solubility can be increased by amphiphilic polymeric carriers. Micellar-type polymer carriers based on amphiphilic block copolymers, liposomes, etc. with encapsulated hydrophobic drugs demonstrate high efficiency, given that they can circulate in the bloodstream for a long time, accumulate in tissues with increased permeability (tumors) and gradually release the drug. These materials include amphiphilic polymers of N-vinylpyrrolidone (PVP) and VP copolymers with triethylene glycol dimethacrylate (VP-TEGDM) synthesized by radical copolymerization in toluene [1]. The advantages of these copolymers include the simplicity of their preparation in combination with wide possibilities for regulating their composition, molecular weight, branching content, nanoparticle sizes, as well as their low cytotoxicity for cells. These copolymers have proved to be potential delivery agents for hydrophobic compounds such as C_{60} fullerene and zinc tetraphenylporphyrinate, and have also been tested as NO-carrying systems of binuclear tetranitrosyl iron complexes with antitumor activity. The aims of this work were to obtain a water-soluble form of TP by its encapsulating in PVP and VP with hexyl methacrylate (HMA) and TEGDM copolymer and to explore the manifestation of interactions between polymers and TP using the self-diffusion measurements by pulsed field gradient (PFG) NMR.

Experimental

The samples of TP, PVP-TP and VP-HMA-TEGDM-TP where investigated in $CDCl_3$ and D_2O solutions. NMR measurements were performed using Bruker Avance III – 500 for high resolution experiments and Bruker Avance III – 400 for PFG experiments on ^{1}H nuclei. The influence of the magnetic field inhomogeneity on the spin echo signal can be used to measure the self-diffusion coefficients. To do this, in the Hahn sequence 90-*τ*-180-*τ* – echo or stimulated spin echo sequence 90-*τ*-90-*τ₁*-90-*τ*-echo a pair of magnetic field gradient pulses of the equal and known amplitude during intervals *τ* is applied. The dependence of the amplitude of the spin echo on the amplitude *g* of the gradient pulse with duration *δ* is given by

$$A(2\tau, \tau_1, g) = A(2\tau, \tau_1, 0)\exp(-\gamma^2 g^2 \delta^2 t_d D),$$

where *γ* – the gyromagnetic ratio, $t_d = \Delta - \delta/3$ – the diffusion time, *Δ* – the interval between gradient pulses and *D* – the self-diffusion coefficient. $A(2\tau, \tau_1, 0)$ contains the factors associated with relaxation. In the present work a series of spin echoes with different gradient pulse amplitudes *g* (diffusion decay) was used to measure the self-diffusion coefficients.

Results

The resonances in the ^{1}H high-resolution spectra of TP as well as PVP were identified and agreed well with the data presented in the literature [2, 3].
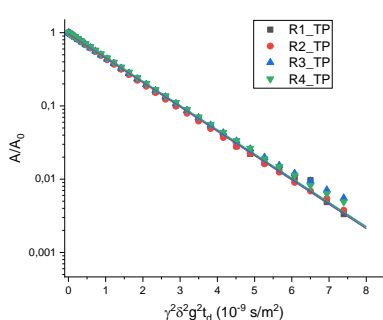
Figure 1. Diffusion decays for TP in CDCl$_3$ solutions
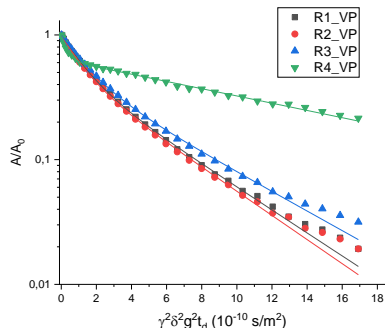
Figure 2. Diffusion decays for TP encapsulated in PVP in D$_2$O solution

The diffusion decays obtained for TP in CDCl$_3$ solutions using different integration regions in ^{1}H spectra (marked with R) are identical and well approximated using a single coefficient $D = 7,63 \cdot 10^{-10}$ m^2/s as shown in Fig. 1. The diffusion decays obtained for TP encapsulated in polymers show non-exponential behavior. The experimental data (dots) presented in Fig. 2 were normalized to the maximum amplitude of the signal in each case and were fitted using biexponential decay (solid lines). The diffusion decays are clearly different for different parts of spectra. This is explained by the different contributions of TP signals to the decay. Range R1_VP corresponds exclusively to the VP signals, while range R4_VP solely correspond to methyl groups of aliphatic chain of TP. Range R2_VP contains small number of TP protons, while R3_VP contains the majority of TP signals. The echo decays less with increasing TP contribution. The biexponential decay in case of R1_VP is predominantly caused by the non-aggregated VP chains and demonstrates the molecular mass distribution, which is also observed in the diffusion decays of neat VP. The contribution of the chains associated with TP increases for range R2_VP and R3_VP, correspondingly. The range R4_VP reflects more accurately the self-diffusion of TP encapsulated in VP polymer. The two self-diffusion coefficients, having values of $2.95 \cdot 10^{-10}$ and $6.7 \cdot 10^{-12}$ m^2/s with relative contributions of 0.4 and 0.6, respectively, were ascribed to the aggregates of different sizes. The corresponding hydrodynamic radii, calculated using Stokes-Einstein relation, are 0.84 and 37.1 nm.

Acknowledgments

References

1. S.V. Kurmaz, N.V. Fadeeva, J.A. Skripets, R.I. Komendant, V.M. Ignatiev, N.S. Emel'yanova, Y.V. Soldatova, I.I. Faingold, D.A. Poletaeva, R.A. Kotelnikova - *Mendeleev Communications*, **32**, 117-119 (2022)
2. J.K. Baker, C.W. Myers - *Pharm Res.*, **8**, 763-70 (1991)
3. K. Dutta, A.S. Brar - J. Polym. Sci. A Polym. Chem., **37**, 3922-3928 (1999)

What is hidden under the FID noise of entangled polymer melt?

Eugeny M. Pestryaev

*Department of Physics, Ufa State Petroleum Technological University, Ufa,
Kosmonavtov St., 1, 450062, Russian Federation*
E-mail: *physics_usptu@mail.ru*

Introduction

It was recently cleared in numerical experiments that the NMR free-induction-decay (**FID**) in entangled polymer melt also contains information about the chain space displacement [1]. Furthermore, the theoretical analysis has disclosed an absolutely unexpected result [2]: The chain intra-molecular residual dipolar coupling (**RDC**) is controlled by its one-dimensional translational self-diffusion inside force tube – the basic abstraction of the reptation model – which replaces the chain interaction with all other chains [3]. The nature of this relationship is specified by a circumstance, that the chain displacement along the tube is accompanied by varying the space orientation of its primitive segments, the second basic abstraction of the reptation model. In other words, in contrary to the conventional NMR-method to measure the self-diffusion coefficient – analyzing the Hahn or stimulated echoes with pulsed field gradient – the situation under consideration does not require a hardware modification, for example, of the standard NMR Fourier-spectrometer to create the space inhomogeneity of any physical parameter inside sample investigated, inasmuch as the Gaussian-coil-tube bends serve as space point markers. During translational diffusion along the tube axis the primitive segments are compelled to reorient after passage from one tube bend to another; this one-dimensional motion causes a specific spin-spin relaxation characterizing the translational self-diffusion of the primitive segment while the chain stays in the tube, i.e. within τ_D [3].

Comparing the theoretical and simulated FIDs in entangled polymer melt

On the other hand, the author's approach [1] allows to theoretically describing the FID shape in polymer melts up to τ_D, whereas earlier in the known experiments a signal was just not registered in this time interval because it dropped below the noise level. For this reason, it was considered the FID long-time tail does not contain the additional information about the dipolar coupling (**DC**). This assumption was successfully disproved in recent work [2], where the asymptotic expression for the high-temperature FID has been derived based on the non-trivial idea of inheriting the RDC by the primitive segments [1]. The essence of assumption is that the primitive segments in the entangled melt at high-temperature also become fluctuating in the NMR time-scale like the Kuhn segments – their mobility at the same time is characterized by so high frequency that its contribution to the transverse relaxation rate becomes negligibly small – therefore, the FID shape is determined only by the primitive segment orientational motion caused by the chain one-dimensional diffusion inside the tube. As a result, the FID, $g(t)$, is represented by two asymptotic scaling expressions for short-time and long-time ranges [2], of which only the second – with index "**T**ail or **T**ube" – is discussed here:

$$g_T(\tau_R < t < \tau_D) \propto \exp\left\{-\langle\frac{s^2(t)}{l_K^2 N_E}\rangle^{\frac{1}{2}} \cdot \ln\left[\frac{\sqrt{12}}{\pi}\langle\frac{l_K^2 N_E}{s^2(t)}\rangle^{\frac{1}{2}} \cdot \frac{\omega}{N_E}t\right]\right\}. \tag{1}$$

Here, l_K^2 is the mean-square length of the Kuhn segments, N_E is their number between successive entanglements along the freely joint chain of length N Kuhn segments; τ_R is the Rouse time; $\langle s^2(t)\rangle$ is the axial mean-square displacement of the chain middle Kuhn / primitive segments along the tube [3]; the FID scale is specified, in turn, by the quadrupole coupling or

intra-segmental DC, ω (rad/s, if it were in experiment). The DC effect is negligibly small due to being under the logarithm that is why; the decay pattern of the long-time tail is totally defined by the first multiplier in exponent (1). To detail the exponents, it is necessary use the explicit expression for $\langle s^2(t)\rangle$ [3]:

$$\langle s^2(\tau_{\mathbf{R}} < t < \tau_{\mathbf{D}})\rangle \propto l_{\mathbf{K}}^2 \left(\frac{t}{\tau_{\mathbf{S}}}\right)^{\frac{1}{2}}; \; \tau_{\mathbf{E}} = N_{\mathbf{E}}^2\tau_{\mathbf{S}} \ll \tau_{\mathbf{R}} \ll \tau_{\mathbf{D}} \tag{2}$$

Additionally introduced $\tau_{\mathbf{S}}$ and $\tau_{\mathbf{E}}$ are the Kuhn segment translation-correlation time and entanglement time, respectively; using this scaling expressions equations (1) can be converted to the form:

$$g_{\mathbf{T}}(\tau_{\mathbf{R}} < t < \tau_{\mathbf{D}}) \propto \exp\left\{-\left(\frac{t}{\tau_{\mathbf{E}}}\right)^{\frac{1}{4}} \ln\left[\frac{\omega\tau_{\mathbf{E}}}{N_{\mathbf{E}}}\left(\frac{12}{\pi^2}\right)^{\frac{1}{2}}\left(\frac{t}{\tau_{\mathbf{E}}}\right)^{\frac{3}{4}}\right]\right\}. \tag{3}$$

It is this FID tail, damped according to the law $\sim exp[-(t/\tau_{\mathbf{E}})^{1/4}]$, was revealed in a strictly specialized long-term experiment with the perdeuterated poly(ethylene-*alt*-propylene) melt [2]. The deuteration allowed observing the signal that provided to account for only orientational mobility of the spin-bearing kinetic units and absence of the inter-molecular DC. The similar properties are also peculiar to the simulated polymer melt [1] corroborating the existence of the long-time tail – according to equation (3) – which represented in figs. 1 and 2 in semi-logarithmic and double-logarithmic scales, respectively.

The simulated FID in these figures is obtained according to its definition [4] reduced by a hypothesis of the pre-averaged intra-segmental DC or quadrupole interaction by the chain backbone isomerization [5]:

$$g(t) = \frac{2}{N-2k}\sum_{i=k}^{N/2} \langle \cos\left\{\omega S_{\mathbf{i}} \int_0^t [3\cos^2(\theta_i(t')) - 1] \, dt'\right\}\rangle; \tag{4}$$

Here, the angular brackets denote the average over Kuhn segments with the same number i for all chains of the simulated monodisperse melt, where each chain consists from N segments. $\theta_i(t)$ is the angle of i-th segment – coinciding with inter-spin vector – relative to an external magnetic field. A chain FID is calculated as the normalized sum of the NMR signals from each individual segment. Besides, expression (4) implicitly includes a dynamic heterogeneity of the segments as well as heterogeneity of their motional anisotropy, hidden in the time-dependence peculiarities of $\theta_i(t)$ and respectively characterized by the correlation time, $\tau_{\mathbf{S}i}$, and intra-segmental order factor, S_i. The subsequent ω-pre-averaging up to ω$/N_{\mathbf{E}}$, as in (3), is realized in the simulation by the Kuhn segment motion due to its higher frequency than that of the primitive segments. Both parameters are constants for the chain middle segments and decrease along the chain end fragments [6]; ω-value in (4) corresponds to a liquid-phase spin-spin relaxation regime. The index value $k=0$ yields the FID for the total chain (curve 1-2 in figs. 1 and 2) that can be observed in experiments; $k=N_{\mathbf{E}}$ yields the FID for only the chain middle constraint Kuhn segments (curve 3-4 in figs. 1 and 2). The FID last version without the signal of the end fragments can be obtained in experiments by subtracting of the slow decaying tail (curve 2 in figs. 1 and 2) caused by these two "dangling" fragments of length $N_{\mathbf{E}}$ each and with theoretical population $p_{\mathbf{E}} \propto 2\cdot N_{\mathbf{E}}/N$.

The total FID (curve 1-2 in figs. 1 and 2) has a typically underestimated population of the tail $p_{\mathbf{E0}} \approx 0.13$ (curve 2 in figs. 1 and 2) relative to the theoretical one. The middle segment FID (curve 3-4 in figs. 1 and 2) indeed demonstrates the slow decaying tail (curve 4 in figs. 1 and 2) – let us call it "reptation tail" – predicted by expression (3b) and having very small population $p_{\mathbf{T}} \approx 0.001 \ll p_{\mathbf{E0}}$. To be exact, $p_{\mathbf{T}}$ determines a fraction of magnetization relaxing according to the stretched exponential $\sim exp[-(t/\tau_{\mathbf{E}})^{1/4}]$, which is linearized in logarithmic axes of fig. 2 and, to conveniently compare the transformations of each curve due to the passage from fig. 1 to fig. 2, the numeration and color of all curves are preserved.

Notice that the reptation tail of the simulated FID (curve 4 in figs. 1 and 2) in contrast to the experimental FID [2] appears already at $t \geq 3 \cdot \tau_E$, where it demonstrates the stretched exponential dependence $\sim exp[-(t/\tau_E)^{1/4}]$, which cannot be confused with a stronger time-dependence $\sim exp[-(t/\tau_E)^{3/5}]$ (curve 2 in figs. 1 and 2), characterizing the FID tail from two chain end fragments. Because of the insufficient signal-to-noise ratio, duration of both simulated FIDs does not reach τ_R ($lg[\tau_R] \approx 4.7$ in fig. 2); therefore, outside this time, their behavior is unknown.
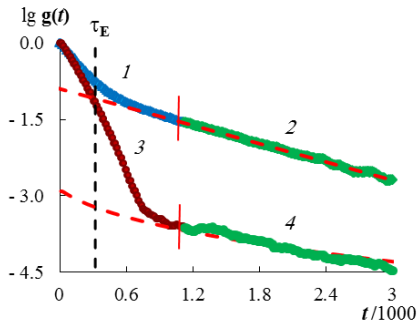
Figure 1. Semi-logarithmic FID time-dependence for the freely jointed chain in the melt (1-2, $N_{TOTAL} = 127$) and for the chain middle Kuhn segments (3-4, $N_{MIDDLE} = 127 - 2\langle N_E \rangle = 98$) according to expression (4a). The green color (2 and 4) denotes the FID tails extrapolated by the dashed red lines to find p_{E0}; the vertical dashed line denotes τ_E.
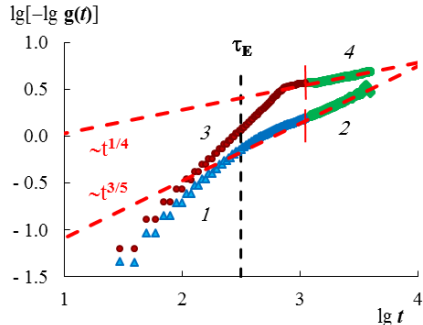
Figure 2. Negative dependences from fig. 1 in the logarithmic scale to reveal the asymptotic linear anamorphosis − the dashed red lines − for the chain middle segments, $\sim t^{1/4}$ (4), and end fragments, $\sim t^{3/5}$ (2). The vertical dashed line denotes τ_E; the colors of all parts of the FIDs are transferred from fig. 1 to correlate them.

Conclusion

Thus, it is shown, that the simulated FID confirms the theoretical equation (3b), which can be considered as a novel approach to describe the FID long-time behavior based on the residual dipolar coupling of the primitive segment [1]. Furthermore, this newly discovered FID tail of the low population indicates transformation of the macromolecule motion into the reptation regime, what gives additional structural-dynamic information about a polymer melt. Moreover, what is most surprising, this information turned out to be available in the experiment due to the existence in the melt of such a seemingly exclusively abstract circumstance as a force tube, which was introduced almost half a century ago to make possible solving the stochastic equation of the polymer chain motion.

References

1. E.M. Pestryaev − *Polym. Sci.: Ser A*, 60, 530-551 (2018).
2. N.F. Fatkullin, T. Korber, E.A. Rossler − *Polymer*, 142, 310-315 (2018).
3. M. Doi, S.F. Edwards. The theory of polymer dynamics − Clarendon pr., Oxford, 1987.
4. A. Abragam. The principles of Nuclear Magnetism − Clarendon pr., Oxford, 1961.
5. Yu.Ya. Gotlib et al − *Polym. Sci. USSR*, 18, 2630-2636 (1976).
6. E.M. Pestryaev − *Polym. Sci.: Ser A*, 62, 766-778 (2020).

Diffusion studies in polymeric membranes plasticized by ionic liquids

Nadezhda V. Pokhvishcheva[1], Alexandr V. Ievlev[2], Maria A. Peshkova[1]
[1]Institute of Chemistry, Saint Petersburg State University, 26 Universitetskiy prospect, 198504, Petergof, St. Petersburg, Russia
[2]Department of Nuclear Physics Research Methods, Saint Petersburg State University, 1 Ulyanovskaya st., 198504, Petergof, Saint Petersburg, Russia
E-mail: n.v.pokhvishcheva@gmail.com

Introduction

NMR diffusometry is a powerful tool for studying various objects and materials; it allows for determining diffusion coefficients for neutral and charged species [1, 2]; moreover, it makes it possible to understand the nature and number of species involved in transport processes in a specific medium. Previously we reported on applicability of NMR diffusometry for research in the field of plasticized polymeric ion-selective sensors (ISSs) [3] and in this contribution we present the results of our further studies.

Diffusion plays an incredibly important role in the process of generating signal of ISSs since their response is closely related to transport phenomena in both the aqueous and polymeric phases. For a stable sensor signal to occur, equilibrium must be established throughout the entire sensor phase, which is essentially a 2-20 μm thick viscous polymeric film, meaning that the sensor response time will be determined by the diffusion coefficients of all species involved in the process. Detection limits are also determined by the diffusion rate, since they are controlled by the transmembrane ion fluxes to/from electrode inner solution [4]. Stability of redox-sensitive sensors and the rate of the solution electrolyte co-extraction are determined by the transport and, in turn, the diffusion coefficients of water microdroplets in the membrane [5]. All this leads to the conclusion that the field of ISSs would greatly benefit from implementation of an accurate method for measuring diffusion coefficients such as NMR-diffusometry.

As a primary research object, we chose a highly promising type of sensors: polymeric membranes containing ionic liquids. The use of ILs in sensors has been extensively studied over the past decade, mainly due to their multifunctional performance. ILs can serve as active sensor components, at the same time plasticizing the polymeric sensing phase [6]. The ionic liquids being used as plasticizers change the viscosity and polarity of the polymeric phase as compared to traditional plasticizers thus heavily affecting the stability of ion-ligand complexes, the ionic distribution coefficients, and the association/dissociation of ionic pairs in the sensing phase. Meanwhile, extensive NMR investigation of the transport and electrolytic properties of pure ILs and their mixtures with liquid solvents is being carried out [2, 7] providing the prerequisites for the successful study of ILs in the composition of the polymeric sensor phase.

Experimental results

One of the most commonly used ionic liquid 1 hexyl-3-methyl-1*H*-imidazol-3-ium bis[(trifluoromethyl)sulfonyl] amide ($[C_6Meim][NTf_2]$) was studied as a plasticizing component in binary bis(2-ethylhexyl)sebacate (DOS) ester-IL mixtures to plasticize PVC membranes. The composition of the PVC-DOS-$[C_6Meim][NTf_2]$ membranes studied by NMR diffusometry are presented in the Table 1. The diffusion coefficients were estimated by means of pulsed field gradient stimulated echo with bipolar gradient (PFG STEb technique). ^{1}H and ^{19}F spectra of the membranes with different IL content in the plasticizing mixture are shown in Fig. 1.

Table 1. The composition of the PVC-DOS-[C$_6$Meim][NTf$_2$] membranes studied by NMR diffusometry

components			target IL content, wt. %	
PVC, mg	IL, mg	DOS, µl	*per plasticizer mass*	*per membrane mass*
60	0	196.9	0	0
	23.1	171.7	11.9	9.7
	49.6	142.7	25.8	20.7
	74.7	115.2	39.3	31.2
	88.2	100.4	46.8	36.8
	107.2	79.2	57.6	44.9
	127.1	57.9	68.7	53.0
	182.7	0	100	75.3
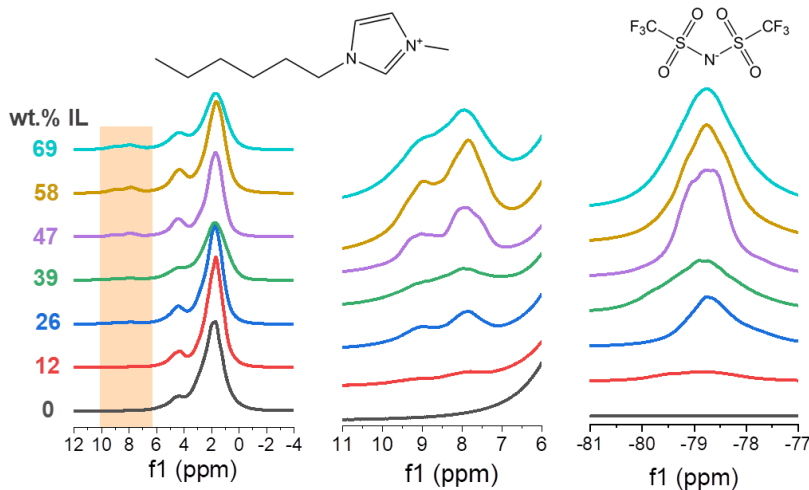
Figure 1. ^{1}H (left, center) and ^{19}F (right) spectra of the membranes with different IL content in the plasticizing mixture (indicated in the legend in wt. %). Center – enlarged domain of ^{1}H spectrum corresponding to imidazolium ring protons.

It was found that spectral lines for all the samples are strongly broadened due to the presence of PVC-DOS matrix. Broadening is mainly associated with an increase in the relaxation times of groups of molecules when interacting with membrane structures that have a significantly lower mobility, similar to that of a solid matter.

The respective dependences of the intensity on the gradient amplitude were fitted with modified Stejscal-Tanner equation: a superposition of the two decaying exponents.

$$I(x) = I_1 \exp(-D_1 x) + I_2 \exp(-D_2 x) \,; \text{ with } x = \gamma^2 G^2 \delta^2 \left(\Delta - \frac{\delta}{3} \right)$$

Where D_i, I_i – the diffusion coefficient and the integral intensity of i-component, respectively; γ – the gyromagnetic ratio; G – the gradient amplitude; δ – the duration of the gradient pulses; and Δ – the time interval between the gradient pulses. Each of the obtained exponents contained a "fast" component with a higher value of the fitting parameter D_1, and a "slower" impact with a lower value of D_2. The D_1 values obtained from the ^{1}H and ^{19}F spectra can be attributed to the diffusion coefficients of imidazolium cation and fluorine-containing

anion, respectively. Diffusion coefficients D_2 for the second ("slow") component obtained for both cation and anion are equal within the margin of error and are almost an order of magnitude lower than the ionic diffusion coefficients. This result may indicate that some amount of the IL diffuses in a form of an ion pair (see Table 2).

Table 2. The diffusion coefficients of the cation (^{1}H) and anion (^{19}F) in the membranes with different IL content.

target IL content, wt. %	^{1}H		^{19}F	
	$D_1\times10^{11}$, m^{2}s^{-1}	$D_2\times10^{12}$, m^{2}s^{-1}	$D_1\times10^{11}$, m^{2}s^{-1}	$D_2\times10^{12}$, m^{2}s^{-1}
11.9	1.316	1.272	1.701	2.375
25.8	1.215	4.392	1.236	5.133
39.3	1.234	4.482	1.211	4.154
46.8	1.198	4.183	1.293	4.686
57.6	1.253	4.221	1.292	5.021
68.7	1.090	3.335	1.173	4.575
100	0.920	2.666	0.928	3.657

We observe the non-monotonic dependence of the diffusion coefficient versus IL content in the polymeric phase: D_1 goes through a maximum at ca. 50 wt. % of IL in the plasticizing mixture. This result is in agreement with the data obtained earlier [3] by means of chronopotentiometry.

Based on the obtained results, we can conclude that NMR diffusometry is a functional instrument for exploration of transport phenomena in polymeric ion-selective membranes. By varying the relative content of IL in the polymeric phase, the viscosity and polarity of sensing PVC membranes can be readily tuned. The observed dependences lead to further explanation of the effect of ILs on the response of polymeric ion-selective sensors.

Acknowledgments

References

1. Price, W.S., *Concepts Magn. Reson.* 1998, *10*, 197–237
2. Umecky, T.; Saito, Y.; Matsumoto, H. ECS Trans. 2019, 25, 23–29
3. N. V. Pokhvishcheva, E.K. Gigiadze, A. V. Kalinichev, A. V. Ievlev, K. V. Tyutyukin, M.A. Peshkova, *Membranes (Basel).* 12, 130 (2022)
4. Z. Szigeti, T. Vigassy, E. Bakker, E. Pretsch. – *Electroanalysis*, 18, 1254-1265 (2006)
5. A.P. Thoma, A. Viviani-Nauer, S. Arvanitis, W.E. Morf, W. Simon. – *Anal. Chem.*, 49, 1567–1572 (1977)
6. N. V. Shvedene, D. V. Chernyshov, I. V. Pletnev. – *Russ. Chem. J.*, LII, 80–91 (2008)
7. Tokuda, H.; Tsuzuki, S.; Susan, M.A.B.H.; Hayamizu, K.; Watanabe, M.. J. Phys. Chem. B 2006, 110, 19593–19600

Photochemical transformations of O-containing radical-cations at low temperatures in CF₃CCl₃ matrix.

Daria A. Pomogailo, Ivan D. Sorokin, Mikhail Ya. Melnikov, Vladimir I. Pergushov, Oleg I. Gromov

Department of Chemistry, M. V. Lomonosov Moscow State University, 119991, Russia, Moscow, Leninskie Gory, 1/3

E-mail: texafirin@ya.ru

Electron Paramagnetic Resonance spectroscopy is widely used to determine the behavior of paramagnetic species, such as ions, radical ions, complexes of transition metals, etc.

Radical cations (RC) are species that have unpaired electrons, similar to radicals, as well as a positive charge, similar to cations. The studies of the mechanisms guiding the reactions of electronically excited radicals and radical ions have attracted considerable interest. This is due to the significance of the processes various substances undergo under extreme conditions. The RC formed upon the irradiation of different solutions of oxiranes in the CF_3CCl_3 matrix at 77 K is described in this study. The purpose of this investigation was to find out how the nature of the substituents in the oxirane ring affected the structure of the resulting RC and its further transformations under the action of light.

Electron Paramagnetic Resonance and UV-vis absorption spectroscopy as well as quantum chemical calculations were used in this investigation. Different types of RC were formed upon the irradiation of solutions of oxiranes (epoxides) in freon-113a (CF_3CCl_3) at low temperatures (77 K) under similar conditions: for cyclopentene oxide and cyclohexene oxide, the RCs with elongated C-C bonds in their oxirane rings were produced. The RC of methyloxirane, 2,3-dimethyloxirane and tetramethyloxirane were stabilized in their ring-open forms (the distance between the carbon atoms in their oxirane rings exceeded the equilibrium length of the C–C bond).

Beside these oxiranes, we studied exo-2,3-norbornene oxide and its corresponding RC since the structure of this precursor molecule included the structural motifs of cyclohexene oxide and cyclopentene oxide for which the photochemical transformations had already been established [1, 2].

The structure and nature of the underlying photochemical transformations of RC were established. It was found that the RC of methyloxirane [3] and 2,3-dimethyloxirane [4] underwent reversible photocyclization concerning the C—C bond in the oxirane cycle, while the tetramethyloxirane RC did not undergo any reactions under the action of light [3].

Upon the action of light, irreversible proton abstraction in the ring-open form of the cyclopentene oxide RC occurred, affecting the bridgehead carbon. This afforded unstable 6-oxabicyclo[3.1.0]hexan-1-yl radicals, which underwent rearrangement to form ring-open terminal C-centered alkyl radicals detected as final products [2]. The RC of cyclohexene oxide underwent similar phototransformations as RC of cyclopentene oxide [1].

It was found that, upon absorption of light, the C–C bond was formed again in the oxirane ring of the exo-2,3-norbornene oxide RC, with the spin and charge both localized in the cycloalkyl fragment. The resulting paramagnetic species is stable at 77 K. In a reaction similar to what was earlier reported for other RC [5], it underwent photoelimination of H_2, affording the 3-oxatricyclo[3.2.1.02,4]oct-5-ene RC.

A sequence consisting of an intramolecular photorearrangement and the photoelimination of molecular hydrogen was found for the RC of exo-2,3-norbornene oxide [6]. Different mechanisms of phototransformations of RCs of some oxiranes are summarized in the scheme 1 [7].
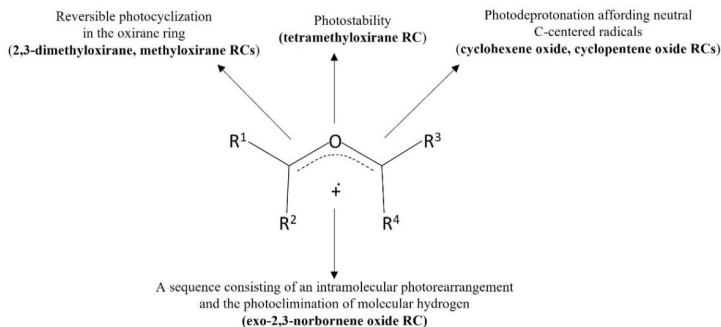
Scheme 1. Different mechanisms of phototransformations of radical cations of oxiranes [7]

Thus, it can be concluded that the structure of the RC dramatically affects the further mechanism of transformations of these RCs under the action of light.

The quantum chemical calculations carried out for different types of RC of oxiranes showed that, upon radiolysis, either RC with elongated bonds between the carbon atoms in the oxirane ring or RC in their ring-open forms were formed.

Using UV-vis and Electron Paramagnetic Resonance spectroscopy allowed us to determine the sequence of photochemical transformations of the afforded RCs. Hence, the conclusion is that the further transformations of RC formed upon radiolysis in freon matrices cardinally depend on the nature of substituents at the oxirane ring.

The observed commonality in the nature of indirect ionization products for various oxirane-derived RCs cannot be extended to other parameters to predict the pathways of their phototransformations.

References:

1. I. Sorokin, O. Gromov, V. Pergushov, D. Pomogailo, M. Melnikov. – *Mendeleev Commun.*, 28 (6), 618-620 (2018).
2. I. Sorokin, O. Gromov, V. Pergushov, D. Pomogailo, M. Melnikov. – *Mendeleev Commun.*, 30 (1), 67–69 (2020).
3. I. Sorokin, O. Melnikova, V. Pergushov, D. Tyurin, V. Feldman, M. Melnikov. – *High Energy Chem.*, 46 (3), 183-193 (2012).
4. *I.* Sorokin, V. Feldman, O. Melnikova, V. Pergushov, D. Tyurin, M. Melnikov. – *Mendeleev Commun.,* 21 (3), 153-154 (2011).
5. M. Tabata, A. Lund. – *Chem. Phys.,* 75 (3), 379-388 (1983).
6. D. Pomogailo, I. Sorokin, O. Gromov, V. Pergushov, M. Melnikov. – *Mendeleev Commun.*, 31 (2), 154–156 (2021).
7. И. Сорокин, О. Громов, В. Пергушов, Д. Помогайло, М. Мельников. – *Вестн. Моск. Ун-та. Сер. 2. Химия.*, 62 (6), 470-480 (2021) (In Russian).

Diastereoisomers of 3-azabicyclo[3.1.0]hexanes spiro-fused with a benzo[4,5]imidazo[1,2-a]indole fragment: structure determinations using NMR methods

<u>*Julia A. Pronina[1]*</u>*, Alexander V. Stepakov[1,2], Stanislav I. Selivanov[1,3]*
[1]*Saint-Petersburg State Institute of Technology (Technical University), Moskovsky prospect 26, 190013, Saint-Petersburg, Russia*
[2]*Institute of Chemistry, State University of Saint-Petersburg, University prospect 26, 198504, Saint-Petersburg, Russia*
[3]*Laboratory of Biomolecular NMR, St. Petersburg State University, 199034, St. Petersburg, Russia*
E-mails: [1]*pronina.iuli05@ yandex.ru;* [3]<u>*nmr.group.spbu@gmaill.com*</u>

Introduction

The analysis of complex NMR spectra is one of the important directions in chemical research now. The development of various strategies in NMR spectroscopy makes it possible to achieve a more accurate and complete determination of the structures of the substances under study. NMR spectroscopy has achieved good results in structural and conformational analysis, in particular in the analysis of relatively small organic molecules [1, 2].

The three-component 1,3-dipolar cycloaddition reaction between 1, 2 and 3 led to two products 4 and 5, which were in the reaction mixture in a ratio 6:1 and were isolated and studied individually using NMR spectroscopy methods. (Figure 1).
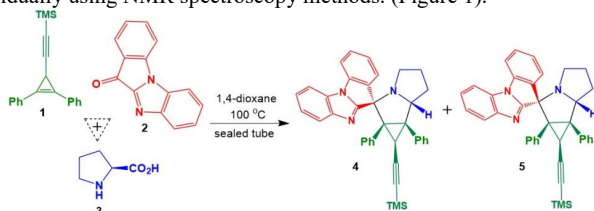

Figure 1. Scheme of reaction and structures of diastereoisomers (4) and (5).

In this thesis the quantitative estimation of the experimental distances by NOESY spectra was carried out in the isolated spin pair approximation (ISPA) [3] and relatively short mixing time ($\tau m = 0.5$ s) was used. The values of the integral cross-peak intensities were reduced to the diagonal and so-called spherical calculation model [4] was implicated. The assumption of the absence of the anisotropy of the total rotational diffusion in the solution of the studied molecules 4 and 5 is based on the relatively low (about 2) calculated value of the diffusion coefficients around the principal axes $D\|/D\perp$ [5]. Moreover, when analyzing the distances between protons in the rigid part of the molecule (H6a`, H1`) and degenerate ortho-protons of mobile aromatic rings (H12,16 and H18,22), only the distance to the nearest of the two protons was taken into account [6], since, according to calculations, the distance to the farthest ortho-proton was significantly (by $1.5 - 2.0$ Å) longer than that of the nearest one, and the contribution of distant protons to the effective NOE was a negligibly small value [7].

Experiments and results

The spatial structure of the major product 4 is shown in Fig. 2 and its proof was quite simply obtained from NOESY spectroscopy data after preliminary identification of all proton signals on base COSY analysis. The most typical for this compound are the following proton-proton spatial interactions (NOEs), which are shown using red asterisks, and the ratios of the

integral intensities of the corresponding cross peaks, which were compared with the calculated values of the corresponding distances obtained by optimizing the geometry of the molecule 4 by the MM2 method.

The discrepancies between the calculated and experimental values of the interproton distances give grounds for assuming the existence of the 4 molecule in solution in the form of a fast exchange on the NMR time scale between two (or more) conformations, which differ from the energetically more preferable conformation (A) of compound 4 by the proximity of H6a` protons and H4`β and the distance from each other of the protons H1 and H4`α. Thus, in experiments on the measurement of NOE, its time-averaged value is observed, which leads to a deviation from the calculated values of the distances for each of the conformers, if they differ significantly from each other and the proximity of protons is characteristic of a minor conformer. Calculations by the MM2 method indicate the possibility of the existence of at least one more minor conformer (B) and, therefore, the dynamic exchange of compound 4 is more complicated.
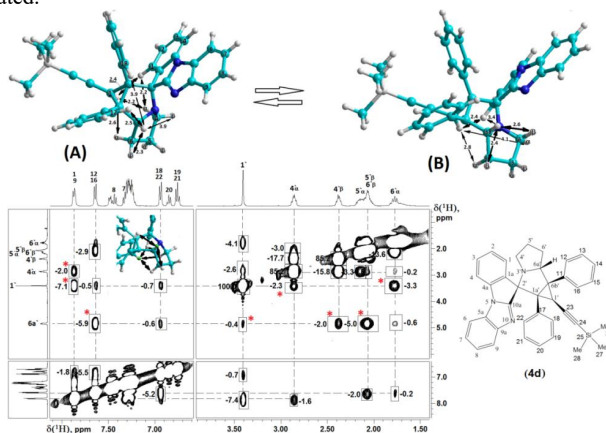
Figure 2. The interproton distances most important for proving the structure and their corresponding cross peaks are shown by double arrows and rectangles on the 3D model of the molecule 4 and on the spectrum, respectively. The calculated (MM2) distance values are given by figures in angstroms (Å), the volume integrals are given in % relatively to the intensity of the diagonal signal of the proton [1]H.

The structure of the minor product 5 was established in a similar way, taking into account the results obtained for the dominant product 4. Comparison of the ^{1}H NMR spectra of these products indicates to significant changes in the chemical shifts in the spectrum of compound 5 compared to 4, which are observed in both its aliphatic and aromatic parts. It should be also mentioned that there is a noticeable broadening of the signals of aliphatic protons compared with the spectrum of compound 4. These broadenings may indicate the existence of a fast dynamic equilibrium in the 5-membered ring in the NMR time scale similar to that described above for 4, but occurring at a slower rate.

Analysis of the NOESY spectrum of compound 5 (Fig. 3) gives an unambiguous answer about its actual structure. The most important source of information about the actual structure of the minor product 5 is undoubtedly the spatial interactions of the ^{1}H proton, which are indicated by double arrows in Fig. 3 (right fragment).

The interaction with the Ha` proton, which has a β-orientation, plays a decisive role in asserting that the minor product 5 is an epimer with respect to the dominant product 4.

125

According to the calculations by the MM2 method, this distance in the **5** epimer should be 2.7 Å, which corresponds to the 6a`/1 cross peak with an intensity of 5.7% in the NOESY spectrum.
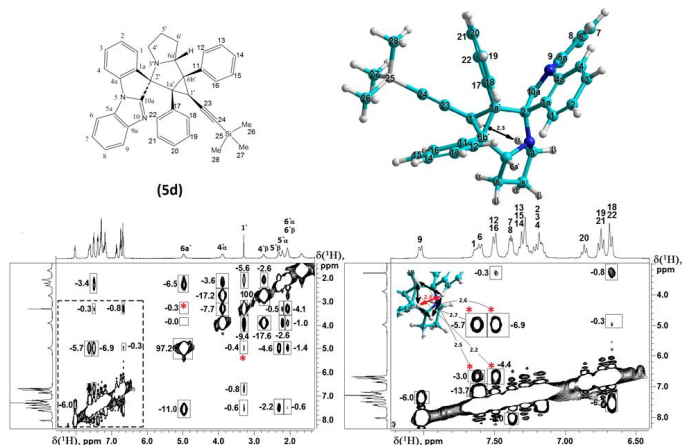

*Figure 3. The interproton distances most important for proving the structure **5** (marked with a red star) and their corresponding cross peaks are shown with double arrows and rectangles on the 3D model of the molecule and on the spectrum, respectively. The calculated (MM2) distance values are given by figures in angstroms (Å), and the volume integrals are given in % relatively to the intensity of the diagonal signal of the proton H1`.*

Conclusion

Thus, the epimeric structure of the minor product 5 was proved by NOE measurements, and the dynamic mobility of the 5-membered aliphatic ring, similar to that observed in the dominant product 4, was found based on the broadening of some signals in both the ^{1}H and ^{13}C spectra. A distinctive point in the case of 5 is the fact that the broadening is observed not only in the aliphatic regions of these spectra, but also in the region of aromatic protons and aromatic carbon-13 atoms. It should also be noted that in the case of product **5**, the conformational equilibrium may shift towards a more energetically favorable conformer (A) compared to the dominant product 4.

Acknowledgments

References

1. W.F. Reynolds, R.G. Enriquez. J. Nat. Prod., 2002, 65, 221–244.
2. M. Jaeger, R.L.E.G. Aspers. Ann. Rep. NMR Sp-py, 2012, 77, ch. 3, 115–258.
3. D. Neuhaus, M.P. Williamson. VCH Publishers Inc., 2000, 619 P.
4. R.A. Bell, J.K. Saunders. Canad. J. Chem, 1970, 48 (7), 1114–1122.
5. D.E. Woessner. J. Chem. Phys., 1962, 36 (1), 1–4.
6. J. Tropp. J. Chem. Phys., 1980, 72 (11), 6035–6043.
7. C.P. Butts, C.R. Jones, Z. Song, T.J. Simpson. Chem. Commun., 2012, 48 (4), 9023–9025.

Handling of the strength of hydrogen bonds involving imidazole ring through the formation of additional non-covalent interactions

Daniil A. Shitov, Elena Yu.Tupikina

Institute of Chemistry, Saint Petersburg State University, Saint Petersburg, Russia
E-mail: shitovsky@gmail.com

Introduction

The imidazole fragment is a key component of many bioactive molecules, drugs and natural compounds. The rate-limiting step, on which processes depend, for example, the transfer of amino acids for assembly into a protein, that ensures such activity of imidazole derivatives is the formation of a hydrogen bond with the imidazole fragment. Thus, controlling the strength of a hydrogen bonding is a direct tool for varying the activity of biological processes involving the imidazole moiety.

For example, imidazole is part of one of the amino acids L-histidine, and the protonated form of L-histidine in the human body interacts with transfer RNA through the formation of a hydrogen bond between the nitrogenous base of t-RNA and imidazole [1] (Figure 1, left). According to X-ray structures of CCDC database, a wide variety of strengths of hydrogen bonds formed by imidazole is due, firstly, to the fact that imidazole can act as both a proton donor and acceptor, and, secondly, imidazole forms additional non-covalent interactions [2-4] (Figure 1, right).
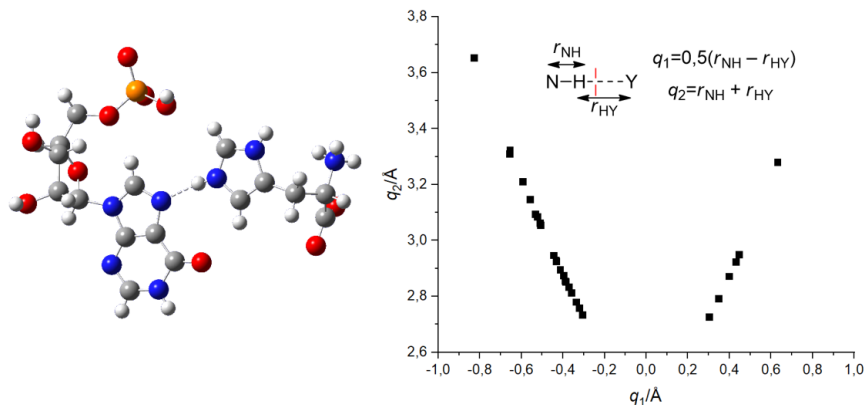
Figure 1. X-ray structure of complex formed by protonated L-histidine and t-RNA nitrogenous base (left). Geometrical parameters of complexes from X-ray structures of CCDC base involving hydrogen bond with imidazole fragment and additional non-covalent interactions (right)

In the figure: $q_1 = 0.5(r_{NH} - r_{HY})$, $q_2 = r_{NH} + r_{HY}$

Model complexes

Imidazole oligomers were chosen as the base model (Figure 2). Additional non-covalent interactions are: the formation of a hydrogen bond imidazole-imidazole, imidazole-proton donor (methanol, dimethylamine), imidazole-proton acceptor (acetone, thioacetone).
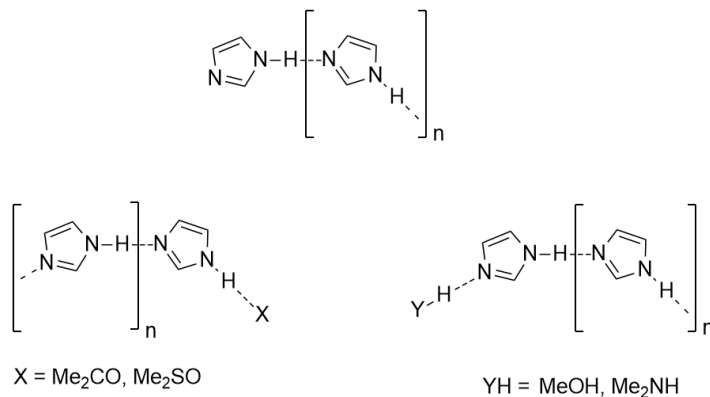
X = Me$_2$CO, Me$_2$SO

YH = MeOH, Me$_2$NH

Figure 2. Investigated complexes containing imidazole fragment with additional non-covalent interactions (n =0,1,2,3

Methods

Model complexes were investigated by the means of non-relativistic quantum chemistry using hybrid functional of electron density B3LYP with dispersion correction D3BJ in triple-ζ correlation-consistent augmented basis set aug-cc-pVTZ. NMR parameters such as isotropic values of chemical shifts of hydrogen bond's protons and spin-spin coupling constants between ^{15}N-^{15}N, ^{15}N-^{1}H nuclei (GIAO method) and parameters of electron density distribution function and their correlation with hydrogen bonding strength were analyzed.

Acknowledgments

References

1. Ślepokura, Katarzyna; Petrus, Rafal. Nucleotide–amino acid interactions in the L-His–IMP·MeOH·H$_2$O complex. *Acta Crystallographica Section C*, 2010.
2. Nagashima, Hideaki; Inoue, Hidenari; Yoshioka, Naoki; An Ideal One-Dimensional Antiferromagnetic Spin System Observed in Hydrogen-Bonded Naphth[2,3-d]imidazol-2-yl Nitronyl Nitroxide Crystal: The Role of the Hydrogen Bond. *The journal of physical chemistry. B*, 2004.
3. Gunawardana, C. A.; Desper, J.; Sinha, A. S.; Đaković, M.; Aakeröy, C. B.; Competition and selectivity in supramolecular synthesis: structural landscape around 1-(pyridylmethyl)-2,2′-biimidazoles. *Faraday Discuss.*, 2017.
4. Xu, Hui; Zhang, Yin; Huang, Jianqiang; Chen, Wanzhi; Copper-catalyzed synthesis of N-fused heterocycles through regioselective 1,2-aminothiolation of 1,1-dibromoalkenes. *Organic letters*, 2010.

An example of the Bloch-Siegert effect in magnetic-resonance sounding

Oleg A. Shushakov [1,2]
[1]*Institute of Chemical Kinetics and Combustion SB RAS, 3, Institutskaya St., 630090 Novosibirsk, Russia*
[2]*Novosibirsk State University, 1, Pirogova St., 630090 Novosibirsk, Russia*
E-mail: o.shushakov@g.nsu.ru

Introduction

Magnetic-resonance sounding (MRS) is a method of remote detection and characterization of aquifers. The MRS is a direct method of detecting underground water, in contrast to the well-known geophysical methods. The MRS allows detecting underground water deposits in the corresponding geologic formations at a depth of down to 100 m or more, depending on the degree of shielding of the electromagnetic field by rocks and electromagnetic noise [1].

An example of the MRS field application

An example of the MRS study was conducted in the Ebro-river basin (Spain) with the Hydroscope produced by the Institute of Chemical Kinetics and Combustion SB RAS and NUMIS PLUS, IRIS Instruments (France). The results of studies using the model without taking into account the interference of electromagnetic shielding and the Bloch-Siegert effect were published earlier [2]. To generate the RF field and receive the MRS signal, eight-shaped antennas were used, first used in [3]. For the Hydroscope device, an antenna consisting of two circles with a diameter of 50 m was used, for the NUMIS device - in the form of two squares of 50x50 m [2]. The lithological cross-section of the Te-27 point is presented in Table 1. The resistivity was 250 ohms*m at depths from 0 to 40 m from the surface and 30 ohms*m over 40 m. The angle of inclination of the geomagnetic field was 55°, and the proton resonance frequency was 1906 Hz ($4.4737 10^{-5}$ T).

Table 1. Lithological log of the Te-27 site, Ebro basin, Spain

Depth (m)	Lithology	Age	Comments
0-1	Clay	Quaternary	Aquitard
1-14	Sandstone	Quaternary	Aquifer
14-50	Marl with gravel	Pliocene	Aquifer
50-105	Marl	Pliocene	Aquitard

Figures 1, show the amplitudes and phases of the MRS for the Te-27 point, depending on the RF pulse intensity, obtained by the Hydroscope device, and the results of their numerical approximation, taking into account the interference of electromagnetic shielding and the Bloch-Siegert effect [1]. The best approximation of the experimental data was obtained by taking into account the interference of electromagnetic shielding and the Bloch-Siegert effect for aquifers from 1 to 14 m with water content of 19% and from 14 to 50 m with water content of 4%. For comparison, the calculated amplitude and phase of the MRS are given taking into account only electromagnetic shielding (without taking into account the Bloch-Siegert effect) for aquifers from 1 to 14 m with water content of 19% and from 14 to 50 m with water content of 4%.
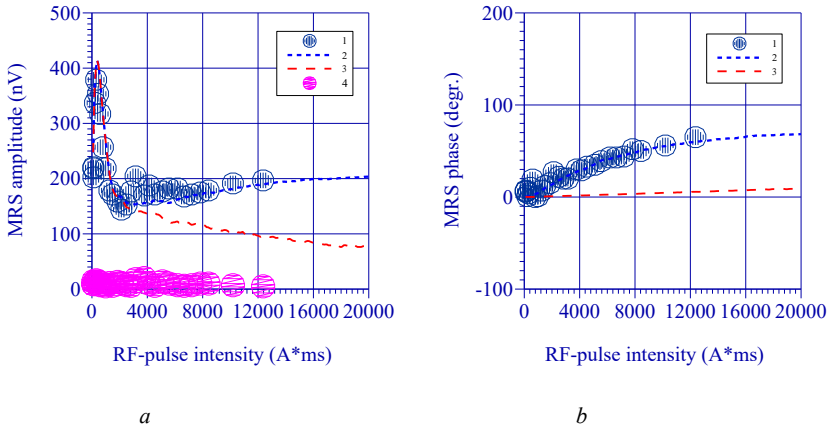
a   *b*

Figure 1. An example of the approximation of the MRS field- data amplitude (a) and phase (b). 1 - field data Te-27, Ebro-River basin (Spain). 2 - approximation with EM shielding and the Bloch-Siegert effect for aquifers 1 -14 m, water content 19% and 14 - 50 m, water content 4%. 3 - calculation with only EM shielding (without the Bloch-Siegert effect) 1 - 14 m, water content 19% and 14 - 50 m, water content 4%. 4 - noise level.

Figure 2 shows an example of a histogram of water content (water content in the rock in%) versus the depth obtained from Figure 1 for the point Te-27. This histogram shows two aquifers: from 1 to 14 m with water content of 19% and from 14 to 50 m with water content of 4%. For comparison, a histogram of the water content versus the depth obtained by approximating the experimental data of Fig. 1 is given, taking into account only electromagnetic shielding (without taking into account the Bloch-Siegert effect) in the form of aquifers from 1 to 14 m with a water content of 19% and from 40 to 50 m with a water content of 25%.
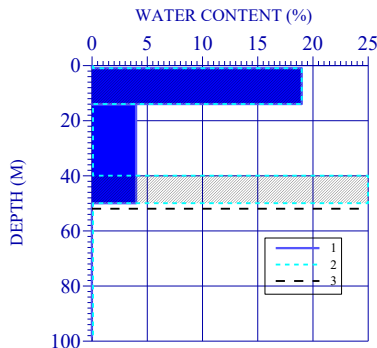
Figure 2. An example of the MRS inversion, Te-27, Ebro-River basin (Spain). 1 - solution with EM shielding and the Bloch-Siegert effect:aquifers 1 - 14 m, water content 19% and 14 - 50 m, water content 4%. 2 – solution with EM shielding only (without the Bloch-Siegert effect): aquifer 1 - 14 m, water content 19% and 40 - 50 m, water content 25%. 3 – the maximum depth of MRS detection with the eight-shaped antenna 2 x 50 m circles [3].

It should be noted that in Fig. 1. 2 the best approximation of the experimental data was achieved by taking into account the interference of electromagnetic shielding and the Bloch-Siegert effect. When taking into account only electromagnetic shielding (without taking into account the Bloch-Siegert effect), the amplitude of the MRS signal in Figure 1 differs 2 times at the maximum RF pulse intensity for experimental data (approximately 12,000 A*ms), the phase of the MRS signal in Figure 1 differs 12 times at the maximum pulse intensity. Therefore, to approximate the experimental data using the model without taking into account the Bloch-Siegert effect, it is necessary to add layers at depths close to the maximum for this type of antenna. For an antenna in the form of a circle with a diameter of 100 m, the maximum depth of the MRS is approximately 100 m. For an antenna in the form of an eight of two circles with a diameter of 50 m, the maximum depth of the MRS is approximately 50 m (Fig. 2). However, in reality, these layers do not exist; they appear only as an artifact of the model without taking into account the Bloch-Siegert effect. Such nonexistent layers were obtained in the previously published work [2] due to the erroneous interpretation of the MRS data without taking into account the Bloch-Siegert effect.

Conclusion

An example of MRS studies in the Ebro-river basin (Spain) shows good approximation of the experimental data considering the interference of electromagnetic shielding and the Bloch-Siegert effect.

The example demonstrates that without taking into account the Bloch-Siegert effect [1] the calculated MRS amplitude and phase differs from the experimental data about 2 and 12 times respectively at the maximum RF pulse intensity.

A nonexistent aquifer from 40 to 50 m can be obtained with the erroneous interpretation of the MRS data without taking into account the Bloch-Siegert effect like in the previously published work [2].

Acknowledgments

References

1. O.A. Shushakov - *Russian Geology and Geophysics*, 63, 831–839 (2022).
2. J.L. Plata, F.M. Rubio - EAGE 67th Conference & Exhibition - Madrid, Spain, Z 99 (2005)
3. D.V. Trushkin, O.A. Shushakov, A.V. Legchenko - *Geophysical Prospecting*, 42, 855-862 (1994).

Local motion of water molecules and Li⁺, Na⁺, Cs⁺ cations in sulfonic cation-exchange membranes studied by spin relaxation of ¹H, ⁷Li, ²³Na, ¹³³Cs nuclei.

<u>*Nikita A. Slesarenko[1]*</u>*, Victor P. Tarasov[1], Alexander V. Chernyak[1,2], Vitaly I. Volkov[1,2]*
[1]Federal Research Center of Problems of Chemical Physics and Medicinal Chemistry RAS, 142432 Chernogolovka, Russia
[2]Osipyan Institute of Solid State Physics RAS, 142432 Chernogolovka, Russia
E-mail: <u>wownik007@mail.ru</u>
https://www.icp.ac.ru

Introduction

NMR relaxation methods allow direct investigation of local molecular and ionic mobility in sulfonic cation-exchange membranes. Among the main problems in the quantitative estimation of the parameters of cation motions is the lack of theoretical works, on the basis of which it would be possible to study the region of diffusion motions characterized by correlation times greater than ω^{-1} (where ω is the NMR frequency, which usually has a value of about 10^9 Hz). To date, there are works performed using ⁷Li and ²³Na NMR relaxation to study the mobility of Li⁺ and Na⁺ counterions in CU-2 type sulfocation exchangers, membranes based on them, and perfluorinated sulfocationite membranes [1–3]. Of particular interest is the study of the mobility of cations in Nafion membrane, which can be considered as a model of homogeneous sulfocationite membranes with well known ionogenic channel microstructure.

Materials

Extruded N117 (thickness 183 μm, equivalent weight (EW)=1100, Dupont, Ion Power Inc.) membranes were used for the experimental characterization of Nafion in salt (Li⁺, Na⁺, Cs⁺) ionic form.

Methods

NMR Relaxation

Spin-lattice T_1 and spin-spin T_2 nuclear relaxation times were measured using *180°-τ-90°* and Carr-Purcell-Meiboom-Gill *(90o - τ -n180°)* pulsed sequences, correspondingly. Longitudinal magnetization M_z recovery and perpendicular magnetization $M_{x,y}$ decay were approximated by exponential dependences (3) and (4), correspondingly for ¹H, ⁷Li, ²³Na, ¹³³Cs nuclei. Spin echo attenuation of ²³Na and ¹³³Cs nuclei was too fast in order to detect a detailed decay curve shape.

$$\frac{(M_0 - M_z)}{2M_0} = \exp(-t/T_1) \tag{1}$$

$$M_x(t) = M_0 \cdot \exp(-t/T_2) \tag{2}$$

M_o is equilibrium nuclear magnetization

Results and discussion

¹H spin- relaxation, water mobility

Spin of ¹H nuclei is 1/2, therefore spin relaxation occurs due to proton dipole-dipole interaction modulated by water molecule mobility. In the case of exponential correlation function relaxation times described by Bloembergen, Purcell, Pound equations.

The temperature dependences of the spin-lattice relaxation time $T_1(T)$ have a minimum at $\omega\tau_{av} = 0.62$, where τ_{av} is average correlation time the value of average correlation time τ_{av} in minimum $T_1(T)$ is $2.46 \cdot 10^{-10}$ sec (Fig. 1).
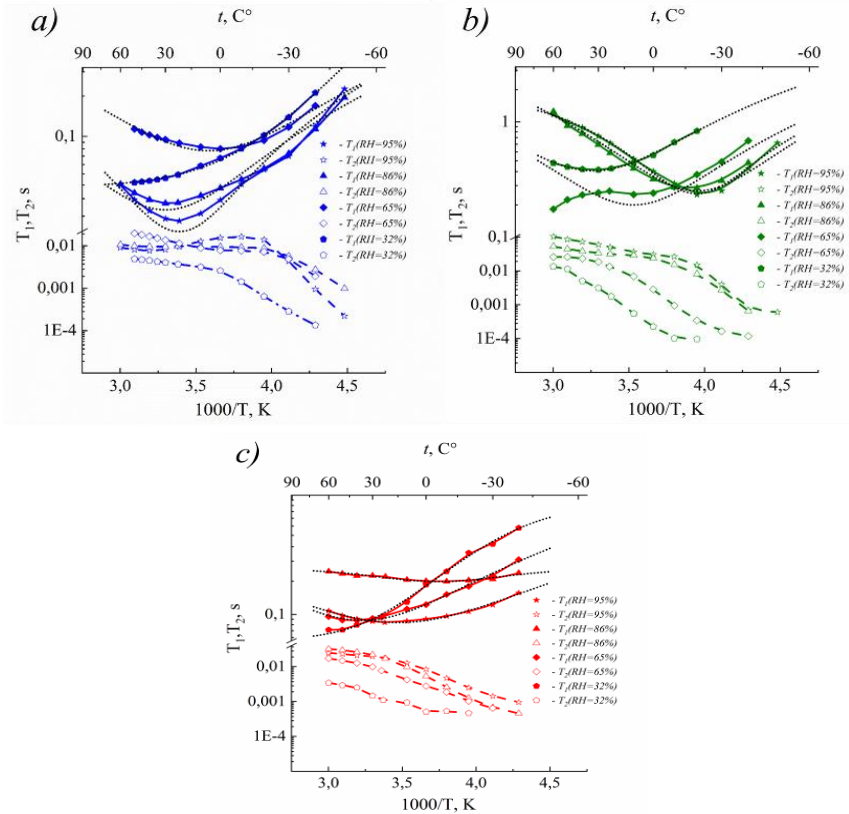
Figure 1. Temperature dependences of water molecules ^1H spin-lattice T_1 and spin-spin T_2 relaxation times of Nafion ionic form a) Li^+, b) Na^+, c) Cs^+ at different relative humidity.

Water self-diffusion coefficient may be estimated from Einstein relation (3).

$$D = l^2/6 \cdot \tau_{av}$$

(3)

where l is average jumping distance.

The values of local water mobility l calculated from the coefficients of water self-diffusion at RH = 65%, 86%, and 95% are comparable with the long hydrogen bond for the ionic forms of Li^+ and Na^+ (Table 1).

Table 1. Calculation of the average jump distance from self-diffusion coefficient D

Ionic form	Li^+				Na^+				Cs^+			
RH, %	32	65	86	95	32	65	86	95	32	65	86	95
l, Å	-	2,0	2,8	3,2	0,6	1,0	1,5	2,1	-	0,9	0,6	1,1

Bearing in mind the approximate calculation of local transport values from the Einstein relation, this is a good match. Therefore, it can be concluded that the macroscopic self-diffusion of water is controlled by the local movement of water molecules through a continuous network of hydrogen bonds, which is formed at a sufficiently high water content λ. For the ionic form of Cs^+, the measured values of the translational jump l are shorter than the length of the hydrogen bond. Water content λ=1.5 at relative humidity=75% in the ionic form of Cs^+. Three water molecules per sulfonate group is not enough to form a continuous network of hydrogen bonds, and this network breaks. Therefore, the rapid local rotation of the water molecule (which causes spin relaxation) does not correlate with the translational jump, since the rotation frequency is higher than the translational frequency.

^{7}Li, ^{23}Na, ^{133}Cs spin relaxation, cation mobilities.

The nuclear spins of ^7Li, ^{23}Na are *3/2*, but ^{133}Cs nuclear spin is 7/2. For these nuclei the main relaxation mechanism is quadrupole relaxation. For nuclear spin = 3/2 in minimum T_1 $(\omega\tau_{av})^2 \approx 1$ and $\tau_{av}=10^{-9}$sec and $3\cdot10^{-9}$ sec for nuclear ^{7}Li and ^{133}Cs, accordingly (Fig. 2).

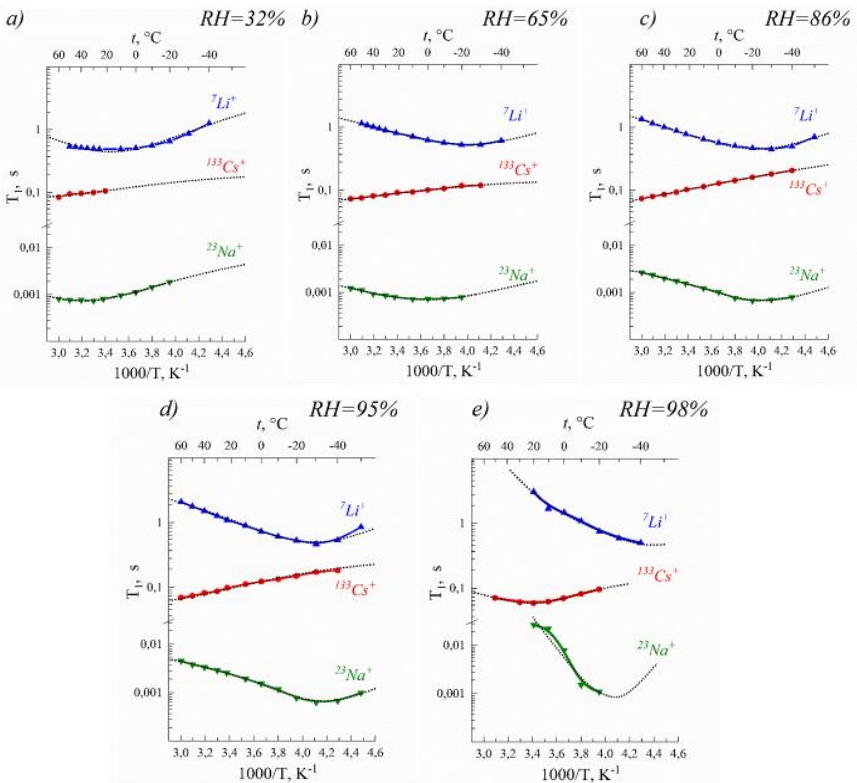*Figure 2. Temperature dependences of cations ^{7}Li, ^{23}Na, ^{133}Cs spin-lattice T_1 relaxation times of Nafion at RH a) 32%, b) 65%, c) 86%, d) 95% and e) 98%*

Using the diffusion coefficient at the temperature of T1 minimum, the length of the translational jump was calculated from the Einstein relation Eq.3. For cation Li^+ l is 0.1, 0.14, 0.14 and 0.18 nm at RH 32%, 65%, 86% and 95%, accordingly. That is closed to water hydrogen bond length. It may be supposed that Li^+ cation translation displacement is controlled by a rearrangement of hydrated water molecules hydrogen bond that explains a symbasis of water and lithium cation self-diffusion behavior. The temperature dependence T_1 (T) ^{133}Cs shows minimum at 20°C (Fig. 2e). Cesium cation at this temperature is $3 \cdot 10^{-11}$ m^2/s. From relation (3) l approximately is 0.7 nm. This value equals to average distance between neighboring sulfonate groups.

Acknowledgments

References

1. V.I. Volkov, A.V. Chernyak, D.V. Golubenko, V.A. Tverskoy, G.A. Lochin, E.S. Odjigaeva, A.B. Yaroslavtsev. Hydration and Diffusion of H^+, Li^+, Na^+, Cs^+ Ions in Cation-Exchange Membranes Based on Polyethylene- and Sulfonated-Grafted Polystyrene Studied by NMR Technique and Ionic Conductivity Measurements Membranes. 2020, 10, 272.
2. V.I. Volkov, S.L. Vasilyak, I.-WW. Park, H.J. Kim, H. Ju, E.V. Volkov, S.H. Choh. Water behavior in perfluorinated ion-exchange membranes. Applied Magnetic Resonance. 2003, 25, 43.
3. V.I. Volkov, N.A. Slesarenko, A.V. Chernyak, V.A. Zabrodin, D. V. Golubenko, V.A. Tverskoy, A.B. Yaroslavtsev. Mobility of Li^+, Na^+, Cs^+ Cations in Sulfocation – Exchange Membranes Based on Polyethylene and Sulfonated Grafted Polystyrene Studied by NMR Relaxation. Membranes and Membrane Technologies. 2022, 4, 189.

Comparison of ion dynamics in a carbon-substituted *closo*-hydroborates NaCB$_9$H$_{10}$, NaCB$_{11}$H$_{12}$ and solid-solution Na$_2$(CB$_9$H$_{10}$)(CB$_{11}$H$_{12}$): ^{1}H and ^{23}Na NMR studies

Alexey V. Soloninin[1], Alexander V. Skripov[1], Olga A. Babanova[1], Roman V. Skoryunov1,
Mirjana Dimitrievska2, Terrence J. Udovic2

[1]*Institute of Metal Physics, Ural Division of the Russian Academy of Sciences, S. Kovalevskoi 18, Ekaterinburg 620990, Russia*
[2]*NIST Center for Neutron Research, National Institute of Standards and Technology, Gaithersburg, MD, 20899-6102, USA*
E-mail: *alex.soloninin@imp.uran.ru*

Introduction

It has been found that the disordered phases of a number of *closo*-hydroborate salts, such as Na$_2$B$_{12}$H$_{12}$, Na$_2$B$_{10}$H$_{10}$, NaCB$_{11}$H$_{12}$, and NaCB$_9$H$_{10}$ exhibit extremely high ionic conductivities [1]. The characteristic feature of these compounds is the occurrence of the order-disorder phase transitions accompanied by abrupt acceleration of both the reorientational (rotational) motion of *closo*-hydroborate anions and the diffusive motion of metal cations. Both Na$_2$B$_{12}$H$_{12}$ and Na$_2$B$_{10}$H$_{10}$ exhibit order−disorder phase transitions (near the temperatures T_{trans} of 520 and 370 K, respectively) accompanied by strong changes in reorientational jump rates of the anions and diffusive jump rates of Na$^+$ cations. The [B$_{12}$H$_{12}$]$^{2-}$ anion and the [B$_{10}$H$_{10}$]$^{2-}$ anion can be modified by replacing one (B−H) vertex with a (C−H) group, yielding the structurally similar icosahedral monocarba-*closo*-dodecaborate anion [CB$_{11}$H$_{12}$]$^-$ and anion [CB$_9$H$_{10}$]$^-$ [2]. The chemically similar NaCB$_{11}$H$_{12}$ and NaCB$_9$H$_{10}$ salts both exhibit noticeably lower respective T_{trans} values near or below room temperature. This leads to liquid-like ionic conductivities for NaCB$_{11}$H$_{12}$ (0.1 S/cm at 380 K) and NaCB$_9$H$_{10}$ (0.03 S/cm at 297 K) [3]. Recently, it has been shown that the order-disorder phase transition is suppressed in mixed-anion solid solutions combining nearly spherical (icosahedral) anions, such as [CB$_{11}$H$_{12}$]$^-$, and ellipsoidal (bicapped-square-antiprismatic) anions, such as [CB$_9$H$_{10}$]$^-$. These solid solutions retain the disordered state with high ionic conductivity down to low temperatures [4]. The mixed-anion solid solution Na$_2$(CB$_9$H$_{10}$)(CB$_{11}$H$_{12}$) shows the highest room temperature ionic conductivity (~0.07 S/cm) among all the studied Na-ion conductors.

In the work, we use ^{1}H and ^{23}Na NMR measurements of the spectra and spin-lattice relaxation rates over wide temperature ranges to compare the anion and cation motional parameters in the *closo*-hydroborate salts and the mixed-anion solid solution.

Experimental results

The proton and ^{23}Na spin−lattice relaxation rates (R_1^H and R_1^{Na}) measured at the resonance frequencies ω/2π = 14, 28 and 23 MHz for NaCB$_{11}$H$_{12}$ as functions of the inverse temperature are shown in Figure 1 (left). The general features of the observed behavior of R_1^H are typical of the relaxation mechanism due to nuclear dipole-dipole interaction modulated by thermally activated atomic motion. For this mechanism, the R_1^H maximum is expected to occur at the temperature, at which the atomic jump rate τ^{-1} becomes nearly equal to the resonance frequency ω. In the case of NaCB$_{11}$H$_{12}$, the relaxation rate maximum is not reached, and near 376 K we observe a 2 orders of magnitude drop of R_1^H accompanied by the change in the sign of temperature dependence of R_1^H and the disappearance of its frequency dependence. This behavior suggests a phase transition accompanied by an abrupt increase in the reorientational jump rate, so that in the high-T (HT) phase the jump rate τ^{-1} becomes much higher than 10^8 s^{-1}. For parametrization of the $R_1^H(T)$ data in the low-T (LT) phase of NaCB$_{11}$H$_{12}$, we have used the standard equation [1] that relates R_1^H and the jump rate τ^{-1},

assuming that the temperature dependence of τ^{-1} is governed by the Arrhenius law with the activation energy E_a. The results of this simultaneous fit to the experimental data in the range 278−376 K are shown by solid curves in Figure 1 (left). The corresponding motional parameters are $\tau_0 = 2.9\,(6) \times 10^{-14}$ s and $E_a = 409\,(7)$ meV. In the high-T phase of NaCB$_{11}$H$_{12}$, the activation energy determined from the slope of the $R_1^H(T)$ data is 177 (8) meV. The activation energies for Na$^+$ diffusion, E_a^d, estimated from the $R_1^{Na}(T)$ slopes are 327 (11) meV for the low-T phase and 152 (8) meV for the high-T phase. Thus, the transition to the high-T phase is accompanied by a strong decrease in the activation energy for cation diffusion. The values of the average activation energies of anions (CB$_{11}$H$_{12}$)$^-$ reorientational motion and cation Na$^+$ diffusion for NaCB$_{11}$H$_{12}$ are summarized in table 1.

The behavior of the proton and ^{23}Na spin-lattice relaxation rates measured for NaCB$_9$H$_{10}$ is shown in Figure 1 (right). For NaCB$_9$H$_{10}$ compound, the relaxation rate maximum is not reached, and between 278 and 287 K, we observe a sharp drop of R_1^H accompanied by the change in the sign of its temperature dependence. Furthermore, the measured relaxation rate above 287 K becomes frequency-independent. These features correspond to the "folding" of the $R_1^H(T)$ maximum due to the abrupt acceleration of anion reorientations at the phase transition. It is important to note that the phase transition occurs at a considerably lower temperature than that observed for NaCB$_{11}$H$_{12}$. Upon cooling, the $R_1^{Na}(T)$ data indicate the continuation of the disordered-phase behavior down to at least 283 K. For the ordered and disordered phases of NaCB$_9$H$_{10}$, the motional parameters of anions and cations are presented in table 1.

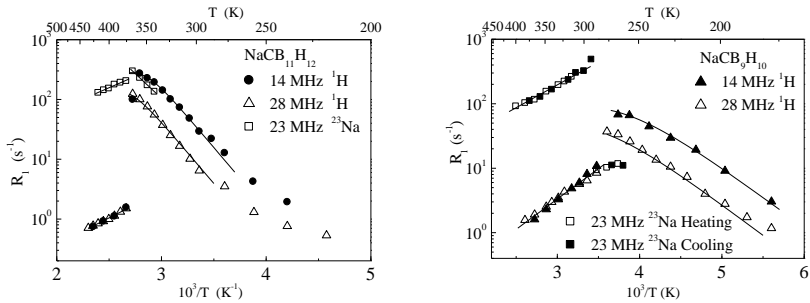*Figure 1. Proton spin-lattice relaxation rates measured at 14 and 28 MHz and ^{23}Na spin-lattice relaxation rates measured at 23 MHz for NaCB$_{11}$H$_{12}$ (left) and for NaCB$_9$H$_{10}$ (right) as functions of the inverse temperature.*

Solid-solution Na$_2$(CB$_9$H$_{10}$)(CB$_{11}$H$_{12}$) sample was prepared by drying the aqueous solution of equimolar amounts of NaCB$_9$H$_{10}$ and NaCB$_{11}$H$_{12}$. The dominant phase of Na$_2$(CB$_9$H$_{10}$)(CB$_{11}$H$_{12}$) has the hexagonal close-packed structure with the lattice parameters a = 6.991(1) Å and c = 11.339(2) Å. This phase is isomorphous to that found for the pristine superionic NaCB$_9$H$_{10}$ above ~310 K, but has a slightly larger unit cell. Figure 2 shows the behavior of the proton spin-lattice relaxation rate R_1^H and the ^{23}Na spin-lattice relaxation rate R_1^{Na} as functions of the inverse temperature. It can be seen that both $R_1^H(T)$ and $R_1^{Na}(T)$ exhibit peaks; however, these peaks are shifted with respect to each other. For parametrization of the $R_1^H(T)$ and $R_1^{Na}(T)$ data, we have used the simplest two-peak model assuming a coexistence of two jump processes. The results of the simultaneous fit at two resonance frequencies are shown by black solid lines in Figure 2. Data of the $R_1^{Na}(T)$ peak in Figure 2

reveals the presence of an inflection point at the low-T slope of this peak; this suggests a coexistence of two jump processes for Na^+ ions. Therefore, for parametrization of the $R_1^{Na}(T)$ data in the range 138–349 K we have used the two-peak model assuming a coexistence of two Na^+ jump processes: localized jump process with E_{a1}=156(5) meV and diffusion process E_a^d=353(11) meV. The value of the activation energy for Na^+ jumps diffusion estimated from the slope of the $R_1^{Na}(T)$ data above 350 K is 135(8) meV. The values of the average activation energies of anions reorientational motion and cation Na^+ diffusion are presented in table 1.

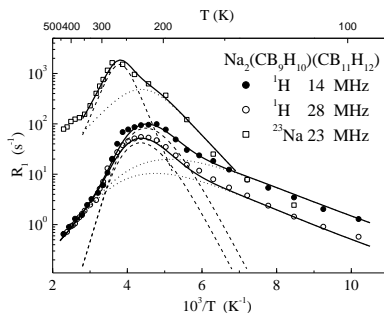*Figure 2. Proton spin-lattice relaxation rates measured at 14 and 28 MHz and ^{23}Na spin-lattice relaxation rates measured at 23 MHz as functions of the inverse temperature. Black solid lines show the simultaneous fit of the two-peak model with Gaussian distributions of the activation energies to the $R_1(T)$ data.*

Table 1. Average activation energies for anions reorientations and Na diffusion in NaCB$_{11}$H$_{12}$, NaCB$_9$H$_{10}$ and Na$_2$(CB$_9$H$_{10}$)(CB$_{11}$H$_{12}$).

Compound	E_a for anion reorientations (meV)	E_a^d for Na diffusion (meV)
NaCB$_{11}$H$_{12}$	409 (7) LT phase, 177 (8) HT phase	327 (11) LT phase, 152 (8) HT phase
NaCB$_9$H$_{10}$	234(8) LT phase, 205(7) HT phase	153 (7) HT phase
Na$_2$(CB$_9$H$_{10}$)(CB$_{11}$H$_{12}$)	147 (9), 430(40)	353 (11), 135(8)

Acknowledgments

References

1. V. Soloninin, M. Dimitrievska, R. V. Skoryunov, O. A. Babanova, A. V. Skripov, W. S. Tang, V. Stavila, S. Orimo, T. J. Udovic. – *J. Phys. Chem. C,* 121, 1000-1012 (2017).
2. V. Skripov, R. V. Skoryunov, A. V. Soloninin, O. A. Babanova, W. S. Tang, V. Stavila, T. J. Udovic. – *J. Phys. Chem. C,* 119, 26912−26918 (2015).
3. W. S. Tang, M. Matsuo, H. Wu, V. Stavila, W. Zhou, A. A. Talin, A. V. Soloninin, R. V. Skoryunov, O. A. Babanova, A. V. Skripov, A. Unemoto, S. Orimo, T. J. Udovic. – *Adv. Energy Mater.,* 6, 1502237 (2016).
4. V. Soloninin, R. V. Skoryunov, O. A. Babanova, A. V. Skripov, M. Dimitrievska, T. J. Udovic. – *J. Alloys Compd.,* 800, 247-253 (2019).

Investigation of the mutual influence of NH·N hydrogen bonds in heterodimers of substituted diaminopyridines by means of quantum chemistry

Anna A. Titova, Elena Yu. Tupikina
Institute of Chemistry, Saint Petersburg State University, Saint Petersburg, Russia
E-mail: aatitova1210@gmail.com

Introduction

Non-covalent interactions are very important for modern design of supramolecular materials with adaptive properties, for example, recovering ability and adaptability. Multiple hydrogen bonds connect proton-donor and proton-acceptor fragments and, unlike single hydrogen bond, such system include cooperative (enhancing) and anti-cooperative (weakening) effects – mutual influence of bonds on each other. So, it's necessary to estimate these effects and consider influence of substituents [1,2]. It can be done systematically using, for example, quantum chemical calculations.

Model systems

In this work we investigate the geometry and NMR parameters of a system with three NH···N hydrogen bonds within a combination DAD-ADA (Figure 1, where D – proton donor, A – proton acceptor) – heterodimers of diaminopyridines with various electron withdrawing and electron donating substituents – by means of quantum chemistry.
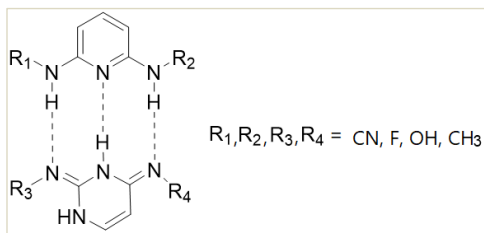
Figure 1. Investigated heterodimers with three hydrogen bonds DAD-ADA and different substituents

Methods

Calculations were performed with Gaussian16 software at B3LYP/6-311G++G(d,p) level and with empirical dispersion correction (GD3BJ). Monomers and dimers of diaminopyridines were optimized, in all structures there were no imaginary frequencies. NMR parameters were calculated at the same of level of theory using GIAO approach.

References

1. Tupikina, E. Y., Denisov, G. S., & Tolstoy, P. M. (**2019**). Anticooperativity of FH···Cl⁻ hydrogen bonds in [(FH)$_n$Cl]⁻ clusters (*n*= 1… 6). Journal of Computational Chemistry, 40 (32), 2858-2867.
2. Grabowski, S. J. (**2013**) Cooperativity of hydrogen and halogen bond interactions. *Theor. Chem. Acc.* **132**, 1–10

The state of concomitant water in system "ionic liquid - aluminum salt"

Milosh Ubovich, *Vladimir V. Matveev*, *Vladimir I. Chizhik*
Faculty of Physics, Saint-Petersburg State University, Russia
E-mail: v.matveev@spbu.ru

Introduction

Liquid electrolytes based on solutions of aluminum salts in ionic liquids (ILs) are considered as promising systems for metal-ion batteries of the next generations. The presence of water may have a negative effect on the properties of electrochemical devices; in particular, it may narrow the electrochemical window. Concomitant (residual) water may appear during the preparation of electrolytes and in some cases it cannot be removed using standard laboratory methods. For example, it was previously shown that standard dehydration procedures were not effective in the removal of water from the aluminum solvation shell in the solutions of $Al(NO_3)_3$ in the ionic liquid "ethylammonium nitrate" (EAN) [1, 2]. At the same time, according to the standard Fisher test, these systems manifest themselves as practically anhydrous, i.e. this test does not detect the water contained in the first solvation shell of the aluminum ion. The objective of this work is to clarify the state of water in an electrolyte based on aluminum salts. The ultimate goal is to find ways to remove or at least reduce the water content in such systems.

Experimental

The sample was prepared using crystalline hydrate $AlCl_3 \cdot 6H_2O$ and ionic liquid [bmim]Cl. Both neat IL and the solution were undergone the standard drying procedure under low pressure ($\approx 10^{-6}$ mbar) and 80 °C but as expected it could not remove the water completely. Therefore, after preparing the sample by gravimetric method the water concentration was verified using integral intensities of the ^1H spectral lines of $[bmim]^+$ and water. As a result, we have determined the following molar ratios for the $AlCl_3 – [bmim]Cl – H_2O$ mixture: 1 Al^{3+}: 5.7 $[bmim]^+$: 7.5 H_2O.

NMR measurements were carried out using Bruker Avance III 500 MHz Spectrometer at 500 MHz for ^1H nucleus and 130 MHz for ^{27}Al one. The examples of spectra are provided in Fig. 1 and 2. We used temperature range between 313 and 363 K.

All NMR measurements were carried out in the Center for Magnetic Resonance of Research Park of Saint Petersburg State University.

Results

Based on the obtained spectra of ^1H and ^{27}Al nuclei, it was concluded that in the studied electrolyte system, water molecules are located in the vicinity of aluminum cations and appear in two nonequivalent structures. The important information is the existence of exchange between these substructures, and the exchange rate can be estimated from the obtained proton spectra. It has also been established that with temperature variation, the concentration of these substructures changes (on the background of the exchange process). Some features of the spectra of quadrupole nuclei ^{27}Al, in particular, of the spectral line width (Fig. 3), allow us to conclude that the symmetry of the environment of aluminum cations has changed with temperature. It is worth noting that the ^{27}Al line in the sample investigated is at least three times broader than the lines in $Al(NO_3)_3$ solutions in EAN or water, see [2], and this fact might be an indirect indication of the partial penetration of the Cl^- ion into the first solvation shell of the Al^{3+} cation.
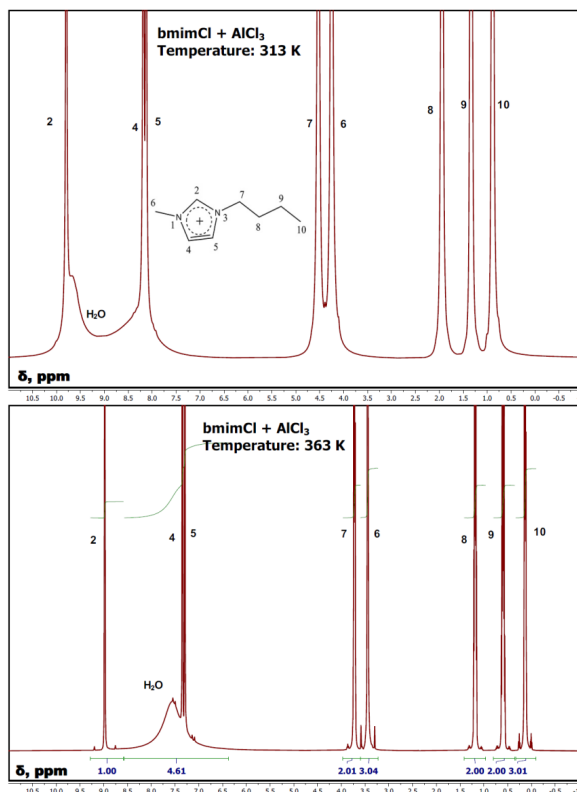
Figure 1. Examples of ^{1}H spectra in the 1m $AlCl_3 \cdot 6H_2O$ solution in [bmim]Cl.
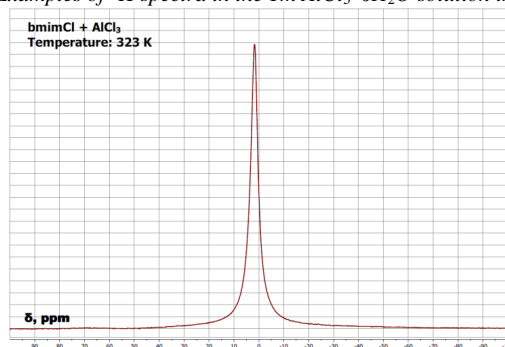
Figure 2. ^{27}Al spectrum of 1 m $AlCl_3 \cdot 6H_2O$ solution in [bmim]Cl ionic liquid at 323 K
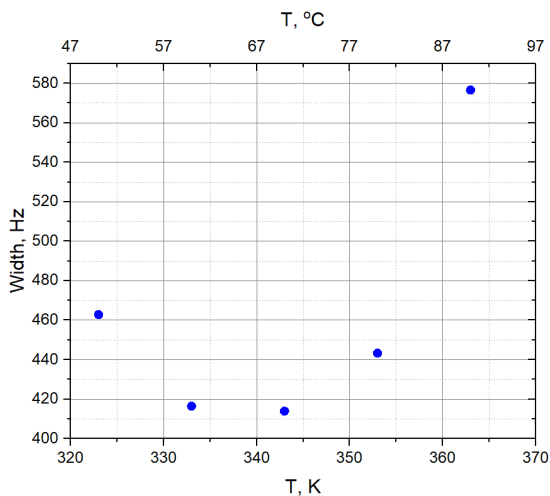
Figure 3. The temperature dependence of the linewidth of ^{27}Al nuclei signal in 1 m $AlCl_3·6H_2O$ solution in [bmim]Cl

Acknowledgments

References

1. Matveev V.V., Ievlev A.V., Vovk M.A., et al. – J. Mol. Liq. 2019. V. 278. P. 239.
2. Matveev V.V., Ievlev A.V., Šoltésová M., et al. – Magn. Reson. Chem. 2021. V. 60. No. 2. p.221.

Polarization dependence of the ODMR spectrum of spin 3/2 vacancy centers in 6H and 15R silicon carbide polytypes

Veyshtort I.P.[1,2], *Skomorokhov A.M.*[1,2]
[1]Ioffe Institute, St. Petersburg 194021, Russia
[2]Laboratory for Diagnostics of Carbon Materials and Spin-Optical Phenomena at Wide-Bandgap Semiconductors, Northern (Arctic) Federal University, Arkhangelsk 163002, Russia
E-mail: igorveyshtort@gmail.com

Introduction

In the last decade, the use of individual defects - vacancies - for quantum computing has become increasingly relevant. It is in this application that the spin centers with spin 3/2 in silicon carbide are an interesting object, which silicon atom vacancies are occupying a certain crystalline position, on which the characteristics of the center depend. It is known that silicon carbide crystallizes in a variety of polytypes, each of which has its own crystal structure.

Silicon vacancies with spin 3/2 were considered. The emission of light along and across the hexagonal crystallographic axis (c-axis) of the 15R-SiC crystal was studied, by analogy with the studies revealed in [1]. The difference between the optical collision of V centers in the 6H and 15R polytypes is studied.

Sample

Sample of silicon carbide 15R-SiC crystal was studied (fig. 1.a). Crystal had a natural isotopic concentration.
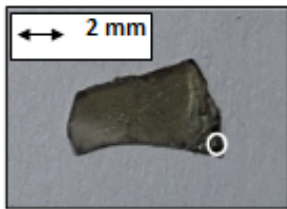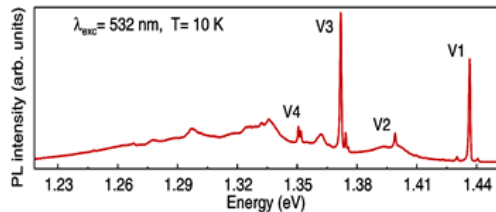
a   *b*
Figure 1. 15R-SiC sample photo (a), low-temperature PL spectra of 15R-SiC sample (b) [2]

Structure of V-centers

The object of the study is negatively charged silicon vacancy centers in SiC. The energy structure of the centers consists of ground and excited states. The principle of the ODMR method lies in the optical change in the difference between the populations of the energy levels of the center due to the action of laser radiation. In this case, transitions through a certain metastable state are induced, as a result of which the populations of the levels of the ground state change. The application of an electromagnetic field of a certain frequency equalizes the population of the levels.

The spin Hamiltonian describes the spin levels: the first term is responsible for the splitting in an external magnetic field, and the second is the splitting of the fine structure of the spin center in an axial crystal field:

$$H = g\mu_B B \cdot S_z + D[S_z^2 - (1/3)S(S + 1)],$$

where g – factor, μ_B - Bohr magneton, B – magnetic field induction, S_z - spin moment projection, D - fine structure splitting, S - spin of center. The values of the fine structure

parameter and the energies of zero phonon lines for the studied types of centers are given in the table (fig. 2).

Scheme of the experiment

Fig. 2 shows optical-electrical scheme of experimental stand. The arrows indicate the wired connections of the devices. The red lines represent the course of the laser beam and the collected luminescence. Focusing on the sample is done with a confocal microscope. Registration is carried out in an asynchronous mode.
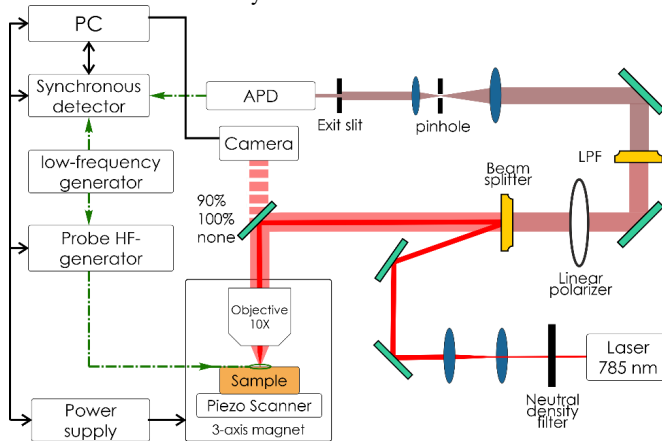

Figure 2. Experimental setup

Experimental data

Turning to the experimental data, let us turn to the PL spectra for 15R. When collecting photoluminescence along the z-axis (n-plane), the spectrum is preserved when the polarizer is rotated by 90 degrees (fig. 4.a). The observed slight increase for the n-plane is due to deviations in crystal orientation. In turn, when collecting from the side face (m-plane), a significant decrease in the level of photoluminescence is observed (fig. 4.b).

Diagram 5 shows the angular dependences of the integral photoluminescence. The cumulative radiation with the m-plane has a clearly visible polarization. Which allows us to conclude that there is splitting in the excited state.

Figure 4 shows the angular dependences of the integral values of individual ODMR lines in both orientations. Incomplete ODMR polarization for the V2 center in 15R is observed for the m-plane. In addition, there is a mixing of polarizations, presumably caused by a local deviation of the z axis from the growth plane of the crystal. A similar result was obtained for the center V3. In turn, the V4 center in the 15R polytype has a completely unpolarized emission.

Results

As a result of the work, the polarization of the PL and ODMR spectra of various centers in the 15R silicon carbide polytype was studied. The effects of different polarizations of radiation from the centers in specific directions for the V2 and V3 centers, as well as the absence of polarization for the V4 center, are found. The presence of a split VS was demonstrated. The results obtained allow us to conclude that it is similar to 6H. However, the differences in the crystal structure necessitate the development of our own theoretical substantiation of the result. The observed polarization effects of radiation make it possible to

a *b* *c*
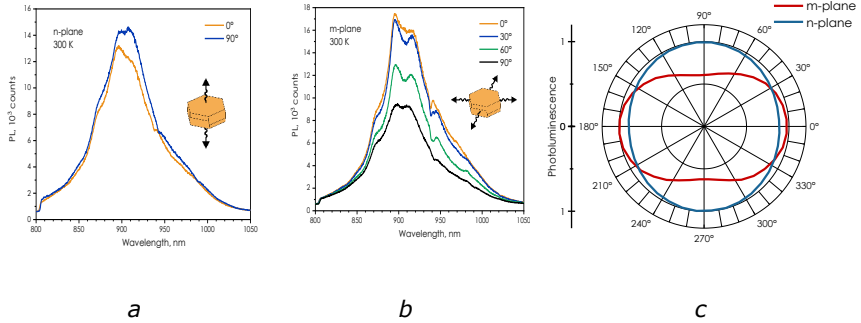
Figure 3. PL spectra for different polarization angles in the n-plane (a) and m-plane (b) orientations. Angular dependences of the integral PL (c)
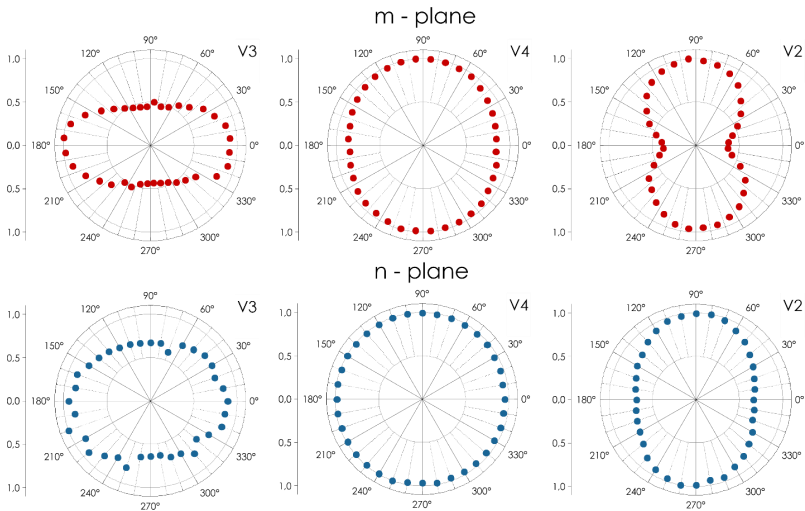
Figure 4. Angular dependences of integral values of ODMR lines for all orientations and centers in 15R-SiC

Draw a preliminary conclusion about the possibility of realizing spin-photon quantum entanglement on the basis of these centers.

Acknowledgments

References

1. Inverted fine structure of a 6H-SiC qubit enabling robust spin-photon interface. I.D. Breev, Z. Shang, A.V. Poshakinskiy et al, NJP Quantum Information 8, 23 (2022).
2. Soltamov V. A. et al. Physical review letters. – 2015. – Т. 115. – №. 24. – С. 247602.

Hydrogen pulverization of metallic cobalt observed by ^{59}Co Internal Field NMR of Co-Zr cermet precursor

Ilya V. Yakovlev[1], Serguei F. Tikhov[1], Olga B. Lapina[1]
[1]*Boreskov Institute of Catalysis, Novosibirsk, Russia*
E-mail: iv_yakovlev@catalysis.ru

Cobalt-zirconium alloys and intermetallic compounds are widely used as magnetic materials, hydrogen storage materials, active gas adsorbers and heterogeneous catalysts. Such binary compounds are often produced by the technique of mechanochemical activation inside high-energy ball mills. This process leads to alteration of the phase composition, defect concentration, particle size and morphology of treated powders. Mechanochemical activation is one of the prospective methods for synthesizing precursors of bulk ceramometal (cermet) catalysts that possess the qualities of both ceramic and metal compounds, which make them mechanically durable and highly heat-conductive. These properties of cermets are especially important in such exothermic processes as Fischer-Tropsch synthesis. The downside of mechanochemical activation is that the resulting powder possesses a very low specific surface area ~ 1 m^2/g, which leads to insufficiently high specific activity of the resulting catalyst. One of the proposed techniques for increasing the activity of such bulk heterogeneous catalysts is high-pressure hydrogen treatment, which was shown to increase the activity of intermetallic bulk catalysts [1, 2]. However, there were no detailed studies of the structural and morphological effects of such hydrogen treatment to explain the increased catalytic activity.

Here, we use the technique of ^{59}Co Internal Field NMR (^{59}Co IF NMR) to investigate the effect of mechanochemical activation and subsequent high-pressure hydrogen treatment on the structure of cobalt nanoparticles in an equiatomic mixture of Co and Zr powders. This technique provides various data on the crystalline and magnetic structure of the studied material as well as its morphology. Over the years, ^{59}Co IF NMR has proven to be an efficient tool for investigation of the structure of various structures of cobalt including bulk Co metal, Co alloys and intermetallic compounds.

In this work, we demonstrate the appearance of small single domain nanoparticles of cobalt that occurred after the high-pressure hydrogen treatment according to ^{59}Co IF NMR data and connect with the increase in specific surface area of the sample. Moreover, this technique has proven to be indispensable in our case since other conventional techniques such as transmission electron microscopy or X-Ray diffraction were not able to detect any changes in the sample after the hydrogen treatment.

Acknowledgments

References

1. Lunin, V.V.; Solovetskii, Y.I. Formirovanie Aktivnoi Poverhnosti Katalizatorov Na Osnove Gidridov Intermetallidov Zr i Hf s Ni, Co i Fe. *Kinet. Catal.* 1985, *24*, 694–698. (In Russian)
2. Lunin, V.V.; Chetina, O.V. Vliyanie Okislitelno-Vosstanovitelnih Processov v Sisteme Intermetallid-Oksid Na Adsorbtsiyu Vodoroda. *Zhurnal Fiz. Him.* 1990, *64*, 3019–3023. (In Russian)

Engineering the Exchange Spin-Waves in Graded Thin Ferro-magnetic Films

Igor Yanilkin[1,2], Amir Gumarov[1,2], Igor Golovchanskiy[3,4], Bulat Gabbasov[1,2],
Roman Yusupov[1], Lenar Tagirov[1,2],

[1]*Kazan Federal University, 420008 Kazan, Russia*
[2]*Zavoisky Physical-Technical Institute, FRC Kazan Scientific Centre of RAS, 420029 Kazan, Russia*
[3]*National University of Science and Technology «MISiS», 119049 Moscow, Russia*
[4]*Moscow Institute of Physics and Technology, 141701 Dolgoprudny, Russia*
E-mail: yanilkin-igor@yandex.ru

Introduction

Nowadays, spin waves are studied intensely in thin ferromagnetic films and heterostructures. In the majority of the reports, homogeneous films or magnonic crystals with a homogeneous periodic structure are investigated. However, the studies of the spin waves in films with artificially created inhomogeneity of magnetic properties across the thickness, known in the literature as graded magnetic materials, have been performed mostly in theory. This work aimed at the experimental investigation of the possibility to engineer the spin wave spectra by means of controlling a magnetic property profile in graded films of Pd-Fe alloy.

Deposition technique

The synthesized collection of epitaxial Pd-Fe alloy films with variable distribution profiles of a composition across the thickness included films with linear, step-like, Lorentzian, Sine, and Cosine film profiles with thicknesses in the range of 50-400 nm [1, 2]. The high-purity (99.95 %) Pd and Fe metals were evaporated from the effusion cells and deposited to a rotating (001) MgO single-crystal substrate. The entire synthesis process was carried out under ultrahigh vacuum ($5 \cdot 10^{-10}$ mbar) in the molecular beam epitaxy (MBE) chamber manufactured by SPECS GmbH. The iron concentration profile in the palladium matrix was realized by a controllable variation of the iron evaporation cell temperature with a fixed palladium cell temperature.

Experimental results

Figure 1 clearly demonstrates the possibility of manipulating the standing spin wave spectrum in thin film structures by varying the magnetization profile.

Analysis of the standing spin wave spectra provided the following common parameters for the ferromagnetic Pd-Fe films: the normalized exchange stiffness constant $D=16$ T·nm^2, the surface pinning coefficient $\alpha_s=-0.05$, the skin layer depth $\sigma_f=170$ nm and the ratio of the effective magnetization to saturation magnetization $M_{eff}/M_s=1.35$. The obtained results indicate that the approach suggested and realized in this work can be applied to engineer the spin waves dispersion in graded ferromagnetic films.
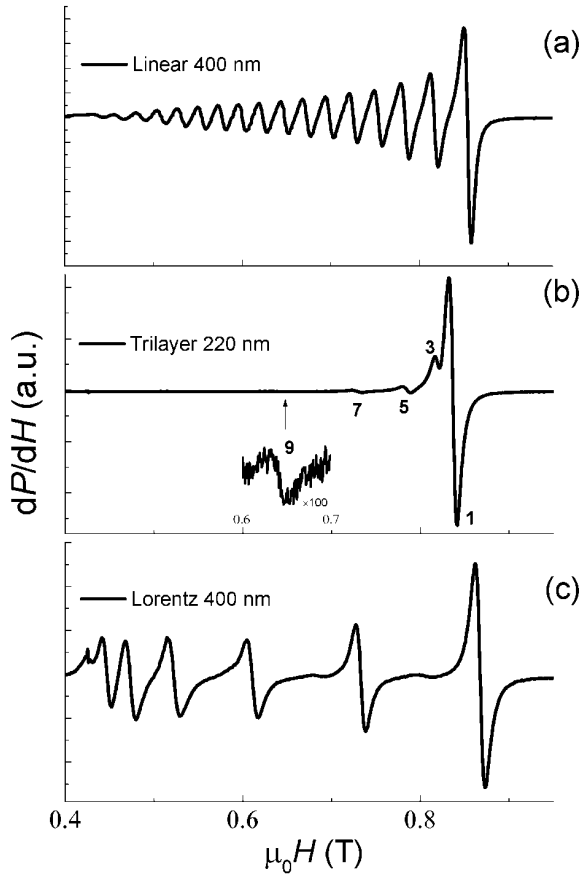
Figure 1. Experimental standing spin-waves resonance spectra of the samples with linear (a), step-like (b) and Lorentz (c) iron distribution at T = 20 K

Acknowledgments

References

1. I.V. Yanilkin et. al. – *Phys. Rev. Mat.*, 6(6), 064406(8) (2022).
2. I.V. Yanilkin et. al. – *Nanomaterials*, 12(24), 4361(12) (2022).

An EPR study on the radiolysis of isolated ethanol molecules in solid argon and xenon: matrix control of radiation-induced generation of radicals in cryogenic media

Pavel V. Zasimov[1], Elizaveta V. Sanochkina[1], Daniil A. Tyurin[1], and Vladimir I. Feldman[1]
[1]Department of Chemistry, Lomonosov Moscow State University, 119991 Moscow, Russia
E-mail: bulgacov2012@yandex.ru

Ethanol (C_2H_5OH) is one of the most important organic molecules widely occurring in different environments on Earth [1] and in the interstellar medium (ISM) [2]. It is believed that this molecule can play a very important role in the formation of interstellar complex organic molecules (iCOMs). In particular, the radiation-induced chemistry of C_2H_5OH in the ISM may lead to a variety of ethers and esters, [3] as well as other iCOMs essential for the origin of life. Thus, the mechanism of ethanol transformation induced by high-energy radiation in icy media of various compositions is of great interest to prebiotic astrochemistry.

Despite the number of studies [4, 5], there are significant gaps in understanding molecular mechanisms of the ethanol transformations induced by radiation of different energy in cold rigid media remain. In particular, the contribution of the primary and secondary processes to the radiation chemistry of ethanol molecules in various media is not fully clear. These issues may be partially resolved using matrix isolation studies with the detection of paramagnetic species by electron paramagnetic resonance (EPR) spectroscopy [6]. In the present work, we focused on the investigation of the radiation-induced transformations of ethanol molecules isolated in solid noble gas matrices (Ar and Xe) at cryogenic temperatures.

Matrix samples were obtained by deposition of gaseous mixtures (CH_3CH_2OH/Ng and CH_3CD_2OH/Ng 1/1000; Ng = Ar or Xe) onto a sapphire rod mounted in a closed-cycle helium cryostat [6]. Complementary experiments were carried out with the addition of Freon-11 ($CFCl_3$) as an electron scavenger. The deposited matrices were irradiated with X-rays (effective energy ca. 20 keV) at 7 K. The EPR spectra were recorded using an X-band (9.4 GHz) spectrometer (SPIN, Russia) with a 100 kHz high-frequency magnetic field modulation and appropriate microwave power (from 10 to 300 µW).

The results of the matrix isolation experiments [7] demonstrate that the radiolysis of ethanol molecules isolated in solid argon mainly leads to the C−C bond cleavage leading to the formation of $CH_3^•$ (methyl) and $HCO^•$ (formyl) radicals. At the same time, the dominant product of ethanol radiolysis in a Xe matrix is α-hydroxyethyl radical ($CH_3^•CHOH$). The α-hydroxyethyl radicals adopt a specific rigid conformation with a non-rotating methyl group at low temperatures, which is an unusual effect for neutral $CH_3^•CHX$ species, and exhibit free rotation in solid xenon only at ca. 65 K. The experiments with the selectively deuterated ethanol (CH_3CD_2OH) provide solid indirect evidence for the primary formation of the ethoxy radical ($CH_3CD_2O^•$) as a result of O−H bond cleavage, which converts to the α-hydroxyethyl radical due to isomerization occurring at 7 K. The observed effect of a matrix (Ar and Xe) on the occurring radiation-induced transformations was explained based on the significant role of "hot" ionic fragmentation and inefficient energy dissipation to medium in the case of Ar. The implications of the obtained results are discussed.

Acknowledgments

References

1. W. V. Kirstine, I. E. Galbally. – *Atmos. Chem. Phys.*, 12 (1), 545–555 (2012)

2. Bergantini, P. Maksyutenko, R.I. Kaiser. – *Astrophys. J.*, 841 (2), 96 (2017).
3. S.B. Charnley, M.E. Kress, A.G.G.M. Tielens, T.J. Millar. – *Astrophys. J.*, 448, 232–239 (1995).
4. G.R. Freeman. – Radiation chemistry of ethanol: A review of data on yields, reaction rate parameters, and spectral properties of transients, *National Standard Reference Data System*, 1974.
5. C. von Sonntag, H.P. Schuchmann. – in *Advances in Photochemistry* (eds. J. N. Pitts Jr., G.S. Hammond, K.Gollnick), John Wiley & Sons, Inc, pp. 59–145 (1977).
6. V.I. Feldman. – in *Application of EPR in Radiation Research* (eds. A. Lund, M. Shiotani), Springer, pp. 151–188 (2014).
7. P.V. Zasimov, E.V. Sanochkina, D.A. Tyurin, V.I. Feldman. – *Phys. Chem. Chem. Phys.*, 2023, https://doi.org/10.1039/D2CP05356J.

Electrophoretic NMR assembly

Extending the capability of conventional NMR instruments

P&L
Scientific

$$\mu = \frac{\phi}{\gamma \delta g \Delta_E E} \qquad z = \frac{\mu k_B T}{De}$$
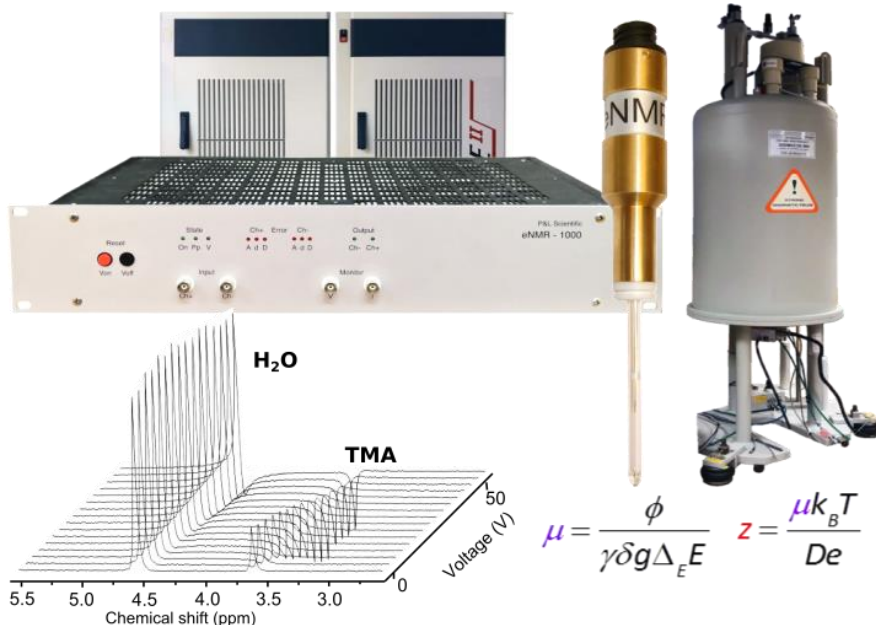
The electrophoretic mobility and the effective charge can be obtained by recording the variation of spectral phase by increasing electric field

Key features

- Well-established scientific background and proven technology
- Operates as add-on for any conventional NMR spectrometer and probe with gradient; requires no additional hardware or software
- Advanced sample cell and RF filter system
- Straightforward embedding of high voltage pulse generation in conventional NMR pulse programs
- Probe and user protection system

info@plscientific.se

Specifications

Output voltage:	0 to ±1000 V
Digital To Analogue converter size:	2×12 bit
Output current	
at ±1000 V:	0 to ±100 mA
at ±500 V:	0 to ±200 mA
Output power:	
Peak power	300 W
Mean power	30 W
Minimum/maximum pulse length:	500 µs / 1 s
Duty cycle:	30 %
Output pulse shapes:	Rectangular
Slew rate:	Greater then 25 V / µs
Settling time (to 2%):	Less than 200 µs for 2 kV step
Stability	
Drift with time	Less than 200 ppm/hr, noncumulative
Drift with temperature	Less than 300 ppm/°C
RF Filters	10 MHz low pass
Power consumption:	80 W for 220 V AC
Dimensions of the main unit:	430×340×90 (fits in standard 19'' rack); weight - 8 kg
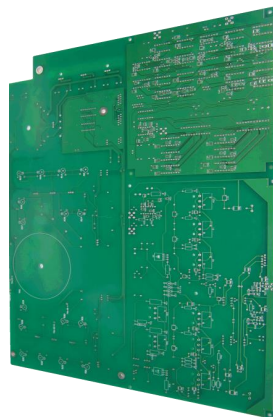
Selected applications

Physical chemistry – ion pairing and association in simple and complex (polyelectrolytes) ionic mixtures.

Batteries and fuel cells - chemically selective measurement of ionic migration.

**Biochemistry** – biomolecular charge and association.

Analytical chemistry – electrophoretic analysis of complex ionic mixtures

Pharmaceutical chemistry – release and association of charged drugs

Metallorganic chemistry – the structure of supramolecular complexes from the observed charge

info@plscientific.se

2D electrophoretic mobility spectroscopy (2D MOSY) based on eNMR

Extending the power of 2D NMR spectroscopy
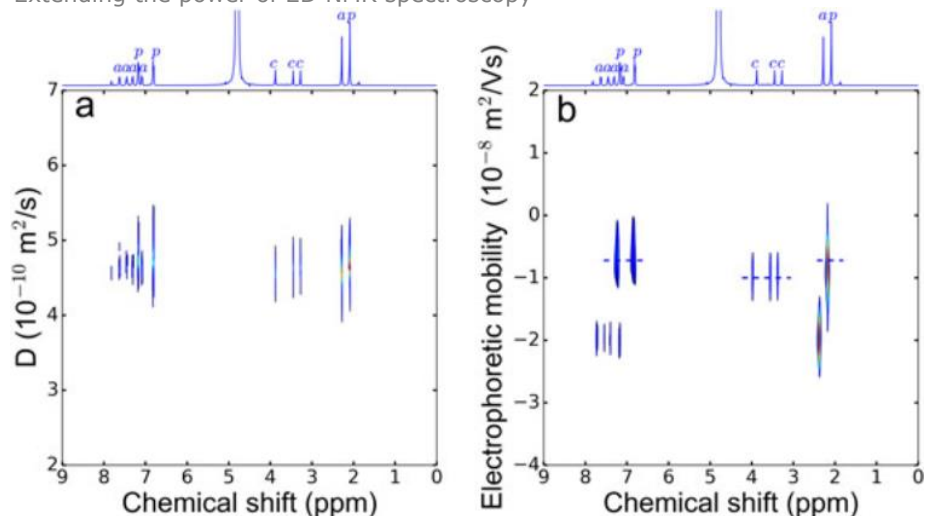
Direct comparison of 2D DOSY (a) and 2D MOSY (b) experiments for a dissolved Thomapyrin® tablet clearly illustrates the superior performance of the 2D MOSY in selection of the different species

Selected articles for eNMR applications

Y. Fang, P.V. Yushmanov, and I. Furó, Assessing 2D electrophoretic mobility spectroscopy (2D MOSY) for analytical applications, Magn. Reson. Chem. 55 DOI: 10.1002/mrc.4558 (2017).

E. Bialik, B. Stenqvist, Y. Fang, Å. Östlund, I. Furó, B. Lindman, M. Lund, and D. Bernin, Ionization of cellobiose in aqueous alkali and the mechanism of cellulose dissolution, J. Phys. Chem. Lett. 7 5044-5048 (2016).

M. Giesecke, F. Hallberg, Y. Fang, P. Stilbs, and I. Furó, Binding of monovalent and multivalent metal cations to polyethylene oxide in methanol probed by electrophoretic and diffusion NMR, J. Phys. Chem. B 120 10358−10366 (2016).

M. Bielejewski, M. Giesecke and I. Furó, On electrophoretic NMR. Exploring high conductivity samples, J. Magn. Reson. 243 17-24 (2014).

L. Patel, O. Mansour, M. Crossman, P. Griffiths, Electrophoretic NMR characterization of charged side chain cationic polyelectrolytes and their interaction with the anionic surfactant, sodium dodecyl sulfate, Langmuir 2019, 35, 28, 9233-9238

info@plscientific.se

Our NMR services

Repair and modification of the NMR spectrometers and hardware components

- RF amplifiers
- Gradient units
- Synthesizer and SGU 400 - 1000 boards
- Power supplies and shim system
- Temperature and MAS controllers

Repair of the NMR probes:

- Solving arcing problems; bad sensitivity and RF tuning/matching
- Replacing broken glass and ceramics in the probe body
- Repairing certain gradient coils in diffusion and high-resolution probes
- Repair of MAS probes; arcing and spinning problem
- Repair of probe accessories for temperature control
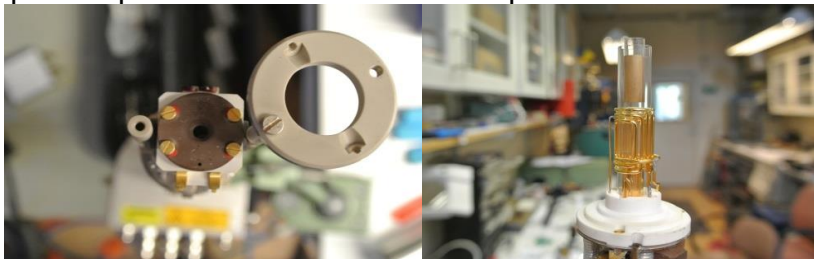
Modification of the NMR probes

- Adaptation of an existing NMR probe to a different spectrometer or NMR frequency.
- Change of RF coil position and configuration
- Adaptation of temperature control components and connectors
- Change of body geometry, dimensions and mounting
- Modification NMR inserts used in several diffusion NMR probes (like Bruker Diff30) to different frequency or double-tuned configuration

Poster Session

Homo- and heteronuclear NMR spectroscopy experiments in studying structure of 3-bromo-3-nitro-1-phenylprop-2-en-1-one

Adyukov I.S., Pelipko V.V., Baichurin R.I., Makarenko S.V.
Herzen State Pedagogical University of Russia, Department of Organic Chemistry,
Laboratory of Nitrocompounds, Center of collective use at the Faculty of Chemistry
"Instrumental methods for the study of nitro compounds, coordination, biologically active substances and nanostructured substances" 48 Moyka River Embankment, Saint Petersburg 191186, Russia
*E-mail:* kohrgpu@yandex.ru
http://kohrgpu.ru, http://ckpo.herzen.spb.ru/?page=organic-chemistry

3-Bromo-3-nitro-1-phenylprop-2-en-1-one **1** is a representative of highly reactive β-functionalized nitroalkenes, that we synthesized according to a literature method [1].

This compound **1** could possibly exist in form of *E*- or *Z*-isomers (C=C) and *s-cis* or *s-trans* conformational isomers (C=O, C=C) which make it an attractive structure for studying by 1D and 2D NMR spectroscopy methods.

The goal of this study was to determine the fine structure of 3-bromo-3-nitro-1-phenylprop-2-en-1-one **1** based on NMR spectroscopy data.
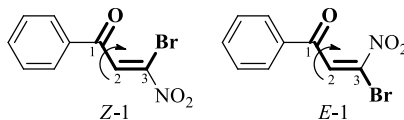
One set of signals in ^{1}H NMR spectrum indicated that compound **1** is stereochemically homogeneous in CDCl$_3$ solution. The C^{2}H proton signal appears as a singlet at 8.49 ppm in the ^{1}H NMR spectrum of bromonitropropenone **1**, and the aromatic ring protons signals appear as multiplets in the ranges of 7.53-7.57 ppm (H^m), 7.67-7.70 ppm (H^p), and 7.94-7.96 ppm (H^o) respectively (Fig. 1). The ^{13}C-{^{1}H} NMR spectrum also contains one set of signals for all structural fragments (Fig. 2).
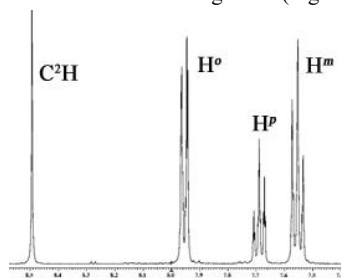
*Figure 1. ^{1}H NMR spectrum of **1** (CDCl$_3$)*
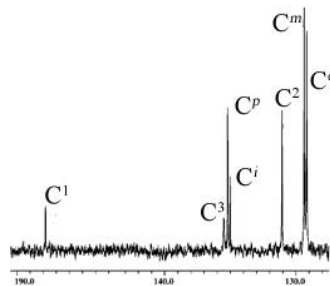
*Figure 2. ^{13}C NMR spectrum of **1** (CDCl$_3$)*

Signals assignment in ^{13}C-{^{1}H} NMR spectra of bromonitropropenone 1 was made by using both ^{1}H-^{13}C HMQC and ^{1}H-^{13}C HMBC experiments. The ^{1}H-^{13}C HMQC spectrum (Fig. 3) revealed cross-peaks between C^{2}H proton signal (8.49 ppm) and carbon atom signal at 131.06 ppm, as well as between signals of aromatic protons H^o (7.94-7.96 ppm), H^p (7.67-7.70 ppm), and H^m (7.53-7.57 ppm) and carbon atoms at 129.18, 135.19, and 129.36 ppm, respectively. The assignment of quaternary carbon atoms signals was based on ^{1}H-^{13}C HMBC experiment results. Specifically, in the ^{1}H-^{13}C HMBC spectrum of compound **1** (Fig. 4), the C^{2}H proton signal (8.49 ppm) formed a single cross-peak with the carbon atom at

135.49 ppm (C^3), while the signal of aromatic ring ortho-protons (7.94-7.96 ppm) showed cross-peaks with the carbon atoms at 178.81 ppm (C^1=O) and 135.00 ppm (C^i).
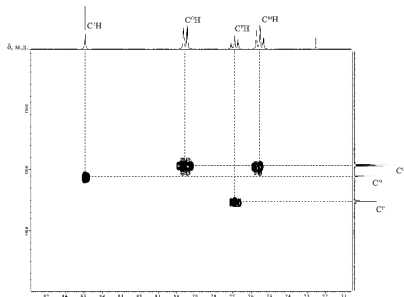
*Figure 3. ^1H-^{13}C HMQC spectrum of **1** (CDCl₃)*
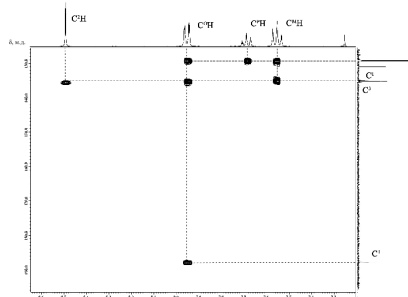
*Figure 4. ^1H-^{13}C HMBC spectrum of **1** (CDCl₃)*

Studying compound 1 by ^1H-^{15}N HMBC method revealed that the nitrogen atom of nitro group corresponds to a signal at -16.3 ppm that forms a cross-peak with a C^2H proton signal (8.49 ppm) which correlates with a literature data [2].

Furthermore ^1H-^1H NOESY experiment (Fig. 5) showed that C^2H and Ho proton signals exhibit a NOE effect, indicating their proximity in space and hence s-cis configuration of the C=C and C=O bonds in the molecule.
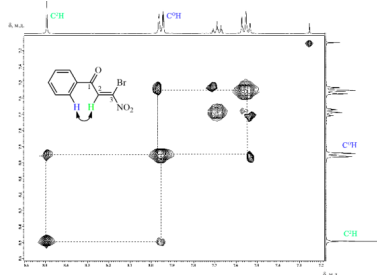
*Figure 5. ^1H-^1H NOESY spectrum of **1** (CDCl₃)*
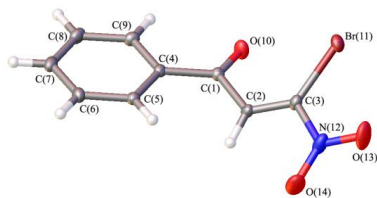
*Figure 6. X-ray analysis of **1***

Assumption about a structure of studying molecule that we had made above is strongly supported by the results of X-ray structural analysis, which prove that compound **1** has a Z-*s-cis* configuration (Fig. 6).

Therefore, by utilizing homo- and heterocorrelation experiments of NMR spectroscopy in studying 3-bromo-3-nitro-1-phenylprop-2-en-1-one **1** allowed a reliable assignment of atoms signals in ^1H, ^{13}C, and ^{15}N NMR spectra, and establish *s-cis* configuration of the molecule.

Acknowlegments

References

1. Choudhury A. R., Manna M. S., Mukherjee S. *Chem. Sci.*, 2017, *8*, 6686-6690.
2. Kuritsyna M.A., Pelipko V.V., Kataeva O.N., Baichurin R.I. et al. *Rus. Chem. Bull.,* 2021, *70*, 1605-1612.

Analysis of thermodynamics properties of Fe(II) spin-crossover complexes by the 1H chemical shifts analysis

<u>*Dmitry Yu. Aleshin*</u>[1], *Alexander A. Pavlov*[1,2], *Igor. A. Nikovskiy*[1], *Yulia V. Nelyubina*[1,2]

[1]*A.N. Nesmeyanov Institute of Organoelement Compounds of Russian Academy of Sciences, Moscow, 119334, Vavilova, 28, Russian Federation*

[2]*Bauman Moscow State Technical University, 105005, 2nd Baumanskaya Str., 5, Moscow, Russia*

E-mail: <u>dima.aleshin26@gmail.com</u>

Introduction

Molecular switches are compounds that can exist in several forms. One of the representatives of this class are spin-transition complexes of 3d-metals, in which switching occurs between two states with different spins. A number of methods are commonly used to study the spin state in solution, typically UV-Vis spectroscopy and nuclear magnetic resonance spectroscopy. In the method of nuclear magnetic resonance, the study of the magnetic susceptibility of a paramagnetic complex in the solution (Evans method) is quite widely used, but it has a high error and cannot be used to accurately determine the enthalpy and entropy of spin transition. Another method is based on the analysis of chemical shifts, but it is necessary to have the temperature dependence of the chemical shift of protons of a high-spin state complex. In our case, complexes (fig. 1) have $T_{1/2}$ close to room temperature and this dependence is not observed for them, so the method needs a large number of independent parameters[1,2] to describe the chemical shifts behavior, because usually for high spin Fe(II) complexes the chemical shifts dependence is linear.
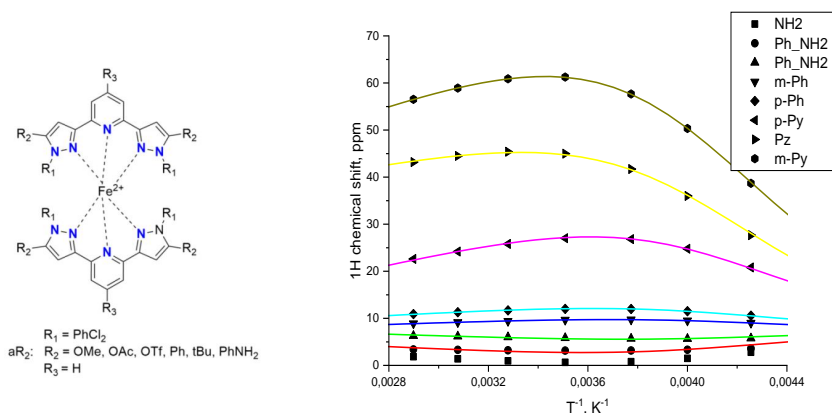
Figure 1. The general view of the studied complexes (left). The example of approximation of ^1H chemical shifts for $[FeLPhNH_2]^{2+}$ (right).

Results

The enthalpies and entropies of the spin transition were determined both by chemical shift analysis and by the Evans method. Also in the poster will be discuss how to avoid

overparametrization in the chemical shift analysis without the observation of high spin dependences.

Acknowledgments

References

1. Holm Petzold et al., ^{1}H NMR spectroscopy eludication in solution of the kinetics and thermodynamics of spin crossover for an exceptionally robust Fe^{2+} complex. Dalton Trans, 2016, 45, p. 13798-13809
2. Dmitry Aleshin et al., Room-temperature spin crossover in a solution of Iron(II) complexes wit N,N'-Disubstituted bis(pyrazol-3-yl)pyridines. ACS Omega, 2021, 6, 48, p. 3311-33121

Induced nonlinear frequency shift of an active ring resonator on a magnonic crystal

Andrey V. Bagautdinov, Alexey B. Ustinov
Saint Petersburg Electrotechnical University "LETI", Professor Popov str., 5, St. Petersburg 197022, Russia
E-mail: freester12@mail.ru

Spin-wave active ring resonators (ARR) find various applications. For example, on their basis, it is possible to create bistable devices [1], narrow-band microwave filters [2, 3], matched filters [4], microwave generators [5-11]. In recent years, developments in the field of artificial intelligence, in particular, reservoir-computing devices based on the principles of magnonics, have become one of the relevant areas [12-14].

As is known, various mechanisms can be used to implement the electronic tuning of the characteristics of magnonic devices. One of the main mechanisms now is magnetic frequency tuning [15]. It is also possible to implement electrical frequency tuning using ferrite-ferroelectric [3, 16], ferrite-piezoelectric [17] and ferrite-semiconductor [18] structures.

The aim of this work was to study the induced nonlinear shift of the resonant frequencies of a magnonic active ring resonator due to the excitation of a pump wave in it.

A schematic representation of an active ring resonator is shown in Fig. 1, *a*. The circuit includes a delay line based on a magnonic crystal (1), a microwave amplifier (2), a tunable attenuator (3), a combiner (4), as well as input (5) and output (6) directional couplers. The magnonic crystal used in the delay line was made of a film of iron-yttrium garnet (YIG) with a thickness of L = 5.5 µm, saturation magnetization M_0 = 153 kA/m and a half-width ferromagnetic resonance curve ΔH = 48 A/m. Twenty grooves with a depth of 0.5 µm and a width of 50 µm were etched on the surface of the film. The formed structure had a period Λ = 150 µm, with the length of the etched part of the film (groove width) a = 50 µm and the length of the non-etched part b = 100 µm. Magnetization of the YIG film was carried out by a permanent magnet with a field strength H = 97.6 kA/ m. A uniform magnetization field was directed in the plane of the film along the grooves. Two short-circuited microstrip antennas with a width of 50 µm and a length of 2 mm were used to excite and receive surface spin waves in the YIG film. The distance between the antennas d was equal to 7 mm. The microwave signal was supplied to the antennas via microstrip transmission lines with a wave resistance of 50 Ω. The microstrip scheme was made by photolithography on a 500 µm thick polycor substrate. The amplifier (2) compensated for the loss of the microwave signal in the delay line and the other components of the ring. A variable attenuator (3) regulated the signal gain in the ring.

The principle of operation of an active ring resonator is as follows. A microwave signal is applied to the input directional coupler (5) and begins to circulate in the ring. After one turnover in the ring, the signal weakens and adds up with the input signal. Then two signals propagate in the ring. After the second turnover, these signals are again combined with the input signal and then three signals propagate in the ring, etc. Thus, in the steady-state regime, the microwave signal circulating in the ring is an infinite sum of damped waves circulating in the ring. Resonance in the ring occurs at certain frequencies satisfying the condition of constrictive interference of circulating waves. At such frequencies, the full phase accumulation of the signal $\Delta\varphi$ is a multiple of 2π [19].

The total gain of the microwave signal in the ring is characterized by an effective gain G, which is defined as the difference between the gain of the amplifier (2) and the loss of the microwave signal in the other elements of the ring. If $G < 0$, then the active ring resonator operates in the microwave signal filtering regime. In the opposite case, the ring generates a microwave signal.
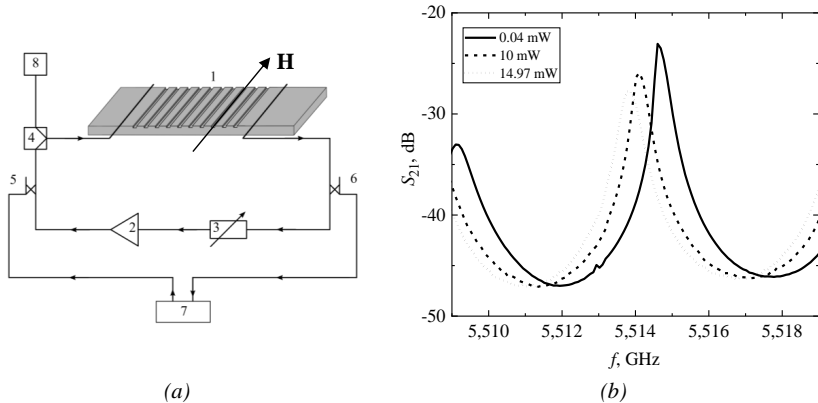
<p align="center">(a)   (b)</p>

Figure 1 – Block diagram of the experimental setup (a), resonant curves at different pump signal strengths (b)

Induced nonlinear shift of resonant frequencies was investigated by measuring the amplitude-frequency characteristics (AFC) of the ARR. To do this, the signal from the vector network analyzer (VNA) (7) was introduced into the ARR using a directional coupler (5). The ARR output signal was output from the ring using a directional coupler (6) and fed to the input port of the VNA. To adjust the frequency of the ARR from the generator (8) through the combiner (4), a microwave pump signal was applied to the magnonic crystal at a certain fixed frequency. This signal caused an induced nonlinear phase shift [20] of a low-power spin wave circulating in the ARR. This phase shift leads to a shift in the resonant frequencies of the ARR. The nonlinear mechanism responsible for the nonlinear effect is the four-wave parametric interaction of spin waves, as in [20].

A typical graph showing the shift of the resonant peak is shown in Fig. 2, *b*. It can be seen from the graph that there were no nonlinear distortions of the shape of the resonant curve, as in the case of bistability [22]. With increasing power of the pump signal, the amplitude of the resonant peak decreased.

Our research shows that the spectrum of resonant frequencies of the ARR can be controlled using a pump signal. The maximum value of the induced nonlinear frequency shift of 1.5 MHz obtained in our experiments is about a quarter of the distance between the resonant frequencies of the ARR. The studied effect can find various applications. For example, it can be used to adjust ARR frequencies, as well as to enter data into magnonic reservoir computers [12-14].

Acknowledgments

References

1. Y. K. Fetisov, P. Kabos, C. E. Patton. Electronics Letters, 32(20), 1894-1895 (1996).
2. V. E. Demidov, B. A. Kalinikos, N. G. Kovshikov, E. Edenhofer, Electronics Letters, **35**(21), 1856-1857 (1999).

<p align="center">161</p>

3. A. B. Ustinov, G. Srinivasan, B. A. Kalinikos, Applied Physics Letters, 92(19), 193512 (2008). DOI: 10.1063/1.2931085

4. A. A. Porokhnyuk, A. B. Ustinov, N. G. Kovshikov, B. A. Kalinikos, Technical Physics Letters, 35(18), 17-27 (2009).

5. W. Ishak, Electronics Letters, 19(22), 930-931 (1983). DOI: 10.1049/el:19830635

6. S. N. Dunaev, Y. K. Fetisov, Electronics Letters, 28(8), 789-791 (1992).

7. B. A. Kalinikos, M. M. Scott, C. E. Patton, Physical review letters, 84(20), 4697 (2000). DOI: 10.1103/PhysRevLett.84.4697

8. A. D. Karenowska, A. V. Chumak, A. A. Serga, J. F. Gregg, B. Hillebrands, Applied Physics Letters, 96(8), 082505 (2010). DOI: 10.1063/1.3318258

9. A. B. Ustinov, A. A. Nikitin, B. A. Kalinikos, IEEE Magnetics Letters, 6, 3500704 (2015). DOI: 10.1109/LMAG.2015.2487238

10. A. B. Ustinov, A. V. Kondrashov, A. A. Nikitin, V. V. Lebedev, A. N. Petrov, A. V. Shamrai, B. A. Kalinikos, In Journal of Physics: Conference Series 1326(1), 012015 (2019). DOI: 10.1088/1742-6596/1326/1/012015

11. S. V. Grishin, et. al., Physical Review Applied, 16(5), 054029 (2021).

12. S. Watt, M. Kostylev, Physical Review Applied, 13(3), 034057 (2020). DOI: 10.1103/PhysRevApplied.13.034057

13. S. Watt, M. Kostylev, A. B. Ustinov, Journal of Applied Physics, 129(4), 044902 (2021). DOI: 10.1063/5.0033292

14. S. Watt, M. Kostylev, A. B. Ustinov, B. A. Kalinikos, Physical Review Applied, 15(6), 064060 (2021). DOI: 10.1103/PhysRevApplied.15.064060

15. V. Gevorkyan, V. Kochemasov, A. Ustinov, Components and technologies, 4(189), 25-32 (2017).

16. A. B. Ustinov, A. V. Drozdovskii, A. A. Nikitin, A. A. Semenov, D. A. Bozhko, A. A. Serga, B. A. Kalinikos, Communications Physics, 2, 137 (2019). DOI: 10.1038/s42005-019-0240-7

17. Y. K. Fetisov, G. Srinivasan, Applied physics letters, 88(14), 143503 (2006). DOI: 10.1063/1.2191950

18. M. A. Morozova, D. V. Romanenko, A. A. Serdobintsev, O. V. Matveev, Y. P. Sharaevskii, S. A. Nikitov, Journal of Magnetism and Magnetic Materials, 514, 167202 (2020). DOI: 10.1016/j.jmmm.2020.167202

19. A. A. Nikitin, A. B. Ustinov, A. A. Semenov, B. A. Kalinikos, Technical Physics, 82(7), 98 (2012).

20. A. B. Ustinov, N. A. Kuznetsov, R. V. Haponchyk, E. Lähderanta, T. Goto, M. Inoue, Applied Physics Letters, 119(19), 192405 (2021). DOI: 10.1063/5.0074824

21. V. V. Vitko, A. A. Nikitin, R. V. Haponchyk, A. A. Stashkevich, M. P. Kostylev, A. B. Ustinov, The European Physical Journal Plus, 137, 1010 (2022). DOI: 10.1140/epjp/s13360-022-03213-5

Increasing the effective relaxation time in Carr-Purcell-Meiboom-Gill sequence

Iskander Khairutdinov, Michael Volkov, Ruslan Zaripov, Marcel Bakirov
Zavoisky Physical-Technical Institute, FRC Kazan Scientific Center of RAS, Kazan, Russia
E-mail: semak-olic@mail.ru

Introduction

It is known that the process of decoherence in the Hahn echo method is characterized by the phase relaxation time of spins (T_2). In the stimulated echo method, in addition to phase relaxation, relaxation is also added due to the interaction of spins with the lattice, which is characterized by its own time (T_1). The amplitude of each CPMG echo signal decreases with its own rate, which is a linear combination of the form $A/T_1 + B/T_2$, where A and B are constants depending on N. In [1], the dependences of all echo signals in the CPMG sequence on the value of the effective angle of rotation φ of spins by pulses up to N=4 are analytically shown. In this case, it was assumed that the pulses act nonselectively, i.e., the impulse rotates all spins of the spectrum by a fixed angle φ. The echo signals of the CPMG pulse sequence were simulated within the framework of the density matrix formalism for an isolated spin S=1/2. Theoretically, it is shown that at small angles φ in the CPMG sequence, stimulated echo signals predominate, and decoherence occurs with time close to T_1. At angles φ close to π, refocused primary echo signals predominate and decoherence occurs with time T_2. As a rule, in real systems $T_1 \geq T_2$. But at small angles of rotation, the absolute magnitude of the echo signals decreases, and it becomes difficult to see them against the background of experimental noise. Thus, one can control the time of the decoherence process by manipulating the rotation angles of microwave pulses in a standard CPMG sequence.

NMR measurements

All NMR measurements were performed by a Bruker Avance 400 NMR spectrometer (Germany) and as suitable nuclear spins the residual protons in deuterated water were used. The liquid was placed in a standard 5 mm glass tube and its ^{1}H NMR spectra were recorded at room temperature. The carrier frequency for the ^{1}H nuclei was 400 MHz, the duration of the 90° pulse for the ^{1}H nuclei was 10 μs, the width of ^{1}H spectra was 3 kHz, the cycle delay was 60 sec, and the number of scans was 4.

The relaxation time T_2 was measured by the primary echo decay method. Its value was 2.35 sec. The relaxation time T_1 was measured by the "inversion-recovery" protocol. Its value was 13.7 sec.

The relaxation time T_{dec} was measured by the CPMG method with a time delay τ=1 sec. The measurements of decay time T_{dec} at different angles of refocusing pulses were performed. The decaying parts of the echo signals were recorded as free induction decays, which then were subjected to a Fourier transform. The dependences of the signal intensity on the total delay time between refocusing pulses were plotted and they were approximated by exponents (Figure 1).

For the refocusing pulses with φ=30º decay time $T_{dec} \approx 0.77 * T_1$. A further decrease in the duration of refocusing pulses leads to a severe decrease in the amplitudes of the NMR signals and they became comparable with the background noise.
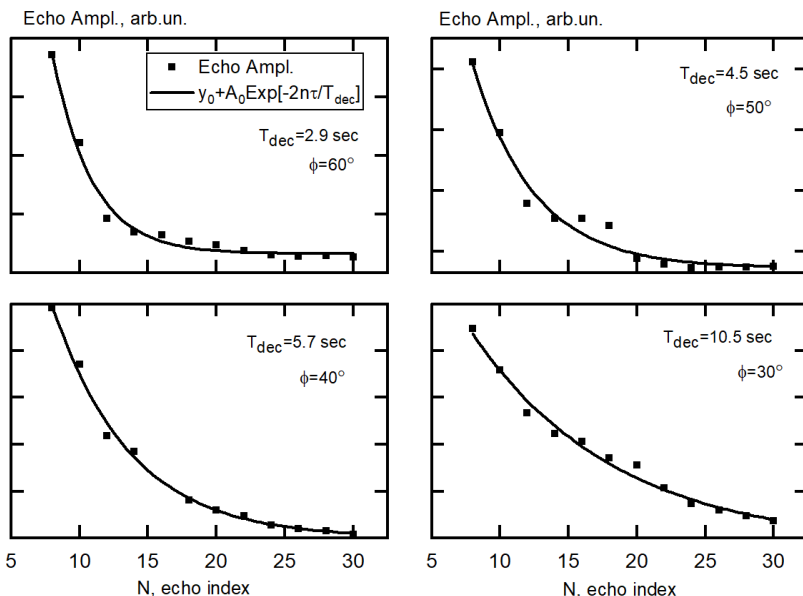
Figure 1. CPMG echo amplitudes (black points) for the residual protons in D_2O at various values of φ. The black lines are monoexponential approximations.

EPR measurements

For EPR measurements, the single-crystal of diamagnetically diluted mononuclear [n-Bu4N]2[Cu(opba)] complex (1%) in the host lattice of [n-Bu4N]2[Ni(opba)] (99%, opba = o-phenylenebis (oxamato)) was chosen [2]. Interest in this crystal is due to the relatively close values of the T_1 and T_2 relaxation times. EPR measurements were performed using Elexsys E580 spectrometer (Bruker, Germany) operating in the X-band. The spectrometer is equipped with the standard cavity ER4118MD5-W1 for X-band measurements. Temperature measurements were carried out using CF935 cryostat and ITC503 temperature controller from Oxford Instruments and all EPR measurements were performed at 80 K. In the CPMG sequence (π/2)x − {τ − (π)y − τ − echo −}n the lengths of the π/2-pulse and π-pulses were set to 16 ns and 32 ns, respectively. Due to technical limitations the delay time τ cannot be set shorter than 260 ns. The effective rotation angle φ was varied by changing Rabi frequency v_1 of π-pulses by using MPFU (microwave pulse former unit). Measurements of the spin-spin relaxation time T_2 was used by registration primary echo (500 nsec). For the measurements of the spin-lattice relaxation time T_1 (3268 nsec) the "inversion-recovery" pulse sequence was applied.

A decrease in the Rabi frequency leads to a decrease in the rotation angles of the refocusing pulses that in turn leads to an increase in the decay time Tdec up to the value 2220 nsec (Figure 2). This value is an order of magnitude 0.7*T_1. A further decrease in the Rabi frequency leads to a strong drop in the amplitudes of the echo signals to such an extent that they become comparable with the background noise.
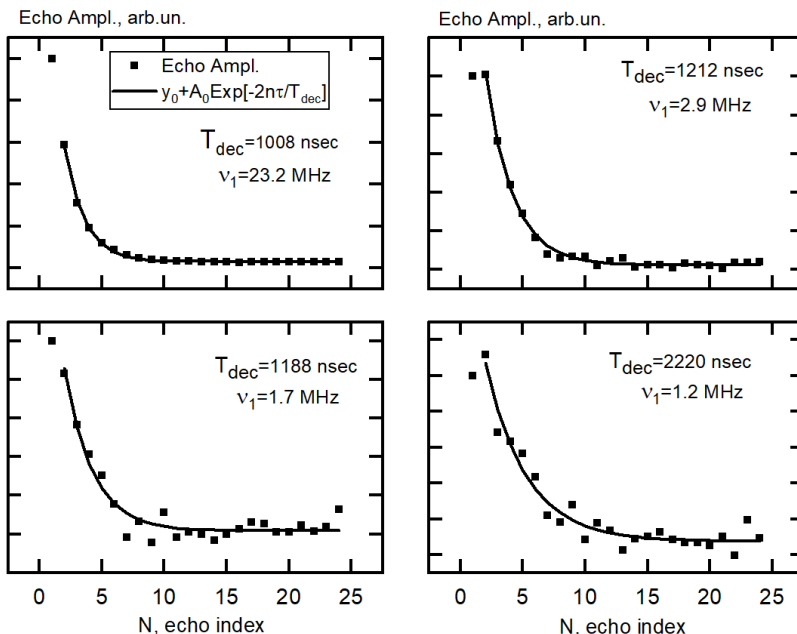
Figure 2. CPMG echo amplitudes (black points) of [n-Bu4N]2[Cu(opba)] *single-crystal at different Rabi frequencies of π-pulses. The black curves are monoexponent approximations. Delay time between pulses τ=300 nsec.*

Acknowledgments

References

1. Zaripov R.B., Khairutdinov I.T., Salikhov K.M., Specific Features of Studying the Paramagnetic Relaxation of Spins by the Carr–Purcell–Meiboom–Gill Method Related to the Superposition of Echo Signals // Russian Journal of Physical Chemistry B. – 2021. – V.15, №3. – P. 389-394.
2. R. Zaripov, E. Vavilova, I. Khairuzhdinov, et al., Beilstein J. Nanotechnol. 8, 943 (2017).

Molecular dynamics simulation of global and local dynamics in lysine based peptide dendrimers with neutral and protonized histidine

Valeriy V. Bezrodnyi[1,2], Emil I. Fatullaev[2], Sofia E. Mikhtaniuk[2], Oleg V. Shavykin[1,2,3], Igor M. Neelov[1,2], Anatoly A. Darinskii[4], Nadezhda N. Sheveleva[1] and Denis A. Markelov[1]

[1]*St. Petersburg State University, 7/9 Universitetskaya nab., 199034 St. Petersburg, Russia*
[2]*St. Petersburg National Research University of Information Technologies, Mechanics and Optics (ITMO University), Kronverkskiy pr. 49, 197101 St. Petersburg, Russia*
[3]*Tver State University, Zhelyabova St., 33, 170100 Tver, Russia*
[4]*Institute of Macromolecular Compounds RAS, Bolshoi pr.31, 199004, St.Petersburg, Russia*
E-mail: kupala-89@mail.ru

Introduction

In recent years several novel peptide dendrimers have been synthesized, studied experimentally and using MD simulation [1-7]. In this study, we used molecular dynamics simulation to study Lys-2His dendrimers with linear histidine inserts in wide temperature range (from 280 K to 340 K) and at two pH: Lys-2His with neutral histidine (His) at normal pH and Lys-2Hisp with protonated histidine (Hisp) at low pH in water. We used MD method described by us earlier [8-11] and functions described in other simulations using BD [12].

Structure

The size and shape of the dendrimer are important for the practical applications of dendrimer in drug and gene delivery. There are various ways to estimate the size of a dendrimer. We used the instant (figure 1) and mean-squares (figure 2) radius of gyration Rg to estimate the size of the Lys-2His and Lys-2Hisp dendrimers.
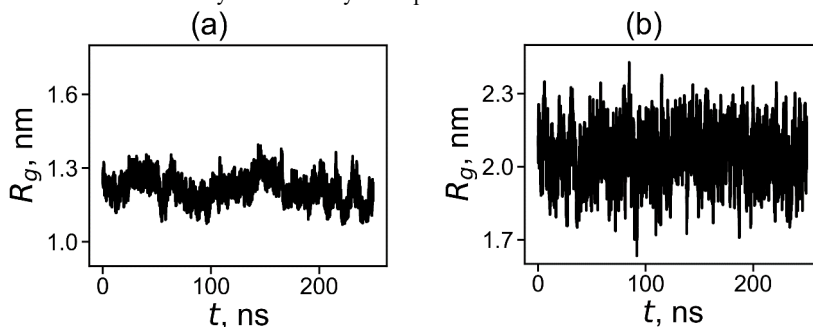
Figure 1. The time evolution of the instant radius of gyration Rg at 310 K for (a) Lys-2His and (b) Lys-2Hisp.

Table 1: The global characteristics of the Lys-2His and Lys-2Hisp dendrimers averaged through whole trajectory time: the radius of gyration R_g (nm), the hydrodynamic radius R_h (nm), the ratio R_h/R_g

Dendrimer	R_g	R_h	R_h/R_g
Lys-2His	1.32	1.22	0.93
Lys-2Hisp	2.05	1.65	0.73

In Figure 2, we plot the average value of R_g for each temperature. The average R_g is significantly larger for the Lys-2Hisp dendrimer with protonated histidines and it is close to Rg or dendrimers with similarly charged 2Lys or 2Arg spacers in dendrimers with repeating units Lys-2Lys and Lys-2Arg correspondingly [4, 6]. The size of Lys-2His with neutral histidine spacers is close to Rg for a dendrimer with neutral double glycine spacers (with Lys-2Gly repeating units).
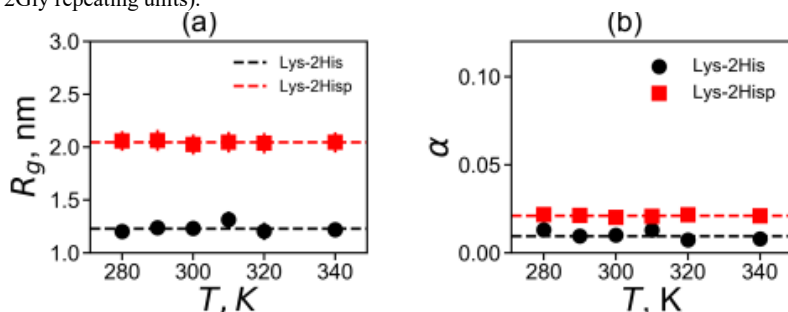
Figure 2. The temperature dependencies of (a) the mean-squared radius of gyration R_g and (b) the shape anisotropy α. All data for Lys-2His and Lys-2Hisp.

The Imidazole Pairing

The radial distributions for neighboring and non-neighboring pairs are shown in Figure 3 at different temperatures. It is easy to see that the results practically independent of temperature. In this case of neighbouring pairs of the studied plane groups, a sharp peak of n_{pairs} exists in the region of them smallest possible distances r = 0.4 nm between plane groups only for neutral His-His pairs. For charged Hisp-Hisp a peak at this distance also exists but its height is negligible. There is a more intense and broader second peaks for His-His and Hisp-Hisp pairs at distances r from 0.6 to 0.9 nm and a smaller third peak at distances close to r = 1.1 nm.

Figure 3. The radial distribution functions $n_{pairs}(r)$ of the centers of imidazole-imidazole (or guanidine-guanidine) groups at different temperatures for pairs between neighboring groups in Lys-2His (a), Lys-2Hisp (b)

References

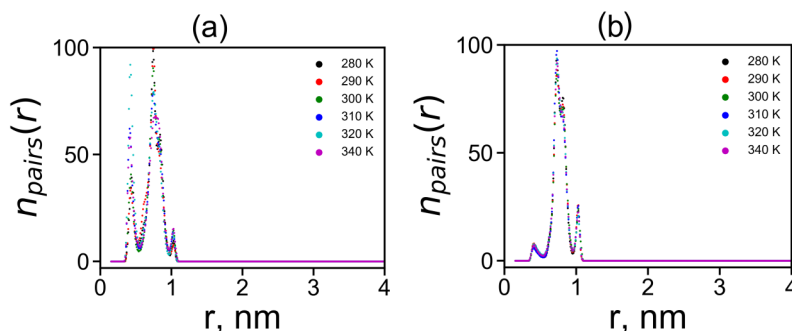1. Sheveleva, N.N.; Markelov, D.A.; Vovk, M.A.; Mikhailova, M.E.; Tarasenko, I.I.; Neelov, I.M.; Lähderanta, E. NMR studies of excluded volume interactions in peptide dendrimers. Sci. Rep. 2018, 8, 8916.
2. Mikhtaniuk S.E., Bezrodniy V.V., Shavykin O.V., Neelov I.M., Sheveleva N.N., Penkova A.V., Markelov D.A. Comparison of Structure and Local Dynamics of Two Peptide Dendrimers with the Same Backbone but with Different Side Groups in Their Spacers//Polymers, 2020, 12, No. 8, 1657
3. Sheveleva, N. N.; Markelov, D. A.; Vovk, M. A.; Mikhailova, M. E.; Tarasenko, I. I.; Tolstoy, P. M.; Neelov, I. M.; Lähderanta, E. Lysine-Based Dendrimer with Double Arginine Residues. RSC Adv. 2019, 9, 18018−18026.
4. Bezrodnyi, V. V.; Shavykin, O. V.; Mikhtaniuk, S. E.; Neelov, I. M.; Sheveleva, N. N.; Markelov, D. A. Why the Orientational Mobility in Arginine and Lysine Spacers of Peptide Dendrimers Designed for Gene Delivery Is Different? Int. J. Mol. Sci. 2020, 21, 9749.
5. Sheveleva, N. N.; Markelov, D. A.; Vovk, M. A.; Tarasenko, I. I.; Mikhailova, M. E.; Ilyash, M. Y.; Neelov, I. M.; Lahderanta, E. Stable Deuterium Labeling of Histidine-Rich Lysine-Based Dendrimers. Molecules 2019, 24, 2481.
6. Bezrodnyi V.V., Mikhtaniuk S.E., O. V. Shavykin, I. M. Neelov, N. N. Sheveleva, D. A. Markelov Size and Structure of Empty and Filled Nanocontainer Based on Peptide Dendrimer with Histidine Spacers at Different pH // Molecules 2021, 26, 6552.
7. Sheveleva N.N., Bezrodnyi V.V., Mikhtaniuk S.E., Shavykin O.V., Neelov I.M., Tarasenko I.I., Vovk M.A., Mikhailova M.E., Penkova A.V., Markelov D.A. Local Orientational Mobility of Collapsed Dendrimers, Macromolecules, 2021, 54, 23
8. Darinskii, A.A., Zarembo, A., Balabaev, N.K., Sundholm, F. Anisotropy of diffusion in a liquid crystalline system of semi-flexible polymer chains, Physical Chemistry Chemical Physics, 2003, 5(11), 2410–2416.
9. Ennari, J., Neelov I. Sundholm, F. Simulation of a PEO based solid polyelectrolyte, comparison of the CMM and the Ewald summation method, Polymer, 2000, 41, 2149.
10. Neelov, I.M., Shavykin, O.V., Ilyash, M.Y., Bezrodnyi V.V., Mikhtaniuk S.E., Darinskii, A.A., Leermakers, F.A.M Application of high-performance computing for comparison of two highly branched lysine molecules of different topology, Supercomputing Frontiers and Innovations, 2018, 5 (3), 60-64
11. Falkovich, S.G., Darinskii, A.A. Mechanism of shear deformation of a coiled myosin coil: Computer simulation. Polymer Science - Series A, 2010, 52(6), 662–670.
12. Shavykin, O.V., Mikhailov, I.V., Darinskii, A.A., Neelov I.M., Leermakers, F.A.M. Effect of an asymmetry of branching on structural characteristics of dendrimers revealed by Brownian dynamics simulations, Polymer, 2018, 146, 256-266

ESR spectroscopy of temperature accessible lowest electronic triplet biradical states of d-elements biologically active 1,10-phenanthrocyanines (bi-1,10-phenanthrolylenes), soft colloidal glasses

Viktor N. Demidov[1], Stanislav M. Sukharzhevsky[2], Evgenia V. Bogomolova[3], Alexandra G. Ivanova[1], Sofia V. Paston[4], Tatiana B. Pakhomova[5]

[1]*I.V. Grebenschikov Institute of Silicate Chemistry of the Russian Academy of Sciences, 199034, Makarova emb., 2, St.-Petersburg, Russia*

[2]*St. Petersburg State University, RC «MRMI», 198504, Universitetskiy ave., 26, Peterhof, Russia*

[3]*V.L. Komarov Botanical Institute of the Russian Academy of Sciences, 197376, Prof. Popova str., 2, St.-Petersburg, Russia*

[4]*Department of Molecular Biophysics and Polymer Physics, St. Petersburg State University, 198504, Universitetskiy ave., 26, Peterhof, Russia*

[5]*Department of Inorganic Chemistry, St. Petersburg State Technological Institute (Technical University), 190013, Moskovsky ave., 24-26/49 lit. A , St.-Petersburg, Russia*

E-mail: vndemidov@mail.ru

Introduction

ESR spectroscopy is one of the effective tools of the investigation of the paramagnetic spin centers (PSC) distribution in the chemical compounds. Investigation of the high-energetic phosphorescence triplet states by ESR method was formed as the independent scientific direction for a long time. In the these decades, the direction connected with investigation of the compounds with stoichiometric concentration of PSC (organic paramagnetic compounds and molecular magnetic compounds) is intensively developing. The third investigations direction of the character and nature of PSC is the studying of the chemical systems being in the thermodynamic equilibrium (quasiequilibrium) when the singlet forms are capable to turn into the radical or biradical states by *thermal way*, not by photochemical activation. The temperature (thermally) accessible radical and biradical forms (triplet biradical, degenerate biradical or monoradical) appear, thereby. Besides, the method developed for investigation of the thermodynamic nonequilibrium structure transitions is likely applicable in this case as well. That pulls together the consideration of strongnonequilibrium $S_0 \rightarrow S_*$ transitions with the successive intercombinatorial conversion S_* into one of the triplet states T_{high} and thermic transitions $S_0 \rightarrow T_{low}$. and shows actuality of the investigation problem of the **temperature accessible radical** and **biradical states** (including triplet states) of the chemical systems in the thermo operated (thermo directed) entropic controllable processes (since energy of these transitions can be too low).

We have previously found that coordination compounds of a new structural class of cyanines: nanoscale chromophore binuclear complexes of d-elements **[$M^{z+}L_n(\mu\text{-}PC)$]$_2$X$_m$** with *electron-rich* 1,10-phenanthrocyanine (**PC**) ligands (**μ-PCH** and **deprotonated μ-PC⁻**) are related as once to a group of complexes with **temperature (thermally) accessible biradical states** [1]. They were synthesized for the first time, we used the original technique of metal-assisted nondehydrogenated $C(sp^2)H$ coupling of coordinated 1,10-phenanthrolines in solutions and melts, which includes as one of the main intermediate stages **nucleophilic heteroaromatic substitution of hydrogen** S_N^H. **PCs** obtained in low temperature melts, when the melts are cooled, form **polymorphous soft colloidal phases** (**glasses**) (they are in an polymorphous glassy state), which, when dissolved in water or organic solvents, pass into a semicolloidal state when monomeric units are in equilibrium with polymer aggregates. Nanostructured aggregates of the micelle type are recorded in solutions of **Zn(II) PC** by nuclear magnetic relaxation, and metal complex polymer "grids"—by dynamic light

scattering. Structured aggregates of **PCs** in solutions scatter red and green laser beams. These compounds exhibit the properties of DNA complexones [2], have a cytostatic effect against tumor cells in vitro (proliferation inhibitors) and demonstrate the ability to inhibit the development of pathogenic fungi (for example, in the case of Co(II)-containing compounds [3]). The effectiveness of the effect of **PCs** of d-elements on biological objects depends on the nature of the complexing agent metal.

ESR spectroscopy in investigation of *electron-rich* 1,10-phenanthrocyanines (bi-1,10-phenanthrolylenes) of d-elements

Using ESR spectroscopy in the solid state for 1,10-phenanthrocyanine (bi-1,10-phenanthrocyanine) complexes (purple forms) $[M^{2+}L_n(\mu\text{-PC})]_2X_4$ of Zn^{2+}, Cd^{2+}, Pd^{2+}, Pt^{2+}, ESR signals (g-factor in the range of values 2.01 - 2.05, in some cases of a very complex form) were recorded, characterizing these compounds as substances with a nonstoichiometric (10^{-2}–10^{-3} spins per molecule) concentration of paramagnetic centers. The nature of the formation of ESR signals in this case is complex and as the most likely scheme, we proposed to consider their occurrence as a result of singlet-triplet $S_0{\to}T_{low}$.-transitions of the compound from the basic singlet state S0 to the temperature accessible electronic lower triplet biradical state T_{low} [4]. Such transitions have been studied recently for a number of organic and metal complex systems [5]. We have previously reported on studies by the ESR method of the electron-rich binuclear bridge diamagnetic Pt(II) 1,10-phenanthrocyanine (bi-1,10-phenanthrolylene) $[Pt(py)_2(\mu\text{-PC}^-)]_2Cl_3$ (purple form) (Pt^{2+} cation: [Xe] $4f^{14}$ $5d^8$) [6]. The obtained results point to the fact that the localization of the paramagnetic spin centers in this compound is too complicated and apparently assumes the existence of the different electron-rich radical states. 1,10-Phenanthrocyanine (bi-1,10-phenanthrolylene) coordination compounds of diamagnetic Zn(II) (purple form) were also studied by the ESR method (Zn^{2+} cation: [Ar] $3d^{10}$) [4]. Main difference of ESR spectra of Zn(II) 1,10-phenanthrocyanine (bi-phenanthrolylene) purple forms in solid glassy state from ESR spectra of Pt(II) 1,10-phenanthrocyanine (bi-1,10-phenanthroline) purple form is that the first is missing thin structure. In present work were investigated ESR spectra of Zn^{2+}, Cd^{2+}, Pd^{2+}, Pt^{2+} complexes $[M^{2+}L_n(\mu\text{-PC})]_2$ X_4 purple forms, soft colloidal biologically active glasses.

Synthesis of electron-rich *purple forms* 1,10-phenanthrocyanines (bi-1,10-phenanthrolylenes) of d-elements

Electron-rich binuclear biologically active 1,10-phenanthrocyanines (bi-1,10-phenanthrolylenes) $[M^{2+}L_n(\mu\text{-PC})]_2X_{2n}$ of Zn^{2+}, Cd^{2+}, Pd^{2+}, Pt^{2+}, *purple forms*, were synthesized based on the *metal-assisted nondehydrogenative* $C(sp^2)H$ coupling methodology of coordinated 1,10-phenanthrolines to ions of d-elements [1] in melt.
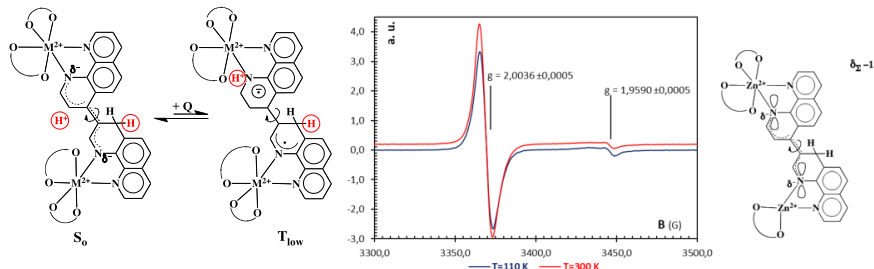
Results and Discussion

The temperature-directed $S_0 \rightarrow T_{low}$-transition is apparently associated with the temperature (*thermally*) activation of intramolecular rotation around the C–C interfragment bond, which binds *dihydro*-1,10-phenanthroline and 1,10-phenanthroline rings (*scheme*). Similarly, this is the case for *bis*(*dibenzo*-[a,i]-*fluorenylidene*), in which a thermally activated transition occurs from the basic singlet state S_0 to the twisted 90° paramagnetic triplet state T_1 and a singlet–triplet energy splitting is 9.6 kcal/ mol [7], as well as in the case of polyparaphenylene (extended viologen) [8] and for bisfluorenylidenebased dihydroacenes [9]. Fig. shows the ESR spectrum of Zn(II) complex in the solid state at various temperatures.

Conclusions

New diamagnetic metal PCs of two types have been studied by ESR spectroscopy: complexes of isoelectronic *redox-inert* Zn^{2+} [Ar]3d^{10} and Cd^{2+} [Kr]4d^{10} cations with fully filled d-shell and PC compounds of *redox*-active Pd^{2+} [Kr]4d^8 and Pt^{2+} [Xe]4f^{14}5d^8 cations with partially filled d-shell with accessible (temperature) states with unpaired electrons. Regardless of the electronic structure of the complexing ion, the ESR spectrum of compounds contains PSC lines that can be interpreted as bridging biradicals that stabilize under thermal excitation of complexes, which confirms the dependence of the integral intensity of the ESR signal in the spectra of complexes on temperature. According to chemical genesis of fragment μ-PC signals in ESR spectra of d-elements ($M^{2+} = Zn^{2+}$, Cd^{2+}, Pd^{2+}, Pt^{2+}) complexes $[M^{2+}L_n(\mu\text{-PC})]_2X_{2n}$ (X= AcO⁻, Cl⁻, I⁻) *purple forms* have been assigned to the *electron-rich* bridge chromophoric1,10-phenanthrocyanine (bi-1,10-phenanthrolylene) μ-PC ligands in the coordination structure of $M^{2+}(\mu\text{-PC})M^{2+}$. The assumed *temperature-directed* $S_0 \rightarrow T_{low}$ - transitions may be associated with the thermal activation of intramolecular rotation around the C–C interfragment bond, which unites the *dihydro*-1,10-phenanthroline and 1,10-phenanthroline rings. It was found that the unusual temperature spectral behavior of metal PCs, manifested in their ESR spectra, is combined with the high microbiological activity of compounds and their ability to bind with DNA macromolecules.

ESR Measurements

The ESR investigation of 1,10-phenanthrocyanine (bi-1,10-phenanthrolylene) complexes *purple forms* of d-elements in the solid state (112,6–300,0 K) has been carried out in the Resource Centre "Magneto-resonance methods of investigation" of the Scientific Park of St. Petersburg State University on the spectrometer ELEXSYS E580 (X-BAND).

Acknowledgments

References

1. V.N. Demidov. – Abstr. Diss. D. Chem. Sci. (in Russ.), St. Petersburg State Technol. Inst. (Techn. Univ.), 2010.
2. E.V. Akulenkova, V.N. Demidov, A.O. Martynova, S.V. Paston. Biophysics. **66** (1), 17-24 (2021).
3. V.N. Demidov, E.V. Bogomolova, L.K. Panina, et al. Med. Probl. Myc. (in Russ.) **20**, No. 2, 66 (2018).

4. V.N. Demidov, S.M. Sukharzhevsky, S.V. Paston, et al. News St. Petersburg State Univ. (in Russ.), Ser.4, Phys., Chem., **4** (62), No. 2, 138-145 (2017).
5. K.K. Kalninsh. Electronic excitation in chemistry. (Inst. Macromol. Comp. RAS, St. Petersburg, 1998. - 323 p. (in Russ.).
6. V.N. Demidov, S.M. Sukharzhevsky, L.N. Vedeneeva, A.V. Zinchenko, T.B. Pakhomova. 15th International School-Conference MAGNETIC RESONANCE AND ITS APPLICATI- ONS (SPINUS-2018). April 1-6, 2018, St. Petersburg, Russia, Abstr., p. 160-162.
7. C. Wentrup, M.J. Regimbald-Krnel, D. Müller, P. Comba. Angew. Chem. Int. Ed. **55** (47), 14600-14605 (2016).
8. J. Casado, S. Patchkovskii, M.Z. Zgierski, et al. Angew. Chem. Int. Ed. **47** (8), 1443 – 1446 (2008).
9. X. Yin, J.Z. Low, K.J. Fallon, et al. Chem. Sci. **10**, 10733–10739, (2019).

Eugenol and piperine proton spectra

Nina Djapic

[1]*University of Novi Sad, Technical Faculty "Mihajlo Pupin", Zrenjanin, Serbia*
E-mail: nidjapic@gmail.com

Introduction

The isolation of natural products from plant material is important part of undergraduate laboratory practice course in organic chemistry. Isolation of trimyristin, carvone, eugenol, anethole, apigenin and piperine are the introduction to the organic chemistry laboratory course techniques. The experiments can be completed in 3 to 4 hours and are excellent examples for the beginning of the undergraduate course in organic chemistry. The isolated and purified compounds are usually analyzed by thin-layer chromatography. The isolated compounds can be prepared for the NMR analysis using deuterochloroform.

Proton spectra of eugenol and piperine

From cloves isolated is eugenol and from black pepper obtained is piperine. The eugenol proton spectrum is depicted in Fig. 1.
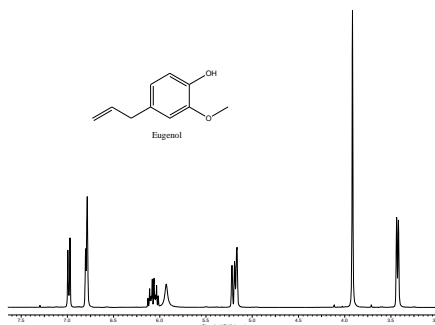

Figure 1. Eugenol proton spectrum
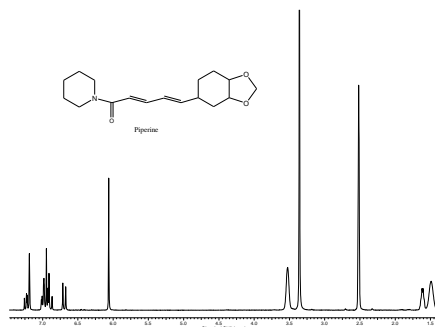
The piperine proton spectrum is depicted in Fig. 2.

Figure 2. Piperine proton spectrum

In case the NMR course is introduced earlier in the semester the obtained spectra can be interpreted.

Development and characterization of novel pervaporation mixed matrix membranes based on carboxymethyl cellulose modified with Zn-based MOF for hybrid process

<u>Maria E. Dmitrenko</u>[1], Anna I. Kuzminova[1], Andrey A. Zolotarev[1], Anastasia D. Chepeleva[1],
Anna I. Mikulan[1], Anton S. Mazur[1], Anastasia V. Penkova[1]

[1]*Saint Petersburg State University, Saint-Petersburg, Russia*
E-mail: <u>m.dmitrienko@spbu.ru</u>
https://go.spbu.ru/rgpenkova

Introduction

Currently, pervaporation is actively used both as an individual method for separating low molecular weight components and in hybrid (combined) processes, for example, for obtaining esters ("reaction + pervaporation"). Successful carrying out of the esterification reaction consists in shifting the equilibrium of the reaction towards the reaction products. Previously, an excess amount of alcohol was added to shift the chemical equilibrium and increase the yield of the ester, which led to the subsequent removal of excess alcohol. The hybrid method "reaction + pervaporation" allows to shift the equilibrium towards the reaction products by removing one of them. The promising industrial implementation of this hybrid process requires the search for new pervaporation membranes with tailored properties. Currently, the solution to this problem can be by creating mixed matrix membranes (MMMs).

In the present work, novel mixed matrix pervaporation membranes based on carboxymethyl cellulose (CMC) modified with Zn-based metal-organic framework (Zn(BIM)Si) were prepared for the enhanced hybrid process "reaction + pervaporation". The structural changes of the developed membranes were studied by spectroscopic methods, in particular, nuclear magnetic resonance (NMR). NMR allowed to evaluate the interaction between Zn(BIM)Si and CMC confirming the complex structure of the obtained MMMs. The additional characterization of the samples was carried out by scanning electron and atomic force microscopies, thermogravimetric analysis, and swelling experiments. Transport properties of the developed MMMs were tested in a hybrid process "reaction + pervaporation" for the production of ethyl acetate.

Acknowledgments

Water molecules mobility in microporous mordenite by molecular dynamics simulation

M.I. Egorova, A.V. Egorov, M.G. Shelyapina

Department of Nuclear-Physics Research Methods, Faculty of Physics, Saint-Petersburg State University

E-mail: maryaverina@gmail.ru

The development of new catalysts on zeolite support requires a detailed understanding of the main regularities in the formation of local microstructure of adsorbed species, as well as factors affecting their molecular mobility in porous systems. In this case, the atomistic molecular dynamics simulation is a promising tool to address the problem. Of course, it should be kept in mind that results of any classical simulation are always sensitive to the used potential model describing the interactions between the molecules. In the present study we focus on the performance of several standard water models to describe water mobility in the micropores of a 3D zeolite with mordenite structure.

Simulations were carried out using the *MDynaMix* package [1]. The simulated system was a fragment of mordenite consisted of 2×2×4 unit cells filled with 384 water molecules. Periodic boundary conditions were used in all three dimensions. The mordenite was considered as a rigid system. Interactions between mordenite and water atoms were a sum of Coulomb and Lennard-Jones (6-12) potentials. Corresponding parameters for mordenite atoms were taken from Refs. [2, 3]. Three different water models: three-site SPC/E [4], flexible SPC-F [5], and five-site TIP5P [6], were considered. Each system was simulated in the *NVT* ensemble at 298 K. Equilibration time was 0.5 ns. The following production run – 1 ns.

Diffusivity and reorientational motion of confined water molecules were studied in detail. A special attention was given to the peculiarities of water motion in various pores.

Acknowledgments

References

1. P. Lyubartsev, A. Laaksonen. − *Comp. Phys. Comm.*, 128, 565-589 (2000).
2. S. Grimme. – *J. Comput. Chem.*, 27, 1787-1799 (2006).
3. H. Fang, P. Kamakoti, P. I. Ravikovitch, et al. – *Phys. Chem. Chem. Phys.*, 15, 12882-12894 (2013).
4. H. J. C. Berendsen, J. R. Grigera, T. P. Straatsma. − *J. Phys. Chem.*, 91, 6269-6271 (1987).
5. K. Toukan, A. Rahman. − *Phys. Rev. B*, 31, 2643-2648 (1985).
6. M. W. Mahoney, W. L. Jorgensen. − *J. Chem. Phys.*, 112, 8910-8922 (2000).

EPR study of mechanically activated calcium gluconate monohydrate irradiated with gamma quanta

A.R. Gafarova [1], G.G. Gumarov [1], R.B. Zaripov [1], D.S. Rybin[2], G.N. Konygin[2]

[1]*Zavoisky Physical-Technical Institute, FRC Kazan Scientific Center of RAS, Kazan 420029, Russian Federation*
[2]*UdmFRC Ural Branch of RAS, Izhevsk, 426067, Russia*
E-mail: albina-gafarova@mail.ru

Calcium gluconate is widely used in the chemical and food industries, it is used as a drug for the treatment of diseases associated with a lack of calcium in the body. Also, interest in the study of this compound is high due to the development of a mechanically activated modified nanodispersed amorphous form of calcium gluconate (MACG), the therapeutic efficacy of which is much higher. It is assumed that the increase in the bioavailability of the drug may be associated with a change in the conformation of the calcium gluconate (GC) molecule after mechanoactivation. Given the great importance of calcium gluconate for industrial and medical applications, it is surprising that its structure remained unexplored for a long time.

The starting material was calcium gluconate monohydrate powder from Sigma Aldrich company (SA). The mechanoactivation of the samples was carried out on a planetary ball mill LAIR. The mechanoactivation time was 120 min. Also samples were irradiated with 1.25 MeV photons with a dose 400 Gy at the Rokus facility. EPR spectra were obtained at room temperature on a Bruker EMX Plus X-band spectrometer and an Elexsys E680 W-band spectrometer.

a) X-band *б) W-band*
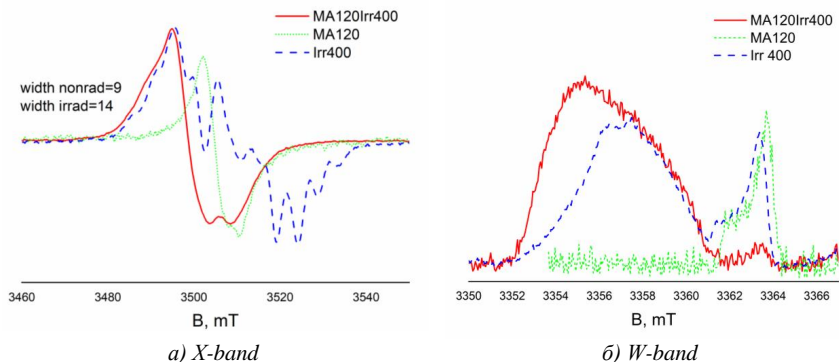
Fig.1. EPR spectra calcium gluconate monohydrate: 1) subjected to mechanical activation (MA120), 2) subjected to irradiation (Irr400) and 3) subjected successively mechanical activation and irradiation (MA120Irr400)

X- and W- band EPR spectra presented in Figure 1: from GC samples, mechanically activated, irradiated, as well as subjected to both types of exposure (MA120Irr400). As found by fitting the spectrum of mechanically activated and irradiated GC consists of three components. The spectrum of mechanically activated GC consists of a single component, while the spectrum of irradiated GC consists of two components (from three corresponding to MA120Irr400).

It should be noted that the shape of the EPR line from the GC sample subjected to mechanoactivation in the W-band indicates the anisotropy of the g factor, and differs significantly (from others) in the practical absence of "tails". This indicates a small width of the resonance line, which is confirmed by model calculations (0.05 mT). Such a narrow line is often observed on paramagnetic centers densely surrounded by cyclic compounds. In the case of GC, δ-gluconolactone could act as such a compound. The formation of a small amount of this substance during mechanical activation was reported earlier [1].

At the same time, subsequent irradiation of a mechanically activated sample of calcium gluconate leads to a significant transformation and shift of the spectrum. In irradiated GC, a broad line is observed, probably corresponding to δ-gluconolactone. This indicates, firstly, that a certain amount of the substance may be contained in the original GC, and secondly, the mechanism of formation of radicals upon irradiation with gamma rays differs markedly from the mechanisms of mechanoactivation. Namely, when irradiated with gamma quanta, the processes of recombination of radicals are greatly hindered in comparison with such processes during mechanical activation.

Preliminary mechanical activation of the sample before irradiation leads to an insignificant broadening of the spectrum in the W-band, which is surprising, since amorphization occurs according to XRD and solid state NMR data. At the same time, in the X-band, on the contrary, a narrower spectrum is observed.

These data, in our opinion, indicate the formation of a certain stable molecular structure, which is probably responsible for the increase in the therapeutic effect of the drug after mechanoactivation.

Acknowledgments

References

1. Изучение состава и структуры глюконата кальция и его механоактивированной (нанодисперсной) формы / Д.Р. Шарафутдинова, Ю.Я. Ефремов, И.Х. Ризванов, [и др.] // Журнал структурной химии, 2010, Т. 51, стр.145-147.

Study of the structure of reaction products of acetyl-containing furancarboxylates with hydrazine hydrate by 1D and 2D NMR spectroscopy

<u>Gomonov K.A.</u>, Pelipko V.V., Baichurin R.I., Makarenko S.V.

Herzen State Pedagogical University of Russia, Department of Organic Chemistry, Laboratory of Nitrocompounds, Center of collective use at the Faculty of Chemistry "Instrumental methods for the study of nitro compounds, coordination, biologically active substances and nanostructured substances" 48 Moyka River Embankment, Saint Petersburg 191186, Russia

E-mail: <u>kohrgpu@yandex.ru</u>

http://kohrgpu.ru, http://ckpo.herzen.spb.ru/?page=organic-chemistry

Alkyl 4-acetyl-5-methylfuran-3-carboxylates **Ia, b** [1], containing two electrophilic centers, are interesting objects for studying the direction of their interaction with hydrazine, a representative of polynitrogen nucleophiles. Theoretically, this reaction can end with the formation of various **II-VII** structures.
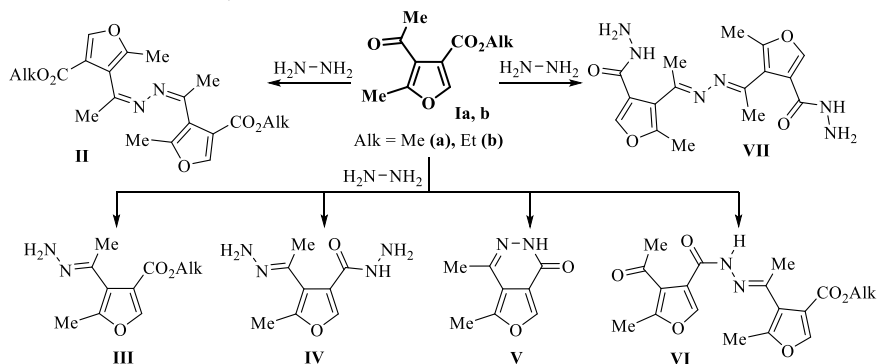
The aim of this work was to study the structure of the reaction products of furan-3-carboxylates **1, 2** with hydrazine using ^{1}H and ^{13}C NMR spectroscopy, including experiments: ^{1}H–^{13}C HMQC and ^{1}H–^{13}C HMBC.

In the structures of the intended proposed products, the following features can be distinguished:

• there is an ester fragment (CO_2Alk) in molecules II, III, VI;

• NH or NH_2 group – in molecules III, IV, V and VII;

• molecules II and VII have internal symmetry.

The implementation of the studied reaction using the ratio of reagents 1:1 led to obtain the crystalline products.

The ^{1}H NMR spectrum of a representative of the synthesized compounds contains signals of the alkyl substituent of the ester fragment (δCH_3 1.22 ppm, t, ^3J 7.1 Hz and δCH_2 4.18 ppm, q, ^3J 7.1 Hz), which confirms the preparation of structures **II**, **III** or **VI** (Fig. 1).

According to the results of studying this molecule by the experiment of the ^{1}H-^{13}C HMQC it turned out that the broadened proton signal at 11.45 ppm (1H) does not correlate with carbon atom signals and therefore belongs to the NH group. This result is consistent only with the structure **VI** of the previously selected (Fig. 2).
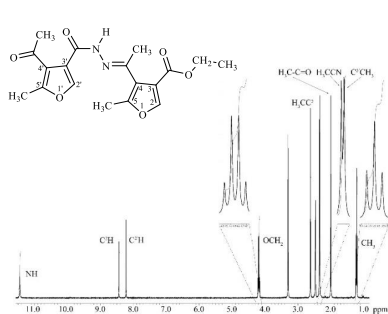
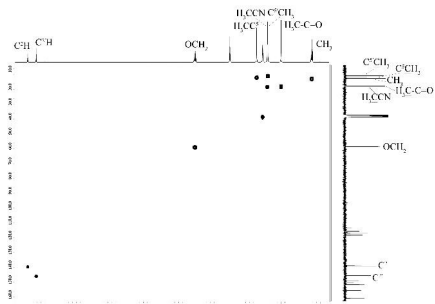Figure 1. *^{1}H NMR spectrum of compound* **VIb** *(DMSO-d_6)*

Figure 2. *^{1}H–^{13}C HMQC spectrum of compound* **VIb** *(DMSO-d_6)*

Indeed, the ^{13}C-{^{1}H} NMR spectrum of the molecule **VI** contain signals of the following structural fragments: 140.52 ppm. (C=N), 153.60 ppm (C=O) and 162.72 ppm. (CO$_2$Alk) (Fig. 3). The assignment of these carbon signals is confirmed by the results of the ^{1}H-^{13}C HMBC experiment (Fig. 4).

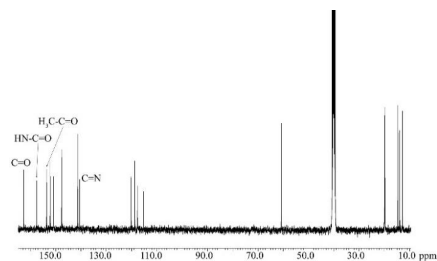Figure 3. *^{13}C NMR spectrum of compound* **VIb** *(DMSO-d_6)*
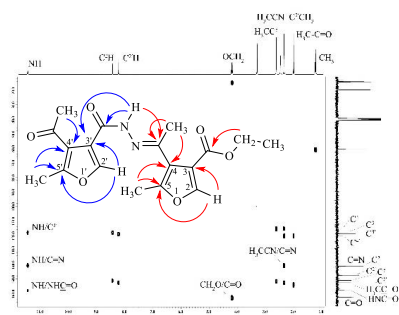
Figure 4. *^{1}H–^{13}C HMBC spectrum of compound* **VIb** *(DMSO-d_6)*

Thus, based on the obtained data of homo- and heterocorrelation experiments of NMR spectroscopy, it was found that the interaction of furan-3-carboxylates **Ia, b** with hydrazine leads to the formation of alkyl 4-(1-{2-[(4-acetyl-5-methylfuran-3-yl)carbonyl]hydrazinylidene}ethyl)-5-methylfuran-3-carboxylates **VIa, b**.

Acknowledgments

References

1. Gomonov, K.A., Pelipko, V.V., Litvinov, I.A., Baichurin, R.I., Makarenko, S.V. Mendeleev Commun. 2023, 33, 11-13.

Pravastatin with transition metal ion studied by NMR

Islamov T.R., Efimov S.V., Klochkov V.V.
Institute of Physics, Kazan Federal University, Kazan, 420008 Russia
E-mail: relifer2000@mail.ru

Introduction

The interaction of organic compounds and metals is an important process in nature. The study of the formation of peptide–metal complexes is a rather popular task due to the need to clarify their structure, reveal the possibility of their modification and practical application [1]. In addition, the formation of a complex of an organic molecule with a metal usually leads to noticeable changes in NMR spectra, which opens the way to study such systems in solution using high-resolution NMR [2]. To simplify the model, small organic molecules – statins – were taken for consideration in our study. Statins are a class of the most common drugs used to lower low-density lipoprotein cholesterol levels. The aim of this study will be to investigate the effect of transition metals on statins using NMR spectroscopy.

Object

The group of statins presents a wide variety of molecules that differ in medical activity, solubility, etc. Pravastatin was chosen as the object due to its solubility in water, which in turn is a biologically native environment. Image of pravastatin in Figure 1.
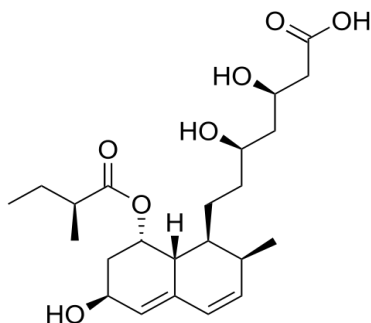
Figure 1. Structural formula of pravastatin

Method

Experiments were carried out on a Bruker Avance II 500 NMR spectrometer. Solution of the pravastatin was prepared in D_2O at the concentration of ~10 mM. One-dimensional proton spectra were acquired; analysis of the data was made in the TopSpin software. Cobalt chloride $CoCl_2$ was dissolved in D_2O and used for titrating the sample.

Results

Figure 2 shows one-dimensional proton spectra for pravastatin with different content of cobalt ions.

As the metal concentration increases, the chemical shift of the protons associated with carbons 15 and 16 changes. The spectral lines also broaden. This effect can be associated with the formation of a complex of pravastatin and cobalt.

In the future, metal complexes of other types of statins with various transition group metals will be considered.
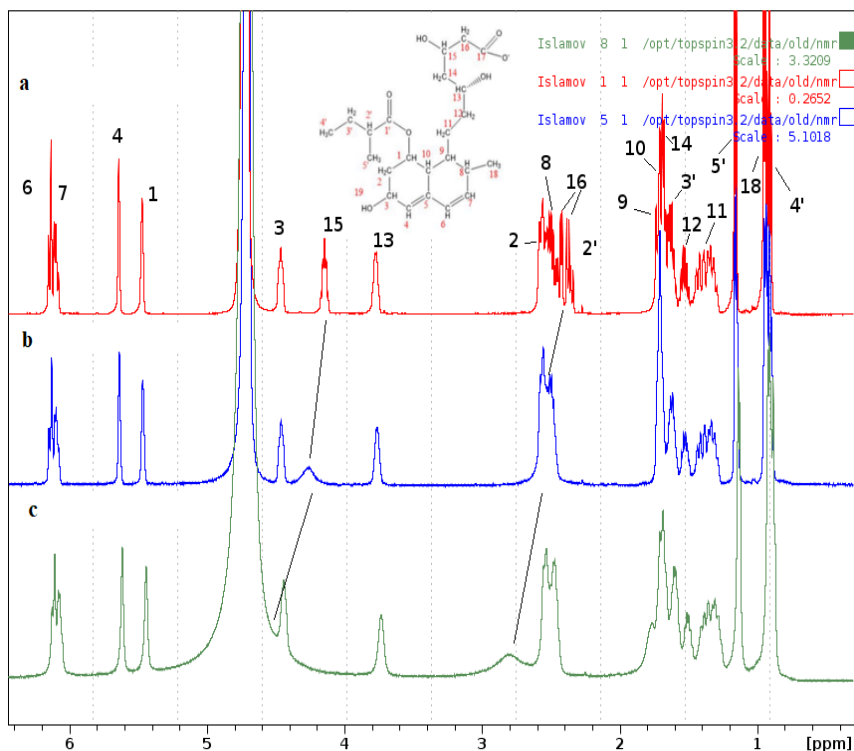
Figure 2. One-dimensional ^1H NMR spectra for pravastatin:(a) solution of pravastatin in D_2O, (b) solution of pravastatin in D_2O with a Co^{2+} ion in a molar ratio of 1/10, (c) solution of pravastatin in D_2O with a cobalt ion in a ratio of 1/5

Acknowledgments

References

1. Caetano-Silva M.E. et al. Peptide-metal complexes: Obtention and role in increasing bioavailability and decreasing the pro-oxidant effect of minerals // Critical Reviews in Food Science and Nutrition, 2021, V. 61, № 9, P. 1470-1489.
2. Shalev D.E. Studying Peptide-Metal Ion Complex Structures by Solution-State NMR // International Journal of Molecular Sciences, 2022, V. 23, № 24, P. 15957.

Deuterium Isotope Effects in Protic Ionic Liquids

Alexander E. Khudozhitkov[1,2], Daniil I. Kolokolov[1,2]

[1]*Boreskov Institute of Catalysis, Siberian Branch of Russian Academy of Sciences, Prospekt Akademika Lavrentieva 5, Novosibirsk 630090, Russia*
[2]*Novosibirsk State University, Pirogova Street 2, Novosibirsk 630090, Russia*
E-mail: alexandr.khudozhitkov@gmail.com

Isotope effects play a pivotal role in chemistry and biology. D-bonds are assumed to be stronger than H-bonds due to quantum effects, mainly the lowering of the zero-point vibrational energy. For instance, the change from protonated to deuterated water increases the strength of the solvent-solvent as well as the solvent-protein hydrogen bonds and thus significantly influences the protein-folding process. What is well established for hydrogen-bonded molecular liquids such as water and methanol is still unclear for hydrogen bonded cations and anions in ionic liquids (ILs). These liquid materials attract increasing interest in science and technology due to their unique properties, which result from the delicate balance of Coulomb interactions, hydrogen bonding and dispersion forces between the charged entities. Specific strength, locality and directionality of the different types of interactions govern the structure, dynamics, and phase behavior of ILs.

It is the purpose of our work to study the influences of isotopic substitution on hydrogen bonding and structural ordering of the model protic ionic liquid (PIL) triethylammonium methanesulfonate [TEA][OMs] by means of deuterium solid-state NMR spectroscopy. We use the N−D deuterons of the triethylammonium cations for probing structural rearrangements, equilibria between static and mobile states and hydrogen bonding depending on selective deuteration of the three ethyl groups. We show that structural changes and interactions vary characteristically with temperature and that the equilibria between static and mobile fractions in the PIL are highly sensitive to deuteration of the alkane chains with respect to both, the transition temperature and the cooperativity of the transition. We demonstrate that solid-state NMR spectroscopy is a suitable method for understanding the origin of changes in thermodynamic, structural and dynamical properties in complex materials caused by isotopic substitution.

Two samples with various quantity of deuterium in cation [TEA-d$_1$][OMs] and [TEA-d$_{16}$][OMs] are prepared and studied with ^{2}H NMR method in a broad temperature range between 67 and 316 K. For the fully deuterated sample the ^{2}H NMR spectra are a superposition of three Pake-doublets with deuteron quadrupole coupling constants (DQCC or Q) for the methyl deuterons (Q$_{CD3}$=52 kHz), the methylene deuterons (Q$_{CD2}$=170 kHz) and the ND deuteron (Q$_{ND}$=147 kHz). The spectra of [TEA-d$_1$][OMs] show only one signal of ND-group with Q$_{ND}$=140 kHz (Fig. 1). Lower value of DQCC for ND deuteron in [TEA-d$_1$][OMs] indicates at stronger hydrogen bond strength compared to fully deuterated sample.

While the DQCCs are sensitive to changes present within a single cation-anion pair, we are also interested to see how isotopic substitution affects the behavior of the whole pair in the solid region. For that purpose, we addressed the dynamically heterogeneous phase between the melting and the crystallization temperatures. Typical ^{2}H spectra measured in this temperature region are shown in Fig.2, exhibiting a Pake patterns and a small narrow line simultaneously. The relative populations of the rigid [TEA]$^+$ cations p_{static} and the mobile fraction p_{mobile} are proportional to the relative intensities of anisotropic and isotropic components of ^{2}H NMR spectrum, respectively. The temperatures where the static and mobile fractions are equally populated at about 236 K for [TEA-d$_1$][OMs] compared to predicted 316 K for [TEA-d$_{16}$][OMs]. Thus, there is an 80 K difference with a preference for the ethyl-deuterated species, suggesting an enormous isotope effect.
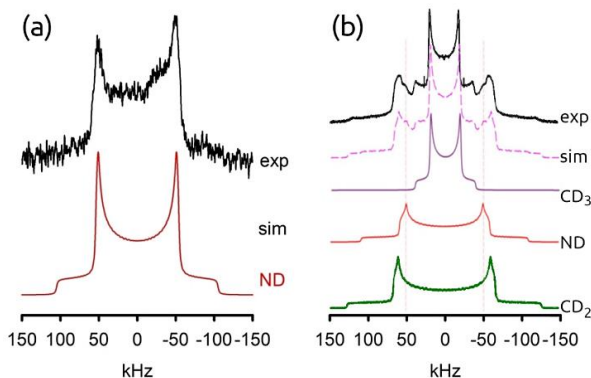
Figure 1.^{2}H NMR spectra of (a) [TEA-d$_1$][OMs] and (b) [TEA-d$_{16}$][OMs] at 113 K.

The thermodynamic parameters of melting transition can be derived from the temperature dependence of equilibrium constant $K_{eq}=p_{mobile}/p_{static}$. In the simplest scenario the temperature dependence of equilibrium constant could be expressed by temperature independent molar standard transition enthalpies and entropies with $\ln K_{eq} = -\frac{\Delta H^0}{RT} + \frac{\Delta S^0}{R}$. The entropy and enthalpy differences are significantly smaller for [TEA-d$_{16}$][OMs] than for [TEA-d$_1$][OMs], which indicates a stronger hydrogen bond formation for [TEA-d$_{16}$][OMs]. A careful thermodynamic analysis shows that the static/mobile transition is governed by the entropy differences which are smaller for [TEA-d$_{16}$][OMs] than for [TEA-d$_1$][OMs], finally leading to a broader transition temperature range for the first. This study underlines the relevance of isotope effects on hydrogen bonding, structural arrangements and ensemble equilibria in protic ionic liquids.

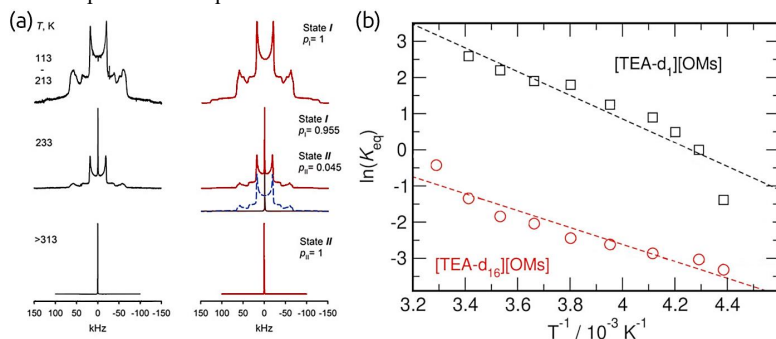*Figure 2.   (a) The ^{2}H NMR spectra of PILs [TEA-d16][OMs] for different temperature ranges showing the static patterns, the heterogeneous phase with both, the mobile and the static states and the pure mobile contribution. (b) van't Hoff plot of the logarithm of the equilibrium constant Keq vs. the inverse temperature.*

Acknowledgments

Nuclear magnetic resonance in eutectic Cs-Li-OAc-H₂O "water-in-salt" solution

Aleksandr Y. Koltsov, Konstantin V. Tyutyukin, Alexandr V. Ievlev

Department of Nuclear Physics Research Methods, Saint Petersburg State University, Saint-Peterburg 198504, Russia

E-mail: st076255@student.spbu.ru

Introduction

If at a certain concentration of the solution, the melting point is less than the melting point of the components separately, and its concentration dependence has a minimum (eutectic point), then such systems are called Deep Eutectic Solvents (DESs). The investigated DESs in our work are solutions of inorganic salts. Their use as ionic liquids (ILs) is promising for use in supercapacitors, as they are easy to prepare, inexpensive, and eco-friendly [1], [2], [3], [4].

Experiment and results

Proton spectra

In this study, 6 samples were made: an aqueous solution of cesium acetate, lithium acetate and their combination. To determine the molality (m), NMR spectra were taken on the protons of each of the samples at 25°C and at 80°C. Measurements at high temperature were necessary to ensure that the samples did not precipitate and that saturated solutions were obtained. The data was received on the Bruker Avance III NMR spectrometer 500 MHz.
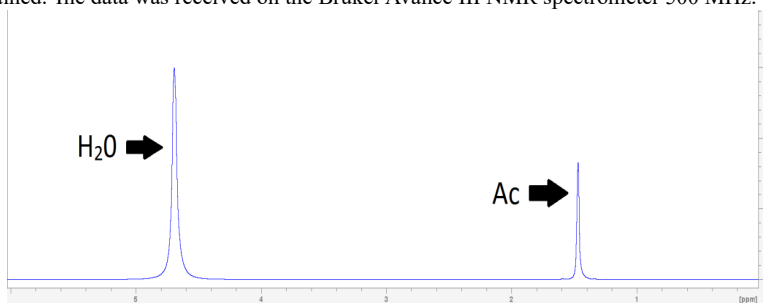
Figure 1. Proton spectrum of the first sample at room temperature

For this, 12 similar spectra were obtained with two lines: water and acetate. Through the ratio of integral areas, the molalities of the solutions given in Table 1 were calculated.

Table 1. Molality of solutions of the studied samples

Sample №	Ratio (Cs-Li)	m calculated		m expected
		25 ˚C	*80 ˚C*	
1	45-0	30.1	30.232	45
2	45-1	26.8	26.962	46
3	45-3	22.0	22.025	48
4	45-5	24.5	24.594	50
5	45-7	38.5	38.46	52
6	0-7	8.30	8.477	7

Diffusion at room temperature

For each sample, the diffusion coefficients of water molecules, acetate anions, and cesium and lithium cations were measured. To do this, spectra were taken at various magnetic field gradients. The pulse sequence "diffSteBp" was used. The measurement results are presented in Table 2.

Table 2. Diffusion coefficients at room temperature

№	^{1}H (H_2O) D, $m^2/s \times 10^{-11}$	^{1}H (OAc) D, $m^2/s \times 10^{-11}$	^{7}Li D, $m^2/s \times 10^{-12}$	^{133}Cs D, $m^2/s \times 10^{-11}$
1	16.21	5.82	-	7.61
2	18.54	6.71	37.02	9.23
3	23.62	8.79	76.91	12.81
4	17.49	5.79	34.46	8.87
5	6.72	1.59	8.87	2.56
6	23.03	7.59	94.28	-

Future measurements

Further work consists in measuring diffusion coefficients and relaxation rates for these samples at various temperatures. This data set will describe the physical model and features of solution dynamics. With their help, it will be possible to determine the possibilities for using lithium acetate and cesium acetate as electrolytes.

Acknowledgments

References

1. V.V Matveev, A.V Ievlev, K.V Tyutyukin, and L.M. Varela, "Comparison of ionic liquids and highly concentrated electrolyte solutions: similarity and differences in structure and in dynamics." // Magnetic Resonance and its Applications. Spinus-2019, Russian Federation: Издательство «ВВМ», СПб., pp. 47,

2. O.A. Kokh, V.V Matveev, A.V Ievlev, K.V Tyutyukin, and L.M. Varela, "Investigation of the molecular mobility of the ionic liquid BmpyrrNTF$_2$ by NMR methods," // Magnetic Resonance and its Applications. Spinus-2021, Russian Federation: Издательство «ВВМ», 2021, p. 215.

3. A.P. Abbott, C.D'Agostino, S.J. Davis, L.F. Gladden, and M.D. Mantle, "Do group 1 metal salts form deep eutectic solvents?" Phys. Chem. Chem. Phys., vol. 18, no. 36, pp. 25528–25537, 2016, doi: 10.1039/c6cp05880a.

4. X. Baokou and M. Anouti, "Physical properties of a new deep eutectic solvent based on a sulfonium ionic liquid as a suitable electrolyte for electric double-layer capacitors," J. Phys. Chem. C, vol. 119, no. 2, pp. 970–979, 2015, doi: 10.1021/jp5110455.

Ways of optimization of the magnonic reservoir computer performances

Alexandr V. Kondrashov[1], Alexey A. Nikitin[1], Andrey A. Nikitin[1], Mikhail Kostylev[2], Alexey B. Ustinov[1]

[1]Department of Physical Electronics and Technology, Saint Petersburg Electrotechnical University "LETI", St. Petersburg, 197022, Russia
[2]Department of Physics, University of Western Australia, Crawley, Western Australia 6009, Australia
E-mail: avkondrashov@etu.ru

Introduction

Reservoir computers (RC) are a particular type of a nonlinear recurrent neural network that is conceptually simple and powerful. The main advantage of RC is a fast training procedure, during which only readout-layer weights are adjusted [1]. Magnonic systems turned out to be a promising candidate for the physical reservoir due to rich diversity of nonlinear effects in magnetic materials and their low thresholds. One of the simplest implementations of the physical magnonic reservoir is a magnonic active ring oscillator (MARO) [2]. Recently A.A. Nikitin et.al. proposed a theoretical model for a nonlinear transient processes of establishing of steady auto-oscillations in a MARO [3]. The numerical model allows evaluating the influence of a broad spectrum of parameters of the active ring on performance characteristics of the magnonic reservoir computer (MRC). In the present work, we demonstrate this capability of the model.

Physical reservoir modelling procedure

A block-diagram of the modelled magnonic reservoir computer is shown in Fig. 1. The main element of the MRC is a magnetostatic surface spin-wave delay line (MSSW DL) consisting of an yttrium iron garnet (YIG) ferrite film placed on top of spin-wave antennae. The output of the MSSW DL is connected to its input through a feedback loop, which consists of an amplifier, a directional coupler, and a variable attenuator. The ferrite film inserts nonlinearity and a time delay that are the most important requirements for a physical system to be suitable as a physical reservoir. The amplifier compensates losses in the circuit. If the compensation is complete, self-oscillations develop in the ring. The directional coupler fans out a small portion of the signal circulating in the ring for further processing and analysis. An electronic attenuator serves for entering data into the ring.

The input data represent an arbitrary sequence of binary pulses consisting of 4200 elements. We define the pulse length as T_p. The binary data sequence is entered into the ring by varying a ring gain coefficient with the electronic attenuator. The ends of its range of attenuation are assumed to be binary values of "0" and "1." Namely, the binary "0" corresponds to a zero loss inserted by the open attenuator. The binary "1" corresponds to some particular non-zero attenuation. Switching between "0" and "1" leads to a transition of the reservoir from "0"-steady-state to "1"-steady-state and vice versa.
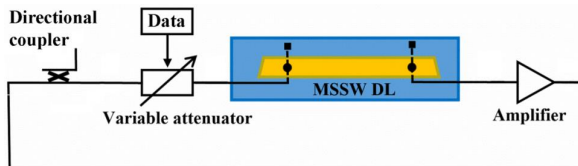

Figure 1. Block diagram of the magnonic reservoir

Parameters of the simulated MARO have following values: external magnetic field H = 1780 Oe; saturation magnetization $4\pi M$ = 1990 G; half width of ferromagnetic resonance ΔH= 0.5 Oe; film thickness L = 5.65 μm; distance between spin-wave antennae l = 7.7 mm; cubic and quintic nonlinear damping coefficients η_1= 2 ns^{-1} and η_2= 2 ps^{-1} respectively. These parameters yield a continuous-wave signal generation at 7.28 GHz and a ring delay time τ_{ring} = 215 ns.

Two tasks were used to evaluate the performance of the reservoir model and analyze ways to improve it. The first is the STM task. The system is trained to remember the binary value entered j pulses ago, by exploiting the information that is still present in the system. This task provides a measure of the "fading" memory present in the MARO. The second is the PC task. While completing the PC task, the reservoir computes parity of the sum of j consecutively entered pulses. This task probes both nonlinearity and memory of the system. STM and PC capacities characterize the efficiency of completion of these two tasks. Higher capacities correspond to higher performance of the reservoir computer. Detailed algorithms for the tasks are described in Ref. [4, 5].

Influence of physical parameters

During the modelling we investigated the influence of the pulse length T_p, ferrite film thickness L, distance between antennas l, ring gain coefficient G_0, and gain variation ΔG on the STM and PC capacities. Fig. 2 shows the obtained dependencies.

Fig. 2(*a*) demonstrates that an increase of the pulse length leads to a decrease in the STM capacity. The effect of STM is present during the transient process of establishing a new steady state upon a sudden variation ΔG in the amplification gain in the ring. We may expect the reservoir to be able to recall past inputs over a period of time that is comparable to the time of completion of the transient process but smaller than it. Therefore, if T_p increases a smaller number of past binary inputs is able to affect a current state of the reservoir. This means that the memory capacity reduces in terms of the number of past inputs. The PC capacity gradually increases with an increase of the pulse length. The reason for this is the shape of the output signal. If the input interval becomes shorter then response of the reservoir becomes linear.
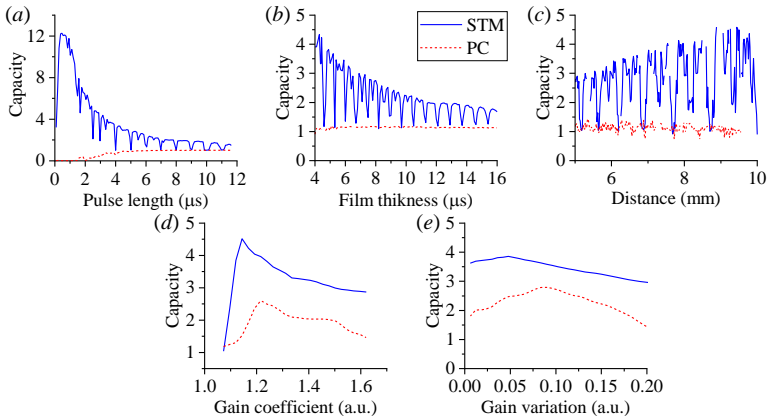
$$G_{ring} = G_0 - \Delta G$$

Figure 2. Dependencies of STM and PC capacities on pulse length(a), Film Thickness(b), distance between antennas(c), ring gain coefficient (d), gain variation(e).

Panels (b) and (c) of Fig. 2 display the capacities obtained for various film thicknesses and distances between antennas, respectively. The modelling was carried out for T_p = 1935 ns. It is clear that an increase of the distance between the antennas makes τ_{ring} longer. In addition, the group velocity of spin waves decreases with a decrease in the film thickness. That also makes τ_{ring} longer, which allows fitting more pulses into the ring length. This leads to an increase of the fading memory of the magnonic RC as well as an increase in the STM capacity. However, these effects also increase signal loss and ultimately, reduce the impact of spin-wave nonlinearity, because the spin-wave signal spends more time in the film while having a smaller amplitude. It leads also to a decrease of the PC task capacity.

Entering the input data into the reservoir proceeds through suddenly changing the ring gain coefficient Gring by a step ΔG. Denote the ring gain for the "0" logic state as Gring = G0. Then the ring gain corresponding to logic "1" is given by the formula as follows

Fig. 2(*c*) shows the influence of G_0 on the values of STM and PC capacities when ΔG was set to 0.07. A gradual increase of G_0 leads to an increase of both capacities. The short-term memory capacity grows faster because it depends on the "fading" memory only. The parity-check capacity increases more slowly, because its value depends on both the "fading" memory of reservoir and nonlinear mixing of inputs. The maximum capacities correspond to G_0=1.14 for the STM task and G_0=1.22 for the PC task. Starting from these values, capacities of both tasks decrease due to an influence of nonlinear damping, which essentially reduces the reservoir memory effect. Near the threshold of self-generation, the amplitudes corresponding to "0" and "1" states are very close. Thus, the transition between the two states is almost instantaneous. Higher gain leads to faster switching between steady states. As a result, for both maximum and minimum values of G_0, new inputs are able to influence the reservoir dynamics during time intervals that are much shorter than the pulse length T_p. The dynamical processes in the ring do not depend on previous states of the system then, and the system has no memory.

Fig. 2(*d*) shows the dependencies of STM and PC capacities on the value ΔG for G_0 fixed at 1.2. One sees that with an increase in ΔG, the capacities first increase, then reach maxima and finally drop. The reason for this behavior is the same as for the behavior of the ring gain. A low ΔG implies a small adjustment of the ring gain. The self-oscillation amplitudes for the original and final states are very close, and it takes a small amount of time to complete the transient process. The fast completion of the process translates into a shorter memory, and ultimately into smaller capacities.

The obtained results demonstrate that upon a careful optimization, the MARO-based reservoir computer will be able to restore past inputs or determine parity of an input sequence up to four inputs back into the past. The improved values of the correlation coefficients translate into values of STM and PC capacities of 3.97 and 2.6 respectively. They are larger by 2 times than experimentally observed.

Acknowledgments

References

1. G. Tanaka, et al, – *Neural Networks*, 115, 100-123 (2019).
2. S. Watt, et al, – *Phys. Rev. Appl.*, 15, 064060 (2021)
3. A. Nikitin, et al, – *J. Appl. Phys.*, 131, 113903 (2022).
4. N. Bertschinger, T. Natschläger, – *Neural Comput.*, 16, 1413-1436 (2004).
5. T. Furuta, et al, – *Phys. Rev. Appl.*, 10, 034063 (2018).

Solid-State ^{13}C NMR of Annealing Nanodiamonds

Anastasia V. Sivtseva[1], <u>Vladilina V. Koryakina[2]</u>, Petr P. Sharin[1]

[1]*V.P. Larionov Institute of Physical-Technical Problems of the North of Siberian Branch of the Russian Academy of Sciences Yakutsk, Russian Federation*

[2]*North-Eastern Federal University, Yakutsk, Russian Federation*

E-mails: [1]sianva@yandex.ru, [2]korvv@empl.s-vfu.ru

Introduction

Diamond nanoparticles represent a unique class of nanosized materials with a variable structure and labile physicochemical properties [1–2]. Nanodiamonds are used as components in polishing compositions, lubricating oils, composite materials, microelectronic elements, as well as selective adsorbents and catalysts. At the same time, a large number of other potential applications, including the use of nanodiamonds as drug carriers, fluorescent markers, an immobilizer of biologically active substances, a sorbent for purifying blood, lymph, etc., are hindered due to the difficulty in obtaining diamond nanoparticles with controlled and reproducible surface chemistry.

An efficient and environmentally friendly method for removing nondiamond carbon and impurities from detonation synthesis nanodiamonds by their thermal oxidation with atmospheric oxygen without significant loss of the diamond component was described in papers [3–4]. Despite a significant number of works devoted to the study of thermal annealing in air, many questions and aspects of the formation of the composition and content of functional structures that affect the chemistry of diamond nanopowders remain open and require clarification and additions.

The purpose of this work is to study by ^{13}C NMR the features of the effect of annealing in air in the temperature range of 200–550 °C on the structure of primary particles of nanopowders obtained by grinding natural diamond and by the method of detonation synthesis.

Methods

The procedure for obtaining nanopowders from natural diamond (NND) and their chemical purification are described in detail in [5]. As samples of the detonation synthesis nanodiamond (DND), we used a highly purified nanopowder of the UDA-S-GO brand produced by the Federal Research and Production Center "Altai" (Biysk).

Stepwise of thermo-oxidation of samples in air at atmospheric pressure was carried out as follows. All samples of diamond nanopowders were poured into separate corundum ceramic cups, placed in a furnace chamber, and heated in air at the following fixed temperature values: 200, 300, 400, 500, and 550 °C. After holding for 1 hour at each given temperature value, one sample of NND and DND was taken out of the oven for further study, and the rest of the samples remained in the furnace chamber. Thus, the total time of stepwise heating of samples of NND and DND nanopowders in air at a temperature of 200 °C was 1 hour, at 300 °C - 2 hours, at 400 °C - 3 hours, at 500 °C - 4 hours and at 550 °C - 5 hours.

NMR measurements were carried out on a high-resolution Avance III 400 MHz spectrometer (Bruker, Germany) with 4 mm MAS broadband probe. ^{13}C MAS spectra were collected at room temperature with the rotation speed of 4 kHz. Number of scans was 1500, pulse length 4 μsec. The ^{13}C chemical shifts refer to tetramethylsilane (TMS). The spectra were processed using the Topspin program.

Results and Discussion

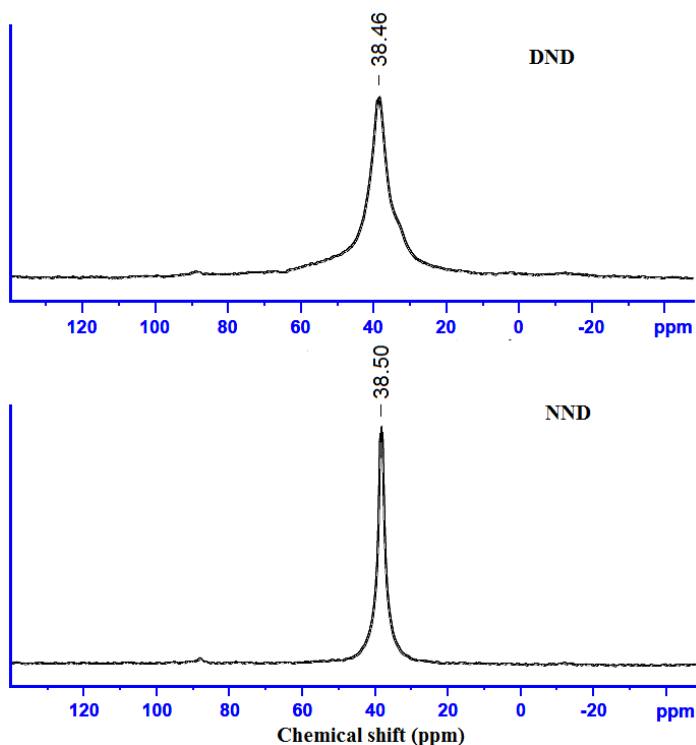The studied samples of NND and DND show an intense line with a peak at about 38.5 ppm. (Fig. 1).

189

Figure 1. ^{13}C MAS NMR spectra of initial DND and NND.

This line is asymmetric, especially in the case of DND, and five components can be deconvoluted. Narrow intense peak with chemical shift δ = 38.6 ppm, which is characteristic of bulk diamond, can be attributed to diamond core carbons with a perfect sp^3 configuration. Slightly wider line with close offset, δ = 34.0 ppm attributed to slightly nonequivalent sp^3 carbons of the diamond core; this non-equivalence may be due to a slight disruption of the tetragonal sp^3 configuration. Broad line with δ = 47.2 ppm comes from a partially disordered shell covering the diamond core. Broad lines at δ = 53.4 and 72 ppm are assigned to the signals of groups CH$_n$ and C-OH, respectively [1, 6]. The proportion of nanodiamond structure components before and after annealing are presented in Table 1.

Table 1. Proportion of nanodiamond structure components before and after annealing in air

Structure components of nanodiamonds	Chemical shift, ppm	NND (%)				DND (%)			
		Initial	400°C	500°C	550°C	Initial	400°C	500°C	550°C
Core sp^{3}dis	34	4.48	7.87	4.70	13.78	10.47	9.50	8.51	10.39
Core sp^3	38.6	85.10	92.13	87.16	75.84	60.03	78.92	75.67	63.79
Shell sp^{3}dis	47.2	10.42	0	7.10	8.41	10.20	5.62	10.79	18.27
Shell CH$_n$	53.8	0	0	1.04	1.97	16.38	4.90	2.34	6.87
Shell C-OH	72	0	0	0	0	2.92	1.06	2.69	0.68

In general, the data obtained using ^{13}C MAS NMR spectroscopy correlate with the data obtained by XPS and Raman methods [7]. The decrease of the number of CH$_n$ groups in DND can be associated with a decrease of graphite-like carbon in the sp^2 state.

Conclusions

Annealing in air in the temperature range of 400–550 °C leads to efficient removal of amorphous and graphite-like carbon in sp^2 and sp^3 states from diamond nanopowders by oxidation with air oxygen. At the same time, for DND, CHn component is more efficiently removed from the shell at 500 °C, and amorphous sp^3 component at 400°C, while for NND, the most optimal temperature range is around 400 °C.

Acknowledgments

References

1. V.Y. Dolmatov– *Russ. Chem. Rev*., 7, 607–626 (2001).
2. A.L.Vereshchagin (in Russian). – *Yuzhno-sibirskii nauchnyi vestnik*., 2, 24–30 (2017).
3. S. Osswald, G.Yuchin, V. Mochalin, S.O. Kucheyev, Y Gogotsi. – *J. Am. Chem. Soc*., 35, 11635–11642 (2006).
4. S. Stehlik, M. Varga, M. Ledinsky, V. Jirasek, A. Artemenko, H. Kozak, L. Ondic, V. Skakalova, G. Argentero, T. Pennycook, J.C. Meyer, A. Fejfar, A. Kromka, B. Rezek – *J. Phys. Chem. C*., 49, 27708−27720 (2015).
5. P.P. Sharin, A.V. Sivtseva, S.P. Yakovleva, M.M. Kopyrin, S.A. Kuz'min, V.I. Popov, L.A. Nikiforov. – *Russ. J. Non-ferrous Metals*., 2020, 4, 456–465 (2020).
6. A.M. Panich– *Diamond Relat. Mater*., 16, 2044–2049 (2007)
7. P.P. Sharin, A.V. Sivtseva, V.I. Popov. – *Powder Metallurgy and Functional Coatings*., 4, 67—83 (2022).

Novel pervaporation membranes based on poly(ester-block-amide) modified with MOFs

Anna I. Kuzminova[1], Maria E. Dmitrenko[1], Anna S. Karyakina[1], Olga A. Mikhailovskaya[1], Anton S. Mazur[1], Anastasia V. Penkova[1]

[1]*Saint Petersburg State University, Saint-Petersburg, Russia*
E-mail: a.kuzminova@spbu.ru
https://go.spbu.ru/rgpenkova

Introduction

Pervaporation is one of the most popular membrane processes that allows the separation of low molecular weight components, including isomer mixtures, azeotropic mixtures, and thermally unstable mixtures. Besides high selectivity, pervaporation is an environmentally-friendly and low energy consuming process with inexpensive and compact equipment. The rapid development of pervaporation requires the search for novel membrane materials with desired properties. One of the effective methods for improving the transport properties of pervaporation membranes is the development of the mixed – matrix membranes (MMMs). The development of MMMs consists in modification of the polymer matrix by introduction of inorganic filler that leads to getting tailoring properties. MMMs combine the simplicity of preparation of polymer membranes with the superior properties of inorganic particles.

In the present work the novel membranes based on poly(ester-block-amide) (PEBA) were prepared by introducing the metal-organic frameworks in the polymer matrix. The improvement of the transport properties of the PEBA/MOFs membranes was expected due to the porous structure, hydrophilic/hydrophobic properties of the MOFs. The characterizations of the polymer samples were studied by nuclear magnetic resonance (NMR), Fourier-transform infrared spectroscopy, scanning electron microscopy, atomic force microscopy, thermogravimetric analysis, swelling experiments, and contact angle measurement. Transport properties of the developed membranes were investigated for water treatment by pervaporation.

Acknowledgments

Development and characterization of novel membranes based on sodium alginate modified with Zr-MOFs.

Anna I. Kuzminova[1], Maria E. Dmitrenko[1], Danila D. Myznikov[1], Roman R. Dubovenko[1], Anton S. Mazur[1], Anastasia V. Penkova[1]

[1]*Saint Petersburg State University, Saint-Petersburg, Russia*
E-mail: a.kuzminova@spbu.ru
https://go.spbu.ru/rgpenkova

Introduction

Dense membranes are used for separation of low molecular weight components, including mixtures of isomers, azeotropic mixtures, and thermally unstable mixtures by evaporating components through the membrane in pervaporation. The separation of mixtures with low molecular weight components by traditional methods is difficult. Currently, the improvement of the transport properties of polymeric membranes occurs due to the creation of mixed matrix membranes (MMMs), by modifying the polymer with an inorganic and/or organic modifier to obtain tailoring properties.

In the present work the novel membranes based on sodium alginate (SA) were prepared by introducing the three metal-organic frameworks (Zr-MOFs): MIL-140A, MIL-140A-AcOH-EDTA and MIL-140A-AcOH into the SA matrix. The improvement of the transport properties of the membranes based on SA modified with Zr-MOFs was expected due to the porous structure, hydrophilic/hydrophobic properties, excellent chemical and thermal stability of the Zr-MOFs. The most important investigation of Zr-MOFs inclusion in SA matrix is analysis of membranes by spectroscopic methods. Among these methods, nuclear magnetic resonance (NMR) is the best tool for the investigation of polymer nanocomposite materials. NMR allowed to study the interaction between Zr-MOFs and polymer SA matrix and to confirm the complex structure of MMMs in the present work. The additional characterizations of the polymer samples were studied by Fourier-transform infrared spectroscopy, scanning electron microscopy, atomic force microscopy, thermogravimetric analysis, and swelling experiments. Transport properties of the developed membranes were investigated by pervaporation during separation of water-isopropanol mixtures at 22 °C.

Acknowledgments

Homo- and heteronuclear NMR methods for signal assignments in ^{1}H and ^{13}C specta of 1-aminoacyloxygermatran

Denis V. Lezov[1], Tatyana A. Kochina[1], Ruslan I. Baichurin[2], Stanislav I. Selivanov[3,1]

[1]*Institute of Chemistry of Silicates of I.V. Grebenshchikov, RAS, emb. Adm. Makarova, 2, 199034 St. Petersburg, Russia*

[2]*Herzen State Pedagogical University of Russia, Department of Organic Chemistry, Moyka River Embankment 48, 191186, St. Petersburg, Russia*

[3]*Laboratory of Biomolecular NMR, St. Petersburg State University, 199034, St. Petersburg, Russia*

E-mails: [1]*lyo-denis@yandex.ru;* [2]*kohrgpu@yandex.ru;* [3]nmr.group.spbu@gmaill.com

Introduction

Hypercoordinated group 14 element compounds have attracted considerable attention. In most germatranes, the germanium atom is pentacoordinated. However, octahedral geometry is often the characteristic of organo-germanium compounds. The secondary bonding between the donor and the germanium atoms causes the hypercoordination phenomenon, resulting in a hexacoordinated germanium atom with a distorted octahedral geometry [1, 2]. For example, octahedral germanium (IV) complexes bearing acetylacetonato ligand possess the promising anticancer activity and display high complex stability in biological media [3]. In [4] the hexa- coordinated germanium complexes catechols and biologically active pyridines (including vitamins) were obtained from GeO_2 Heptacoordinated trichlorogermyl[tris(2-methoxyphenyl)]methane of a tricapped tetrahedral structure was obtained by Y.Takeuchi with co-author [5]. S. Karlov and co-authors [6] reported that germaspirobis (ocanes) $[RN(CH_2CHR'O)_2]_2Ge$ may possess four-, five-, and six-coordinated Ge atoms. Among them, octahedrally hexacoordinated Ge atoms with the N atoms occupying cis-positions are thermodynamically the most stable.

The germatrane cycle is significantly more resistant to hydrolytic cleavage than the silatrane one, which makes it possible to use germatranes as a transport agent for biologically active fragments into living cells [7]. At the moment, a wide range of germatranes containing organic substituents at the germanium atom are known [8]. Among them, the 1-acyloxygermatranes $RC(O)OGe(OCH_2CH_2)_3N$ should be especially distinguished. The choice of a carboxylic acid as a substituent has a significant effect on the biological activity of germatranes.

The use of NMR spectroscopy for establishing the structure of germatranes (Figure **1**) has a rather long history, which is described in the review [9]. The importance of the first NMR works (in the early 80s) of the two most active research groups from the Siberian Branch of the Russian Academy of Sciences under the guidance of M.G. Voronkov and from the Institute of Organic Synthesis (The Latvian Academy of Sciences) under the guidance of É. Lukevics should be noted. It is not surprising that from these groups (predominantly synthetic chemists by training) such well-known NMR-specialists as V.A. Pestunovich, V.K. Voronov [10], S.N. Tandura, A.V. Kisin, E.E.

Y=O, S, CH2, NR, OCH2

Figure 1. The structure and numbering of germatranes

Liepins and É.L. Kupće [11, 12] later emerged, some of them continue active NMR studies [13, 14]. The methodological and technical revolution in NMR spectroscopy at the end of the 1970s made it possible to carry out studies (exotic for that time) on almost all magnetic nuclei and so the works of these two groups on the study of germatranes on the rare nuclei ^{13}C, ^{15}N, [17]O, [73]Ge appeared [15]. However, ^{1}H NMR turned out to be the least informative because of

high level symmetry of germatranes and the effects of strong coupling AA`XX`-type of protons in $(NCH_2CH_2O)_3$ system. The introduction of substituents at positions 3, 7, and 10 of the atrane core complicates the ^{1}H spectrum too much [9], the analysis of which is a separate goal.

Experiments and results

The main goal of this work is to identify signals in the ^{1}H and ^{13}C NMR spectra of 1-aminoacyloxygermatran (**1**) using homo- and heteronuclear correlation methods J-resolved COSY, COSY, NOESY, HSQC, and HMBC. Figure **2** shows fragments of the ^{1}H and J-COSY spectra, which greatly facilitate the analysis of overlapped regions of the proton spectrum and the isolation of multiplet signals and also the measurement of the scalar constants [2,3]J_{H-H}.
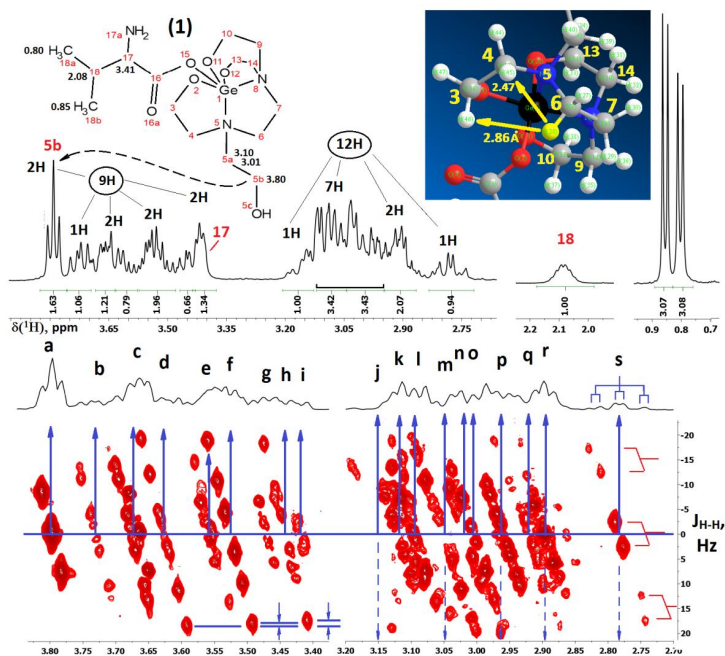

*Figure 2. ^{1}H (left) and J-resolved COSY (right) spectra of 1-aminoacyloxygermatran (**1**). Multiplet structure and shifts of some signals are shown by arrows. Fragment of calculated (MM2) spatial structure of compound (**1**) and atom numbering are presented in a rectangle.*

In the ^{1}H NMR spectrum of compound (**1**) a significant dispersion of signals is observed both in the region of 3.85 – 3.35 ppm, in which the signals of eight protons of the -O-CH_2-groups and the C[17]H proton at 3.41 ppm are located (d, J = 4 Hz, 1H) and in the region of 3.20-2.70 ppm, where the signals of all 12 protons of the N-CH_2 groups are situated. Integration of the signals (see Fig. 2, left) shows that only the region 3.12 – 2.94 ppm turns out to be too overloaded, since there are signals of 7 of the 12 methylene protons at different nitrogen atoms. The multiplet signals of other protons (-N-CH_2-CH_2-O-) belong to weakly coupled spin systems of the AB-XY type and are quite well distinguishable. The only exceptions are the signals of the methylene protons of the mobile fragment N[5]C[5a]H_2C[5b]H_2OH,

one of which ($C^{5b}H_2$) has a characteristic triplet structure at 3.80 ppm, and for the second one the chemical shift difference of geminal protons is equal to 0.087 ppm. So, they form an AB-system in the region 3.15 – 2.97 ppm (see Fig. **3**). The belonging of signals to pseudoequatorial or pseudoaxial protons is easily determined on the basis of the Karplus dependence of vicinal constants on the dihedral angle [16], which leads to the following set of constants for the protons of the ethane fragment in rigid cyclic structures: the sum of the constants (i.e., the multiplet width) for the equatorial proton is always less than for axial. Therefore, the signals with a triplet structure found in the J-COSY spectrum at 3.63 (**d**), 3.53 (**f**) and 3.44 (**h**) ppm (the sum of the constants is about 30 Hz) belong to axial protons, and the signals at 3.73 (**b**), 3.67 (**c**), and 3.56 (**e**) ppm. respectively, equatorial (the sum of the constants is about 22 Hz). The existence of a geminal constant $^2J_{ax-eq} \approx -12$ Hz between axial and equatorial protons and their spatial proximity ($r_{ax-eq} = 1.78$ Å), made it easy to establish 3 pairs of –OCH$_2$-: protons: "**b-d**", "**c-f**" and "**h-e**". These pairs are especially well seen in the NOESY spectrum (Fig. **3**) as intense negative (blue) cross peaks near the diagonal with a positive (red) signal orientation.
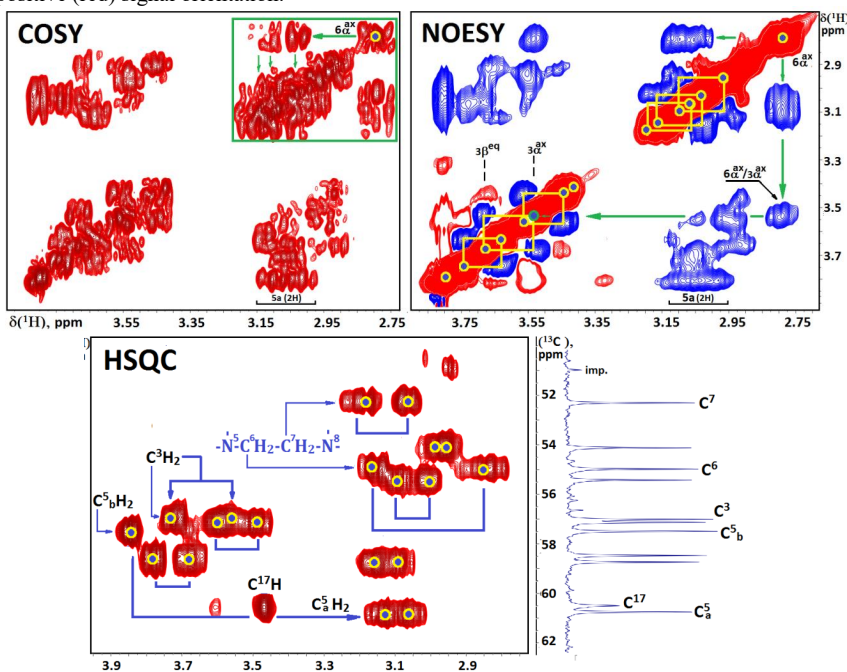

*Figure 3. Fragments of ^{13}C (right) and (left to right) COSY, NOESY and HSQC spectra of 1-aminoacyloxygermatran (**1**). Most important for ^1H and ^{13}C signal assignments scalar and through space interactions (NOEs) are shown by different color lines and arrows.*

Similar geminal pairs of protons can also be found in the region where the signals of NCH$_2$- groups are located. Among them, the signals of protons of the $N^5C^6H^2C^7H_2N^8$ group are the most interesting, since all their signals should be in the region of 3.20–2.70 ppm. Consequently, any of their spatial interactions with the protons of the O–CH$_2$- groups will indicate the spatial proximity of the single $N^5C^6H_2C^7H_2N^8$ fragment to the protons of the

nearest -CH$_2$O- fragment of the neighboring germatrane cycle. This problem was solved by comparing the cross peaks in the COSY and NOESY spectra (Fig. **3**). The first of them clearly shows that the signal at 2.78 ppm (**s**), which has the structure of a triplet of doublets (td, J$_{H-H}$ = 12.6, 12.6, 4.8 Hz, 1 H) and, therefore, it is an axial proton. It has scalar and spatial (NOE) cross peaks only within the 3.20 – 2.98 ppm. region and, consequently, this is one of the axial protons of the desired ethane fragment C^{6}H$_2$-C^{7}H$_2$. Moreover, there is one more cross-peak in the spectrum, linking this proton with the axial proton (at 3.53 ppm. **f**) of one of the -OCH$_2$- groups. According to calculations, only the α-proton at the C^3 atom can be such a proton. So, we can make the reasonable assignments of proton and carbon signals for two adjacent germatrane cycles: Ge-N^5-C^{6}H$_2$-C^{7}H$_2$-N^8 and Ge-N^5-C^{4}H$_2$-C^{3}H$_2$-O^2 (See ^{1}H and ^{13}C assignments in Fig. **3**). Additional independent HMBC data fully confirm the obtained results.

Conclusion

Using various homo- and heteronuclear NMR experiments (J-COSY, COSY, NOESY, HSQC, HMBC), the identification of signals in the ^{1}H and ^{13}C NMR spectra was made for a 1-aminoacyloxygermatran (**1**). The obtained values of chemical shifts and scalar constants ^{2,3}J$_{H-H}$ are the basis for the further active use of NMR spectroscopy in the structural and conformational analysis of new germatrane derivatives with potential biological activity.

Acknowledgments

References

1. S. Gonzalez-Montiel, R. Cea-Olivares, V. Jancik et al. Heteroatom Chem., 2009, 20, 45–49.
2. N.W. Alcock. Adv. Inorg. Chem. Radiochem., 1972, 15, 1–58.
3. R.T. Mertens, S. Parkin, S.G. Awuah. Inorganica Chim. Acta, 2020, 503, 119375.
4. E.N. Nikolaevskaya, P.G. Shangin et al. Inorganica Chim. Acta, 2019, 495, 119007.
5. Y. Takeuchi, Y. Takase. J. Organomet. Chem., 2004, 689, 3275–3277.
6. S.S. Karlov, E.Kh. Lermontova, M.V. Zabalov et al. Inorg. Chem. 2005, 44, 4879–4886.
7. A. Han, L. Li, K. Qing, X. Qi, L. Hou et al. Bioorg. Med. Chem. Lett., 2013, 23, 1310–1314.
8. F. Ye, X. Song, J. Liu, X. Xu, Y. Wang et al., Chem. Biol. Drug Des. 2015, 86, 905–910.
9. S.S. Karlov, G.S. Zaitseva. Chem Heterocycl Compds, 2001, 37, 1325–1327.
10. V.K. Voronov, M.G. Voronkov. Journal of Molecular Structure, 1980, 67, 285–287.
11. É. L. Kupće, É. Lukevits. Khimiya Geterotisiklicheskikh Soed., 1989, 5, 701–703.
12. E. Kupce, R. Freeman. J. Magn. Reson., 1995, A 115, 273–276.
13. Ē. Kupče, L. Frydman, A.G. Webb, J.R. J. Yong. T.D.W. Claridge. Nature Reviews Methods Primers, 2021, 1, Article number: 27.
14. V.K. Voronov. Vestnik RAN, 2022, 92 (9),893–899.
15. E. Lippmaa, M. .Mägi,; M.F. Larin, V.A. Pestunovich, M.G. Voronkov. J. Organomet. Chem. 1979, 171, 301−308.
16. M. Karplus. *J. Am. Che. Soc., 1963, 85 (18), 2870-2871.*

Molecular Dynamics Study of the Process of Extraction Purification of Model Fuel

<u>Kenan Mammadhasanov</u>[1], Sabina A. Seidova[2], Andrei V. Komolkin[1], Minaver D. Ibragimova[2]
[1]*Faculty of Physics, Saint Petersburg State University, 199034, St. Petersburg, Russia*
[2]*Y. H. Mammadaliyev Institute of Petrochemical Processes of Ministry of Science and Education of Republic of Azerbaijan, AZ 1025, Baku, 30 Khojaly ave., Azerbaijan*
E-mail: <u>mammadhasanov@yandex.ru</u>
E-mail: <u>sabina.seidova.ai@mail.ru</u>

Introduction

Currently, the development of effective and economical methods for cleaning the diesel fraction, which ensure the ecology of the fuel, is relevant. Therefore, it is promising to use an alternative hydrogen-free technology in the process of upgrading the diesel fraction, in particular, the extraction purification method, which demonstrates a number of advantages over the existing traditional purification method.

One of the directions in the development of extraction purification methods is the use of solvents – ionic liquids – that obey the principles of "green" chemistry as an extractant in the extraction process.

The unique properties of ionic liquids, such as chemical and thermal stability, low volatility, low toxicity, high selectivity with respect to the extracted components, easy regeneration and the possibility of reuse without reducing the extraction ability, make ionic liquids attractive in the extraction purification of petroleum fractions. In this regard, the replacement of organic volatile solvents in the process of extraction purification with "green solvents" – ionic liquids has become one of the actively developed approaches to solving the environmental problem associated with the negative impact of traditional solvents on the environment.

In order to improve the method of ion-liquid extraction purification, it is of great interest to study the process of selective purification by modern computer methods, often by the method of molecular dynamics simulation.

Computer model

Simulation of the process of extraction purification of model diesel distillate with thiophene-3-trimethylammonia thiophene-2-carboxylate ionic liquid was carried out using the AKMD molecular dynamics program.

The model fuel was a mixture of n-hexane, thiophene and m-xylene. The content of thiophene corresponded to the content of sulfur compounds in the real straight-run diesel fraction and amounted to 0.85 wt%, and the content of m-xylene was 16 wt%. The model fuel and the ionic liquid were placed in the simulation cell as layers. Simulation was performed in *NpT* ensemble at normal pressure. Temperature of the system changed during simulation from +75 °C down to –50 °C in order to estimate temperature dependence of extraction ability of the ionic liquid. Total simulation time was 0.6 μs.

Results and discussion

During simulation, some of the thiophene molecules were attracted by the thiophene-based ionic liquid. Concentration of thiophene in the layer of 6 Å around ionic liquid was higher than in bulk fuel.

Efficiency of the thiophene-based ionic liquid for the extraction purification of model fuel with respect to N-methylpyrrolidonium acetate is discussed in the report.

Tautomeric transformations N- and C-acyl derivatives of tetrahydro-1,4-diazepines

N.A. Anisimova[1,2], D.A. Melkova[1]
[1]*The Herzen State Pedagogical University of Russia, St. Petersburg, Russia*
[2]*Saint-Petersburg State University of Industrial Technologies and Design, St. Petersburg, Russia*
E-mail: mall30@mail.ru

It is well known that diazepines are structural fragments of biologically active natural (streptocarbazoles A and B1) and synthetic compounds. Based on diazepines, a wide range of drugs have been already obtained. For example, diazepines are used as effective tranquilizers (diazepam, lorazepam), hypnotics (bromazepam, phenazepam), and CNS depressants [1].

The interaction of 14-membered azamacrocycle (**1**) with chloroacetic acid chloride was used to obtain representatives of N-(**2**) and C-(**3a, b**) acyl derivatives of tetrahydro-1,4-diazepines according to the procedure we previously described [2]. Separation of N- and C-acyl diazepines was carried out by column chromatography.
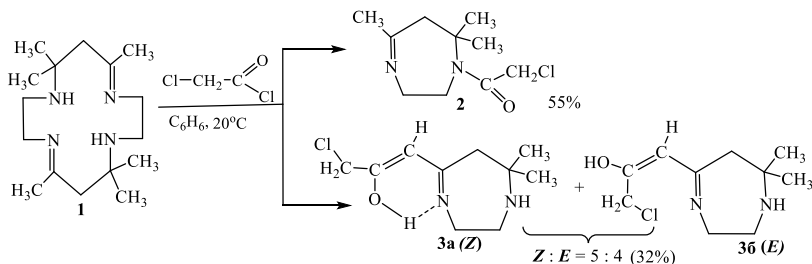

Figure 1. Interaction of 14-membered azamacrocycle (1) with chloroacetic acid chloride

Using ^{1}H, ^{13}C NMR, HMQC, HMBC, COZY spectroscopy, we studied the tautomeric transformations of the obtained N-(**2**) and C-(**3a,b**) acyl derivatives of tetrahydro-1,4-diazepines. It was shown that N-acyldiazepine (**2**) exists in the CD_3OD solution in the keto-imine form, while C-acyldiazepines (**3a,b**) exist in the enol-imine form. In a DMSO solution, both types of acyldiazepines (**2, 3 a,b**) acquire the corresponding keto- and enol-enamine forms.
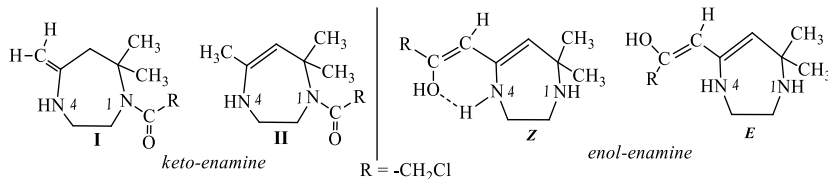

Figure 2. Keto and enol-enamine forms of diazepines (2,3 a,b) in DMSO solution

References

1. N. A. Meanwell, M.A. Walker. – *Comprehensive Heterocyclic Chemistry III*, 13, 183-235 (2008).
2. N. A. Anisimova, D. A. Melkova. – *Russian Journal of General Chemistry,* 12, 2809-2815 (2022).

Cogwheel phase cycling for T_2-T_2 exchange NMR

Ivan Mershiev, Galina Kupriyanova

Institute of Physics, Mathematics and Information Technology, Immanuel Kant Baltic Federal University, 236041, Kaliningrad, Russia

IMershiev@kantiana.ru

Introduction

T_2-T_2 exchange experiment is an NMR method used for observing molecular mobility and fluid dynamics in porous media. By obtaining a two-dimensional T_2 relaxation times distribution, it is possible to find correlation between sites with different relaxation rate and study the effects of molecular exchange. However, the pulse sequence is susceptible to effects of field inhomogeneity, as undesired spin echoes interfere with CPMG echo train. In this work, we propose a phase cycling scheme for T_2-T_2 exchange with enhanced suppression of artifacts.

Cogwheel phase cycling

Cogwheel phase cycling is a method for constructing phase cycles proposed by M. Levitt [1]. It is based on selection of relative phases for different parts of the pulse sequence, or "pulse blocks", depending on the overall change of coherence order at the end of the block. Phases within the pulse block may be cycled independently.
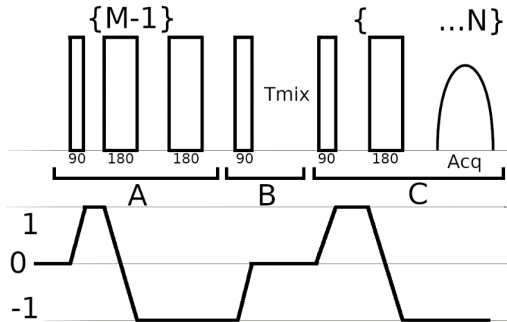

Figure 1. Pulse sequence and coherence pathway diagrams for T_2-T_2 exchange experiment.

T_2-T_2 exchange sequence can be divided into three blocks A, B and C: first, a CPMG sequence with variable number of refocusing pulses; second, a single 90° pulse that returns magnetization to the longitudinal direction, followed by a mixing delay; and a second GPMG sequence for signal acquisition. For phase cycling within CPMG blocks, we chose an 8-step variant of EXORCYCLE phase cycling scheme: [$\varphi_{90°}$, φ_{Acq}; $\varphi_{180°}$]=[0 0 1 1 2 2 3 3; 1 3 0 2 1 3 0 2]. It proved itself reliable for cancelling FID signals and additionally compensating for the effects of field inhomogeneity. According to [1], the relative phases of phase blocks depend on change of coherence order at the end of each block. Pulse sequence starts at coherence level 0, and signal detection corresponds to coherence level -1. Relative coherence changes between blocks will be p_0=[0, p^0_{AB}, p^0_{BC}, -1]=
[0, -1, 0, -1]. Using the prediction formulas for optimal cogwheel parameters

$$N = (p_{max} + 1 + |p^0_{AB}|)(p_{max} + 1 + |p^0_{BC}|) - 4|p^0_{AB}||p^0_{BC}|$$
$$\Delta\gamma_{AB} = (signp^0_{AB})(p_{max} + 1 - |p^0_{BC}|)$$
$$\Delta\gamma_{BC} = (signp^0_{BC})(p_{max} + 1 - |p^0_{AB}|)$$

leads to [N, $\Delta\gamma_{AB}$, $\Delta\gamma_{BC}$]=[2, -1, 0], where N is a number of required phase steps and $\Delta\gamma$ is a relative phase change. The overall phase cycling scheme, obtained by combining cogwheel phases with EXORCYCLE phases for CPMG sequences, is shown in Table 1.
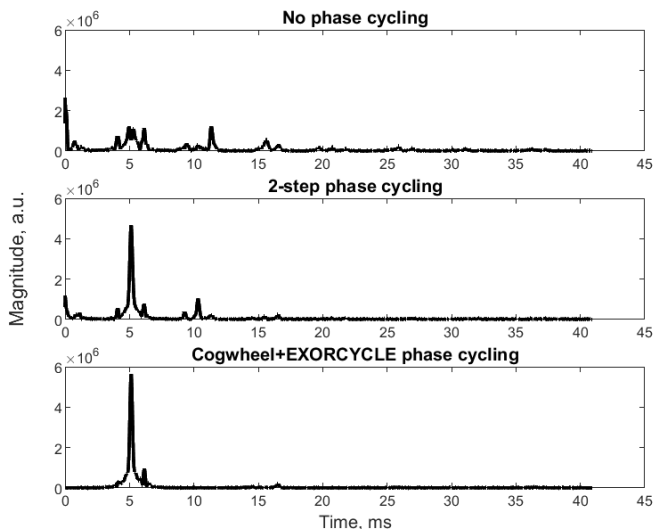

Figure 2. Comparison of echo signals detected using T_2-T_2 exchange sequence (M=6, N=1) using different phase cycling schemes.

Experimental results

To test the phase cycling scheme, T_2-T_2 experiments were performed with the detection of a single echo at the third block of pulse sequence, i. e. at N=1. The inhomogeneity of the 300 mT magnet field in the probe volume was 100 ppm. Compared to 2-step phase cycling, 16-step phase cycling provides full suppression of FID signal and enhanced suppression of most artifacts at multiples to T_{echo} and T_{mix}, as well as a 20% increase of echo magnitude. The results can be used to improve T_2-T_2 exchange NMR measurements in low and inhomogeneous fields.

Table 1.

Phase cycling	$90°_M$	$180°_M$	$90°_{mix}$	$90°_N$	$180°_N$	Acq.
Ref.[2,3], 2 steps	0 0	1 1	0 2	0 0	1 1	1 3
Cogwheel+EXORCYCLE, 16 steps	0 0 1 1	1 3 0 2	2 2 3 3	0 0 1 1	1 3 0 2	0 0 1 1
	2 2 3 3	1 3 0 2	0 0 1 1	2 2 3 3	1 3 0 2	2 2 3 3
	2 2 3 3	3 1 2 0	0 0 1 1	2 2 3 3	3 1 2 0	2 2 3 3
	0 0 1 1	3 1 2 0	2 2 3 3	0 0 1 1	3 1 2 0	0 0 1 1

References

1. Levitt M.H., Madhu P.K., Hughes C.E. Cogwheel phase cycling // J. Magn. Reson. 2002. Vol. 155, № 2. P. 300–306.
2. D'Eurydice M.N. et al. T_2-Filtered T_2-T_2 Exchange NMR // J. Chem. Phys. 2016. Vol. 144, № 20.
3. Montrazi E.T. et al. Simultaneous acquisition for T_2-T_2 Exchange and T_1-T_2 correlation NMR experiments // J. Magn. Reson. Elsevier Inc., 2018. Vol. 289. P. 63–71.

Molecular dynamics study of complex formation of the dendrigraft DG2 with charged oligopeptides AED, GED and ED

Emil I. Fatullaev[1], Sofia E. Mikhtaniuk[1], Valerii V. Bezrodnyi[2], Oleg V. Shavykin[1,3,4], Igor M. Neelov[1,5]

[1]*ITMO University, Kronverkskiy pr. 49, 197101 St. Petersburg, Russia*
[2]*St. Petersburg State University, 7/9 Universitetskaya nab., 199034 St. Petersburg, Russia*
[3]*Lomonosov Moscow State University, Leninskie Gory 1-2, 119991 Moscow, Russia*
[4]*Tver State University, Sadoviy per., 35, 170102 Tver, Russia*
[5]*Institute of Macromolecular Compounds RAS, Bolshoy pr.V.O. 31, St. Petersburg, Russia*
E-mail: i.neelov@mail.ru

Introduction

Dendrimers and dendrigrafts are widely used as nanocontainers for drug delivery and biological molecule transport. Lysine-based dendrimers and dendrigrafts are preferred due to their lower toxicity compared to synthetic analogues. The aim of this study was to investigate the possibility of complex formation between a lysine dendrigraft (DG2) and 16 peptides (AED, GED, and ED).

The model and method

Molecular dynamics simulations were used to study the interaction between the lysine dendrigraft DG2 and the therapeutic peptides AED, GED, and ED. The potential energy in the MD method included the energy of valence bonds, valence and dihedral angles, as well as the energy of van der Waals and Coulomb interactions. The Gomacs program with Amber forcefield, Tip3p water model and PME method for electrostatic interactions were used in all simulations.

The equilibrium properties of complexes

To determine the number of peptides in dendrigraft-peptide complexes, a simple local criterion was used:

$$r_{ij} < s \cdot r_{ij,min}$$

This criterion measured the distance between the i-th atom of the dendrimer and the j-th atom of the tetrapeptide, and compared it to the distance at which the potential of non-bonded interactions reached a minimum for the respective types of atoms i and j. If at least one peptide atom and one dendrigraft atom satisfied the criterion, it was assumed that the peptide is in complex.

The time dependencies of the gyration radius of complexes are shown on Figure 1. The average size of the complex with AED peptide is 1.73 nm according to the local criteria, the size of dendrigraft in this complex is 1.57 nm. For the complex with GED peptides these values are 1.67 nm and 1.55 nm, for the complex with ED peptide 1.63 nm and 1.56 nm respectively. The Figure 2abc depicts the instantaneous numbers of 16AED, 16GED, and 16ED peptide molecules in complexes with dendrigraft DG2 at various times. The slope of initial linear section of the peptide number versus time characterizes the rate of complex formation. A molecule of peptide consisting of only two negatively charged amino acids (ED) forms the complex faster due to its small size (easier penetration into the dendrigraft interior and uniform charge distribution). It is evident that this number swings mainly between 14 and 16 for all systems. The average number of peptide molecules in three complexes is close to 15. Therefore, the ability of dendrigraft to transport these peptide molecules is pretty equal independently of presence of hydrophobic alanine or glycine residues in the peptide.
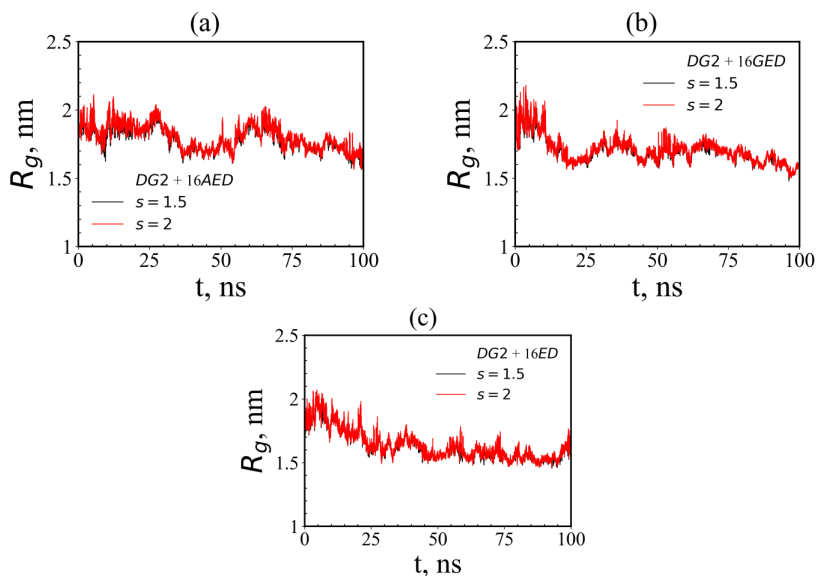
Figure 1. Dependences on time of the gyration radius Rg(t) of complexes for systems: (a) DG2+16AED, (b)DG2+16GED, (c) DG2+16ED at T=300 K, P=1 atm
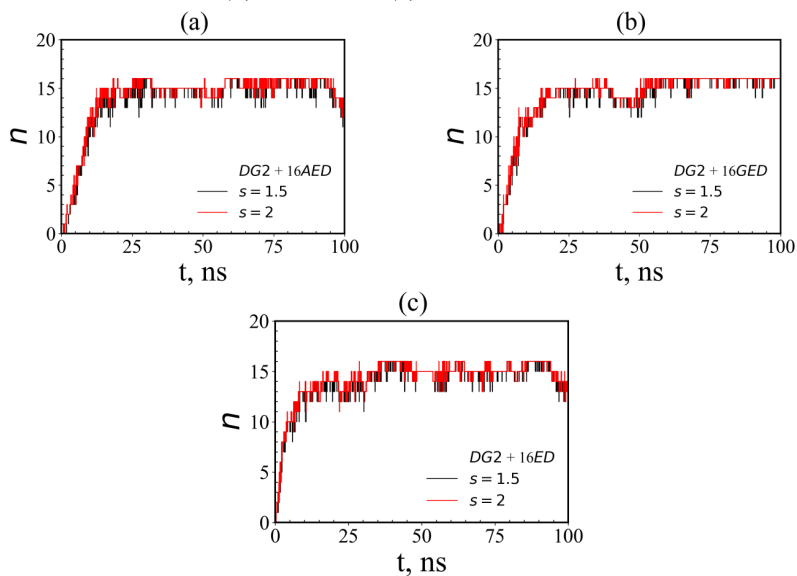

Figure 2. Dependences on time of the number of peptides in complexes for systems: (a) DG2+16AED, (b)DG2+16GED, (c) DG2+16ED at T=300 K, P=1 atm

These dendrigrafts can be used in the future to deliver molecules of these and similar therapeutic peptides to various cells and organs [1-41].

Acknowledgments

References

1. Sheveleva N.N., Markelov D.A., Vovk M.A. Mikhailova, M.E., Tarasenko I.I, Neelov I.M., E.Lähderanta. Scientific Reports, 2018, 8, 8916.
2. Sheveleva N.N., Markelov D.A., Vovk M.A., Tarasenko I.I, Neelov I.M., E.Lähderanta, 2019, RSC Adv. 9, 18018.
3. Sheveleva N.N., Markelov D.A., Vovk M.A., Tarasenko I.I, Mikhailova M.E., Neelov I.M., 2019, Molecules, 24, 2481.
4. M.Gorzkiewicz, O.Kopec, A.Janaszevska, I.I.Tarasenko, N.N.Sheveleva, I.M. Neelov, B.Klajnert, Bioorg.Chem. 2020, 95, 103504.
5. M. Gorzkiewicz,, A.Konopka, A.Janaszewska, A., I.I.Tarasenko, V.V.Bezrodnyi. I.M. Neelov, B.Klajnert, Int. J. Mol. Sci., 2020, 21 (9), 3138.
6. Denkewalter R.G., Kolc J., Lukasavage W.J., US Patent, 1983, № 4410688.
7. Neelov, I. M., Markelov D.A, Falkovich S.G., Ilyash M.Y., Okrugin B.M., Darinskii A.A., Polymer Science, 2013, 55, 154.
8. S. Falkovich, D. Markelov, I. Neelov, and A. Darinskii. J. Chem. Phys. 2013, 139, 064903.
9. Neelov, I., Markelov D., Falkovich S.G., Paci E., Darinskii A., Tenhu H., Dendrimers in Biomedical Applications, (London: RSC) 2013, 99-114.
10. Gotlib, Y.Y., Darinskii, A.A., Neelov, I.M., Balabaev, N.K. Macromolecules, 1980, 13(3), pp. 602–608
11. Darinskii A., Lyulin A., Neelov I., Makromolekulare Chemie - Theory and Simulations (Macromolecular Theory and Simulations), 1993, 2, 523.
12. Neelov I.M., Adolf D.B., Lyulin AV., Davies G.R. J. Chem. Phys., 2002, 117,4030.
13. Zarembo, A., Balabaev, N.K., Neelov, I.M., Sundholm, Darinskii, A.A., F. PCCP, 2003, 5(11), 2410–2416.
14. Neelov I.M., Adolf D.B., McLeish T.C.B., Paci E., Biophys. J., 2006, 91, 3579.
15. Gowdy, J., Batchelor, M, Neelov, I, Paci, E. J. Phys. Chem. B, 2017, 121, 9518.
16. Neelov I.M., Binder K., Macromolecular Theory and Simulations, 1995, 4, 1063.
17. Neelov, I.M., Binder, K. Macromol. Theory&Simul., 1995, 4(1), pp. 119–136,
18. Ennari J., Neelov I., Sundholm F., Polymer, 2000, 41, 4057.
19. Ennari J., Neelov I., Sundholm F., Polymer, 2001, 42, 8043
20. Darinskii A., Gotlib Yu., Lukyanov M., Lyulin A., Neelov I., Progress in Colloid & Polymer Science, 1993, 91, 13.
21. Ennari J., Neelov I., Sundholm F., Comput. Theor. Polym. Sci., 2000, 10, 403.
22. Ennari J., Elomaa M., Neelov I., Sundholm F., 2000, Polymer, 41, 985.
23. Darinskii A., Gotlib Yu., Lyulin A., Neelov I., Vysokomolek. Soed.. Ser,A 1991, 33, 1211 (translation to English: Polymer Science, 33,1116).
24. Ennari J., Neelov I., Sundholm F., Polymer, 2004, 45, 4171.
25. Ennari J., Neelov I., Sundholm F., Polymer, 2000, 41, 2149
26. Mazo M.A., Shamaev M.Y., Balabaev N.K., Darinskii A.A., Neelov I.M., Physical Chemistry Chemical Physics, 2004, 1285.
27. Okrugin B., Ilyash M., Markelov D., Neelov I., Pharmaceutics, 2018, 10, 129.
28. Neelov I.M., Adolf D.B., 2003, Macromolecules, 36, 6914.
29. Neelov I.M., Adolf D.B., 2004, J. Phys. Chem. B, 108, 7627.
30. O.V.Shavykin, I.M.Neelov, A.A.Darinskii. PCCP, 2016, 18, 24307

31. Shavykin O.V., Mikhailov I.V., Darinskii A.A., Neelov I.M., Leermakers F.A.M., Polymer, 2018,146, 256.
32. Okrugin B.M., Neelov I.M., Leermakers F., Borisov O.V.,Polymer,2017,125 292.
33. Shavykin O.V., Leermakers F., Neelov I.M., Darinskii A.A.,Langmuir, 2018,34, 1613.
34. Mikhtaniuk, S.E., Bezrodnyi, V.V., Shavykin, O.V., Neelov I.M., Penkova, A.V., Markelov, D.A., Polymers,2020,12(8),1657.
35. Shavykin, O.V., Neelov, I.M., Borisov, O.V., Darinskii, A.A., Leermakers, F.A.M.,Macromolecules, 2020, 53(17), pp. 7298–7311.
36. Bezrodnyi, V.V., Shavykin, O.V., Mikhtaniuk, S.E., Neelov I.M., Sheveleva, N.N., Markelov, D.A., International Journal of Molecular Sciences, 2020, 21, 1–22, 9749.
37. NN Sheveleva, VV Bezrodnyi, SE Mikhtaniuk, OV Shavykin, IM Neelov, D.A.Markelov, Macromolecules, 2021, 54 (23), 11083.
38. N.N. Sheveleva, I.I. Tarasenko, M.A. Vovk, M.E. Mikhailova, I.M. Neelov, D.A.Markelov, International Journal of Molecular Sciences, 2023, 24 (2), 949.
39. OV Shavykin, SE Mikhtaniuk, EI Fatullaev, IM Neelov, FAM Leermakers, A.A.Darinskii, International Journal of Molecular Sciences, 2023, 24 (3), 2078.
40. E.I.Fatullaev, O.V.Shavykin, I.M.Neelov, M.E. Brito, C.Holm, A.A.Darinskii, International Journal of Molecular Sciences 24 (4), 3063.
41. M.E. Brito, S.E. Mikhtaniuk, I.M. Neelov, O.V. Borisov, C.Holm, International Journal of Molecular Sciences, 2023, 24 (3), 2763.
42. Sadovnichy, V.; Tikhonravov, A.; Voevodin, V.; Opanasenko, V. "Lomonosov": Supercomputing at Moscow State University. In Contemporary High Performance Computing: From Petascale toward Exascale; Chapman and Hall/CRC: Boca Raton, FL, USA, 2013; pp. 283–307.

Investigation of complex formation by Lys-2Leu dendrimer with oligopeptides of different degree of hydrophobicity

Emil I. Fatullaev[1], Sofia E. Mikhtaniuk[1], Valerii V. Bezrodnyi[2], Oleg V. Shavykin[1,3,4], Igor M. Neelov[1,5]

[1]*ITMO University, Kronverkskiy pr. 49, 197101 St. Petersburg, Russia*
[2]*St. Petersburg State University, 7/9 Universitetskaya nab., 199034 St. Petersburg, Russia*
[3]*Lomonosov Moscow State University, Leninskie Gory 1-2, 119991 Moscow, Russia*
[4]*Tver State University, Sadoviy per., 35, 170102 Tver, Russia*
[5]*Institute of Macromolecular Compounds RAS, Bolshoy pr.31, 199004,St. Petersburg, Russia*
E-mail: i.neelov@mail.ru

Introduction

Dendrimers are nanoscale molecules that are composed of a central core, branched repetitive blocks, and end groups. However, high-generation dendrimers are not suitable for biomedical applications due to the high number of charged end groups, which makes them toxic. One way to overcome this issue is to use lower-generation peptide dendrimers and modify them with amino acid inserts between all branching points. This study aims to explore the possibility of using the lysine dendrimer Lys2Leu, which has leucine amino acid dipeptide spacers, as drug carriers for delivering 16 biologically active tetrapeptides such as Ala-Glu-Asp-Gly (AEDG), Ala-Gly-Ala-Gly (AGAG), and Ala-Leu-Leu-Gly (ALLG).

The model and method

To investigate the interaction between the dendrimer and peptides, molecular dynamics simulations were conducted in an aqueous solution with explicit counterions at a temperature of T=310 K and a pressure of P=1 atm using the Gromacs 4.5.6 software package [1-41]. The snapshots of the first system with AEDG peptides at times t =0 ns and t = 300 ns are shown on Figure 1.
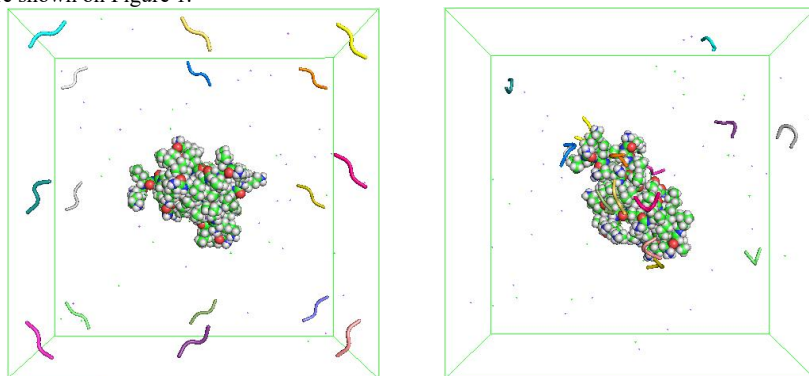

Figure 1. Initial and final stages of formation of the dendrigraft DG2 and 16 AEDG peptide complex at t = 0 (left) and t = 300 ns (right)

The equilibrium properties of complexes

The results revealed that negatively charged AEDG peptides formed the most stable and compact complexes with dendrimer Lys-2Leu, with 8 out of 16 peptides forming these complexes (see Table 1). The most hydrophobic peptide ALLG formed a complex with 6 out

of 16 peptides, whereas the AGAG peptide formed a complex with only 2 out of 16 peptides. The study also investigated the internal structure of the formed complexes, and the radial atom group density distribution functions were obtained.

Table 1. The radius of gyration of Lys-2Leu dendrimer in complex Lys-2Leu+16AEDG (or 16AGAG and 16ALLG), the radius of gyration of complex Lys-2Leu+16AEDG (or 16AGAG and 16ALLG), and the number of peptide molecules in complex Lys-2Leu+16AEDG (or 16AGAG and 16ALLG). Two parameters s=1.5 and 2 were used to determine that any peptide's atom is close to any dendrimer's atom, and, as can be seen from the table, the results are practically independent of the parameter's value)

	K2L-16AEDG		K2L-16AGAG		K2L-16ALLG	
	s=1.5	s=2	s=1.5	s=2	s=1.5	s=2
$Rg^{lc}_{complex}$	1.41	1.44	1.22	1.25	1.27	1.30
$Rg^{lc}_{dendrimer}$	1.12	1.12	1.11	1.11	1.06	1.06
n^{lc}	7.85	8.25	2.29	2.63	6.05	6.39

While the electrostatic interaction between the positively charged end groups of the dendrimer and the negatively charged groups of the peptides played a significant role in the formation of complexes, hydrophobic interactions were also important for transferring hydrophobic molecules by the dendrimer with hydrophobic inserts.

Acknowledgments

References

1. Sheveleva N.N., Markelov D.A., Vovk M.A. Mikhailova, M.E., Tarasenko I.I, Neelov I.M., E. Lähderanta; Scientific Reports, 2018, 8, 8916
2. Sheveleva N.N., Markelov D.A., Vovk M.A., Tarasenko I.I, Neelov I.M., E.Lähderanta, 2019, RSC Adv. 9, 18018.
3. Sheveleva N.N., Markelov D.A., Vovk M.A., Tarasenko I.I, Mikhailova M.E., Neelov I.M., 2019, Molecules, 24, 2481
4. M.Gorzkiewicz, O.Kopec, A.Janaszevska, I.I.Tarasenko, N.N.Sheveleva, I.M. Neelov, B.Klajnert, Bioorg.Chem. 2020, 95, 103504.
5. M. Gorzkiewicz,, A.Konopka, A.Janaszewska, A., I.I.Tarasenko, V.V.Bezrodnyi. I.M. Neelov, B.Klajnert, Int. J. Mol. Sci., 2020, 21 (9), 3138.
6. Denkewalter R.G., Kolc J., Lukasavage W.J., US Patent, 1983, № 4410688.
7. Neelov, I. M., Markelov D.A, Falkovich S.G., Ilyash M.Y., Okrugin B.M., Darinskii A.A., Polymer Science, 2013, 55, 154.
8. S. Falkovich, D. Markelov, I. Neelov, and A. Darinskii. J. Chem. Phys. 2013, 139, 064903.
9. Neelov, I., Markelov D., Falkovich S.G., Paci E., Darinskii A., Tenhu H., Dendrimers in Biomedical Applications, (London: RSC) 2013, 99-114.
10. Gotlib, Y.Y., Darinskii, A.A., Neelov, I.M., Balabaev, N.K. Macromolecules, 1980, 13(3), pp. 602–608
11. Darinskii A., Lyulin A., Neelov I., Makromolekulare Chemie - Theory and Simulations (Macromolecular Theory and Simulations), 1993, 2, 523.

12. Neelov I.M., Adolf D.B., Lyulin AV., Davies G.R.; J. Chem. Phys., 2002, 117,4030.
13. Zarembo, A., Balabaev, N.K., Neelov, I.M., Sundholm, Darinskii, A.A., , F. PCCP, 2003, 5(11), 2410–2416
14. Neelov I.M., Adolf D.B., McLeish T.C.B., Paci E., Biophys. J., 2006, 91, 3579.
15. Gowdy, J., Batchelor, M, Neelov, I, Paci, E. J. Phys. Chem. B, 2017, 121, 9518.
16. Neelov I.M., Binder K., Macromolecular Theory and Simulations, 1995, 4, 1063.
17. Neelov, I.M., Binder, K. Macromol. Theory&Simul/, 1995, 4(1), pp. 119–136
18. Ennari J., Neelov I., Sundholm F., Polymer, 2000, 41, 4057.
19. Ennari J., Neelov I., Sundholm F., Polymer, 2001, 42, 8043
20. Darinskii A., Gotlib Yu., Lukyanov M., Lyulin A., Neelov I., Progress in Colloid & Polymer Science, 1993, 91, 13.
21. Ennari J., Neelov I., Sundholm F., Comput. Theor. Polym. Sci., 2000, 10, 403.
22. Ennari J., Elomaa M., Neelov I., Sundholm F., 2000, Polymer, 41, 985.
23. Darinskii A., Gotlib Yu., Lyulin A., Neelov I., Vysokomolek. Soed.. Ser,A 1991, 33, 1211 (translation to English: Polymer Science, 33,1116).
24. Ennari J., Neelov I., Sundholm F., Polymer, 2004, 45, 4171.
25. Ennari J., Neelov I., Sundholm F., Polymer, 2000, 41, 2149.
26. Mazo M.A., Shamaev M.Y., Balabaev N.K., Darinskii A.A., Neelov I.M., Physical Chemistry Chemical Physics, 2004, 1285.
27. Okrugin B., Ilyash M., Markelov D., Neelov I., Pharmaceutics, 2018, 10, 129.
28. Neelov I.M., Adolf D.B., 2003, Macromolecules, 36, 6914.
29. Neelov I.M., Adolf D.B., 2004, J. Phys. Chem. B, 108, 7627.
30. O.V.Shavykin, I.M.Neelov, A.A.Darinskii. PCCP, 2016, 18, 24307
31. Shavykin O.V., Mikhailov I.V., Darinskii A.A., Neelov I.M., Leermakers F.A.M., Polymer, 2018,146, 256.
32. Okrugin B.M., Neelov I.M., Leermakers F., Borisov O.V., Polymer, 2017, 125, 292.
33. Shavykin O.V., Leermakers F.A.M., Neelov I.M., Darinskii A.A., Langmuir, 2018, 34, 1613.
34. Mikhtaniuk, S.E., Bezrodnyi, V.V., Shavykin, O.V., Neelov I.M., Penkova, A.V., Markelov, D.A., Polymers,2020,12(8),1657
35. Shavykin, O.V., Neelov, I.M., Borisov, O.V., Darinskii, A.A., Leermakers, F.A.M.,Macromolecules, 2020, 53(17), pp. 7298–7311
36. Bezrodnyi, V.V., Shavykin, O.V., Mikhtaniuk, S.E., Neelov I.M., Sheveleva, N.N., Markelov, D.A., International Journal of Molecular Sciences, 2020, 21(24), 1–22, 9749
37. NN Sheveleva, VV Bezrodnyi, SE Mikhtaniuk, OV Shavykin, IM Neelov, D.A.Markelov, Macromolecules, 2021, 54 (23), 11083
38. N.N. Sheveleva, I.I. Tarasenko, M.A. Vovk, M.E. Mikhailova, I.M. Neelov, D.A.Markelov, International Journal of Molecular Sciences, 2023, 24 (2), 949
39. OV Shavykin, SE Mikhtaniuk, EI Fatullaev, IM Neelov, FAM Leermakers, A.A.Darinskii, International Journal of Molecular Sciences, 2023, 24 (3), 2078
40. E.I.Fatullaev, O.V.Shavykin, I.M.Neelov, M.E. Brito, C.Holm, A.A.Darinskii, International Journal of Molecular Sciences 24 (4), 3063
41. M.E. Brito, S.E. Mikhtaniuk, I.M. Neelov, O.V. Borisov, C.Holm, International Journal of Molecular Sciences, 2023, 24 (3), 2763
42. Sadovnichy, V.; Tikhonravov, A.; Voevodin, V.; Opanasenko, V. "Lomonosov": Supercomputing at Moscow State University. In Contemporary High Performance Computing: From Petascale toward Exascale; Chapman and Hall/CRC: Boca Raton, FL, USA, 2013; pp. 283–307.

The SCF study of micelle formation of the amphiphilic hybrid molecules consisting of a polylysine dendron with several hydrophobic tails

<u>*Sofia E. Mikhtaniuk*</u>[1], *Emil I. Fatullaev*[1], *Valerii V. Bezrodnyi*[2], *Oleg V. Shavykin*[1,3,4], *Anatoly A. Darinskii*[5], *Igor M. Neelov*[1,5]

[1]*ITMO University, Kronverkskiy pr. 49, 197101 St. Petersburg, Russia*
[2]*St. Petersburg State University, 7/9 Universitetskaya nab., 199034 St. Petersburg, Russia*
[3]*Lomonosov Moscow State University, Leninskie Gory 1-2, 119991 Moscow, Russia*
[4]*Tver State University, Sadoviy per., 35, 170102 Tver, Russia*
[5]*Institute of Macromolecular Compounds RAS, Bolshoy pr.V.O. 31, St. Petersburg, Russia*
E-mail: <u>*i.neelov@mail.ru*</u>

Introduction

Dendromicelles, which are hybrid molecules consisting of dendritic and linear units, show great potential for drug delivery due to their unique properties. Lysine dendrons are specifically well-suited for this purpose because of their low cytotoxicity and ability to break down naturally. In this study, we used the SCF approach to investigate the formation and characteristics of spherical micelles made of hybrid linear-dendritic molecules with multiple linear hydrophobic tails, which could be used for drug delivery applications.

The model and method

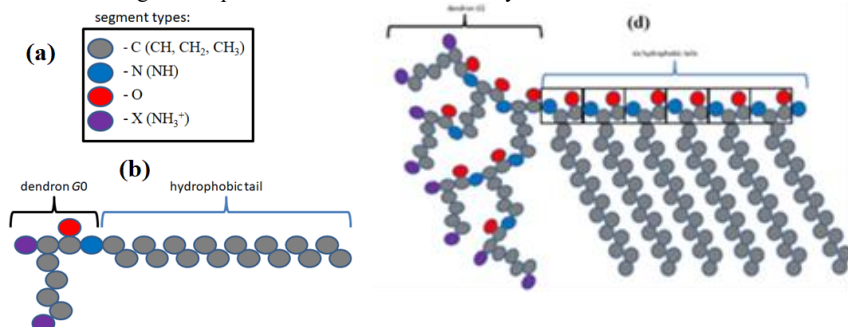The Figure 1 depicts the schematic models of hybrid linear-dendritic molecules.

Figure 1. The united atom model of surfactant molecules: (a) segment types, (b)dendron of 0-th generation with one hydrophobic tail (d) dendron of 2-nd generation with six hydrophobic tails.

First, we identified the barriers between different micelle morphologies by analyzing the relationships between the large thermodynamic potential, chemical potential, and aggregation number. The results revealed that the spherical morphology is most common at short tail length values, while the cylindrical morphology becomes more dominant as the tail length increases. The lamellar morphology only takes over at higher tail length values.

We also studied the relationship between the inner structure of the spherical micelles and the structure of the hybrid molecules. It was found that splitting a single hydrophobic tail into smaller ones reduced the aggregations number and the core radius whereas increasing the total number of hydrophobic segments in the linear part of molecule increases these characteristics (see Figure 2a,b). These findings could have important implications for the development of dendromicelles for drug delivery applications (1-41).
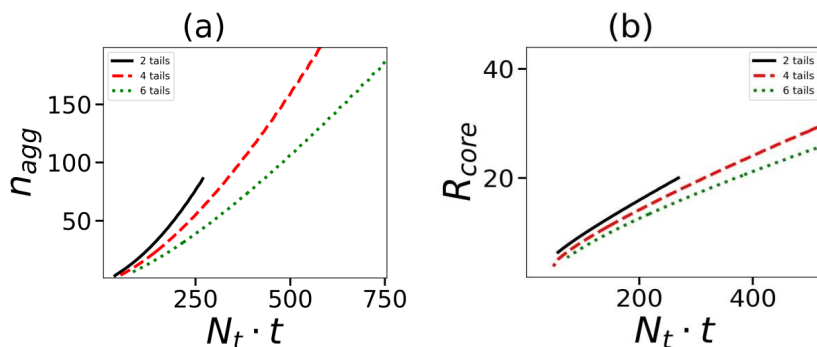
Figure 2. Dependences of the aggregation number nagg (a) and micelle core size Rcore (b) on the total number of monomers in the tails Nt · t for hybrid molecules G = 4

Acknowledgments

References

1. Sheveleva N.N., Markelov D.A., Vovk M.A., Mikhailova M.E., Tarasenko I.I, Neelov I.M., E. Lähderanta; Scientific Reports, 2018, 8, 8916
2. Sheveleva N.N., Markelov D.A., Vovk M.A., Tarasenko I.I, Neelov I.M., E.Lähderanta, 2019, RSC Adv. 9, 18018.
3. Sheveleva N.N., Markelov D.A., Vovk M.A., Tarasenko I.I, Mikhailova M.E., Neelov I.M., 2019, Molecules, 24, 2481
4. M.Gorzkiewicz, O.Kopec, A.Janaszevska, I.I.Tarasenko, N.N.Sheveleva, I.M. Neelov, B.Klajnert, Bioorg.Chem. 2020, 95, 103504.
5. M. Gorzkiewicz,, A.Konopka, A.Janaszewska, A., I.I.Tarasenko, V.V.Bezrodnyi. I.M. Neelov, B.Klajnert, Int. J. Mol. Sci., 2020, 21 (9), 3138.
6. Denkewalter R.G., Kolc J., Lukasavage W.J., US Patent, 1983, № 4410688.
7. Neelov, I. M., Markelov D.A, Falkovich S.G., Ilyash M.Y., Okrugin B.M., Darinskii A.A., Polymer Science, 2013, 55, 154.
8. S. Falkovich, D. Markelov, I. Neelov, and A. Darinskii. J. Chem. Phys. 2013, 139, 064903.
9. Neelov, I., Markelov D., Falkovich S.G., Paci E., Darinskii A., Tenhu H., Dendrimers in Biomedical Applications, (London: RSC) 2013, 99-114.
10. Gotlib, Y.Y., Darinskii, A.A., Neelov, I.M., Balabaev, N.K. Macromolecules, 1980, 13(3), pp. 602–608
11. Darinskii A., Lyulin A., Neelov I., Makromolekulare Chemie - Theory and Simulations (Macromolecular Theory and Simulations), 1993, 2, 523.
12. Neelov I.M., Adolf D.B., Lyulin AV., Davies G.R. J. Chem. Phys., 2002, 117, 4030.
13. Zarembo, A., Balabaev, N.K., Neelov, I.M., Sundholm, Darinskii, A.A., , F. PCCP, 2003, 5(11), 2410–2416
14. Neelov I.M., Adolf D.B., McLeish T.C.B., Paci E., Biophys. J., 2006, 91, 3579.
15. Gowdy, J., Batchelor, M, Neelov, I, Paci, E. J. Phys. Chem. B, 2017, 121, 9518.
16. Neelov I.M., Binder K., Macromolecular Theory and Simulations, 1995, 4, 1063.
17. Neelov, I.M., Binder, K. Macromol. Theory&Simul/, 1995, 4(1), pp. 119–136

18. Ennari J., Neelov I., Sundholm F., Polymer, 2000, 41, 4057.
19. Ennari J., Neelov I., Sundholm F., Polymer, 2001, 42, 8043
20. Darinskii A., Gotlib Yu., Lukyanov M., Lyulin A., Neelov I., Progress in Colloid & Polymer Science, 1993, 91, 13.
21. Ennari J., Neelov I., Sundholm F., Comput. Theor. Polym. Sci., 2000, 10, 403.
22. Ennari J., Elomaa M., Neelov I., Sundholm F., 2000, Polymer, 41, 985.
23. Darinskii A., Gotlib Yu., Lyulin A., Neelov I., Vysokomolek. Soed.. Ser,A 1991, 33, 1211 (translation to English: Polymer Science, 33,1116).
24. Ennari J., Neelov I., Sundholm F., Polymer, 2004, 45, 4171
25. Ennari J., Neelov I., Sundholm F., Polymer, 2000, 41, 2149
26. Mazo M.A., Shamaev M.Y., Balabaev N.K., Darinskii A.A., Neelov I.M., Physical Chemistry Chemical Physics, 2004, 1285.
27. Okrugin B., Ilyash M., Markelov D., Neelov I., Pharmaceutics, 2018, 10, 129.
28. Neelov I.M., Adolf D.B., 2003, Macromolecules, 36, 6914.
29. Neelov I.M., Adolf D.B., 2004, J. Phys. Chem. B, 108, 7627.
30. O.V.Shavykin, I.M.Neelov, A.A.Darinskii. PCCP, 2016, 18, 24307
31. Shavykin O.V., Mikhailov I.V., Darinskii A.A., Neelov I.M., Leermakers F.A.M., Polymer, 2018,146, 256.
32. Okrugin B.M., Neelov I.M., Leermakers F.A.M., Borisov O.V., Polymer, 2017, 125, 292.
33. Shavykin O.V., Leermakers F.A.M., Neelov I.M., Darinskii A.A., Langmuir, 2018, 34, 1613.
34. Mikhtaniuk, S.E., Bezrodnyi, V.V., Shavykin, O.V., Neelov I.M., Penkova, A.V., Markelov, D.A., Polymers,2020,12(8),1657
35. Shavykin, O.V., Neelov, I.M., Borisov, O.V., Darinskii, A.A., Leermakers, F.A.M.,Macromolecules, 2020, 53(17), pp. 7298–7311
36. Bezrodnyi, V.V., Shavykin, O.V., Mikhtaniuk, S.E., Neelov I.M., Sheveleva, N.N., Markelov, D.A., International Journal of Molecular Sciences, 2020, 21(24), 1–22, 9749
37. NN Sheveleva, VV Bezrodnyi, SE Mikhtaniuk, OV Shavykin, IM Neelov, D.A.Markelov, Macromolecules, 2021, 54 (23), 11083
38. N.N. Sheveleva, I.I. Tarasenko, M.A. Vovk, M.E. Mikhailova, I.M. Neelov, D.A.Markelov, International Journal of Molecular Sciences, 2023, 24 (2), 949
39. OV Shavykin, SE Mikhtaniuk, EI Fatullaev, IM Neelov, FAM Leermakers, A.A.Darinskii, International Journal of Molecular Sciences, 2023, 24 (3), 2078
40. E.I.Fatullaev, O.V.Shavykin, I.M.Neelov, M.E. Brito, C.Holm, A.A.Darinskii, International Journal of Molecular Sciences 24 (4), 3063
41. M.E. Brito, S.E. Mikhtaniuk, I.M. Neelov, O.V. Borisov, C.Holm, International Journal of Molecular Sciences, 2023, 24 (3), 2763
42. Sadovnichy, V.; Tikhonravov, A.; Voevodin, V.; Opanasenko, V. "Lomonosov": Supercomputing at Moscow State University. In Contemporary High Performance Computing: From Petascale toward Exascale; Chapman and Hall/CRC: Boca Raton, FL, USA, 2013; pp. 283–307.

Modeling of nonlinear spin-wave transient processes in magnonic active-ring oscillators

<u>Andrey A. Nikitin</u>[1], A.A. Nikitin[1], A.B. Ustinov[1], M.P. Kostylev[2]

[1]*Department of Physical Electronics and Technology, St. Petersburg Electrotechnical University, St. Petersburg 197376, Russia*
[2]*Department of Physics, University of Western Australia, Crawley, W.A. 6009, Australia*
E-mail: aanikitin@etu.ru

Nonlinear spin-wave processes in magnonic active-ring oscillators (MARO) are of great interest. From a fundamental point of view, these systems are used for observing a wide variety of nonlinear wave phenomena [1-6]. From a practical point of view, MAROs are prospective candidates for applications in microwave signal generation and processing [7-9]. Recently, it has been shown that MAROs hold promise for implementing magnonic physical reservoir computers (PRC). To convert a MARO into a PRC, one just needs to control the ring gain coefficient as a means of data input into the reservoir [10-12]. A change in the ring gain results in an onset of a nonlinear transient process of a slow approach to a new steady auto-oscillation amplitude. The transient process underlies the MARO performance as a PRC. Therefore, it is important to have a good understanding of the process. This motivated us to numerically model nonlinear spin-wave transient processes induced in magnonic active-ring oscillators due to variation of the ring gain. This is the goal of the present work.

The MARO consists of a microwave directional coupler, an electronic variable attenuator, an amplifier, and a spin-wave delay line (Fig. 1). A directional coupler is used to fan out a small part of the generated signal from the ring. An arbitrary waveform generator and electronic attenuator controls the ring gain. An amplifier provides for positive feedback. The key component of the MARO is the nonlinear spin-wave (magnonic) delay line.
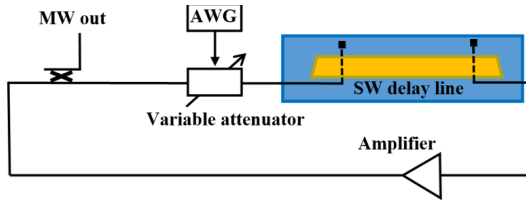

Figure 1. Sketch of the MARO

The spin-wave delay line represents a piece of a single-crystal yttrium iron garnet (YIG) film. Two microwave transducers ("spin-wave antennas") are used to convert a microwave signal into a spin wave and to pick up the spin-wave signal after some distance of its propagation in the film and convert it back into a microwave signal. The propagation of spin waves in MAROs based on an YIG film demonstrates a highly nonlinear behavior. Two types of nonlinear processes are relevant to this work, and both exploit the fundamental process of the nonlinear four-wave interaction. These are nonlinear damping [13] and the nonlinear phase shift (see e.g. [14, 15]). In accordance with these works, two following differential equations describe the nonlinear evolution of the spin-wave amplitude and phase:

$$\frac{\partial u}{\partial z} + \frac{\upsilon_1}{V_g}u^3 + \frac{\upsilon_2}{V_g}u^5 + \frac{\eta}{V_g}u = 0 \ \text{ and } \ \frac{\partial \varphi_{NL}}{\partial z} + \frac{N}{V_g}u^2 = 0.$$

Here $u = m/\sqrt{2}M_0$ is the dimensionless spin-wave amplitude, m is the small-signal dynamic magnetization component, M_0 is the saturation magnetization, φ_{NL} is the nonlinear phase shift, $V_g = \partial\omega/\partial k$ is the group velocity, $N = \partial\omega/\partial|u|^2$ is the cubic nonlinear self-

interaction coefficient, $\eta = 2\pi\gamma\Delta H$ is the linear damping parameter, $|\gamma| = 2.8$ MHz/Oe is the gyromagnetic ratio, ΔH is the half width of the ferromagnetic resonance curve, $\upsilon_1 = 2\pi\gamma\, d\Delta H \big/ d\,|u|^2$ and $\upsilon_2 = 2\pi\gamma\, d^2\Delta H \big/ d\,|u|^4$ are the cubic and quintic nonlinear damping parameters, respectively.

We employ the equations above to model the propagation of a spin wave between the antennas. The spin wave signal from the output antenna is then "re-injected" into the film with its amplitude increased by the amplifier amplification gain and the process of modelling repeats. [16, 17]. Figure 2 shows the simulated dynamics of the MARO for 45 μs. We assume that the ring closes at t=0. The calculations performed for the following set of the parameters: $H = 1780$ Oe, $4\pi M_0 = 1990$ G, $\Delta H = 0.5$ Oe, a film thickness $L = 5.65$ μm, a distance between the spin wave antennas $l = 7.7$ mm, and self-oscillation frequency of 7.28 GHz, $\upsilon_1=2$ ns^{-1}, $\upsilon_2=2$ ps^{-1}. As seen from Fig. 2, the behavior of the signal amplitude is a sequence of sharp upward jumps that are followed by a gradual quasi-exponential decrease in the signal amplitude. The duration of this process coincides with the SW delay time in the YIG film of τ = 215 ns. The position of a jump corresponds to the moment when the signal transmits through the amplifier. The increase in the amplitude is caused by the amplifier gain $G_1 = 254$, which overcompensates the linear spin-wave losses by 1.3 times. In the early stage of developing of auto-oscillations on the ring (t < 32 μs, see inset I to Fig. 2), an increase in the signal amplitude is observed after each circulation cycle. The amplitude grows by 1.3 times with respect to the preceding circulation cycle. In this stage, linear damping is the only relaxation process present on the ring. For t > 32 μs (see inset II to Fig. 2) the amplitude of the circulating signal becomes large enough to introduce additional nonlinear losses. The nonlinear losses lead to suppression of the amplitude growth, and ultimately, to stabilization of the auto-oscillation amplitude at some level. This happens for t = 35 μs. A decrease of the of the amplifier gain coefficient down to $G_2 = 229$ inserted by the electronic attenuator induces an imbalance between the signal gain and its nonlinear decay (t > 38.7 μs, see inset III to Fig. 2). This triggers a gradual decrease of amplitude of the circulating signal down to a new steady state.
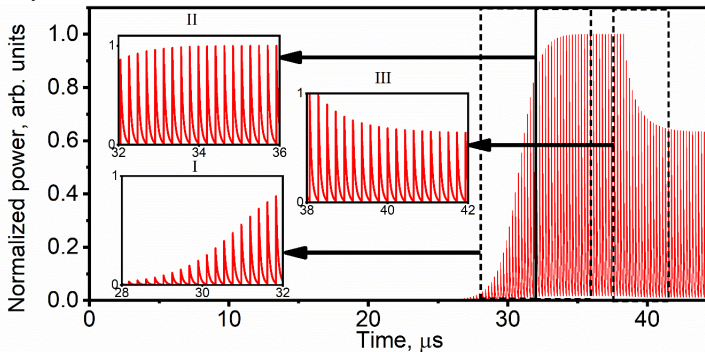

Figure 2. The nonlinear spin-wave transient processes in MARO

Acknowledgments

References

1. B. A. Kalinikos, N. G. Kovshikov, and A. N. Slavin. Envelope solitons and modulation instability of dipole-exchange magnetization waves in yttrium iron garnet films. – Sov. Phys. JETP, vol. 67, pp. 303-312, 1988.
2. M. Wu, B. A. Kalinikos, L. D. Carr, C. E. Patton. Observation of spin-wave soliton fractals in magnetic film active feedback rings. – Phys. Rev. Lett., vol.96, p. 187202, 2006.
3. V. Kondrashov, A. B. Ustinov, B. A. Kalinikos, H. Benner. Chaotic microwave self-generation in active rings based on ferromagnetic films. – Tech. Phys. Lett. vol. 34, pp. 492–494, 2008.
4. M. Wu. Nonlinear spin waves in magnetic film feedback rings. – Solid State Physics, vol. 62, pp. 163–224, 2010.
5. Y. Xiong et al. Experimental parameters, combined dynamics, and nonlinearity of a magnonic-opto-electronic oscillator (MOEO). – Rev. Sci. Instrum., vol. 91, p. 125105, 2020.
6. V. V. Vitko et al. Bistable behavior of active ring resonator on surface spin waves. – The European Physical Journal Plus, vol. 137, p. 1010, 2022.
7. J. C. Sethares, M. R. Stiglitz, I. J. Weinberg. Magnetostatic wave oscillator frequencies. – Journal of Applied Physics, vol. 52, pp. 2273–2275, 1981.
8. B. Ustinov, A. V. Kondrashov, I. Tatsenko, A. A. Nikitin, M. P. Kostylev. Progressive development of spin wave chaos in active-ring oscillators. – Phys. Rev. B., vol. 104, p. L140410, 2021.
9. J. Q. Anderson, P. P. Janantha, D. A. Alcala, M. Wu, and L. D. Carr. Physical realization of complex dynamical pattern formation in magnetic active feedback rings. – New J. Phys., vol. 24, p. 033018 2022.
10. Watt, S., Kostylev, M.: Reservoir Computing Using a Spin-Wave Delay-Line Active-Ring Resonator Based on Yttrium-Iron-Garnet Film. Phys. Rev. Applied. vol. 13, p. 034057, 2020.
11. S. Watt, M. Kostylev, A. B. Ustinov, B. A. Kalinikos. Implementing a magnonic reservoir computer model based on time-delay multiplexing. – Phys. Rev. Applied, vol. 15, p. 064060, 2021.
12. S. Watt, M. Kostylev, A. B. Ustinov. Enhancing computational performance of a spin-wave reservoir computer with input synchronization. – J. Appl. Phys., vol. 129, p. 044902, 2021.
13. M. M. Scott, C. E. Patton, M. P. Kostylev, and B. A. Kalinikos. Nonlinear damping of high-power magnetostatic waves in yttrium–iron–garnet films. – J. Appl. Phys., vol. 95, pp. 6294-6301, 2004.
14. B. Ustinov, and B. A. Kalinikos. Power-dependent switching of microwave signals in a ferrite-film nonlinear directional coupler. – Appl. Phys. Lett., vol. 89, p. 172511, 2006.
15. B. Ustinov, and B. A. Kalinikos. A microwave nonlinear phase shifter. – Appl. Phys. Lett., vol. 93, p. 102504, 2008.
16. A. Nikitin, et al. Theoretical model for nonlinear spin-wave transient processes in active-ring oscillators with variable gain and its application for magnonic reservoir computing. – J. Appl. Phys., vol. 131, p. 113903, 2022.
17. V. Kondrashov et al. Numerical simulation of performance of magnonic reservoir computer based on active-ring oscillator. – J. Magn. Magn. Mater., vol. 563, p. 169968, 2022.

New methods of magnetic resonance theranostics

Yury V. Bogachev, <u>Anastasia V. Nikitina</u>, Marina N. Shishkina
Department of Physics, Saint Petersburg Electrotechnical University, St Petersburg, Russia
E-mail: <u>yu.bogachev@mail.ru</u>, <u>nastya_nikitina1996@mail.ru</u>

Introduction

The methods of MR-theranostics that have already found clinical application or are at the stage of preparation for clinical testing, in which the therapeutic effect of various physical fields occurs under the control of MRI, are considered in [1]. These methods include MRI-guided high-intensity focused ultrasound surgery (tumor ablation), radiation (X-ray) therapy, proton therapy and radiofrequency therapy. Interest in MR-theranostics is growing rapidly. The materials presented in this report cover promising methods of MR-theranostics that are under research, such as MRI-guided laser therapy, MRI tracking in stem cell therapy, MR-guided therapy using MRI-theranostic agents based on magnetic nanoparticles [2].

MRI-guided laser therapy

One of the main methods of laser therapy is photodynamic therapy (PDT), used intensively for the treatment of cancer [2(2)]. To increase the efficiency of PDT, the delivery of photosensitizers using magnetic nanoparticles (MNPs) was proposed [2(9)].

A theranostic system based on MNPs coated with human serum albumin and bacteriochlorin derivatives for the treatment of cancer was investigated in mouse colon xenograft models [2(23)], which would meet the requirements for MRI-guided photodynamic cancer therapy. MRI was used to study the rate and dynamics of accumulation of MNPs and the drug in tumors.

An original method of destroying cancer cells using a two-photon scheme using nanoparticles and riboflavin (vitamin B2) molecules that are injected into cancer cells and irradiated with a laser is proposed in [2(25)]. Observations have shown that 50 days after the introduction of nanoparticles and their periodic laser irradiation, the growth of cancer cells stopped, and the tumor volume decreased by 90%.

Another promising area of application of laser therapy under the control of MRI is catheter embolization of blood vessels. The use of magnetic colloidal nanoparticles based on iron oxide in a biologically inert and thermostable shell made of silicon dioxide, chitosan and gelatin as means of hyperthermic embolization with heating by a radio frequency electromagnetic field is described in [2(29)]. A more attractive method of heating nanoparticles during hyperthermic embolization, an alternative to radiofrequency, may be local exposure to a laser beam [2(30)], including by means of an optical fiber inserted through a catheter [2(31)].

MRI tracking in stem cell therapy

Magnetic resonance imaging with the use of various contrast agents has the greatest prospects for stem cell tracking in vivo.

Paramagnetic compounds of gadolinium Gd^{3+} and manganese Mn^{2+} were used for labeling of various stem cells. For example, Gd_2O_3 nanoparticles were used for labeling and monitoring of hematopoietic cells [2(48)]. Gadolinium chelate nanoparticles were labeled with human MSCs (hMSCs) for cancer diagnosis using the hMSCs homing property on cancerous tumors. Stem cells detected an early tumor (≈ 3 mm^3) within 2 hours using 4.7 T MRI and optical imaging [2(50)]. Manganese oxide nanoparticles coated with silicon oxide were used for tagging and tracking of MSCs [2(55)].

Currently, the most studied systems for MRI tracking of stem cells are superparamagnetic nanoparticles based on iron oxide. Preparations of iron oxide nanoparticles have been used to label and track various types of stem cells after their transplantation, such

as bone marrow stromal stem cells, embryonic stem cells, neural stem cells, hematopoietic progenitor cells [2(56)], [2(57)].

MRI tracking of cells with magnetic nanoparticles in vivo is able to track several hundred cells. In vivo detection of about five hundred cells implanted in the rat brain was demonstrated using a 7 T MRI scanner [2(63)]. The possibility of detecting a small number of cells or even individual cells has also been demonstrated. Single mammalian cells labeled with magnetic nanoparticles in a cellular phantom were visualized on a 1.5 T scanner [2(66)].

Stem cell MRI tracking technologies will be further improved to increase sensitivity and specificity in cell tracking and quantification. It should be noted that labeling cells with a contrast agent cannot be used to study the viability of transplanted cells, their function or ability to differentiate into desired phenotypes. To determine the functional state of the transplanted cells and their subsequent therapeutic effect, the method of multimodal visualization with direct and indirect labeling may be the most useful.

MRI-theranostic agents

Recently, much attention has been paid to the development of multimodal theranostic MRI agents that would not only have high contrast efficiency, but also have the ability to accumulate in the places of the disease and have a therapeutic effect on certain human organs and tissues.

Among such developments, it is possible to distinguish a combination of a contrast substance and a drug, a contrast substance and a neutron capture therapy, a contrast substance and a thermal therapy, a contrast substance and a photodynamic therapy, etc.

To overcome the low efficiency of targeting and side effects of drugs used in chemotherapy, magnetic nanoparticles (MNPs) combined with chemotherapeutic drugs and drugs with small interfering RNAs have been developed [2(94)], which have proven highly effective in the fight against various types of cancer. Higher MR sensitivity and anticancer efficacy were achieved when MNPs were paired with doxorubicin (a potent anticancer agent) and used to treat liver cancer in rats and rabbits [2(95)].

Minimally invasive magnetic heating therapy uses iron oxide-based MNPs to generate heat (using an external alternating magnetic field) in certain areas of the tumor. This method has been used to treat various types of cancer, such as brain cancer [2(99)], breast cancer [2(100)], prostate cancer [2(101)] and liver cancer [2(102)]. The advantage of this method is that they can be injected directly into the tumor before the start of thermotherapy, where they apparently remain almost completely, which allows for repeated treatment.

MRI contrast agents based on Gd have been tested for neutron capture therapy. Various Gd-containing polymers have been studied to increase the accumulation of gadolinium in the tumor. Core-shell nanoparticles from Gd and calcium phosphate (Gd-DTPA/CaP) have been synthesized [2(106)]. Antitumor evaluation was performed for single and multiple administration of Gd-DTPA/CaP nanoparticles. Observation of tumor suppression after neutron irradiation revealed no significant differences in antitumor efficacy between single and multiple injections. In addition, Gd nanoparticles with a chitosan shell [2(107)], complex compounds of gadolinium and boron [2(108)] and the use of liposomes as a Gd delivery agent [2(109)] were studied for neutron capture therapy. After neutron irradiation, the group treated with liposomes with Gd showed a 4-fold higher degree of tumor suppression.

References

1. Yu.V. Bogachev, A.V. Nikitina, V.V. Frolov, V.I. Chizhik. - *Technical Physics*, 65 (9), 1427 – 1435 (2020).
2. Yu.V. Bogachev, A.V. Nikitina, M.N. Shishkina. – *LETI Transactions on Electrical Engineering & Computer Science*, 16(1), 5-24 (2023).

Investigation of NMR relaxation properties of contrast agents based on magnetic nanoparticles

Nikitina A.V.[1], Bogachev Yu.V.[1], Marchenko Ya.Yu[2].

[1]*Department of Physics, Saint-Petersburg Electrotechnical University "LETI", 5, prof. Popov st., Saint-Petersburg, 197376, Russia,*

[2]*Petersburg Nuclear Physics Institute, National Research Centre "Kurchatov Institute", 188300 Gatchina, Russia*

E-mail: nastya_nikitina1996@mail.ru

Introduction

The use of contrasting agents is a widespread method of increasing the contrast of the MR image area of interest. An analysis of modern research in this field shows that negative contrast agents based on magnetic nanoparticles (MNPs) open up wide opportunities not only in diagnostics, but also in therapy. In order to improve the understanding of the behavior of MNPs in proton-containing biological solutions, within the framework of this work, studies of particles with different core composition and with different shells were carried out.

Studies of NMR relaxation and stability of negative contrast agents with different nucleis and shells

MNPs with a core composition of the $M_{gx}Z_{ny}Fe_{3-x-y}O_4$ type were investigated. The following synthesis methods were used: the method of co-precipitation with carbonate and the method of co-precipitation with alkali. For all the studied MNP samples, regardless of the method of preparation, the efficiency of the transverse relaxation r2 is significantly higher than the efficiency of the longitudinal relaxation r1. The concentration dependences of the rate of transverse R2 nuclear magnetic relaxation of water protons for a number of samples were nonlinear. The analysis of these dependencies shows a decrease in the relaxation efficiency of these MNP with an increase in the concentration of MNPs in solution. This indicates the instability of these MNP in an aqueous solution and that their aggregation ability to form clusters increases with an increase in the concentration of MNPs in solution.

Studies have been conducted on MNPs with the same core composition, but with different shells and with a depending on the storage time. During the analysis of the obtained measurement results, it was determined that the relaxation efficiency of r2 is significantly greater than the relaxation efficiency of r1 for all types of MNP. In a sample of MNPs with a PDDA shell, the relaxation efficiency of r1 could not be determined either in the first or in the second year of storage, since the determination of the relaxation time T_1 takes longer than T_2, and the particles being in a magnetic field are even more prone to aggregation. At the same time, according to the change in r2, it can be concluded that over time, the particles in this shell significantly lose their contrasting properties. The samples of MNPs with CH60 and CH60-DEX shells performed well not only from the side of good contrasting properties (relatively high r2 values), but also from the side of stability: the relaxation efficiency indicators of r1 and r2 remained at a high level even after a year.

Conclusion

Thus, the results obtained suggest that the studied magnetic nanoparticles can potentially be used as negative contrast agents in MRI [2].

References

1. Gao M.,et al.// Biomaterials 2017. Vol. 133. P. 165–175.
2. NMR Relaxation Efficiency of Aqueous Solutions of Composite $M_{gx}Z_{ny}Fe_{3-x-y}O_4$ Nanoparticles/Bogachev,Y.V., Nikitina,A.V., et al.//AMR, 2017, V.48, I.7, P.715–722

Low-field Bench-top NMR analysis of pharmaceutical, food products in chemical laboratory

Boris P. Nikolaev, *Yaroslav Yu. Marchenko*

Saint-Petersburg Technopark, Engineering Centre API, Saint-Petersburg, Russian Federation
E-mail: *nikolaevhpb@gmail.com*

Introduction

The development of small nonexpensive NMR magnets from permanent FeNdB, SmCo materials with field strength H up to 2 T are now in progress. Compact bench-top NMR spectrometers don't demand the highly cost helium cryoagents and may be installed nearby chemical reactor. The disadvantages of nonsufficient spectral resolution are overcame by measurement of resonance in small probe volume and smart compensation of inhomogeneities by special shimming procedures and application of different hyper-polarization techniques. The advance in size decreasing of chip electronics, micro-coils and introduction of alternative detection schemes makes possible to create small bench-top NMR spectrometers with satisfactory spectral characteristics for structural study of small organic molecules at resonance frequency 40, 60, 80 MHz of nuclei ^{1}H, ^{13}C, ^{19}F, ^{31}P [1, 2].

The immediate estimation of product quality is the important task of quality control in chemical industry and laboratory practice. Bench-top NMR spectroscopy provides essential complement to HPLC, FTIR in control assay of technological operations. Nowadays the intense growth of pharmacy industry of drugs and consumer food products demands new innovative analysis at each step of technological chain.

Results and Discussion

Quantitative and qualitative determination of different species in one formulation by NMR method is the base of simultaneous acquisition of spectral finger-print of components from single spectrum. NMR assay of pharmaceuticals and consumer food ingredients gives way to counter adulteration [3]. As example of such facility the NMR spectra of coffee extracts from different retail samples demonstrate the ability of low-field NMR method to differentiate soluble and ground roasted coffee specifications Fig.1.

The application of new techniques of strong suppression of proton aqueous signal and 2D NMR measurements in COSY, TOCSY regimes facilitates the robust assignment of resonance lines in spectra. The decreased content of coffein in spray-dryied coffee is observed in NMR of aqueous extracts compared to ground roasted forms [3]. The formic, acetic, lactic and citrate acids were observed spectrally in the both brands but at different ratio. Fatty acids from heat transformed lipids give rise to generation of lines in high field 2-3 ppm. Intense nonresolved signals at 3-4 ppm have saccharide origin. The results of coffee assay suggest the possibility to monitor level of adulteration in coffee product in retail trade. Commercially available drug formulations of caffeine, acetylsalicylic acid, paracetomol, metformine in mixture with excipients can be analysed in solutions by recording ^{13}C NMR spectrum.

2D NMR spectra are efficient instrument to separate the nuclei resonance from active substance from excipient as shown Fig.2.
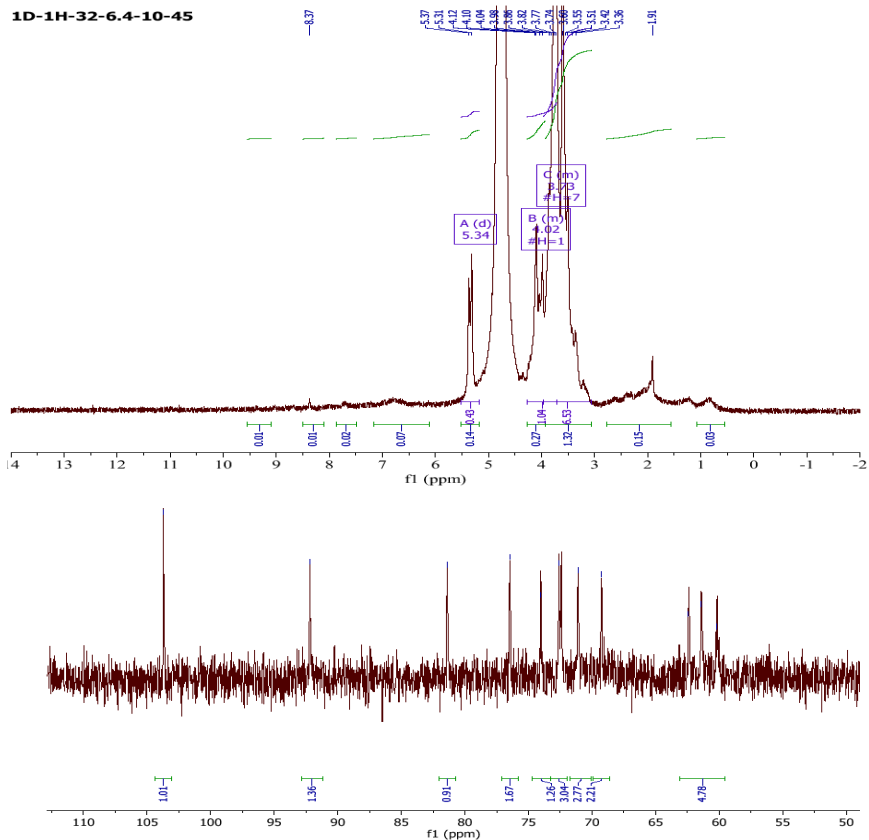
Figure 1. ^1H, ^{13}C NMR spectra of spray-dried Nescafe coffee in ^2H_2O at 60 MHz Spinsolve (Magritek GmbH).
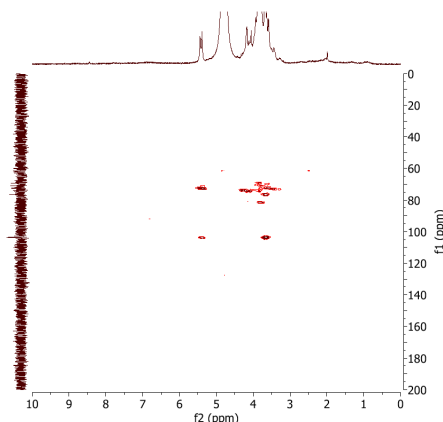
Figure 2. 2D Heteronuclear Multiple Bond Correlation Spectrum of spray-dried Nescafe coffee in ^2H_2O at 60 MHz Spinsolve (Magritek GmbH).

On line recording of chemical reactions of synthesis of adducts from halogen and alkylmetal through the transfer halogen and hydrogenation of substrate is a productive way for real time examination of chemical process in batch and microreactor mode [4]. The continuous monitoring of mixing spectrally different solutions in flow cell of bench-top spectrometer Spinsolve is performed. To study the chemical process in such mode the final reactant from microreactor flows through the magnet hole of NMR spectrometer and enters back to the reactor. To optimize measurement the liquid reactant flows continually to RF receiver cell of spectrometer by soft inert tubing with internal diameter 4 mm. The flow rate 2-5 ml/min is sufficient to get the nondistorted specta with sensitivity at concentration 1 mM. The conducted experiments with microreactor synthesis of 5-hydroxymethylfurfural demonstrate the possibility to realize the continuous real-time analysis in situ during production of chemical by-products for "green" chemistry.

Acknowledgments

References

1. E.Danielly, J.Perlo, B.Blumich, F.Casanova. Highly Stable and Finely Tuned Magnetic Fields Generated by Permanent Magnet Assemblies. Phys.Rev.Letters, 2013, v.110, p. 180801.
2. K. Singh, B. Blümich, NMR spectroscopy with compact instruments, Trends Analyt. Chem. (2016), p. 12–26.
3. M.Defernez, E, Wren, A.D.Watson,Y.Gunning, I.J.Colquhon, G. Le Gall, D.Williamson, E.Kate Kemsley. Low-field ^1H NMR spectroscopy for distinguishing between arabica and robusta ground roast coffees. Food Chem. 2017, v.216, p.106-113.
4. K.Meyer, S.Kern, N.Zientek, G.Guthausen, M.Maiwald. Process control with compact NMR. Trends in Anal.Chem. 2016, v.83, p.39-52.

Configuration Determination of Regioisomeric Spirocyclopropanes Using NMR Spectroscopy Methods

Pelipko V.V., Pilipenko I.A., Baichurin R.I., Makarenko S.V.
Herzen State Pedagogical University of Russia, Department of Organic Chemistry,
Laboratory of Nitrocompounds, Center of collective use at the Faculty of Chemistry
"Instrumental methods for the study of nitro compounds, coordination, biologically active substances and nanostructured substances" 48 Moyka River Embankment, Saint Petersburg 191186, Russia
E-mail: kohrgpu@yandex.ru
http://kohrgpu.ru, http://ckpo.herzen.spb.ru/?page=organic-chemistry

The study of the interaction of 1-bromo-1-nitro-3,3,3-trichloropropene with phenylmethylpyrazolone showed that the reaction leads to the formation of two regioisomeric spiro-fused nitrocyclopropanes **1**, **2**, similarly to the reactions of bromonitroacrylates [1]. The products can be separated by silica gel column chromatography. The isolated regioisomers **1**, **2** are very attractive objects for studying the structure by 1D and 2D NMR spectroscopy experiments due to their rigidly fixed structure.

In the ^{13}C NMR spectra the signals of C^2 atom appear at 52.8–56.0 ppm in the form of doublets with a characteristic J-coupling constants $^1JC^2\text{-}H^2$ = 169.7–172.7 Hz, and the signals of C^1 atom appear at 69.6–72.4 ppm in the form of doublet-doublets with constants $^1JC^1\text{-}H^1$ = 189.7–194.0 and $^2JC^1\text{-}H^2$ = 4.0–4.9 Hz (Fig. 1), which confirms their cyclopropane nature [2, 3, 4]. The observed in the ^{1}H NMR spectra of compounds **1**, **2** J-coupling constants of the methine protons of the cyclopropane ring ($^3JH^1\text{-}H^2$ = 6.6-6.8 Hz) indicates their *trans* configuration (Fig. 2).
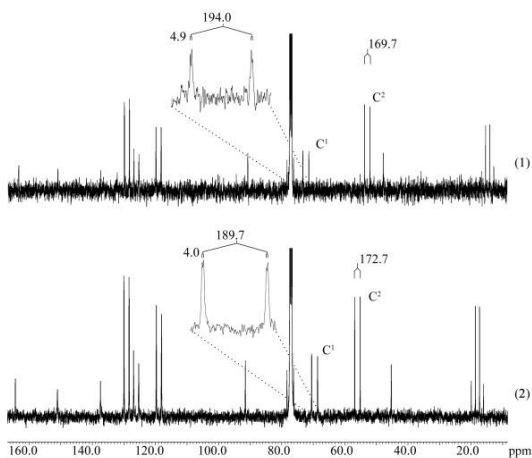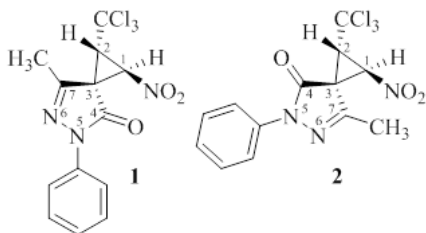
*Figure 1. ^{13}C NMR spectrum of spectrum of compounds **1**, **2**(CDCl$_3$)*
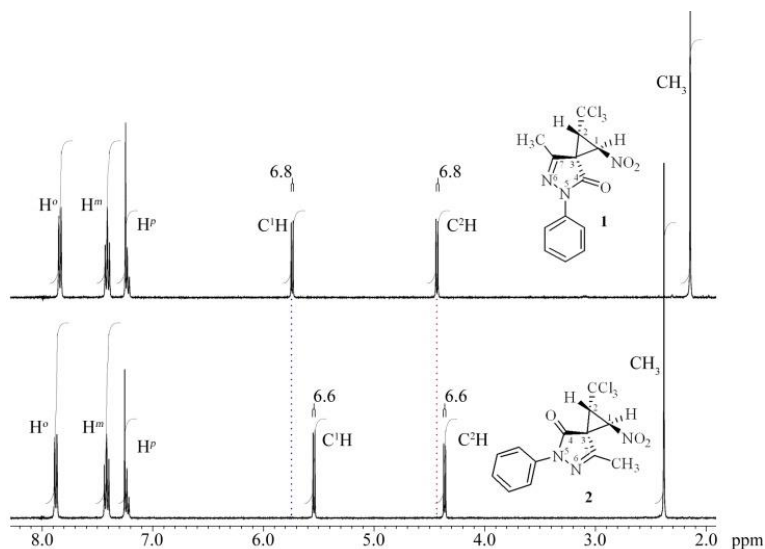
Figure 2. *¹H NMR spectrum of compounds **1, 2***(CDCl₃)

In turn, the results of 1H-1H NOESY experiments for individual diastereomers obtained with a variable value of mix. time (τ 0.5, 1, 1.5, 2 sec) show NOE correlations of C2H/CH₃ (heterocycle) protons for diastereomer 1 and C1H/CH₃ (heterocycle) for diastereomer

(Fig. 3, 4). The presence of these correlations indicates the realization for diastereomer 1 of such an arrangement of spirocycles, in which the methyl group of pyrazolone and the nitro groups are on the same side of the cyclopropane ring, while for diastereomer 2, this position is occupied by the methyl and trichloromethyl groups.
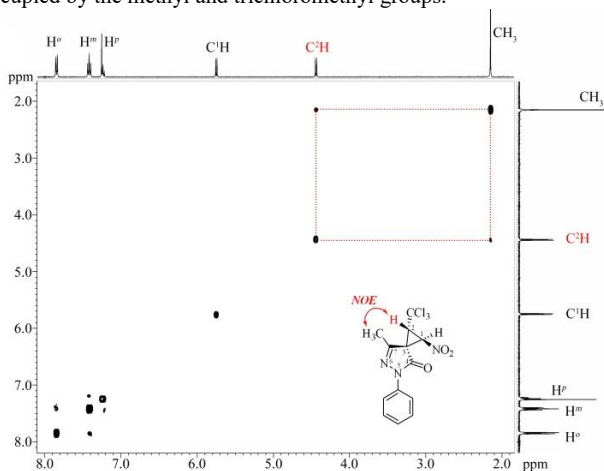
Figure 3. *¹H-¹H NOESY spectrum of compound **1*** (CDCl₃)
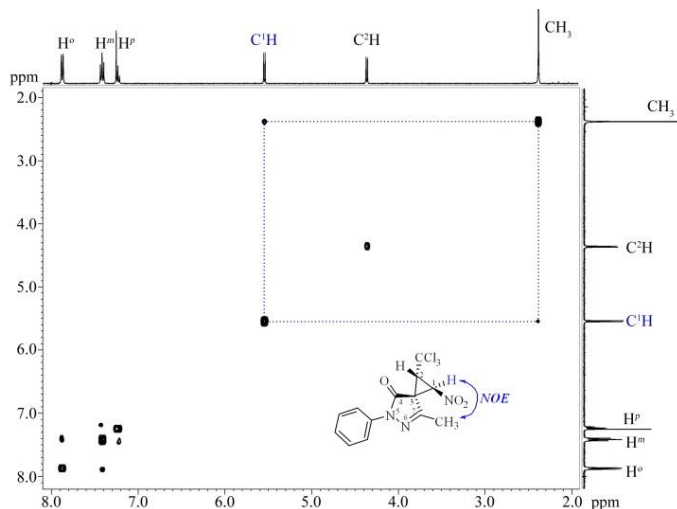
*Figure 4. ^1H-^1H NOESY spectrum of compound **2** (CDCl$_3$)*

Thus, the study of compounds **1**, **2** using 1D and 2D NMR spectroscopy experiments made it possible to establish the fine structure of the obtained regioisomeric spirocyclopropanes.

References

1. M.M. Pavchenko, V.V. Pelipko, K.A. Lyssenko, S.V. Makarenko, R.I. Baichurin. *In Magnetic resonance and its applications. Spinus-2018*, 221-222 (2018).
2. V.V. Pelipko, R.I. Baichurin, S.V. Makarenko. *In Magnetic Resonance and its Applications*, 230-231 (2020).
3. A.J. Gordon, R.A. Ford. The Chemist's Companion. New York: Wiley, 1972.
4. R. Silverstein, F. Webster, D. Kimle. Spectrometric Identification of Organic Compounds: BINOM. Laboratoriya Znanii. Moscow, 2012.

Investigation of biosilification mechanisms by experimental EPR methods and calculated DFT method on the example of orthosilicic acid oligomers

Alina Petrova [1], Alexander Rodionov [1], Marat Gafurov [1]

[1]*Institute of Physics, Kazan Federal University*
E-mail: mamatovaalinka@mail.ru

Introduction

The main process of biosilification is the oligomerization of silicic acids $n(SiO_2)m(H_2O)$. The influence of the environment of the silicon atom on the oligomerization process can be one of the important factors of biosilification.

The study of orthosilicic acid by experimental methods of EPR and the teretic method of DFT

In this work, quantum-chemical and EPR studies of $Si(OH)_4$ powder as a model compound acting as the main oligomerization reagent were carried out. The EPR spectra of the $Si(OH)_4$ powder were acquired with Bruker X-band spectrometer ESP 300. To obtain paramagnetic centers, the samples were irradiated with URS-55 X-ray setup at room temperature with the irradiation dose of 10 kGy. As a result of X-ray irradiation, a group of lines in the EPR spectra for the g-factor of 2 appears (Fig. 1). The studies performed by the microwave saturation method showed that this group of lines belongs to at least two types of paramagnetic centers.
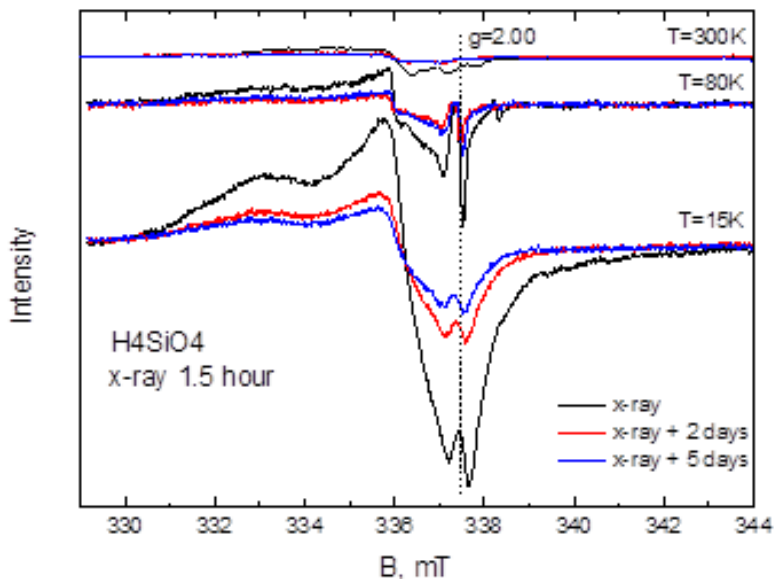
Figure 1. EPR spectra of $Si(OH)_4$ sample.

The easily saturated narrow EPR line with g=2.00 and a shape characteristic of the axial symmetry of the center can be attributed to the so-called E'-centers, which are quite well studied in the literature [1]. The nature of the paramagnetic centers, to which such a spectrum of complex structure can be assigned, is the subject of further study.

Novel fishing technique

The DFT method was used to calculate the EPR parameters (HFI constant and g-factor) for $Si(OH)_4$, $Si(OCH_2CH_3)_4$, and model oligomers with the degree of oligomerization from 1 to 6 Si atoms using the ORCA software package [2].

Acknowledgments

References

1. F. Neese. Wiley Interdisciplinary Reviews: Computational Molecular Science **2**, 73, 2012.
2. Galukhin, et al. Magn. Reson. Solids 20, 18203. 2018

Slowdown of spin-lattice relaxation of quadrupole nuclei in crystals by additional magnetic excitation

Andrey M. Rochev, Vladimir M. Mikushev, Elena V. Charnaya, Dmitriy Yu. Nefedov, Dmitrii Yu. Podorozhkin

Faculty of Physics, St. Petersburg State University, St. Petersburg
E-mail: v.mikushev@spbu.ru

Introduction

The spin-lattice relaxation time T_1^{Σ} measured by nuclear magnetic resonance (NMR) depends on the efficiency of the spin-phonon interaction in solid materials and is drastically affected by defects and paramagnetic centers [1]. The effectiveness of the "impurity" mechanism of nuclear spin-lattice relaxation (SLR) and its significant contribution to the value of T_1^{Σ} even at a low concentration of paramagnetic centers in the crystal volume, for example, in the case of uncontrolled impurities in purified samples, are due to the strong coupling of the paramagnetic centers with lattice vibrations and nearest nuclear spins, and also due to spin diffusion in the spin system of nuclei, which equalizes the nuclear magnetization over the sample [2]. The thermodynamical condition for the participation of spin diffusion in "impurity" relaxation can be written as

$$\left| \alpha_{loc} - \alpha_l \right| < \left| \langle \alpha_I \rangle - \alpha_l \right|, \qquad (1)$$

where $\langle \alpha_l \rangle$ is an inverse lattice temperature, $\langle \alpha_I \rangle$ average inverse spin temperature in the sample, α_{loc} inverse local spin temperature near paramagnetic centers.

It has been revealed in numerous studies of stationary saturation of the NMR signal that the saturation process is similar to the reverse process of nuclear SLR: there is a "crystalline" saturation mechanism due to direct transitions in the nuclear spin system stimulated by a steady resonance field and an "impurity" (or "defect") saturation mechanism due to paramagnetic centers, local overheating of the nuclear spin system near these centers, and the spin diffusion [3]. At the same time, local overheating of the nuclear spin system near a certain paramagnetic center under the resonance magnetic excitation leads to suppression of the contribution of this center to relaxation according to Eq. (1). This makes it possible to separate the mechanisms of SLR of quadrupole nuclei and to measure the times T_1^{lat} of lattice relaxation and T_1^{imp} of impurity relaxation in the presence of a stationary saturating field [4].

Sample and experiment

As a model sample for the application of the nuclear SLR slowdown technique, we used a sodium fluoride NaF single crystal, in which there are two spin systems, a spin system of quadrupole sodium nuclei and that of fluorine nuclei with the spin 1/2, which do not have quadrupole moments. The presence of uncontrolled impurities, paramagnetic and non-paramagnetic, in the NaF crystal was monitored using elemental analysis by atomic emission spectrometry with inductively coupled plasma on ICPE-9000 (Shimadzu). The elemental analysis showed the following concentrations of impurities: Ca (310±40) mg/kg; Mg (10.5±1.4) mg/kg; Fe (7.93±1.02) mg/kg; Zn (6.1±0.8) mg/kg; Sr (3.1±0.4) mg/kg. The study of the NaF crystal on the SQUID magnetometer Quantum Design MPMS VSM demonstrated the weak magnetization of the order of 10^{-7} emu/g in the field of 100 Oe emerged because of uncontrolled paramagnetic centers.

The nuclear magnetization restoration after a 180° pulse (inversion recovery protocol) was monitored using a Bruker Avance III 400 spectrometer optimized for solids. The controlled stationary magnetic saturation of the NMR line at the Larmor frequency was

characterized by the saturation factor $Z^{st}=A^{st}/A_0$, where A^{st} and A_0 were the integral intensities of the NMR signals after a 90° pulse under additional saturation and without it.

Results and discussion

The dependence of the relative integral intensity of the ^{23}Na NMR signal $Z(t)=A(t)/A^{st}$ on the time interval t between the 180° and 90° pulses was measured under additional weak long electromagnetic pulses at the Larmor frequency, which produced saturation of the sodium nuclear spin system to the value Z^{st} in the range from 1 to 0.1.

When the spin temperature averaged over the crystal volume was negative, which corresponds to $Z(t)<0$, the restoration of nuclear magnetization follows the exponential law

$$Z(t) = Z^{st}\left[1-(1+b)\exp(-t/\tau_1)\right], \quad (2)$$

where b takes into account the imperfect magnetization inversion and τ_1 is the restoration time. For the positive spin temperature averaged over the sample volume ($Z(t)>0$), the magnetization recovery could be better described not by a single exponential, unlike [5], but by the sum of two exponentials for any factors Z^{st} of stationary saturation:

$$Z(t) = Z^{st}\left[1-\rho_1(1+b)\exp(-t/\tau_1)-\rho_2\exp(-(t-t_0)/\tau_2)\right], \quad (3)$$

where ρ_1 and ρ_2 show the normalized weights of the exponentials in Eq. (3) ($\rho_1+\rho_2=1$), t_0 corresponds to the time when the spin temperature changes the sign. Experimentally found values of ρ_1 and ρ_2 at 293 K are shown in Fig. 1. The results obtained showed that the time τ_2 is longer than τ_1. Moreover, the second exponential emerged only at Z^{st} below a particular stationary saturation.
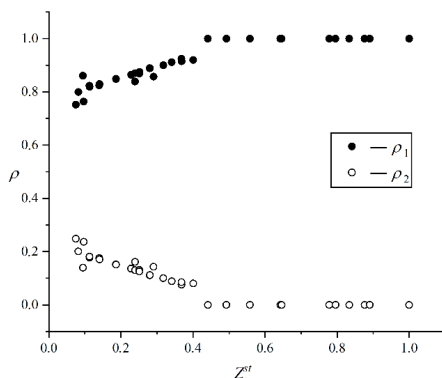
Figure 1. The dependence of the coefficients ρ_1 and ρ_2 on the [23]Na saturation factor.

The dependence of the restoration times τ_1 and τ_2 on the saturation factor Z^{st} is shown in Fig. 2. Since the general analysis of relaxation under stationary saturation, which neglects the role of impurities, predicts the linear decrease of the restoration time with decreasing the saturation factor

$$\tau = T_1^{\Sigma}/Z^{st}, \quad (4)$$

the straight line shown for the $\tau_1(Z^{st})$ dependence in Fig. 2 should extend to T_1^{Σ} at $Z^{st}=1$. This agrees with the experimental data obtained. The emergence of the contribution to nuclear spin relaxation with τ_2, which is longer than τ_1 (see Fig. 2), means the suppression of the impurity relaxation as a result of strong enough saturation. Such suppression can occur only at positive spin temperatures, namely, at $t>t_0$. When impurity relaxation breaks down, nuclear

relaxation runs only due to spin-phonon coupling as in crystals with perfect structure. Then the straight line, which fits the $\tau_2(Z^{st})$ dependence in Fig. 2, should extend to T_1^{lat} at $Z^{st} = 1$.
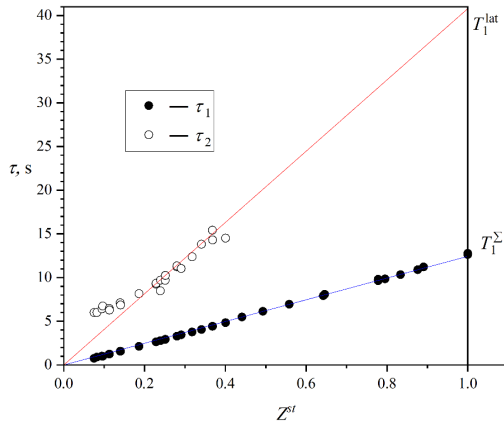
Figure 2. The dependence of the ^{23}Na restoration times on the stationary magnetic saturation factor Z^{st}.

The two-exponential restoration of the ^{23}Na nuclear magnetization in the sodium fluoride crystal under additional stationary magnetic saturation of the NMR signal most likely indicates the incomplete suppression of impurity spin-lattice relaxation. It can be caused by local heating of the spin system insufficient to fulfil the condition (1) for all paramagnetic centers in the crystal volume. As a result, the magnetization restoration for the ρ_1 part of the nuclear spins is characterized by the shorter τ_1 time, while spin relaxation for the ρ_2 part of the nuclear spins runs due to spin-phonon coupling and is characterized by the larger τ_2 time. Moreover, according to Fig. 2 the number of nuclear spins for which the "impurity" component of spin-lattice relaxation is suppressed increases with increasing the intensity of the stationary resonance field and decreasing the saturation factor Z^{st}. Note that measurements for the fluorine nuclei proved the absence of impurity relaxation suppression.

Acknowledgments

References

1. A. Abragam, M. Goldman. *Nuclear Magnetism: Order and Disorder*. – Claredon Press, Oxford, 1982.
2. G.R. Khutsishvili. – *Sov. Phys. Uspekhi*, 8, 743-768 (1966).
3. A.A. Kuleshov, V.M. Mikushev, A.L. Stolypko, E.V. Tcharnaya. – *Akust. Zh.*, 35, 473-476 (1989).
4. E.V. Charnaya, V.M. Mikushev, A.M. Ulyashev, D.A. Yas'kov. – *Physica B: Condens. Matter,* 292, 109-113 (2000).
5. V.M. Mikushev, E.V Charnaya, M.K. Lee, L.-J. Chang. – *Results Phys.*, 12, 1202 (2019).

Synthesis and NMR structure of Michael adducts derived from phosphine-catalyzed reaction of sesquiterpene lactone arglabin with nucleobases

Alexey V. Salin, Andrey A. Shabanov, Laura G.K. Bernal, Asiya R. Salakhetdinova
A.M. Butlerov Institute of Chemistry, Kazan Federal University, Kremlevskaya 18, Kazan, 420008, Russian Federation
E-mail: salin555@mail.ru

Introduction

Sesquiterpene lactone arglabin **1** isolated from *Artemisia glabella* is used in medicine to treat breast, colon, ovarian and lung cancers [1]. The antitumor activity of arglabin is known to occur through competitive inhibition of farnesyl transferase, which is involved in prenylation of Ras proto-oncogene. Since oncogenic forms of Ras proteins are detected in many types of cancer, the defarnesylation inhibits proliferation of tumor cells.

Michael adducts of sesquiterpene lactones are considered as promising prodrugs with more selective anticancer activity [2, 3]. The selective cytotoxicity of Michael adducts is attributed to their ability to undergo retro-Michael reaction in cancer cells, thus generating *in situ* the parent lactone. In this work, we aimed to perform diversity-oriented synthesis of Michael adducts derived from sesquiterpene lactone arglabin with nucleobases.

Results and Discussion

Recently, we developed a novel method allowing functionalization of α-methylene-γ-butyrolactones with different types of pronucleophiles under tertiary phosphine organocatalysis [4]. Herein, we report first synthesis of Michael adducts 2a-d derived from arglabin 1 and nucleobases as the nitrogen pronucleophiles using n-PBu3 as the catalyst (Scheme 1).
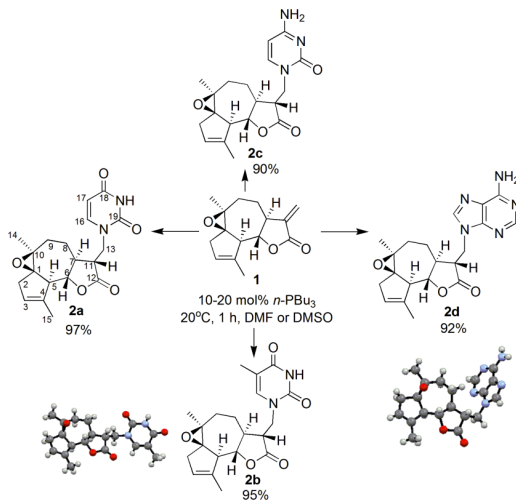
Scheme 1. Synthesis of Michael adducts of arglabin with nucleobases

Michael adducts **2a-d** were obtained in good to excellent yields within 1 h at room temperature. The reactions with pyrimidine bases provided selective formation of N1-alkylated products **2a-c**, and with adenine – N9-alkylated product **2d**. Nucleoside thymidine

was totally unreactive, since its N1 center is linked to the 2'-deoxyribose ring, and the remaining N3 center could not be alkylated. The reaction with guanine could not be performed due to the insolubility problem. The structures of products **2a-d** were studied using ^{1}H, ^{13}C{^{1}H}, DEPT, COSY, NOESY, HSQC, and HMBC NMR techniques. Tables 1 and 2 show signal assignments in ^{1}H and ^{13}C{^{1}H} NMR spectra of adduct **2a** made from analysis of the 2D NMR spectra. Figure 1 shows the ^{1}H–^{1}H COSY spectrum of **2a**, from which all correlations for protons can be found. Absolute configuration at the created C11 stereocenter in adducts **2b** and **2d** was determined to be *R* by single-crystal X-ray diffraction. Configuration at C11 stereocenter in other adducts was assigned by analogy.

*Table 1. Signal assignment in ^{1}H NMR spectrum of **2a** (CDCl$_3$, 400 MHz)*

H atom	Chemical shift (δ, ppm), multiplicity, and integral intensity
NH	8.71 (s, 1H)
H16	7.52 (d, J = 8.0 Hz, 1H)
H17	5.70 (dd, J = 8.0, 2.3 Hz, 1H)
H3	5.61 – 5.55 (m, 1H)
H6, H$_A$13	4.18 – 4.05 (m, 2H)
H$_B$13	3.98 (dd, J = 14.5, 3.0 Hz, 1H)
H5	2.85 (br d, J =8 Hz, 1H)
H$_A$2	2.81 – 2.71 (m, 1H)
H11	2.56 (ddd, J = 12.7, 5.3, 2.9 Hz, 1H)
H$_A$9, H$_B$2	2.21 – 2.09 (m, 2H)
H$_A$8, H$_B$9, H15	2.02 – 1.87 (m, 5H)
H7, H$_B$8	1.56 – 1.41 (m, 2H)
H14	1.34 (s, 3H)

*Table 2. Signal assignment in ^{13}C{^{1}H} NMR spectrum of **2a** (CDCl$_3$, 100.6 MHz)*

C atom	Chemical shift (δ, ppm)	C atom	Chemical shift (δ, ppm)
C12	176.4	C5	52.4
C18	163.2	C7	49.5
C19	151.2	C11	46.7
C16	146.0	C13	44.8
C4	140.1	C2	39.6
C3	125.2	C9	33.5
C17	102.4	C14	22.7
C6	83.5	C8	22.6
C1	72.4	C15	18.2
C10	62.8		

Cytotoxic profiles of **2a-d** using normal and cancer cell lines were studied. Adduct **2a** showed selective activity against cervical carcinoma M-Hela (IC$_{50}$=21.6±1.7 μM, SI=3.3). This result is superior to that of arglabin **1** (IC$_{50}$=28.0±2.2 μM, SI=0.4) and dimethylamino-arglabin (IC$_{50}$=32.5±2.6 μM, SI=0.3) currently used in medicine.
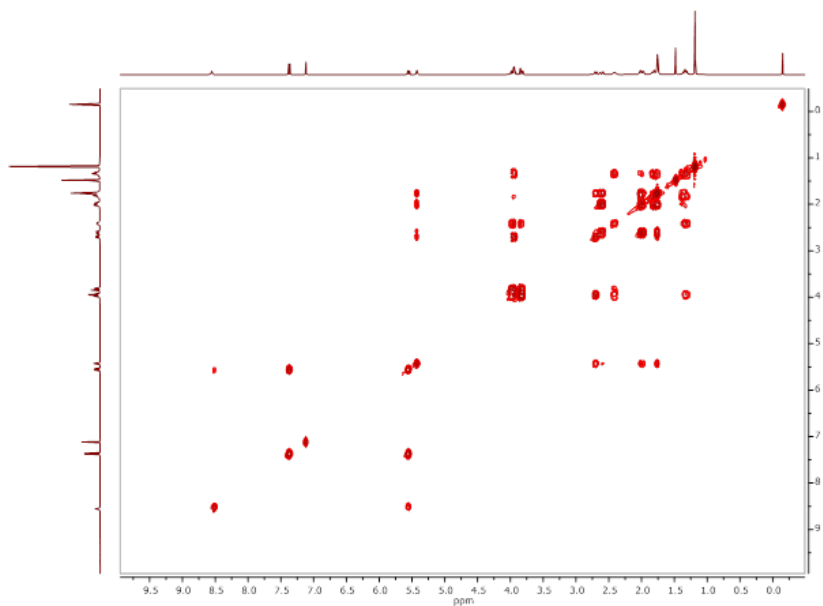
*Figure 1. ^1H–^1H COSY spectrum of **2a** (CDCl$_3$, 400 MHz)*

Acknowledgments

References

1. S.H. Lone, K.A. Bhat, M.A. Khuroo. – *Chem.-Biol. Interact.*, 240, 180-198 (2015).
2. T.R. Valkute, E.K. Aratikatla, N.A. Gupta, S. Ganga, M.K. Santra, A.K. Bhattacharya. – *RSC Adv.*, 8, 38289-38304 (2018).
3. Janecka, A. Wyrębska, K. Gach, J. Fichna, T. Janecki. – *Drug Disc. Today*, 17, 561-572 (2012).
4. V. Salin, D.R. Islamov. – *Org. Biomol. Chem*., 17, 7293-7299 (2019).

The environment effect on the intramolecular mobility of pillar[5]arene

L.V. Sharipova[1,2], B.I. Khayrutdinov[1,2], Yu.F. Zuev[1]

[1]*Kazan Institute of Biochemistry and Biophysics, FRC Kazan Scientific Center of RAS, Kazan 420111, Russian Federation*
[2]*Institute of Physics, Kazan Federal University, Kazan 420008, Russian Federation*
E-mail: lv.sharipova@yandex.ru

Introduction

One of the actual problems of modern supramolecular chemistry is the development of principles for the design of macrocyclic compounds capable of recognizing biologically important substrates. Pillar[n]arenes are new class of macrocyclic compounds which are capable of forming "guest-host" complexes. Important properties of pillar[n]arenes are planar chirality, biocompatibility and non-cytotoxicity, possibility step-by-step functionalization, a tubular spatial structure and the ability to encapsulate small molecules in it. These properties of pillar[n]arenes make it possible to prolong the action of the encapsulated drug, which reduces the number of side effects and increases its therapeutic efficacy. The aim of this work is to study the dynamic properties of an aqueous solution of decaammonium salt 4,8,14,18,23,26,28,31,32,35-deca(carboxymethoxy) pilar[5]arene.

Results

In this work, NMR spectroscopy was used to study the effect of external environmental conditions (temperature and pH values of the solution) on the dynamic properties of pillar[5]arene. To characterize mobility of the hydroquinone fragment of pillar[5]arene, the Carr-Purcell-Meiboom-Gill pulse sequence was used. From the analysis of the CPMG spectra, the chemical exchange rate constant of the dynamic process was obtained at various temperature and pH values of the solution. The thermodynamic parameters of the conformational exchange of proton in the hydroquinone fragment of pillar[5]arene were determined from the temperature dependence of the chemical exchange rate constant. Based on experimental data, the influence of environmental conditions on the intramolecular dynamics of the processes occurring in the pillar[5]arene was shown.

Acknowledgments

Identification of diosmin in *Hyssopus officinalis* L. by ^{1}H NMR spectroscopy.

Anzhelika V. Sheremeta, Vasiliy A. Ivlev, Anastasia A. Murtazina, Alina Y. Polukhina, Luiza A. Miridonova, Vasiliy G. Vasil'ev

Peoples' Friendship University of Russia (RUDN University), 6 Miklukho-Maklaya Street, Moscow, 117198, Russian Federation
E-mail: anzhelika.sheremeta@mail.ru

Introduction

Plants are important renewable resources of the biosphere, whose processing methods should be waste-free and produce not only composite materials, but also valuable individual biologically active substances for obtaining a wide range of food, medical and technical means and preparations. Assessment of the content of biologically active substances (BAS) in biomass should be based on environmentally safe, express, precision instrumental methods of analysis. The assortment of such methods is very wide - various types of chromatography, spectrophotometry and infrared spectrometry, mass spectrometry. All of them have one or another disadvantage: the need to isolate the target component or its chemical modification, complex and time-consuming sample preparation, low accuracy, etc. NMR spectroscopy of multicomponent extracts of metabolites is free from complicated sample preparation, derivatization and the need for standard samples.

Hyssopus officinalis

Hyssopus officinalis L., commonly known as hyssop, is a herbaceous plant in the Lamiaceae family. It is native to Southern Europe, the Middle East, and the region surrounding the Caspian Sea [1].

Hyssop has been used for its medicinal properties for centuries. It contains a variety of compounds, including flavonoids, tannins, and essential oils, which are believed to have anti-inflammatory, antiseptic, and expectorant properties [1]. It has been used to treat respiratory infections, digestive problems, and skin conditions. In addition to its medicinal properties, hyssop is also used as a culinary herb. Its leaves have a slightly bitter, minty flavor and are used to flavor soups, stews, and sauces. Hyssop is also used to flavor liqueurs and is a common ingredient in the liqueur Chartreuse [2].

Hyssop is a hardy plant that grows well in full sun and well-drained soil. It can be propagated from seeds or cuttings and is often grown in herb gardens.

Identification of diosmin

Hyssopus officinalis L. is a medicinal plant that is rich in polyphenolic compounds. These compounds have been shown to have antioxidant, anti-inflammatory, and antimicrobial properties, making them important for human health. There are several methods that can be used to identify and characterize the polyphenolic compounds of *Hyssopus officinalis* L. [3].

In the research [4] ultraviolet–visible (UV) spectroscopy was used to determine of the total flavonoid content of hyssop leaves and one-dimensional nuclear magnetic resonance (NMR) spectroscopy was used to elucidate diosmin structure.

The flavonoid composition of the hyssop plant was studied using high-performance liquid chromatography and NMR spectroscopy in research [5]. The presence of diosmin as the main flavone was detected. The maximum levels of this compound are found in the sepals and leaves, which account for 51 and 40.5%, respectively, of the total diosmin content of the whole plant.

Crushed leaves of a commercial sample of hyssop were analyzed in this research. The following solvents and standard samples were used: dimethyl sulfoxide-d_6 (≥99.9%, Sigma-

Aldrich, CAS number 2206-27-1), a standard sample of diosmin (CAS number 520-27-4). The samples were analyzed on a spectrometer JEOL JNM ECA-600, Japan.

To develop a technique for the identification of individual BAS in the extract, it is important that at least one signal of each BAS does not overlap with the others. To achieve this, a ^{1}H NMR spectrum of a standard sample of diosmin (Figure 1) as one of the main biologically active substances of *Hyssopus officinalis* L.was registered. Also, a ^{1}H NMR spectrum of an extract of hyssop, obtained in the laboratory from hyssop leaves by direct extraction with deuterated dimethyl sulfoxide, was registered.
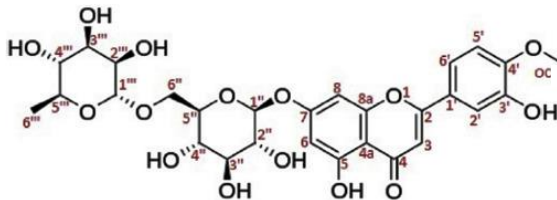
Figure 1. The chemical structure of diosmin [4]

Comparing the ^{1}H NMR spectra of a *Hyssopus officinalis* L. extract and standard sample of diosmin (Figure 2), we can observe the next signals of diosmin which do not overlap with the signals of other BAS: δ 12.93 (s, ^{1}H, OH-5), 9.46 (s, ^{1}H, OH-3′), 7.57 (dd, J = 8.5, 2.2 Hz, ^{1}H, H-6′), 7.44 (d, J = 2.2 Hz, ^{1}H, H-2′), 7.13 (d, J = 8.7 Hz, ^{1}H, H-5′), 6.82 (s, ^{1}H, H-3), 6.76 (d, J = 2.1 Hz, ^{1}H, H-8), 6.46 (d, J = 2.1 Hz, ^{1}H, H-6). The coupling constants of these signals also coincide. This leads to the conclusion that presented signals can be used to identify diosmin in the extract of *Hyssopus officinalis* L. by ^{1}H NMR spectroscopy.
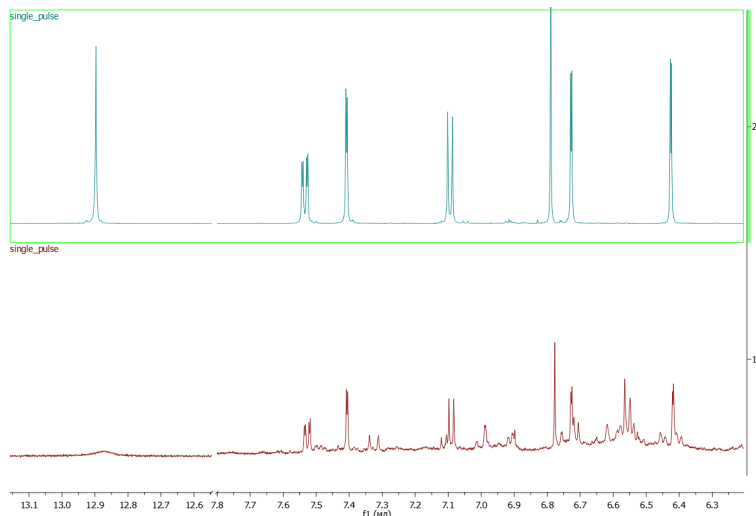
Figure 2. Stack of ^{1}H NMR spectra in DMSO-d_6: 1) leaf extract of Hyssopus officinalis L., 2) standard sample of diosmin

Practical application

In summary, there are several analytical techniques that can be used to identify and characterize the polyphenolic compounds of *Hyssopus officinalis* L., including HPLC, LC-MS, FTIR spectroscopy, NMR spectroscopy, and HRMS. These techniques can provide valuable information about the structure, composition, and properties of the polyphenolic compounds, which can be used to better understand their biological activities and potential health benefits.

It is proposed to use this approach for determination of diosmin in extracts from leaves of *Hyssopus officinalis* L. by ^{1}H NMR spectroscopy as an alternative method for the qualitative determination. Using the considered signals it is also possible to quantify the diosmin content in *Hyssopus officinalis* L by ^{1}H NMR spectroscopy because this method is free from complicated sample preparation, derivatization and the need for standard samples.

Acknowledgments

References

1. F. Fathiazad, S. Hamedeyazdan A Review on Hyssopus officinalis L.: Composition and Biological Activities. – African Journal of Pharmacy and Pharmacology. – 2011, 5(17), pp. 1959-1966.
2. S. Kumar, A. K. Pandey Chemistry and biological activities of flavonoids: an overview. – Sci. World J. – 2013.
3. M. N. Ivashev, O.A. Andreeva, V.A. Bandjukova, T.D. Dragaleva. Extraction of diosmin from plants of the genus Vicia and Hyssopus officinalis and its effect on blood coagulation (in Russian). – Pharm. Chem. J. – 1995, № 10, pp. 39-41.
4. Z. Soheilikhah, M. Modarresi, N. Karimi, A. Movafeghi. Qualitative and quantitative analysis of diosmin content of hyssop (Hyssopus officinalis) in response to salinity stress. – Heliyon. – 2021, 7(10), p. e08228.
5. F. R. Marin, A. Ortuño, O. Benavente-Garcia, J. A. Del Rio. Distribution of flavone glycoside diosmin in Hyssopus officinalis plants: changes during growth. – Planta medica. – 1998, 64(2), pp. 181-182.

Optimization of the duration of ^{31}P-NMR analysis of lignin functional composition

S.L. Shestakov, A.Yu. Kozhevnikov, Yu.A. Sypalova, N.S. Sukherina
Northern (Arctic) Federal University named after M.V. Lomonosov
E-mail: laston85@mail.ru

Lignin is a natural aromatic polymer which content is from 20 to 35 % of wood. Nowadays lignin is considered as the waste after cellulose isolation, and is not widely used.

According to common considerations, lignin is a complex macromolecule based on three monomer sub-units: guaiacylic links (G), which are the derivatives of conipherylic alcohol; syringylic links (S), the derivatives of synapic alcohol; *p*-hydroxyphenylic links (H), the derivatives of cumaric alcohol. The structure of lignin is amorphous and branched due to presence of simple etheric and carbon-carbon bonds.

Nowadays is actual the issue of lignin recycling to various useful products, in particular, lignins are used as sorbents. One of the important parameters of such products is the number of sorption centers in macromolecule, for example, the hydroxyl groups. Thus, it's actual the analysis of polymer functional composition via the determination of the fraction of each sort of OH-groups. The hydroxyl groups in lignin macromolecule are located in different chemical surrounding, which allows to differ them during the NMR analysis. One of the effective methods of such analysis is ^{31}P-NMR, which includes the preliminary phosphytilation of OH-groups with special agent. Nevertheless, most of suggested methodics require the significant duration of spectrum recording. We adjusted the experimental parameters for working process optimization. As the test sample, we used the lignin of raspberry stalks (*Rubus Idaeus L.*). Pulse length (12 µs) and acquisition time (1.13 s) were constant during the experiments series, other parameters (delay time, number of scans, sample weight mass) were varied.

As a result of experiments series we determined the parameters that allow to shorten the time of experiment from 3.5 h to 13 min without spectra quality loss (lowering of resolution and signal-to-noise ratio). The values of varied parameters and signal-to-noise ratio are represented in Table 1.

Table 1. Signal-to-noise ratio in experiments.

Sample weight, mg	Delay, s	Signal-to-noise ratio
15	25	41,33
15	5	19,09
40	5	38,03

As the example, fig. 1 represents the ^{31}P-NMR spectra of raspberry stalks lignin, registered under equal experimental conditions (pulse length 12 µs, acquisition time 1.13 s, delay 5 s, number of scans 128), but with different sample weight mass (varied from 15 to 40 mg).
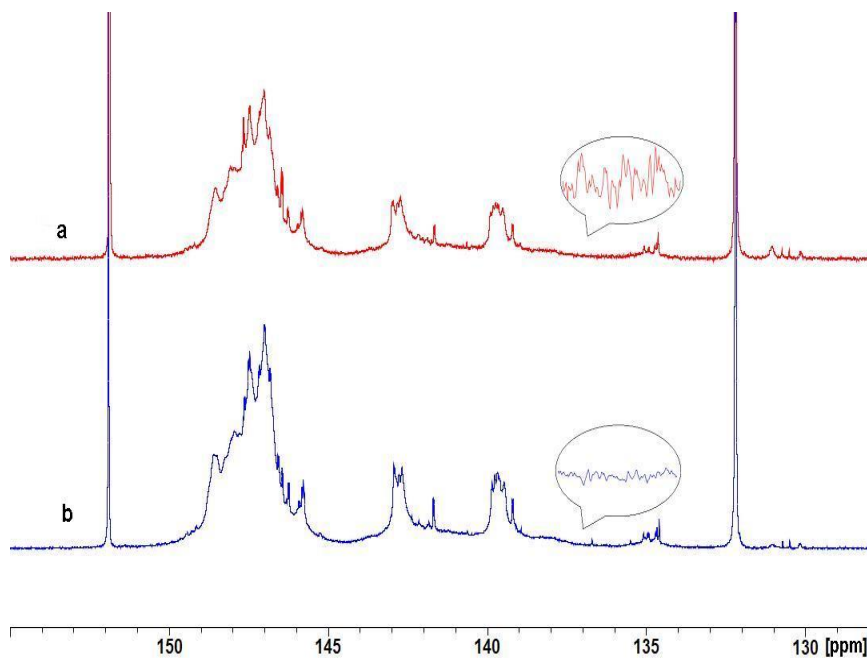
Figure 1. ^{31}P-NMR spectra of raspberry stalks lignin, registered for sample weights 15 mg (a) and 40 mg (b).

Mechanical Relaxation of PPI and PAMAM Dendrimers of Low Generations

Nadezhda N. Sheveleva,[1] Ivan N. Fadeenko,[1] Andrei V. Komolkin,[1] Denis A. Markelov[1]
[1]St. Petersburg State University, 7/9 Universitetskaya nab., St. Petersburg 199034, Russia
E-mail: n.n.sheveleva@spbu.ru

Introduction

Dendrimers are hyperbranched synthetic macromolecules with a perfectly symmetrical tree-like structure [1]. The reason is the global demand for new nanomolecules and materials based on them, which can be used in advanced technologies and medicine. Therefore, the optimization of synthesis methods and the development of new strategies, that allow the creation of dendrimers with different morphology and functionalization, contribute to the emergence of new types of dendrimers [2–4]. The behavior of dendrimers in solution remains the most studied due to their use in biomedical applications [5–7] as nanocontainers for gene and drug delivery. The field of creating new materials based on dendrimer macromolecules and the use of dendrimers as nanomodifiers for already utilized materials develops [8,9].

The development of the theory of mechanical relaxation of dendrimers began with analytical studies using a simplified viscoelastic model. However, within the framework of this model, it is quite difficult to predict the effects determined by volume interactions, the mobility of the dendrimer as a whole, and the intermacromolecular mobility/interactions as well as the influence of the chemical structure of the dendrimer monomer unit. Thus, in the first experimental rheological studies of dendrimers or hyperbranched polymers, the analysis of experimental data was usually carried out without taking into account the specific tree-like topology of macromolecules.[10–12]

The aim of this work is a comprehensive study of the mechanical properties of polyamidoamine (PAMAM) and polypropylene imine (PPI) dendrimers of the second generation in a melt. For comparative analysis, we use the MD simulation results for the polybutylcarbosilane (PCS) dendrimer obtained by us earlier in [13,14].

Simulation details

We have performed atomistic molecular dynamics (MD) simulations of these dendrimers. The atomistic model of united atoms was used, in which only ionized hydrogen atoms in NH_2 groups were explicitly taken into account. The simulation box with periodic boundaries contained 27 dendrimers for each system. Molecular dynamics simulations were performed in the GROMACS package [15] and OPLS force field [16]. At the preliminary stage of equilibration of the systems, the V-rescale thermostat [17] at 600 K was used, which was triggered every 0.1 ps, and Berendsen barostat [18] at 1 atm and $\tau_p = 1$ ps for 100 ns for PPI and 500 ns for PAMAM dendrimers. The lengths of these trajectories were sufficient for the systems to "forget" the initial configurations. Further, each system was simulated in the NPT ensemble using the Langevin thermostat at different values of the coupling constant $\tau_T = 0.005, 0.05, 0.5$ ps in order to vary the friction in the systems. For the highest value of τ_T, we have simulated ten replicas to have a better statistics at long times. This equilibration was performed at least for 100 ns for each system. The final trajectories were obtained in NVT ensemble during 600 ns for PPI and 1200 ns for PAMAM dendrimers.

Results

It has been shown that the mechanical relaxation in the tension relaxation region (at high frequencies or short times) of PPI and PAMAM G2 is very different from PCS G2 (Fig.1). This is due to the less dense core of PPI and PAMAM G2 than in PCS G2, as well as to the presence of entanglements between dendrimers due to hydrogen bonding, which are absent in PCS. In this regard, a significant change in the absolute value of the slope of the

dynamic modulus from 0.7 (for PCS G2) to 0.4-0.45 (for PPI and PAMAM G2) is observed. However, most likely, that for higher generations, the difference in *G(t)* at short times between PCS and the studied dendrimers may significantly decrease or disappear, since the neighboring PPI and PAMAM dendrimer macromolecules will not be able to penetrate into the core region.
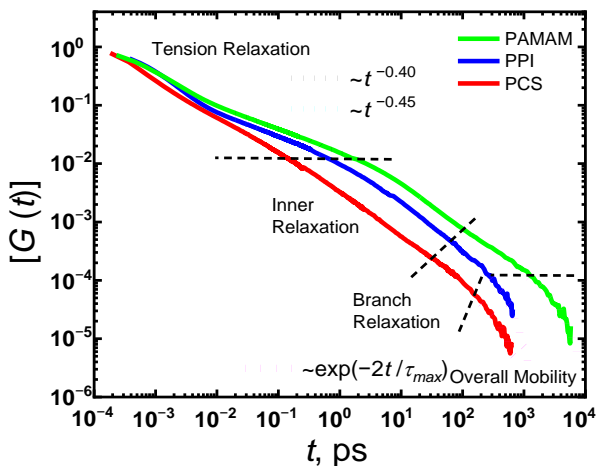

Figure 1. Double-logarithmic representation of the normalized shear-stress relaxation modulus [G(t)] = G(t)/G(0) of melts for PAMAM and PPI dendrimers. The data for PCS melt are presented for comparison from Ref. [13].

In the intermediate and high-frequency region, the mechanical relaxation of PAMAM slows down compared to PPI and PCS. Moreover, as for PAMAM, the region is observed where $G'(\omega) > G''(\omega)$. This effect is associated with the presence of intermolecular entanglements due to hydrogen bonding. The presence of entanglements between PAMAM dendrimers is also confirmed by the slowdown of rotational diffusion.

Thus, hydrogen bonding strongly affects the mechanical relaxation of dendrimer melts. Therefore, tuning the chemical structure of the dendrimer can be used to improve the mechanical properties. We believe that our comprehensive research contributes to the systematization of knowledge about the rheological properties of dendrimers.

Acknowledgments

References

1.   Mintzer, M.A.; Grinstaff, M.W. Biomedical Applications of Dendrimers: A Tutorial. *Chem. Soc. Rev.* 2011, *40*, 173–190, doi:10.1039/B901839P.
2.   Sowinska, M.; Urbanczyk-Lipkowska, Z. Advances in the Chemistry of Dendrimers. *New J. Chem.* 2014, *38*, 2168, doi:10.1039/c3nj01239e.
3.   Kang, T.; Amir, R.J.; Khan, A.; Ohshimizu, K.; Hunt, J.N.; Sivanandan, K.; Montañez, M.I.; Malkoch, M.; Ueda, M.; Hawker, C.J. Facile Access to Internally Functionalized

Dendrimers through Efficient and Orthogonal Click Reactions. *Chem. Commun.* 2010, *46*, 1556–1558, doi:10.1039/b921598k.

4.   Hecht, S. Functionalizing the Interior of Dendrimers: Synthetic Challenges and Applications. *J. Polym. Sci. Part A Polym. Chem.* 2003, *41*, 1047–1058, doi:10.1002/pola.10643.

5.   Chis, A.A.; Dobrea, C.; Morgovan, C.; Arseniu, A.M.; Rus, L.L.; Butuca, A.; Juncan, A.M.; Totan, M.; Vonica-Tincu, A.L.; Cormos, G.; et al. Applications and Limitations of Dendrimers in Biomedicine. *Molecules* 2020, *25*, 3982, doi:10.3390/molecules25173982.

6.   Dias, A.P.; da Silva Santos, S.; da Silva, J.V.; Parise-Filho, R.; Igne Ferreira, E.; Seoud, O. El; Giarolla, J. Dendrimers in the Context of Nanomedicine. *Int. J. Pharm.* 2020, *573*, 118814, doi:10.1016/j.ijpharm.2019.118814.

7.   Gorzkiewicz, M.; Konopka, M.; Janaszewska, A.; Tarasenko, I.I.; Sheveleva, N.N.; Gajek, A.; Neelov, I.M.; Klajnert-Maculewicz, B. Application of New Lysine-Based Peptide Dendrimers D3K2 and D3G2 for Gene Delivery: Specific Cytotoxicity to Cancer Cells and Transfection in Vitro. *Bioorg. Chem.* 2020, *95*, 103504, doi:10.1016/j.bioorg.2019.103504.

8.   Kuang, T.; Chang, L.; Fu, D.; Yang, J.; Zhong, M.; Chen, F.; Peng, X. Improved Crystallizability and Processability of Ultra High Molecular Weight Polyethylene Modified by Poly(Amido Amine) Dendrimers. *Polym. Eng. Sci.* 2017, *57*, 153–160, doi:10.1002/pen.24396.

9.   Zhao, H.; Liao, B.; Nian, F.; Zhao, Y.; Wang, K.; Pang, H. Synthesis and Characterization of a PAMAM Dendrimer-Based Superplasticizer and Its Effect on the Properties in Cementitious System. *J. Appl. Polym. Sci.* 2018, *135*, 1–11, doi:10.1002/app.46550.

10.   Uppuluri, S.; Morrison, F.A.; Dvornic, P.R. Rheology of Dendrimers. 2. Bulk Polyamidoamine Dendrimers under Steady Shear, Creep, and Dynamic Oscillatory Shear. *Macromolecules* 2000, *33*, 2551–2560, doi:10.1021/ma990634u.

11.   Kwak, S.-Y.; Ahn, D.U. Processability of Hyperbranched Poly(Ether Ketone)s with Different Degrees of Branching from Viewpoints of Molecular Mobility and Comparison with Their Linear Analogue. *Macromolecules* 2000, *33*, 7557–7563, doi:10.1021/ma991569r.

12.   Wu, W.; Driessen, W.; Jiang, X. Oligo(Ethylene Glycol)-Based Thermosensitive Dendrimers and Their Tumor Accumulation and Penetration. *J. Am. Chem. Soc.* 2014, *136*, 3145–3155, doi:10.1021/ja411457r.

13.   Dolgushev, M.; Markelov, D.A.; Lähderanta, E. Linear Viscoelasticity of Carbosilane Dendrimer Melts. *Macromolecules* 2019, *52*, 2542–2547, doi:10.1021/acs.macromol.8b02250.

14.   Sheveleva, N.N.; Dolgushev, M.; Lähderanta, E.; Markelov, D.A. Mechanical Relaxation of Functionalized Carbosilane Dendrimer Melts. *Phys. Chem. Chem. Phys.* 2022, *24*, 13049–13056, doi:10.1039/D2CP00805J.

15.   Abraham, M.J.; Murtola, T.; Schulz, R.; Páll, S.; Smith, J.C.; Hess, B.; Lindahl, E. GROMACS: High Performance Molecular Simulations through Multi-Level Parallelism from Laptops to Supercomputers. *SoftwareX* 2015, *1–2*, 19–25, doi:10.1016/j.softx.2015.06.001.

16.   Matsui, M.; Akaogi, M. Molecular Dynamics Simulation of the Structural and Physical Properties of the Four Polymorphs of TiO 2. *Mol. Simul.* 1991, *6*, 239–244, doi:10.1080/08927029108022432.

17.   Bussi, G.; Donadio, D.; Parrinello, M. Canonical Sampling through Velocity Rescaling. *J. Chem. Phys.* 2007, *126*, 014101, doi:10.1063/1.2408420.

18.   Berendsen, H.J.C.; Postma, J.P.M.; van Gunsteren, W.F.; DiNola, A.; Haak, J.R. Molecular Dynamics with Coupling to an External Bath. *J. Chem. Phys.* 1984, *81*, 3684–3690, doi:10.1063/1.448118.

Application of ^{1}H and ^{13}C NMR spectroscopy for the determination of the key parameters of vegetable oils

Mark Smirnov, Galina Kupriyanova

Institute of Physics, Mathematics and Information Technology, Immanuel Kant Baltic Federal University, 236041, Kaliningrad, Russia

E-mail: smirnov.mark2015@yandex.ru

http://kantiana.ru

Introduction

The method of nuclear magnetic resonance spectroscopy has been successfully used for a long time to study the composition of vegetable oils, their quality, and to establish their authenticity [1-3]. The widespread use of NMR in this area is due to the high degree of repeatability of the experiment and the indestructibility of the sample. One of the important indicators of the quality of oils is the degree of unsaturation and the proportions of various acyl groups. The degree of unsaturation is used to predict chemical and physical properties and allows us to assess the degree of rancidity of the finished product. Chemical tests are traditionally used to assess this indicator. One of these tests is to determine the iodine number IN [4]. The method consists in adding iodine, and further determining the number of grams of iodine attached at the place of double bonds to 100 g of fat. However, this method is time consuming. There are also classical methods that include various stages of oil transesterification, as well as gas chromatography methods that subject the sample to significant processing, which leads to oxidation of the samples and the appearance of various artifacts. The NMR method lacks these disadvantages.

The purpose of this work was to determine two important parameters of vegetable oils using ^{1}H and ^{13}C NMR spectroscopy: the iodine number and the percentage of free fatty acids (%FFA).

Vegetable oils consist of more than 90% triacylglycerides (TAG), which are a product of esterification of three carboxylic acids and triatomic alcohol glyceride. The oils also contain diacylglycerides (DG), which are a glyceride consisting of two fatty acids associated with a glycerol molecule. Monoglycerides (MG) are also present in small amounts. However, in the oil there are also so-called free fatty acids (FFA), which are not part of TAG, MG and DG, and whose percentage determines such a parameter as the acidity of vegetable oil. This parameter directly determines the taste properties of vegetable oil, if its value is higher than normal, the oil is rancid.

Samples

Ten oil samples were studied in the work: 3 samples of olive oil Virgin Olive oil (Spain 2022), Virgin Olive oil (Borges, 2021), Olive oil (Riviera Komili, Turkey); 4 samples of soybean oil, subjected to technological processing; 2 samples of sunflower oil (Yudum, Turkey) and one sample of unrefined sesame oil (KOTA'NYI, GOURMET, Мексикаб 2021).

Experiment

High-resolution ^{1}H and ^{13}C NMR spectra were recorded on a Varian 400 MHz NMR spectrometer at B = 9 T.

^{1}H NMR spectra were registed using standard parameters: the number of scans is 16, the relaxation delay is 1 second, and the experiment time is about 1 minute.

^{13}C NMR spectra were recorded both with the suppression of the proton signal (with decoupling) and without the suppression of protons for the correct assignment of signals. Experiment parameters ^{13}C: the number of scans is 256, the relaxation delay is 1 second, the signal gain is 54, and the experiment time is about 10 minutes.

Results and discussion

1. Calculation of the iodine value

To determine the iodine number (IN) of the studied samples of vegetable oils, the method proposed in [5] was used. The iodine number of vegetable oil can be determined based on the number of protons bound to carbon atoms, which in turn are linked by double bonds [6]. The chosen technique is based on the value of the integral intensity of the multiplet at δ = 4.2 ppm, which refers to protons that form the TAG glycerin skeleton. The multiplet at δ=5.3 ppm is also taken into account which is responsible for the signal of protons of the methyl group of glycerol. Figure 1 shows the spectra of sesame and olive oils with spectral regions highlighted at 4.2 ppm and 5.3 ppm. The relative intensities of the overlapping signals were estimated using the Magic Plot program.
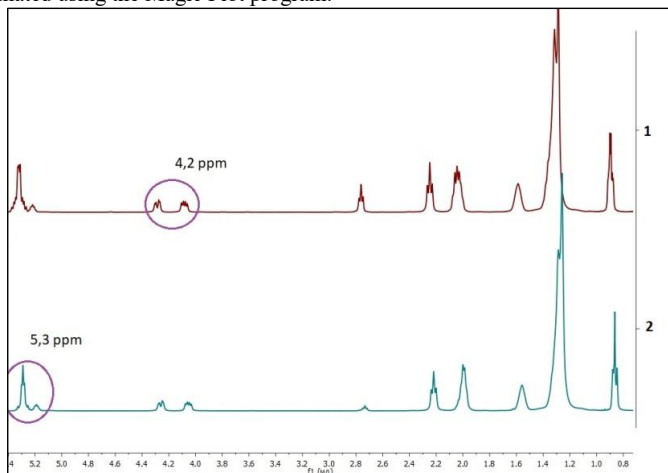
Fig.1. ^{1}H NMR spectra of oils:1. Sesame oil;2.Olive oil Borges 2021.

The obtained values of the iodine number (Table 1) perfectly matched the literature data for the corresponding types of oils [7]. Nevertheless, it should be noted that the data on IN for soybean oils No. 3 and No. 4 differ. This may be due to the fact that the soybean oil samples were subjected to hydration. According to the data presented, it can be seen that soybean oils No. 1 and No. 2, as well as sesame oil, have higher values of the iodine number than olive oil.

Table 1.

Sample	Iodine number	% FFA
Sesame	116,45	1,38
Sunflower	81,38	-
Soybean №1	124,15	2,011
Soybean №2	132,59	0,31
Soybean №3	108,43	1,85
Soybean №4	118,57	-
Olive oil (Spain 2022)	85,52	0,7
Olive oil (Borges 2021)	81,58	0,99
Sunflower oil (Yudum)	80,98	3,14
Olive oil (Komili)	80,67	8,1

2. Calculation of the percentage of the free fatty acids.

Figure 2 shows high-resolution ^{13}C NMR spectra of sesame and olive oils. Separately, the spectral region 173 - 178 ppm is highlighted. To determine the percentage of free fatty acids (%FFA) in the sample, the method proposed in the article [8] was used. The technique is based on estimates of integral signal intensities in the ^{13}C NMR spectrum in the region δ = 170 – 180 ppm (fig.2).

This spectral region is formed by the signals of carbon nuclei, which are part of the carbonyl group (C = O) of fatty acids. The method used is based on the fact that the signals in the region δ = 174 – 178 are attributed to the nuclei of the ^{13}C carbonyl group of free fatty acids, i.e. those that are not part of MG, DG and TAG. Intense signals in the region of δ = 173 – 174 ppm will, on the contrary, come from the nuclei of ^{13}C atoms that are part of triglycerides [1]. Using the methodology proposed in [8], the percentage composition of free fatty acids in the studied samples was determined (Table 1). However, it was not possible to calculate this indicator in all samples. Extra virgin olive oil cold-pressed olive oils have a very low level of free acids, so it is not always possible to determine the values of %FFA less than 1% [7]. According to the data [7], the following indicators can be expected %FFA:

1. Olive oils of the highest quality (extra virgin olive oil) – up to 0.8 %;
2. Less quality olive oils (virgin olive oil) – 0.8 – 2%;
3. Oils of the lowest grade have over 2%.
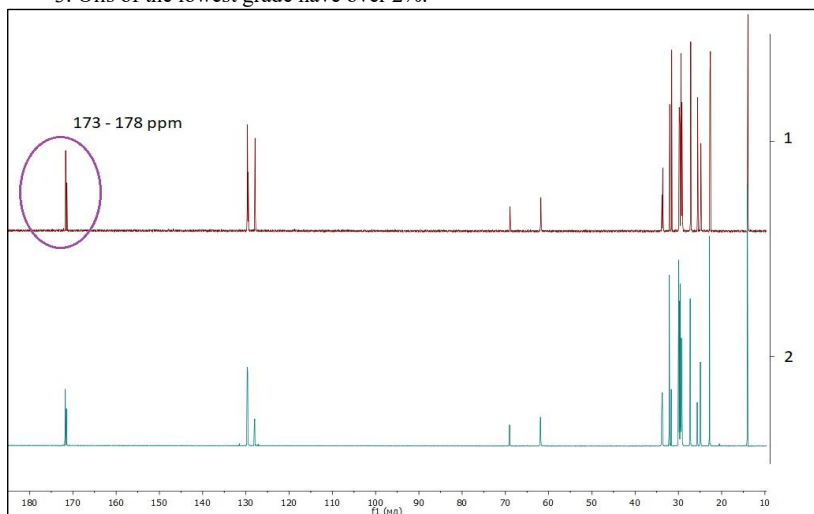
Fig.2. ^{13}C NMR spectra of oils (with decoupling): 1. Sesame oil; 2. Olive oil Spain 2022.

From the data we have obtained, it can be seen (Table 1) that the sample of olive oil (Spain) is an olive oil of the highest standard. A good acidity index was also found in the Borges 2021 sample, although the FFA parameter is slightly higher than the limit of permissible values for olive oils of the highest grades. The Riviera Komili olive oil sample showed a very high FFA value (more than 3%). It can be seen that the FFA parameter for sunflower and soybean oils is much higher, which is a reflection of the process of additional processing of these oils.

Thus, using the methods of ^{1}H and ^{13}C NMR spectroscopy, the parameters characterizing the quality of vegetable oils, such as the iodine number and the percentage of

free fatty acids, were determined. A qualitative agreement was achieved with the parameters IN, FFA obtained earlier by chemical methods for olive, soybean and sunflower oils.

References

1. Raffaele Sacchi. ^{1}H and ^{13}C NMR of virgin olive oil. An overview / Raffaele Sacchi, Francesco Addeo, Livio Paolillo // Magnetic Resonance in Chemistry. – 1997. – Vol.35 – S.133 – 145;
2. Mark Smirnov, Ivan Mershiev, Galina Kupriyanova. ^{1}H high-resolution NMR spectrometry and relaxometry for soybean oil research. Magnetic Resonance and its Applications. Spinus-2021. Proceedings. Saint Petersburg State University, 2021. 282 pp. ISSN 2542–2049;
3. Mark Smirnov, Ivan Mershiev, Alexsander Musalenko, Galina Kupriyanova. ^{1}H NMR study of soybean oils. Magnetic Resonance and its Applications. Spinus-2020. Proceedings. Saint Petersburg State University, 2020. 308 pp. ISSN 2542-2049;
4. Пассет Б. В., Антипов М. А. - Практикум по техническому анализу и контролю в производстве химико-фармацевтических препаратов и антибиотиков. - Москва: Медицина, 1981, 272 с.;
5. Ondrej Hendl. Rapid method for determination of iodine numbers of vegetable oils: Master's Theses. – Western Michigan University, 1996 – 59 с.
6. Nielsen LV. Studies on the relation between unsaturation and iodine value of butterfat by high resolution nuclear magnetic resonance (NMR). Milchwissenschaft 1976;31:598–602
7. Olive oil acidity [Electronic resource]. - Access mode: https://en.wikipedia.org/wiki/Iodine_value;
8. Maria Enrica Di Pietro. NMR Determination of Free fatty acids in Vegetable Oils / Maria Enrica Di Pietro, Alberto Mannu, Andrea Mele // Processes. – 2020. - 8, 410;

Topical problems of ^{15}N NMR spectroscopy.

<u>Vladislav V. Stanishevskiy[1]</u>, Alla K. Schestakova[2], Vyacheslav A. Chertkov[1]

[1]*Department of Chemistry, Moscow State University, Moscow, 119991 Russia*
[2]*State Scientific Research Institute of Chemistry and Technology of Organoelement Compounds, Moscow, 105118 Russia*
E-mail: Stvladislav@yandex.ru

Introduction

The present work is devoted to the analysis of current problems of ^{15}N NMR spectroscopy in studies of structure and properties of nitrogen-containing compounds.

The major nitrogen isotope is ^{14}N, whose nucleus is quadrupole. The signals in the ^{14}N NMR spectra show extremely short relaxation times due to the quadrupole properties of these nuclei (spin 1) for the vast majority of organic compounds, which makes these spectra of little information. On the contrary, the minor isotope ^{15}N has spin ½ and acceptable for registration of NMR spectra. However, at natural content (0.38%) in NMR spectra ^{1}H and ^{13}C appropriate satellite signals appear too weak to extract information about the *J*-couplings with ^{15}N. So, the availability of ^{15}N-enriched compounds is the key practical problem in these studies. Therefore, the search for new methods for the synthesis of nitrogen-enriched compounds is the primary task of solving them. Interest in these objects is determined by their special role as model systems for in-depth study of the properties of nitrogen-containing compounds and the mechanisms of their transformations, including, among other things, metabolic processes in living systems.

Results

An original way to synthesize a series of ^{15}N-enriched compounds from ^{15}N-enriched ammonium salts was developed and their ^{1}H, ^{13}C and ^{15}N NMR spectra were fully analyzed.

This methodology was successfully applied to obtain [^{15}N]benzamide and double enriched [^{2}H$_5$, ^{15}N]benzamide. A two-step synthesis of [^{15}N]aniline from [^{15}N]benzamide was performed providing the product of high chemical and isotopic purity. ^{13}C NMR spectra of benzamide isotopomers was decoded to give the couplings involving ^{15}N nucleus and isotopic chemical shifts.
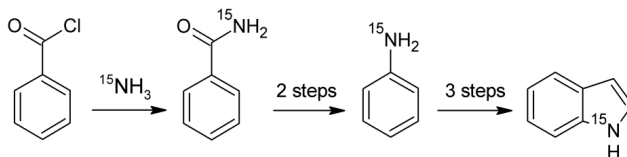
Scheme 1

An original scheme for the synthesis of [^{15}N]indole from [^{15}N]aniline was developed [1]. Elucidation of all of the 1D and 2D NMR spectra made it possible to measure unambiguously the exact values of the couplings ^{1}H-^{1}H, ^{15}N-^{1}H and ^{13}C-^{15}N. The totality of all NMR spectra obtained in this work can serve as an important reference point to establish structure of new aromatic heterocycles.

An analysis of modern literature data and the results of our experiments show that ^{15}N chemical shifts, as well as ^{1}H-^{15}N and ^{13}C-^{15}N spin couplings, are highly informative spectral parameters. Here we show for the first time, that the isotope-chemical shifts of ^{13}C nuclei caused by the replacement of the ^{14}N nucleus by ^{15}N can also provide valuable information about the molecular structure.

The series of quantum-chemical calculations of chemical shifts ^{15}N and spin-spin coupling constants ^{13}C-^{15}N for a representative series of conformationally rigid nitrogen-

containing compounds has been performed. An approach for the determination of the spin-spin coupling constants signs was developed using the statistical processing of the obtained correlation dependences [2].

Using [^{2}H$_5$, ^{15}N] benzamide as an example, it is shown that the use of nitrogen-enriched compounds can provide systematic error-free and qualitatively new information on the dynamics of these compounds in solution. The temperature-dependent waveforms of the amide proton signals were processed using the DNMRD5 software package. Isotopic enrichment of the benzene ring with deuterium atoms avoided the overlapping of the amide proton signals with the aromatic signals.

To determine the rotation barrier of the benzamide under study, we used dynamic NMR spectroscopy. During the rotation around the amide bond the chemical exchange of non-equivalent amide protons occurs. In turn, dynamic NMR spectra are quite sensitive to the rate of this exchange and provide a powerful and well-established way to extract kinetic parameters using variable temperature NMR experiments.

Fig. 1. The temperature-dependent lineshupes of the amide protons of [^{2}H$_5$, ^{15}N]benzamide.
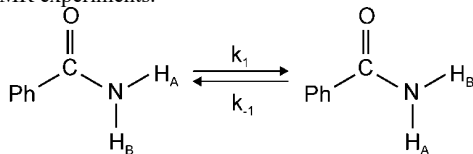
Scheme 2

The presence of the ^{15}N nucleus in the molecule makes it possible to obtain signals with good resolution due to the absence of quadrupole broadening from the ^{14}N nucleus. This inevitably leads to the appearance of splitting on the ^{1}H nucleus. However, they are quantitatively taken into account in the course of adequate software (DNMRD5) data processing. Additional deuteration of the benzene ring prevents unwanted overlapping of amide protons with aromatics. We used DMSO-D$_6$ because of its respective liquid phase temperature range as it includes the entire high temperature region where amide proton signal collapse occurs. It is also critical to obtain accurate rotational dynamics parameters.

We also studied a number of ^{15}N-enriched benzylideneanilines containing substituents in the ortho-position of the benzene ring, which is far from the nitrogen isotope label. We have shown that these objects can be used as pH-induced molecular switches. Under the action of the acid, the azomethine nitrogen is protonated and conditions are created for the formation of an intramolecular hydrogen bond with the substituent (Fig. 3). Our calculations have shown that the geometry of the molecule can change dramatically in this case. This proceeds due to the fact that in a neutral molecule, the substituent and lone pair of nitrogen, in common repel each other. The protonation of greatly alters the balance of intramolecular forces, which causes rotation of the those removed benzene ring. We estimate numerically (DFT) the molecular switching energy of [^{15}N]orthofluorobenzylideneaniline to be ~7 kcal/mol, which is one of the highest values for this type of molecular switches.

E, kcal/mol

Fig. 2. A cross-section of the potential energy surface if [^{15}N]orthofluorobenzylidenaniline B3LYP, 6-311++g(2d,p)

Fig. 3. Molecular pH-controlled switching of [^{15}N]orthofluorobenzylidenaniline.

We calculated the cross-section of the potential energy surface of [^{15}N]orthofluorobenzylidenaniline and its protonated form around the dihedral angle φ (C1-C2-C3-N), Fig.1. It is well visible that the position of the global minimum of the molecule changes in the transition to the protonated form, which is explained by the formation of a strong intramolecular hydrogen bond between the fluorine and hydrogen atoms of the quaternized nitrogen atom.

According to quantum chemical DFT modelling, the distance between the fluorine and hydrogen atoms is about 1.98 Å, which can be supported experimentally in NMR spectra in the formation of a long-range spin-spin coupling constant through the hydrogen bond.

Thus from the ^{1}H NMR spectra of [^{15}N]orthofluorobenzylidenaniline a spin-spin coupling constants of $^5J_{F-H}$ = 1.32 Hz was determined.

Fig. 4. NMR spectra of [^{15}N]orthofluorobenzylidenaniline a spin-spin coupling constants of NH$^+$.

Conclusions

Thus, our research confirms that ^{15}N NMR spectroscopy is a powerful tool for establishing the structure and properties of nitrogen-containing compounds.

References

1. V.V. Stanishevskiy, A.K. Shestakova, V.A. Chertkov. *Chem. Heterocycl. Compd.* (2023), *in the press*.
2. V.V. Stanishevskiy, A.K. Shestakova, V.A. Chertkov. *Appl. Magn. Reson.*, **53**,1693-1713 (2022)

Effect of addition of lithium and aluminum salts on molecular mobility in ethylammonium nitrate. A molecular dynamics simulation study

Milosh Ubovich, Andrei V. Egorov, Vladimir. I. Chizhik
Faculty of Physics, Saint-Petersburg State University, Russia
E-mail: ubovich.milosh@yandex.ru

Introduction

The interest in the study of alkylammonium nitrate protic ionic liquids (AN PILs) has increased significantly in the recent decades. PILs consist of only ions, but, unlike "classical" salts, they are in a liquid state at relatively low temperatures (up to approximately $100^{o}C$). These compounds attract the attention of researchers due to their astonishing properties, such as high thermal stability, high boiling point, low vapor pressure, etc. PILs are employed in diverse electrochemical applications (for instance, lithium ion batteries, fuel cells, etc.). AN PILs have a relatively low cost and toxicity, and besides they are characterized by an exceptional combination of properties. Ethylammonium nitrate (EAN) is a typical substance among AN PILs. EAN consists of ethylammonium cation (EA^{+}, see Fig. 1) and nitrate anion (NO_3^{-}). Mixtures of EAN and two different salts (namely, aluminum nitrate $Al(NO_3)_3$ and lithium nitrate $LiNO_3$) were chosen as the objects of the present study. It is important to compare the behavior of mixtures depending on the type of salt added.
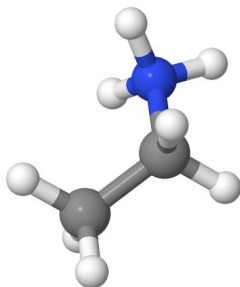
Figure 1. The schematic representation of the ethylammonium nitrate cation (hydrogen – white, nitrogen – blue, carbon – grey)

An attempt was performed to investigate the mechanisms of changes in molecular mobility, when adding salts to the EAN, applied the molecular dynamics (MD) simulations. The main purpose was not only to quantify the kinetic characteristics of the components in the mixture at their different ratios but also to identify the relationship between the peculiarities of the local structure of mixtures and the character of processes of rotational reorientations of ions.

Simulation details and results

The pure ionic liquid (EAN without added salts) and mixtures containing $Al(NO_3)_3$ and $LiNO_3$ were simulated by the MD method. The simulation was carried out in a cubic cell with periodic boundary conditions in the NPT ensemble at 298 K and 1 atm. employing the MDynaMix simulation package [1]. The temperature was kept constant with a Nose-Hoover thermostat [2, 3]. The pressure was maintained with a Hoover barostat [4]. The EA^{+} cation was modeled applying the potentials described in Ref. [5, 6]. A model nitrate anion (Fig. 2) was treated as a 4-site planar structure with the central nitrogen atom and three oxygen atoms at the distance of 1.22 Å with all O-N-O angles of 120° [7]. Its intermolecular interactions

were described by the sum of Coulomb and Lennard-Jones (6-12) potentials. Three different potential parameter sets, taken from Refs. [5, 8, 9], were considered. The interaction potential of the model lithium ion and aluminum ion were also the sum of Coulomb and Lennard-Jones (6-12) potentials. The potential parameters were described in Ref. [10] for Li^+ and in Ref. [11] for Al^{3+}. Simulation time was 1 ns.
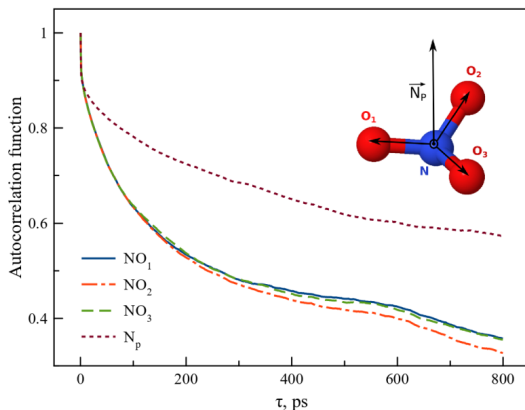
Figure 2. An example of autocorrelation functions of intramolecular vectors in the nitrate anion for EAN with 5 mol. % aluminum nitrate, potential parameter sets taken from Ref. 8.

The self-diffusion coefficients, radial distribution functions, and reorientation times of the intramolecular vectors of the nitrate anion (reorientation times were obtained from autocorrelation functions, an example of the functions is shown in Fig. 2) were calculated for each model systems. A detailed analysis of the influence of added salts of various types on the translational motions of the system components and the processes of reorientation of the nitrate has been fulfilled.

It is planned to compare the results obtained with experimental NMR data (NMR diffusometry and NMR relaxation).

Acknowledgments

References

1. Lyubartsev A. P., Laaksonen A. – Comp. Phys. Comm. 2000. V. 128. No. 3. P. 565.
2. Nose S. – Mol. Phys. 1984. V. 52. No. 2. P.255.
3. Martyna G. J., Tobias D. J., Klein M. L. – J. Chem. Phys. 1994. V. 101. No. 5. P. 4177.
4. Martyna G. J., Tuckerman M. E., Tobias D. J., et al. – Mol. Phys. V. 87. No. 5. P. 1117.
5. Umebayashi Y., Chung W.-L., Mitsugi T., et al. – J. Comput. Chem. Jpn. 2008. V. 7. No. 4. P. 125.
6. Choe J., Kim K., Chang S. – Bull. Korean Chem. Soc. 2000. V. 21. P. 200.
7. Ebner C., Sansone R., Hengrasmee S., et al. – Int. J. Quant. Chem. 1999. V. 75. P. 805.
8. Megyes T., Balint S., Peter E., et al. – J. Phys. Chem. B. 2009. V. 113. No. 13. P. 4054.
9. Laaksonen A., Kovacs H. – Can. J. Chem. 1994. V. 72. P. 2278.
10. Dang L.X. – J. Chem. Phys. 1992. V. 96. P. 6970.
11. Faro T. M. C., Thim G. P., Skaf M. S. – J. Chem. Phys. 2010. V. 132. P. 11450.

Atomic mobility in metallic sodium confined to porous glass

<u>*A.V. Uskov*</u>[1], *D.Yu. Nefedov*[1], *E.V. Charnaya*[1], *Yu.A. Kumzerov*[2], *A.V. Fokin*[2]

[1]*Physics Department, St. Petersburg State University, St. Petersburg 198504, Russia*
[2]*A.F. Ioffe Physico-Technical Institute RAS, St. Petersburg 194021, Russia*
E-mail: <u>*a.uskov@spbu.ru*</u>

Introduction

Sodium is a promising material for production of solid state batteries because of low price compared to lithium, enhanced safety and high power density. Metallic sodium is one of candidates for production of anodes for high energy solid sate batteries (SSB). Knowing the effects of nanostructuring becomes crucial because modern anodes have developed internal microstructure which is required for obtaining better mechanical and electrical properties of SSB [1].

Nanostructuring has a strong influence on atomic mobility and electronic properties of small metallic particles. NMR is a perfect method for investigation of atomic mobility in small metallic particles. Previously the magnetisation recovery curves were used for investigation of atomic mobility in liquid and solid gallium [2]. The gallium has two isotopes ^{69}Ga and ^{71}Ga with the same spin, but different resonance frequencies and quadruple moments. It simplifies analysis of recovery curves. Sodium has only one stable isotope, thus in current work we compare recovery curves obtained in different magnetic fields.

Methods

The correlation time of atomic mobility could be determined by analysis of magnetization recovery curves. The time dependence of magnetization for nuclei with spin 3/2 could be described with [3]:

$$\frac{M(t)}{M_0} = 1 - b\left[\frac{4}{5}\exp\left(-\frac{C\tau_c t}{1+4\omega_0^2\tau_c^2}\right) + \frac{1}{5}\exp\left(-\frac{C\tau_c t}{1+\omega_0^2\tau_c^2}\right)\right]\exp\left(-\frac{t}{T_{1m}}\right), (1)$$

where M_0 is an initial magnetisation, b accounts for a nonideal inversion of magnetisation, C is a constant of quadruple interaction, ω_0 is a Larmor frequency, τ_c is the correlation time of atomic motion, T_{1m} is a time of longitudinal relaxation due to magnetic interaction, which is inversely proportional to temperature.

The samples were produced by embedding the liquid sodium into porous glass with the average pore size 23 nm under pressure 10 *kBar*. The pore size distribution was measured using nitrogen porosimetry on Quadrosorb SI. The samples were gradually cooled to room temperature and cut into pieces with size 3x3x5 mm. The NMR measurements were performed using Bruker Avance 400 and Bruker Avance 750 pulse NMR spectrometers in temperature range from 190 to 293 K. The temperature changed not faster than 0.5 K/min. The period of temperature stabilization was not less than 20 minutes. At every temperature the longitudinal magnetisation recovery curve was measured using the inversion recovery protocol with the two180^o and 90° pulses.

The magnetic interaction is not affected by nanostructuring [4]. Thus contribution of T_{1m} could be determined in bulk sodium where impact of atomic motion on magnetic relaxation is less compared to nanostructured sodium. The T_1 relaxation time in bulk sodium is govern by magnetic relaxation at low temperatures. The measurements of T_1 relaxation times were performed for bulk metallic sodium at temperatures from 18 to 293 K.

Results

The recovery curves obtained at temperatures 190 and 293 K are presented at Figure 1. It was found that the magnetization recovery depends on magnetic field and recovery time becomes longer at higher field and shorter at higher temperature. The recovery curves obtained at temperatures higher than 250 K were fitted using Eq. (1) where $\omega_0^2\tau_c^2 = 1$. This procedure allowed determining values C and τ_c. At lower temperatures the correlation times become longer and value of $\omega_0^2\tau_c^2$ becomes much more than unity. In this case Eq. (1) simplifies to:

$$\frac{M(t)}{M_0} = 1 - b\left[\frac{4}{5}\exp\left(-\frac{Ct}{4\omega_0^2\tau_c}\right) + \frac{1}{5}\exp\left(-\frac{Ct}{\omega_0^2\tau_c}\right)\right]\exp\left(-\frac{t}{T_{1m}}\right) \quad (2)$$

Expression (2) was used for fitting experimental curves in order to obtain value of $C\tau_c^{-1}$ at temperatures lower than 250 K.
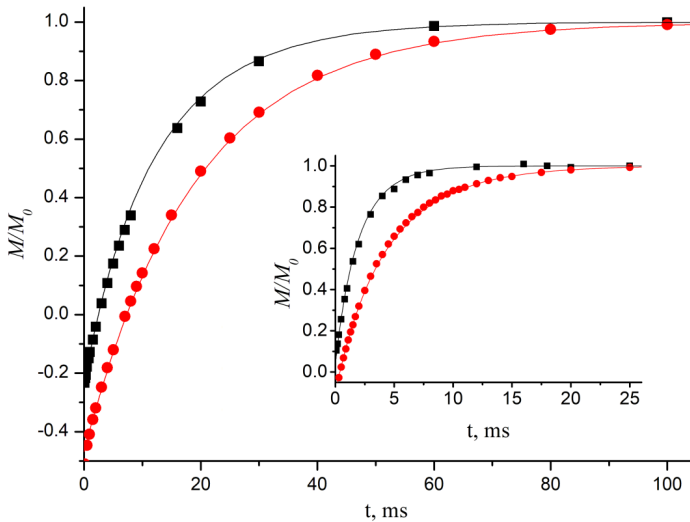
Figure 1. The magnetization recovery curves at 190 K. Black squares correspond to Bruker Avance 400, red circles correspond to Bruker Avance 750. The magnetization recovery curves obtained at 293 K are presented in the insert. The lines are fittings using Eq. (1).

The C value weakly depends on temperature [2], thus the correlation time of atomic motion could be determined for lower temperatures as well. The obtained values of correlation times are presented at *Figure 2*. The correlation time has the thermal activation dependence

$\tau_c = \tau_0 \exp\left(-\frac{E_0}{k_B T}\right)$ where E_0 is an activation energy, k_B is the Bolzmann constant. Thus the dependence of $\ln(\tau_c)$ on T^{-1} is a straight line. The proportionality factor gives the value of activation energy $E_0 = (0.114 \pm 0.007)\,eV$.
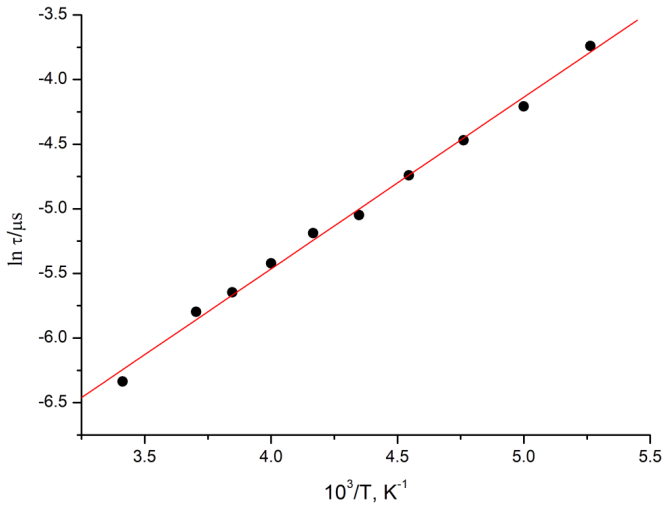
Figure 2. The dependence of the correlation time on T^{-1}.

Acknowledgments

References

1. C. Zhao, L. Liu, X. Qi, Y. Lu, F. Wu, J. Zhao, Y. Yu, Y. Hu, L. Chen. – *Adv. Energy Mater.*, 8, 1703012 (2018).
2. D.Y. Nefedov, E.V. Charnaya, A.V. Uskov, A.O. Antonenko, D.Y. Podorozhkin, Y. A. Kumzerov, A.V. Fokin. – *Phys. Solid State*, 63, 1739-1743 (2021).
3. E.V. Charnaya, T. Loeser, D. Michel, C. Tien, D. Yaskov, Y.A. Kumzerov – *Phys. Rev. Let.*, 88, 097602 (2002).
4. D.Y. Nefedov, A.O. Antonenko, D.Y. Podorozhkin, A.V. Uskov, E.V. Charnaya, M.K. Lee, J.L. Chang, J. Haase, D. Michel, Y.A. Kumzerov. – *Phys. Solid State*, 59, 362-367 (2017).

Freezing and melting transitions and atomic mobility in the nanoconfined Ga-Sn eutectic alloy

A.A. Vasilev[1], D.Yu. Nefedov[1], A.V. Uskov[1], E.V. Charnaya[1], Yu.A. Kumzerov[2], A.V.Fokin[2]
[1]Physics Department, St. Petersburg State University, St. Petersburg 198504, Russia
[2]A.F. Ioffe Physico-Technical Institute RAS, St. Petersburg 194021, Russia
E-mail: Allisher93529@yandex.ru

Introduction

Investigations of properties of gallium and gallium alloys in bulk and in nanocomposites are of great interest for modern applied physics [1, 2]. Phase transitions and size effects in such systems attract the increasing attention of investigators.

The present study has been carried out by using NMR technique, which is a powerful instrument for obtaining information about the internal structure of metallic liquids and solids. The ^{71}Ga and ^{69}Ga NMR measurements were performed for a binary eutectic Ga-Sn alloy, embedded into two opal matrices with different sizes of silica spheres, with a view to study the polymorphism, atomic mobility, and electron-nuclear coupling in Ga-Sn nanocomposites.

Experiment

The synthetic opal matrix is composed of silica spheres arranged in the cubic close packing. The mean sphere diameters in two opal matrices under study were $D_1 = 160$ nm and $D_2 = 375$ nm according to atomic force microscopy. The octahedral and tetrahedral voids between silica spheres form a regular interconnected pore network.

The binary Ga-Sn alloy with a composition of 91.5 at.% Ga and 8.5 at.% Sn was embedded into opal matrices under pressure up to 10 kbar. The composition of the alloy was close to the eutectic point [3]. At room temperature, the alloy in both opal matrices was in the melted state, which is in agreement with its phase diagram [3]. The samples for NMR studies were cut from the loaded opals in the shape of parallelepipeds $3 \times 3 \times 6$ mm. The surfaces of the samples were cleaned from the rest of the bulk alloy.

Studies were carried out using a Bruker Avance 400 NMR pulse spectrometer at magnetic field 9.4 T within a temperature range from 145 to 300 K. We observed NMR signals for the ^{71}Ga and ^{69}Ga isotopes. The NMR spectra were obtained as Fourier transforms of free-induction decays after 90° pulses. The Knight shift for gallium isotopes was referenced to NMR signals from a GaAs single crystal.

Results

The relative ^{71}Ga NMR signal intensity from liquid gallium during the cooling-heating cycle is presented in Fig. 1 for two samples. One can see the quite different hysteretic behavior for the nanocomposites under study. Fig. 1b shows two phase transition steps under both freezing and melting. On the other hand, two phase transition steps can be seen in Fig 1a under freezing and one phase transition step is seen under melting. Note that temperature ranges of the occurrence of supercooled melts were remarkably different.

Fig. 2 illustrates the temperature dependences of the ^{71}Ga Knight shift for the Ga-Sn alloy embedded into both opals. The data correspond to cooling down until complete freezing of confined melts.
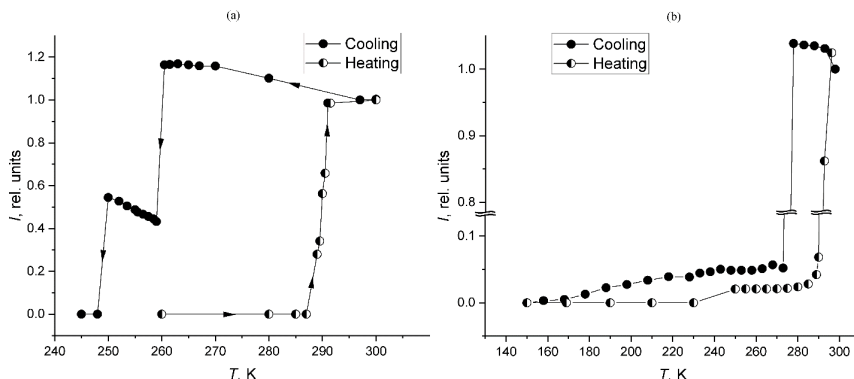
Figure 1. The temperature dependences of the ^{71}Ga signal relative integral intensities for the full freezing-melting cycles for loaded opals with mean diameter of silica spheres 160 nm (a) and 375 nm (b).

The emergence of clear steps in the NMR signal intensity upon freezing of the confined alloy shown in Fig. 1 demonstrates the complex structure of solid Ga-Sn. In agreement with previous studies of crystallization of pure gallium under nanoconfinement [4-6] we can suggest that the gallium-rich segregates in the nanostructured eutectic Ga-Sn alloy have different crystalline symmetries due to enhanced polymorphism. The two polymorph structures formed in the opal with $D_2 = 375$ nm have quite different melting temperatures. One of these temperatures is close to the melting point of α-Ga. In contrast, two different crystalline modifications of gallium-rich segregates in the opal with $D_1 = 160$ nm melted at close temperatures.

Fig. 2 demonstrates that the pore sizes affect the value and the temperature dependence of the Knight shift in the melted alloy.
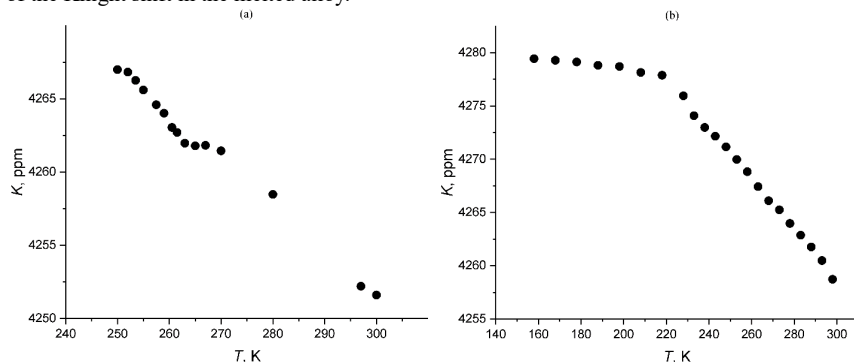
Figure 2. The temperature dependence of the ^{71}Ga Knight shift under cooling for samples with mean diameter of silica spheres 160 nm (a) and 375 nm (b).

To study atomic mobility in confined alloys, NMR measurements of the spin-lattice relaxation time T_1 for ^{71}Ga and ^{69}Ga in bulk alloy and alloy embedded into opals were carried out at room temperature. Remarkable acceleration of nuclear spin relaxation under

nanoconfinement was observed for both gallium isotopes. This acceleration was treated as a result of the increase in the rate of quadrupole relaxation for the alloys within pores. The quantitative treatment based on theoretical models developed in [6] revealed the pronounced slowdown of atomic diffusion in confined melts in agreement with the strong increase of the correlation times τ_c of atomic mobility. It was found that the values of τ_c correlated to the sizes of silica spheres in the opal matrices: the smaller sphere diameter, the longer correlation time. For the opal with $D_1 = 160$ nm the correlation time of atomic mobility increased by ten times compared to the correlation time in the bulk Ga-Sn alloy. Note that NMR provides a unique opportunity to measure the local atomic mobility in confined melts.

Acknowledgments

References

1. Z. Li, Y. Guo, Y. Zong, K. Li, S. Wang, H. Cao, C. Teng. Nanomaterials **11**, 2246 (2021).
2. G. Bo, L. Ren, X. Xu, Y. Du, S. Dou. Adv. Phys.: X **3**, 1446359 (2018).
3. T. J. Anderson, I. Ansara. J. Phase Equilib. **13**, 181 (1992).
4. C. Tien. E. V. Chanaya, W. Wang, Y. A. Kumzerov, D. Michel. Phys. Rev. B **74**, 024116 (2006).
5. E. V. Charnaya, C. Tien, W. Wang, M. K. Lee, D. Michel, D. Yaskov, S. Y. Sun, Yu. A. Kumzerov. Phys. Rev. B **72**, 035406 (2005).
6. E. V. Charnaya, T. Loeser, D. Michel, C. Tien, D. Yaskov, Yu. A. Kumzerov. Phys. Rev. Lett. **88**, 097602 (2002).

Investigation of transmission characteristics of active ring resonator on nonlinear ferrite-ferroelectric delay line

Vitalii Vitko, Andrey Nikitin, Alexey Ustinov

Department of Physical Electronics and Technology, St. Petersburg Electrotechnical University "LETI", 197376 St. Petersburg, Russia

E-mail: vitaliy.vitko@gmail.com

Introduction

Recently the interest to the active ring resonators (ARRs) on spin-wave delay lines incredibly grow up due to a wide variety of unique nonlinear and dispersion properties dependent on choice of the mutual orientation of the magnetic film and the external magnetic field. The ARRs are used to observe a wide variety of nonlinear phenomena such as generation of monochromatic or chaotic signals, the bright and dark spin-wave solitons [1, 2], as well as bistability and foldover effects due to positive or negative frequency shifts [3-6], and also to neuromorphic calculations based on the principles of magnonics [7,8].

Note that the tuning of the resonance modes in spin-wave ARR is realized only by changing the external magnetic field. This method is characterized by low speed and high power consumption. Well known that an utilization of layered ferrite-ferroelectric (FF) structures allow one to realize a rapid electrical tuning of the spectrum of spin-electromagnetic waves (SEW) [9] as well as to observe the nonlinear effect such as bistability [10]. Studies of the transmission characteristics of ARR on FF delay lines have been carried out only in the linear regime [11]. The purpose of this work is to investigate the transmission characteristics of a nonlinear ferrite-ferroelectric ARR.

Numerical simulation of dispersion and transmission characteristics

Consider the ARR on FF structure shown in Fig. 1. Two directional couplers are used for the microwave signal input and output. A microwave amplifier and a tunable attenuator are used to control the power level of the circulating signal. The FF structure is magnetized to saturation by a homogeneous external magnetic field perpendicular to the direction of the wave propagation in order to realize the conditions for surface SEW propagation [12].

Following the Ref. [6] the theoretical model described dispersion and transmission characteristics ARR on FF structure have been developed. During the consideration both the electrical nonlinearity of the ferroelectric layer and the magnetic nonlinearity of spin waves in a ferrite film have been taken into account. The wave nonlinearity in the ferroelectric structure is manifested due to the dependence of the dielectric permittivity of the ferroelectric layer on the external electric field [13]. The nonlinearity of spin waves is described qualitatively in accordance with the Landau-Lifshitz equation through a change in the length of the magnetization vector **M** of a ferrite film with an increase in the amplitude of spin waves [14]. Nonlinear dynamic in FF structures are caused simultaneously by changes in the electric field and the amplitude of spin waves [15].

The numerical simulation has been carried out for the following parameters: thickness of ferrite layer was 5.54 μm, saturation magnetization was 1750 G, half-width of the ferromagnetic resonance curve was 0.5 Oe, the distance between antennas was 3.5 mm, the ferroelectric layer thickness was 250 μm, and dielectric permittivity was varied from 1500 to 1300. Following the work [6] in order to achieve the high nonlinear coefficient the external magnetic field was varied from 3200 Oe to 3203.6 Oe. In calculation, the input power is assumed to be -20 dBm. As is known, the SEW dispersion characteristic in two-layered FF

structure consists of two dispersion branches. We consider the lower dispersion branch in order to observe the tuning by both the electric and magnetic fields.
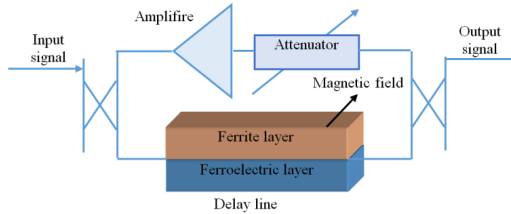
Figure 1. ARR on the FF structure

Fig. 2. shows the results of numerical simulation of nonlinear dispersion and transmission characteristics. The dispersion and transmission characteristics corresponding to the linear regime are shown by dotted lines. Solid lines show the characteristics calculated for various magnetic field (see Fig. 2 (a) and (b)) and various dielectric permittivity (see Fig. 2 (c) and (d)). The magnetic nonlinearity is dominant at low input signal power. It manifests itself on the dispersion characteristics as negative nonlinear frequency shift (see Fig. 2 (a)). The transmission characteristic becomes two-valued slightly above the threshold value (see the hysteresis loops in Fig. 2 (b) and (d)). The hysteresis loops on the nonlinear transmission characteristic are followed in counterclockwise direction as shown by the arrows in Fig. 2 (b) and (d). One can see in Fig. 2 (a) that increase in the external magnetic field leads to the shift of the dispersion branch to the high frequencies. The increase in external magnetic field by 3.6 Oe leads to frequency shift of the resonance mode from 11.15 GHz to 11.16 GHz, which corresponds to the intermodal frequency range of 10 MHz. One can see in Fig 2 (c) and (d) that the variation in the dielectric permittivity from 1500 to 1300 leads to decrease in the level of the transmission characteristic and a narrowing of the hysteresis from 3 MHz to 1 MHz. In addition, the electric tuning of the resonance mode is 5 MHz.
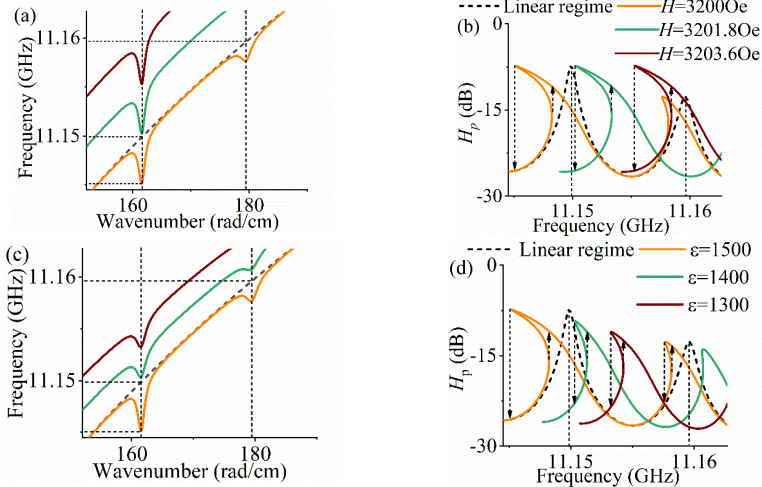
Figure 2. Fragments of the nonlinear dispersion and transmission characteristics of ARR on FF structure for various magnetic field (a) and (b), respectively, as well as for various dielectric permittivity (c) and (d), respectively.

Conclusion

The numerical calculation of nonlinear transmission characteristics of ferrite-ferroelectric ARR is carried out. It is shown that an increase in the amplitude of the microwave signal leads to a negative nonlinear frequency shift of the resonance modes. The transmission characteristic becomes two-valued slightly above the threshold value. The hysteresis loops on the nonlinear transmission characteristic are followed in counterclockwise direction. The increase in external magnetic field from 3200 Oe to 3203.6 Oe leads to frequency shift of 10 MHz, which corresponds to the intermodal range. The variation in the dielectric permittivity from 1500 to 1300 allows one to tune the resonance mode to 5 MHz. However, it leads to decrease in the level of the transmission characteristic and a narrowing of the hysteresis from 3 MHz to 1 MHz. Dual electronic tuning allow one to accurately adjust the resonance mode frequency as well as to control the frequency range of the hysteresis on the nonlinear transmission characteristic.

Acknowledgments

References

1. B. Ustinov et al. – *Phys. Rev. B,* 104 (14), L140410 (2021).
2. M. Wu. – *Phys. Solid State*, 62, 163-224 (2010).
3. V. V. Vitko et al. – *J Phys Conf Ser,* 2103 (1), 012059 (2021).
4. V. V. Vitko et al. – *IEEE Magn. Lett.,* 9, 1-4 (2018).
5. P. A. P. Janantha, B. Kalinikos, M. Wu. – *Phys. Rev. B,* 95, (6), 064422 (2017).
6. V. V. Vitko et al. – *Eur. Phys. J. Plus,* 137 (9), 1010 (2022).
7. S. Watt, M. Kostylev, A. B. Ustinov. – *J. Appl. Phys.,* 129 (4), 044902 (2021).
8. A. Nikitin et al. – *J. Appl. Phys.,* 131 (11), 113903 (2022).
9. V. E. Demidov et al. – IEEE Trans Microw Theory Tech, 51 (10), 2090-2096 (2003).
10. Y. K. Fetisov et al. – *Appl. Phys. Lett.*, 113 (2), 022903 (2018).
11. A. Nikitin et al. – *Tech. Phys.,* 57, 994-997 (2012).
12. A. Nikitin et al. – *J. Appl. Phys.,* 122 (1), 014102 (2017).
13. G. A. Smolensky et al. Physics of ferroelectric phenomena (in Russian). – Science. Leningrad, 1985.
14. D.D. Stancil and A. Prabhakar. Spin Waves: Theory and Applications – Springer, NY, 2010.
15. M. A. Cherkasskii, A. A. Nikitin, B. A. Kalinikos. – *J. Exp. Theor. Phys.,* 122, 727-733 (2016).

On the possibility of using nuclear magnetic resonance to create a quantum computer based on a top-down approach

V.K. Voronov

Irkutsk National Research Technical University, 664074, Irkutsk, Russia
E-mail: vladim.voronov1945@yandex.ru

Introduction

The report proposes to substantiate the use of the phenomenon of nuclear magnetic resonance (NMR) to solve problems related to the creation of true quantum computers. In this regard, it should be noted that an elementary quantum algorithm was implemented for the first time with the help of NMR. An elementary version of Shor's algorithm was also implemented in a quantum NMR processor containing seven q-bits. In the late nineties of the twentieth century - the beginning of the twenty-first century, the use of NMR to solve the problem of creating a quantum computer began to be considered unpromising. The scientific achievements of the last twenty years or so allow us to return to the idea of using the NMR phenomenon at a new level to solve the problem associated with the design of a quantum computer. Itis proposed to do this using NMR signals transformed by the phenomenon of chemically induced dynamic polarization of nuclei.

Fundamental capabilities of NMR in solving the problem of creating a cable-stayed processor

All (or almost) of the research carried out to date related to the creation of a quantum computer is based on the search for suitable individual quantum objects. Therefore, we can talk about the use of the ideology "from below to the top". It is believed that the creation of a really working quantum processor on the basis of such individual objects (qubits), suitable for the implementation of the quantum counting procedure, is a matter of technique. There are a number of problems along the way (in particular, scaling and decoherence problems) that prevent (at least for now) a successful solution to this problem. Since the substantiation of the idea of a quantum computer, many different compounds have been synthesized to date, many different materials have been created, including two-dimensional materials (the first among them is graphene). The question arises: "Is it possible to try to use them in order to a priory creates the necessary mathematical resource, the elements of which, while remaining within the laws of quantum physics, could be used in calculations?" If we proceed from a positive answer, it should be concluded that they should be analogues of the elements of a classical computer, i.e. first of all they could act as triggers. That's how we come to the top-down idea. Only now they must be nanotriggers, i.e. elements functioning on the basis of the laws of quantum physics. The most complete one of the possible variants of a quantum processor based on the "top to bottom" approach is set out in the works [1 - 3]. Their proposed method of constructing a true quantum computer does not replace, much less abolish, the bottom-up approach. It's just another way to create a device that performs computational processes using the law and the provisions of quantum physics. The fundamental condition in our case should be the periodic appearance in a sample in a magnetic field for some time of a paramagnetic particle - a radical in which there is an ultrafine or electron-nuclear interaction between the spins of resonant nuclei and an unpaired electron spin. The result of this is, ultimately, a characteristic transformation of the NMR spectrum due to the phenomenon of chemical polarization of nuclei [4]. This fact schematically reflects Fig. 1a. It presents a signal of proton magnetic resonance from CH_3 group under conditions of chemically polarized resonant nuclei [4].

CH₃

a	*b*
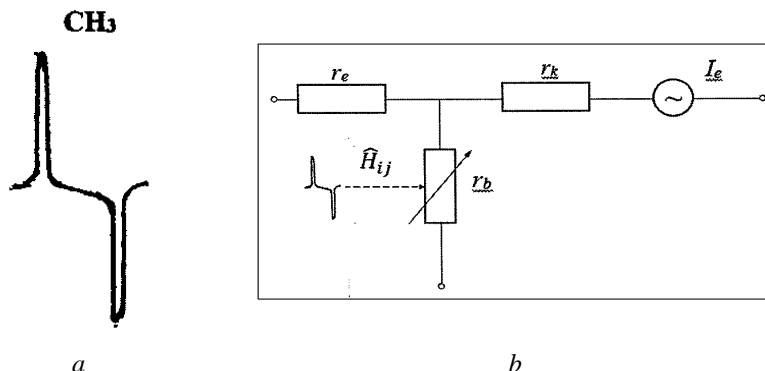
Fig. 1. (a) NMR signal of CH₃ protons under conditions of chemically polarized resonant nuclei; (b) a simplified equivalent circuit for including a nanotransistor with a control quantum dot $\hat{H}_{ij}$ in the base circuit (the indices correspond to the emitter – e, collector – k, base – b).

The above-mentioned transformation of the NMR spectrum is a consequence of the ultrafine interaction, which is described by a member of the Hamiltonian species $\hat{H}_{ij} \sim J_i J_k$ (here i refers to the spins of electrons, k to the spin spins of nuclei, J is the spin-spin bond constant of the corresponding electrons and nuclei. It will change the magnetic field at a frequency corresponding to the transition between the two states (Fig. 1b). In turn, this will lead to a periodic change in the current that make up the nanotrigger. The nanotrigger proposed herein can ultimately be used to perform all those logical operations on which the computational process is based. Such a nanotrigger is essentially an inverter capable of independently performing the logical negation operation of NOT. Adding new elements to it ensures the implementation of other logical operations necessary for the execution of the account. The device created in this way is an additional electronic unit built into a classical computer. Its purpose is, first of all, to expand the capabilities of existing computers in solving problems related to the analysis of a large amount of data bank.

Conclusion

Scientific achievements of the last twenty years or so allow us to return to the idea of using the NMR phenomenon to create a true quantum computer. It is proposed to do this using a top-down approach. It allows you to create a device that includes a block containing about 1010 nanotriggers based on nanoribbons of a two-dimensional material, in particular, graphene. These nanotriggers should act as qubits - bits of quantum counting. Each nanotrigger is controlled by a quantum dot acting on the principle of self-organization. The control point has two states with substantially different magnetic properties. It is created on the basis of a substance whose molecules are characterized by intramolecular rearrangement. From nanotriggers, a logical block with the property of reversibility is formed in order to perform the logical operations underlying quantum computing. To do this, you need to control the states of the qubit system. It is shown that it can be carried out using the phenomenon of chemical polarization of nuclei, realized in specially selected conditions of NMR detection. An equivalent scheme of a nanotrigger with a control element in the base circuit is described, which is essentially a ready-made inverter capable of independently performing a logical operation NOT. Adding new elements to such a nanotrigger ensures the implementation of the logical operations necessary for carrying out other logical operations.

References

1. V.K. Voronov Quantum-dot Controlled Electronic Block Triggering a Quantum Computation Procedure. International Journal of Information Technology and Computer Science. 2020; v.12, p. 42-48.
2. V.K. Voronov, O.V. Dudareva, L.A. Gerashchenko 2D Material-based Quantum Logic Gate Operating Via Self Organization of Quantum Dots. Global Journal of Science Frontier Research: A. 2020, v. 20, p.13-20.
3. V.K. Voronov. The Application of Generalized Rayleigh Equation for Description of Periodic Intramolecular Rearrangements, Including Valence Tautomerism. International Journal of Theoretical Physics. 2021, v. 60, p. 924–928
4. E.G. Bagryanskaya, R.Z. Sagdeev, Dynamic and stimulated nuclear polarisation in photochemical radical reactions, Russ. Chem. Rev. 2000, v. 69 (11), p. 925–945.

Applied possibilities of using the ^{35}Cl NQR line in KClO$_3$.

Timothey Zhivotikov[1], Anton S. Mazur[2], Alexandr V. Ievlev[3]
[1]Special Educational and Scientific Center "Academic Gymnasium named after D.K. Faddeev" of Saint-Petersburg State University, Saint Petersburg, Russia
[2]Resourse center MRMI of Research park Saint-Petersburg State University, Russia
[3]Department of Nuclear Physics Research Methods, Saint Petersburg State University, 199034, 7/9, Universitetskaya nab., Saint Petersburg, Russia
E-mail: a.ievlev@spbu.ru

Introduction

One of the radio frequency methods for studying the physicochemical properties of substances in a solid state of aggregation is the method of Nuclear Quadrupole Resonance (hereinafter referred to as NQR). Due to the high resolution of radio frequency methods, their use allows both scientific research and the use of the NQR method to solve various applied problems. The method is based on the fact that the frequency of the NQR spectral line, as well as its shape, directly depends on the structure of the crystal lattice, i.e. the nearest environment of an atom whose nucleus has a quadrupole magnetic moment. Nuclei with a spin greater than or equal to 1 have this property. Due to this dependence on the nearest environment, the NQR line has many experimental applications. In this work, the dependence of the NQR line frequency of the ^{35}Cl isotope on temperature is experimentally recorded, i.e., in fact, the kinetic energy of vibrations of the nearest environment of the Chlorine atom in the crystalline powder of Bertolet's salt KClO$_3$.

Experiment section

For For this series of experiments, about 800 milligrams of salt were used. The substance was packed in a 5 mm glass flask and placed in the resonant circuit of the sensor of the Tecmag Redstone NMR/NQR spectrometer, which is located in the MRMI resource center of the St. Petersburg State University Science Park. By recording the NQR spectra of chlorine with a change in temperature in the sensor, a set of their resonant frequencies was obtained. Initially, the temperature was recorded by a thermocouple built into the sensor, and in order to achieve uniform heating of the sensor and the sample with a change in temperature, the wait was at least 10 minutes. Figure 1 shows a set of spectra recorded at different temperatures, in the range from -35 to 105 ˚C. It can be seen that the NQR line shifts towards lower values in frequency with increasing temperature. By approximating the spectra by lines of the Lorentz form, the positions of the centers of the spectral lines were determined with high accuracy.

To influence an external magnetic field, a self-made solenoid with an inner diameter of 5 cm, a wire thickness of 0.75 mm, a solenoid length of 13 cm, and a wire wound in four layers was used. To create a direct current in the solenoid, a current source was used in the range from 0 to 10 A with the possibility of stabilization with an accuracy of 0.01 A. The radio-frequency coil of the resonant circuit was placed perpendicular to the direction of the magnetic field vector of the solenoid. In this case, it should be taken into account that the asymmetry parameter of the electric field gradient on the chlorine nuclei in Bertolet's salt is equal to zero.

The obtained experimental points and the data presented in the literature [1] are shown in Figure 2. (The graph is presented as a dependence of temperature on frequency for further processing.) Each set of points is extrapolated by parabolas (formula 1), which are also shown in Figure 2. Parameters the obtained curves are presented in Table 1.

$$f = f_0 + k(T - T_0)^2 \qquad (1)$$
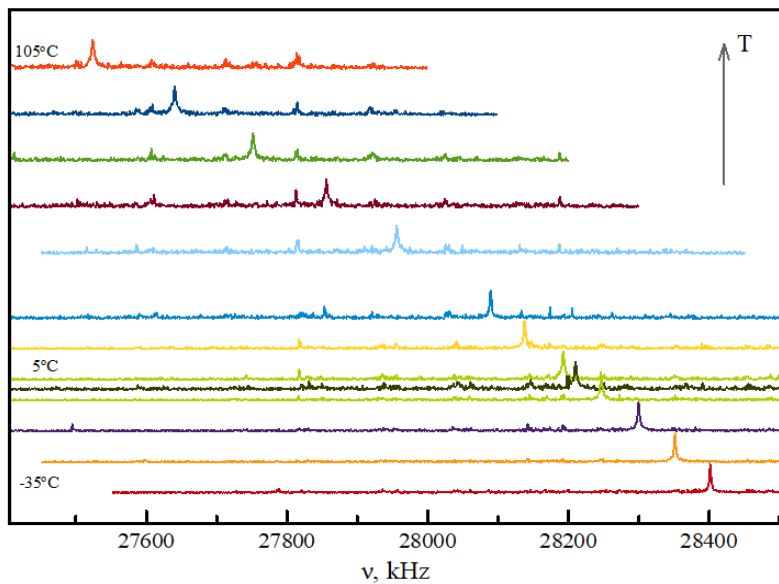
Figure 1. A set of spectra at different temperatures.
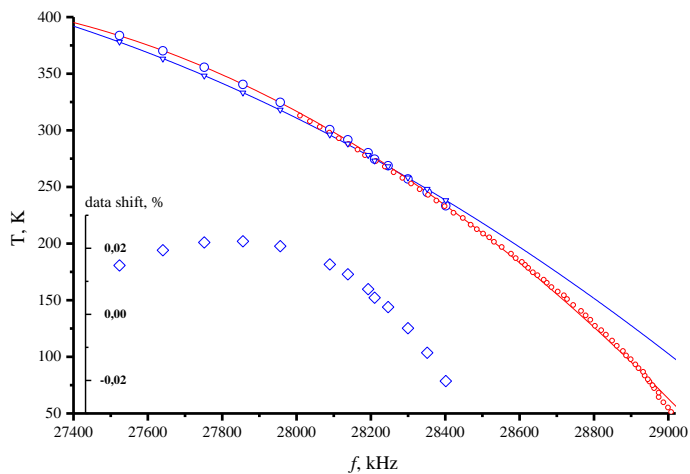
Figure 2 Temperature dependences of ^{35}Cl NQR frequencies (red circles, published data; blue triangles, experimental data; blue circles, corrected experimental data). The inset shows the amount of adjustment relative to the original data as a percentage.

Table 1. Coefficients of extrapolation curves of literature and experimental data.

	f_0, kHz	$k \cdot 10^{-6}$	T_0, K
Literature [1]	26850	-76.9	418.4
Experiment	26212	-45.5	456.1

It can be seen that for the experimental data there is a deviation from the curve obtained by processing the literature data. Using the results of data processing, it is possible to correct the experimental temperature values obtained by the instrument's thermocouple. The conversion results are also shown in Figure 2. The inset in Figure 2 shows the amount of temperature correction required.

It is known that when an external magnetic field is applied in NQR studies, the effects of Zeeman splitting appear and the shape of the NQR line changes [2]. The NQR line is broadened and, relative to the central resonant frequency (f_0), features appear on it at frequencies (f_Z) proportional to the magnitude of the external magnetic field (H) and the value of the gyromagnetic ratio (γ) of the nucleus under study:

$$f_0 - f_Z = \pm\gamma H \qquad (2)$$

Figure 3 shows a set of NQR spectra on ^{35}Cl nuclei in Berthollet salt obtained at different currents in the solenoid of an external magnetic field. Analyzing the shape of the spectra, it was possible to plot the dependence of the external magnetic field strength on the current, which is shown in Figure 4. It can be seen that at current values from 0 to approximately 0.3 A, the dependence of the field strength on the current applied to the solenoid has a linear dependence. At high values of the current, the determination of the frequencies f_Z is conditional, since additional effects begin to appear that affect the shape of the spectrum.
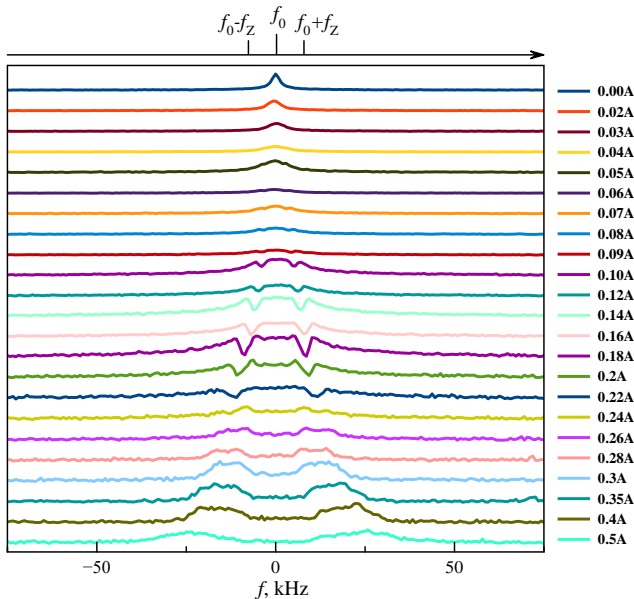
Figure 3. A set of NQR spectra on ^{35}Cl nuclei in KClO$_3$ at different currents in the solenoid.
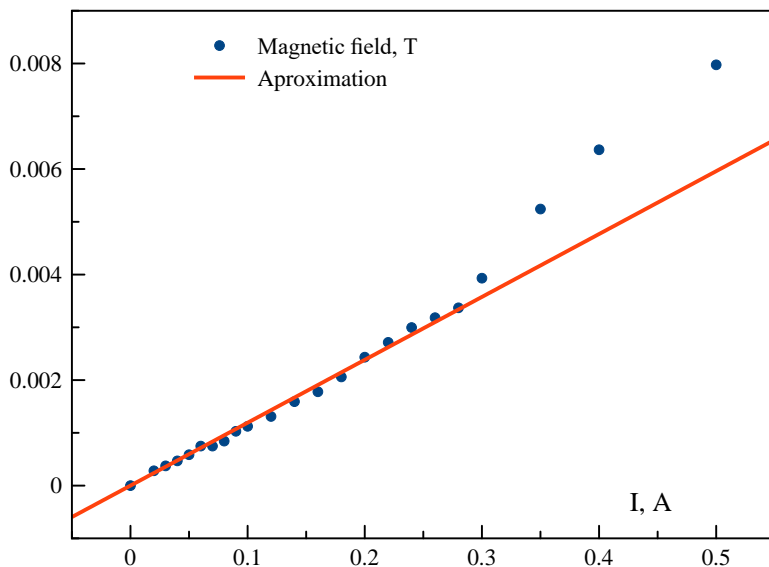
Figure 4. The dependence of the magnitude of the magnetic field on the current.

Conclusion

Thus, as a result of NQR studies of Bertolet's salt in a wide temperature range, it was shown that there is a correlation between the resonance frequency and the temperature at which the spectra were recorded. In this case, the dependence of the frequency on temperature is well described by a second-order polynomial (parabola), which is in good agreement with the available literature data. By processing the data of this curve, it is possible to correct the thermocouple of the NQR spectrometer in order to refine subsequent temperature studies in other experiments.

In turn, the application of the NQR method for calibrating the magnetic field strength of the solenoid can be used in parallel, for example, with the use of Hall sensors, especially at low magnetic field strengths. In addition, it was possible to estimate the maximum limit of the magnetic field strength for NQR on ^{35}Cl nuclei in Bertolet's salt, where this calibration technique is applicable: it is approximately 3.3 mT.

Acknowledgments

References

1. L. PMeasurement of temperature and temperature gradient in millimeter samples by chlorine NQR/ Janko Lužnik, Janez Pirnat, Zvonko Trontelj / 2009Applied Physics A 96(4):1023-1026 DOI: 10.1007/s00339-009-5137-y
2. R. B. Creel, S. L. Segel, L. A. Anderson. – *J. Chem. Phys.*, **50**, 4908-4913 (1969).

Development and characterization of novel ultrafiltration membranes based on cellulose acetate modified with Zn-based MOFs

Andrey A. Zolotarev[1], Anna I. Kuzminova[1], Maria E. Dmitrenko[1], Roman R. Dubovenko[1], Margarita E. Puzikova[1], Anton S. Mazur[1], Anastasia V. Penkova[1]
[1]*Saint Petersburg State University, Saint-Petersburg, Russia*
E-mail: andrey.zolotarev@spbu.ru
https://go.spbu.ru/rgpenkova

Introduction

Ultrafiltration is the most actively applied membrane method in various industrial fields, such as food, chemical, microbiological, water treatment, etc. The creation of novel ultrafiltration membranes with improved transport and antifouling properties is required due to the constant growth of requirements for the purity of the resulting product and tightening environmental regulations. Nowadays, active research is ongoing for the use of cellulose acetate (CA) biopolymer as a matrix for ultrafiltration membranes. However, membranes based on CA have the disadvantage as decreased filtration productivity due to significant membrane fouling. To solve this problem, the modification of CA membranes was carried out with synthesized porous Zn-based metal organic frameworks (MOFs).

In this work, porous membranes based on CA modified with Zn-based MOFs (Zn(SEB), Zn(BDC)Si and Zn(BIM)) were developed for the enhanced ultrafiltration. The influence of various pore-forming agents, membrane formation conditions, and content of Zn-MOFs on the structure of ultrafiltration CA membranes was studied. The structure of the developed membranes was investigated by NMR spectroscopy, scanning electron and atomic force microscopies. The membrane surface hydrophilicity was evaluated by the contact angle measurements. The membrane performance was tested in ultrafiltration of industrially important feed - bovine serum albumin (BSA) solution. It was found that modification with Zn-MOFs significantly improved the transport and antifouling properties of ultrafiltration CA membranes.

Acknowledgments

Poems about School

* * *

Чижик-Spinus, где ты был?
– «Я сигнал за хвост ловил!
Сделал я ему "Фурье" –
Закружилось в голове!»

Цели Spinus'а просты:
Дать научные мосты!
Пусть у вас здесь будет шанс
Пообщаться «в резонанс»!

В Школе здесь научат всех
Сочетать с наукой смех,
Дискотеки с Э-Пе-эР,
Я-Ка-эР и Я-эМ-эР!

В Школе много новых лиц,
Будем превращать их в птиц:
Вдруг хотя б одной из ста
Дастся «Нобель-высота»!

2010

* * *

Spinus, Spinus, where you were?
Did you dive in the Resonance world?
– "Yes! I dived with my great joy –
Resonance is a pleasant toy!"

"Spinus" school invited you
To look for a knowledge clue.
We will show the signal birth
In the field of our Earth!

If you wish to have success,
At the School achieve progress!
We will teach you all to fly
In the scientific sky!

We desire you to get
Many victories-побед!
It will be a good surprise
If you catch the Nobel prize!

2010

Author Index

Magnetic Resonance and its Applications
Proceedings

Saint Petersburg State University
March 27 — 30, 2023